Minerals Research Institute
of Western Australia

REPORT NO. 10502

CuBAS - Structural and sedimentological reconstruction and fluid flow simulations for copper exploration in the Yeneena Basin – Paterson Orogen, WA

Results of research carried out as MRIWA Project M10502

at CSIRO and Curtin University

by

Heather A. Sheldon, Chirantan Parui, Thomas Poulet, Susanne Schmid, Giovanni Spampinato, Valentin Zuchuat, Christopher Kirkland, Janne Liebmann

April 2026

Distributed by: MRIWA
1 Adelaide Terrace
Perth WA 6000
to which all enquiries should be addressed

Acknowledgements

MINISTER FOR MINES AND PETROLEUM

Hon. David Michael MLA

CHIEF EXECUTIVE OFFICER, MINERALS RESEARCH INSTITUTE OF WESTERN AUSTRALIA

Nicole Roocke

[LEAD POSITION OF PROJECT ORGANISATION/DEPARTMENT], [ORGANISATION/DEPARTMENT NAME]

Principal Research Scientist at CSIRO Mineral Resources

LEAD INVESTIGATOR

Susanne Schmid (2023-2025); Thomas Poulet (since 2025)

AUTHORS:

Heather A. Sheldon, Chirantan Parui, Thomas Poulet, Susanne Schmid, Giovanni Spampinato, Valentin Zuchuat, Christopher Kirkland, Janne Liebmann

REFERENCE

The recommended reference for this publication is:

Sheldon, H. A., Parui, C., Poulet, T., Schmid, S., Spampinato, G., Zuchuat, V., Kirkland, C. & Liebmann, J. (2025). CuBAS - Structural and sedimentological reconstruction and fluid flow simulations for copper exploration in the Yeneena Basin – Paterson Orogen, WA. Results of research carried out as MRIWA Project M10502. MRIWA report 10502, 162pp. DOI 10.71342/106693231035

This report is available from the national Library of Australia

PARTICIPATING ORGANISATIONS

KEYWORDS AND TAGS

Sedimentary-hosted copper, mineral system, basin analysis, fluid flow modelling, Yeneena Basin, Paterson orogen

DISCLAIMER

CSIRO advises that the information contained in this publication comprises general statements based on scientific research. The reader is advised and needs to be aware that such information may be incomplete or unable to be used in any specific situation. No reliance or actions must therefore be made on that information without seeking prior expert professional, scientific and technical advice. To the extent permitted by law, CSIRO (including its employees and consultants) excludes all liability to any person for any consequences, including but not limited to all losses, damages, costs, expenses and any other compensation, arising directly or indirectly from using this publication (in part or in whole) and any information or material contained in it.

CSIRO is committed to providing web accessible content wherever possible. If you are having difficulties with accessing this document please contact csiro.au/contact.

ACKNOWLEDGEMENT OF COUNTRY

CSIRO acknowledges the Traditional Owners of the lands, seas and waters of the area that we live and work on across Australia and pays its respects to Elders past and present. CSIRO recognises that Aboriginal and Torres Strait Islander peoples have made, and will continue to make, extraordinary contributions to Australian life including in cultural, economic, and scientific domains.

Published 2026 by the Minerals Research Institute of Western Australia

This report is published in digital format (PDF) and is available online at

https://www.mriwa.wa.gov.au/research-projects/project-portfolio/

CONTACT

Minerals Research Institute of Western Australia

1 Adelaide Terrace

Perth WA 6000

+61 8 6180 4340

mail@mriwa.wa.gov.au

https://www.mriwa.wa.gov.au/

Executive Summary

Copper (Cu) plays a fundamental role in modern society due to its critical importance in enabling a clean energy future. Although sedimentary-hosted Cu deposits account for ~14% of global Cu production (the second-highest contributor after porphyry-Cu), they typically have higher ore grade and medium-high tonnage, making them an important resource type for Cu. Current exploration for this resource type has become challenging as undiscovered deposits are increasingly limited to areas deeper and buried under thick cover (sedimentary rock units or regolith), making them difficult to detect using traditional approaches (e.g., surface mapping, anomalies in soil and stream sediments). To address this issue, we applied a mineral systems approach that integrates components from basin analysis, enabling predictive targeting for sedimentary-hosted mineral systems. The workflow was tested using the Neoproterozoic Yeneena Basin (Paterson Province, Western Australia) as a case study to evaluate its effectiveness in reducing the exploration search space for sedimentary-hosted Cu.

The Yeneena Basin formed in the Tonian Period in response to widespread NE–SW directed crustal extension. It was subsequently inverted during the Miles and Paterson crustal shortening events. Multiple mineralisation events occurred during basin development and deformation, creating the Nifty Cu deposit as well as numerous known sub-economic occurrences of Cu mineralisation. Mineralisation is largely hosted in the Broadhurst Formation, a fine-grained organic-rich marine mudstone.

The project was organised in three modules demonstrating different aspects of the workflow: (1) Data collection and analysis to determine the present-day structural and sedimentological framework of the Yeneena Basin; (2) 4D reconstruction of the Yeneena Basin; and (3) Fluid flow modelling.

Module 1 included (i) geophysical interpretation of present-day basin architecture; (ii) structural analysis of the mapped surface geology and drill core data; and (iii) geochronology to refine the timing of sediment deposition and the Miles event. Depth to basement was estimated by geophysical inversion combined with previous interpretations and other constraints, resulting in a 3D surface that was utilised in subsequent components of the project. Magnetic and gravity geophysical data were reprocessed to facilitate identification of faults, which were combined with previously mapped structures to produce a comprehensive fault network map for the Yeneena Basin and surroundings. Previously published structural data from surface geological mapping and logging of oriented drill cores were combined with new structural observations from nine oriented drill cores that had not previously been logged. The combined dataset revealed folding consistent with NE-SW shortening during the Miles event. Uranium-Lead (U-Pb) dating of calcite provided a minimum depositional age of 927 ± 33 Ma for the Broadhurst Formation.

Module 2 used (i) subsidence modelling, (ii) construction and restoration of cross-sections and (iii) stratigraphic forward modelling to reconstruct the basin's evolution through time. Subsidence modelling showed that the Yeneena Basin likely formed in an extensional setting akin to a passive margin, with rapid subsidence during deposition of the Coolbro Sandstone waning to a much lower subsidence rate during deposition of the Broadhurst Formation and overlying units.

The outputs of Module 1 informed the construction of five NE-SW cross sections, including one through the Nifty Cu deposit. Restoration of four of these sections using the line-length balancing technique showed that NE-SW shortening during the Miles tectonic event was accommodated first by folding and later by reverse reactivation of normal faults. The restored sections reveal the existence of basement highs in the early stages of basin evolution. These highs bound a series of sub-basins, one of which hosts the Nifty Cu deposit.

Stratigraphic forward modelling was conducted on two scales, producing a large, supra-basin scale model (620 x 560 km) and a smaller, more detailed model in the area of the cross-sections from Module 2 (84 x 90 km). The large-scale model revealed aspects of the source-to-sink sediment pathways and distribution of potential Cu source and host rocks in the Yeneena Basin. This model could be used to address conceptual questions about the basin's evolution, such as the consequences of exposure or burial of the Rudall Complex during sediment deposition. The small-scale model was built using input from the structural restoration work, and provided a detailed 4D distribution of porosity and sediment types in the basin. This was used to inform the porosity-permeability distribution in a model of thermal convection in the undeformed basin (Module 3).

Module 3 used fluid flow modelling to test hypotheses regarding fluid sources and pathways in the sedimentary-hosted copper mineral system. Models explored (i) brine migration; (ii) release of fluid from an over-pressured compartment; (iii) thermal convection; and (iv) upward fluid flow in the deformed basin. Evaporites in the contemporaneous and adjacent Officer Basin were shown to be a plausible source of brine for the sedimentary-hosted Cu mineral system in the Yeneena Basin. Brine migration was shown to be highly sensitive to the dip and permeability anisotropy of the basin fill. Brine was most likely to accumulate in the sub-basin closest to the brine source, but may have reached more distant sub-basins depending on the dip and permeability of the sedimentary strata. Accurate simulation of brine migration was shown to be very challenging, but an alternative method based on analytical solutions could be used to predict brine pooling locations that may be critical for mineralisation.

Having accumulated at depth in a sub-basin, the brine would need to be mobilised upwards to account for mineralisation in the Broadhurst Formation. Modelling showed that fluid release from an over-pressured compartment could not generate sufficient upward flow to create economic mineralisation. Thermal convection may have been a viable mechanism for upward flow, with convective upwellings creating regions of fluid penetration into the Broadhurst Formation. Other mechanisms such as metamorphic fluid production or deformation-driven flow may have been active later in the basin history. A model of upward flow in the deformed basin showed that permeability enhancement (e.g., fracturing around a fault tip) and blind faults may have been required to enable fluid to penetrate into the low-permeability Broadhurst Formation in order to account for mineralisation there.

The workflow followed in this project is both sequential (i.e., the output of one step informs subsequent steps) and iterative (i.e., new insights were fed back into earlier models to improve their outputs). Fluid flow modelling was tightly integrated with other modules throughout the project. Together, the components of the workflow provide a holistic understanding of the mineral system in the Yeneena Basin. Application of this workflow to other Proterozoic basins in WA and beyond can help explorers to reduce the exploration search space for sedimentary-hosted Cu.

Table of Contents

Terms, Abbreviations and Acronyms

CSCBA: Complete spherical cap Bouguer gravity anomaly

MOOSE: Multiphysics Object-Oriented Simulation Environment - an open-source, parallel finite element framework used in this project for simulating fluid flow

MSWD: Mean square weighted deviation

RTP: Reduced to pole

SFM (method): Stratigraphic Forward Modelling - a method of simulating sediment deposition/erosion in response to basement subsidence, uplift, changing sea level and sediment supply.

SFM (model): Stratigraphic Forward Model – a model produced by Stratigraphic Forward Modelling

TMI: Total magnetic intensity

List of Figures

List of Tables

1 Introduction

The Yeneena Basin in Western Australia contains the sedimentary-hosted copper (Cu) deposit at Nifty mine (54.84 Mt at 1.41% Cu; Metals X Limited 2017), as well as numerous sub-economic prospects at Maroochydore, Ghoosewacker, Finch, and Rainbow (Reed et al. 1995; Ferguson et al. 2005). While these discoveries were made primarily through outcropping gossans and soil anomalies, current exploration within the basin remains challenging due to thick regolith cover of ~300 m (Czarnota et al. 2009). In such scenarios, employing a mineral systems approach integrating basin analysis and fluid flow modelling allows for more efficient exploration by combining geological, geochemical, and geophysical data to unravel the mineralisation processes, fertility, and timing of ore formation from metal source to sink (Figure 1; McCuaig et al. 2018). Central to this integrated approach is reconstruction of the basin's stratigraphic and structural history in four dimensions, which sheds light on fluid flow pathways, the spatial distribution of host rocks, ore-forming processes, and preservation potential (Schmid 2022). This report describes the outcomes of MRIWA project M10502, which used the Yeneena Basin as a case study to demonstrate the effectiveness of such an integrated workflow in reducing the exploration search space for sedimentary-hosted Cu.

1.1 Minerals research/industry challenge and background

Cu is extensively used in renewable energy technologies and plays a vital role in the global energy transition. The International Copper Association noted that global demand for Cu is projected to soar to around 50 million tonnes per year by 2050, which is twice as much as 2020. A recent study highlighted that with all currently identified reserves and planned projects, the projected demand can be met between now and 2035 (Guj and Schodde 2025). However, in the long run, new Cu discoveries are required to meet the net zero goal by 2050 (Guj and Schodde 2025). Cu deposits can be broadly classified into: (1) porphyry, (2) sedimentary-hosted, (3) iron oxide copper-gold, (4) volcanogenic massive sulphide, (5) magmatic deposits, and (6) others (Singer 2017). Although sedimentary-hosted Cu deposits account for ~14% of total global production (Guj and Schodde 2025), they have generally higher ore grade than porphyry Cu (~70% of total global production) with medium to high tonnage, making them an important resource type for Cu (Mudd and Jowitt 2018).

Current exploration for sedimentary-hosted Cu has become challenging as prospective new deposits are deeper and buried under thick cover – sedimentary rock units or regolith (Singer 2017) – making them difficult to detect using traditional approaches (e.g., surface mapping, anomalies in soil and stream sediments). Additionally, a lack of progress in understanding the processes involved in the formation of sedimentary-hosted Cu deposits, has resulted in poor knowledge of the critical parameters in these mineral systems.

In the Yeneena Basin multiple mineralisation events occurred during basin development and subsequent deformation, adding complexity to the mineral exploration challenge (Raye et al. 2025). The exploration industry needs a new approach to unravel these complex mineral systems and reduce the search space in potentially mineralised basins.

1.2 Objectives of the research

The overarching objective of this project is to evaluate the effectiveness of a sedimentary-hosted mineral systems workflow, one that integrates key components of basin analysis (Figure 1), in reducing the exploration search space for sedimentary-hosted Cu deposits within the Yeneena Basin. To address this broad objective, we deconstruct it into a series of targeted research questions, each designed to test specific aspects of the workflow.

In line with the project's overarching aim, a critical first step involves examining the existing geological framework of the Yeneena Basin. This step enables the integration of existing published data and knowledge into the sedimentary-hosted mineral systems workflow (Figure 1), providing both contextual grounding and empirical constraints. In doing so, it facilitates the identification of key knowledge gaps that the project seeks to address. The Geological Survey of Western Australia has mapped the Yeneena Basin at the 1:100,000 scale and has published many reports detailing its geological characteristics (Hickman and Clarke 1993; Bagas 2000; 2005; Williams and Bagas 1999). Earlier research has largely focused on the depositional environment (Kunzmann et al. 2021), depositional age of the sedimentary rocks (Maidment et al. 2008; Clark et al. 2023; Kohanpour et al. 2024), sediment provenance (Clark et al. 2023; Kohanpour et al. 2024), ore-forming processes at Nifty (Haynes and Mazzoni 1993; Anderson et al. 2001; Raye et al. 2025) and other prospects (Reed et al. 1995; Haynes and Mazzoni 1993), Cu mineralisation ages (Huston et al. 2020; Ribeiro et al. 2023; Raye et al. 2025), regional mineral systems (Gorczyk et al. 2025; Maidment et al. 2008; 2017), Proterozoic crustal evolution (Cawood and Korsch 2008; Bagas 2004), and Palaeogeographic development (Martin et al. 2017).

Despite this extensive body of work, significant knowledge gaps remain, particularly in understanding the basin’s large-scale structural framework, its sedimentary architecture, and the dynamics of fluid migration through faults and aquifers. These gaps are a barrier to predictive exploration. This project seeks to address these limitations by investigating the following research questions:

1. How did the structural architecture of the basin evolve through geological time, and what implications does this have for fluid and metal migration?
2. Can stratigraphic forward modelling effectively reconstruct the distribution of potential host and source sedimentary rocks within the basin?What insights can fluid-flow simulations provide on the pathways and migration scenarios of metal-bearing fluids within strata and fault networks?

1.3 Scope

The project utilised existing commercial, open source and CSIRO in-house tools/workflows to implement a mineral systems approach to sedimentary-hosted Cu mineralisation in the Yeneena Basin. Development of new tools or substantial modification of existing tools was out of scope for this project.

2 Project Approach and Structure

The project utilised a mineral systems approach to advance understanding of sedimentary-hosted Cu mineralisation and reduce the exploration search space in the Yeneena Basin. Mineral systems analysis involves evaluation of: 1) the source of metals, mineralising fluids, and fluid composition; 2) fluid migration pathways; 3) energy for driving fluid flow; 4) ore forming processes; and 5) residual fluid discharge (Wyborn et al. 1994; McCuaig et al. 2010; Hagemann et al. 2016). For sedimentary-hosted mineral systems the analysis must consider sedimentary facies variations, depositional environments and subsidence/burial history, as these factors influence the distribution of potential metal source and host rocks and the existence, permeability and geometry of fluid pathways. Figure 1 summarises the mineral systems analysis workflow for sedimentary-hosted mineral systems, highlighting the components that were included in this project.

The work was organised into 3 modules with associated milestones:

Module 1: Data collection and analysis to determine the present-day structural and sedimentological framework of the Yeneena Basin

- Milestone 1: Geophysical interpretation of present-day basin architecture
- Milestone 2: Collection of structural, petrophysical and sedimentological data on drill core
- Milestone 6: Geochronology to constrain sediment provenance and timing of diagenesis, metamorphism and mineralisation

Module 2: 4D reconstruction of the Yeneena Basin through time

- Milestone 3: Subsidence analysis from drill core data to understand porosity evolution and variations in basin subsidence
- Milestone 4: 2D cross sections based on structural measurements and geophysical and sedimentological interpretations
- Milestone 5: 2.5D reconstruction based on 2D cross sections, to constrain key aspects of basin architecture prior to deformation
- Milestone 7: 3D stratigraphic forward modelling to understand the distribution of potential host and source rocks in the basin

Module 3: Fluid flow modelling

- Milestone 8: 2D or 3D simulations of fluid flow through the stratigraphic framework and fault architecture of the basin through time

The modules were inter-connected, with each module providing input for the next. Strong connections between the project components enabled the researchers to deliver insights that go far beyond the outcomes of individual modules and milestones.

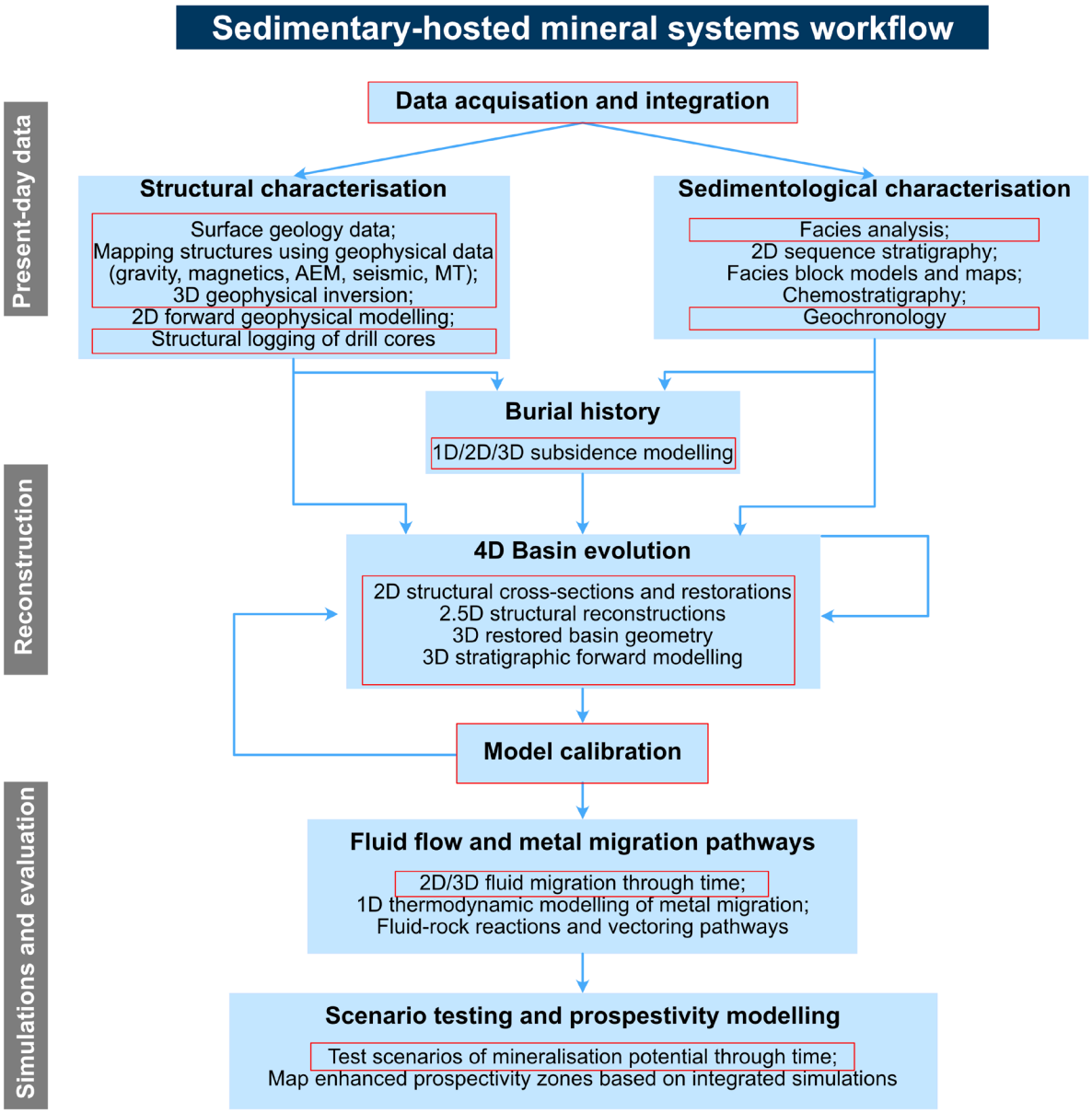

Figure 1. Analysis workflow based on a mineral systems approach for sedimentary-hosted Cu. Red boxes indicate the components that were addressed in this project.

3 Geological Background

3.1 Tectonic and magmatic history

The Yeneena Basin forms part of the Centralian Superbasin, which developed during the Neoproterozoic in response to NE–SW crustal extension across central, western, and southern Australia and comprised of four super-sequences (Walter et al. 1995). The basin formed in the Tonian Period and was situated along the eastern edge of the Fortescue Basin of the Archean Pilbara Craton, unconformably overlying the Paleoproterozoic–Mesoproterozoic Rudall Complex (Bagas 2004; Grey et al. 2005; Kohanpour et al. 2024). The Rudall Complex recorded magmatism between ~1804–1762 million years ago (Ma; Kalkan Supersuite) and ~1590–1550 Ma (Krackatinny Supersuite), as well as deformation events linked to the Parnngurr Orogeny occurring at ~1680 Ma and ~1375–1275 Ma (Gardiner et al. 2018). The Tonian Yeneena Basin developed contemporaneously to the Officer Basin to the S-SE, and is overlain by the Phanerozoic Canning Basin and other younger Mesozoic–Quaternary sequences (Figure 2).

After deposition, the Yeneena Basin and the underlying Rudall Complex underwent two major shortening events, referred to as the Miles and Paterson events. The Miles event was characterised by NE–SW directed shortening, which was accompanied by regional lower greenschist facies metamorphism (Bagas 2004), although its exact age remains debated (Kelsey et al. 2024). Argon-Argon ($^{40}Ar/^{39}Ar$), muscovite and potassium (K)-feldspar ages suggest that the deformation associated with the Miles event took place between ~680 and 630 Ma (Durocher et al. 2003). The granites of the O'Callaghan Supersuite (~654–603 Ma; Figure 2) were intruded toward the end-phase of the Miles event that resulted in contact metamorphism reaching mid-amphibolite grade (Wilson et al. 2020). The subsequent Paterson event, dated to around 550 Ma, was associated with NNE–SSW shortening (Durocher et al. 2003). In contrast to the Miles event, it did not cause any regional metamorphism within the Yeneena Basin.

3.2 Stratigraphy

The Neoproterozoic Yeneena and Officer Basins formed contemporaneously, and their respective lithostratigraphic units exhibit time-correlative relationships and lateral facies variations (e.g., Grey et al. 2005; Kunzmann et al. 2021). This suggests a shared depositional history and regional-scale sedimentary processes operating across both basins during their formation, with the Officer Basin representing the proximal part of the source-to-sink system, whereas the Yeneena Basin corresponds to its more distal part (Grey et al. 2005).

3.2.1 Yeneena Basin

The sedimentary fill of the Yeneena Basin is subdivided into two groups: the Throssell Range Group and the overlying Lamil Group (Figure 2; e.g., Grey et al. 2005).

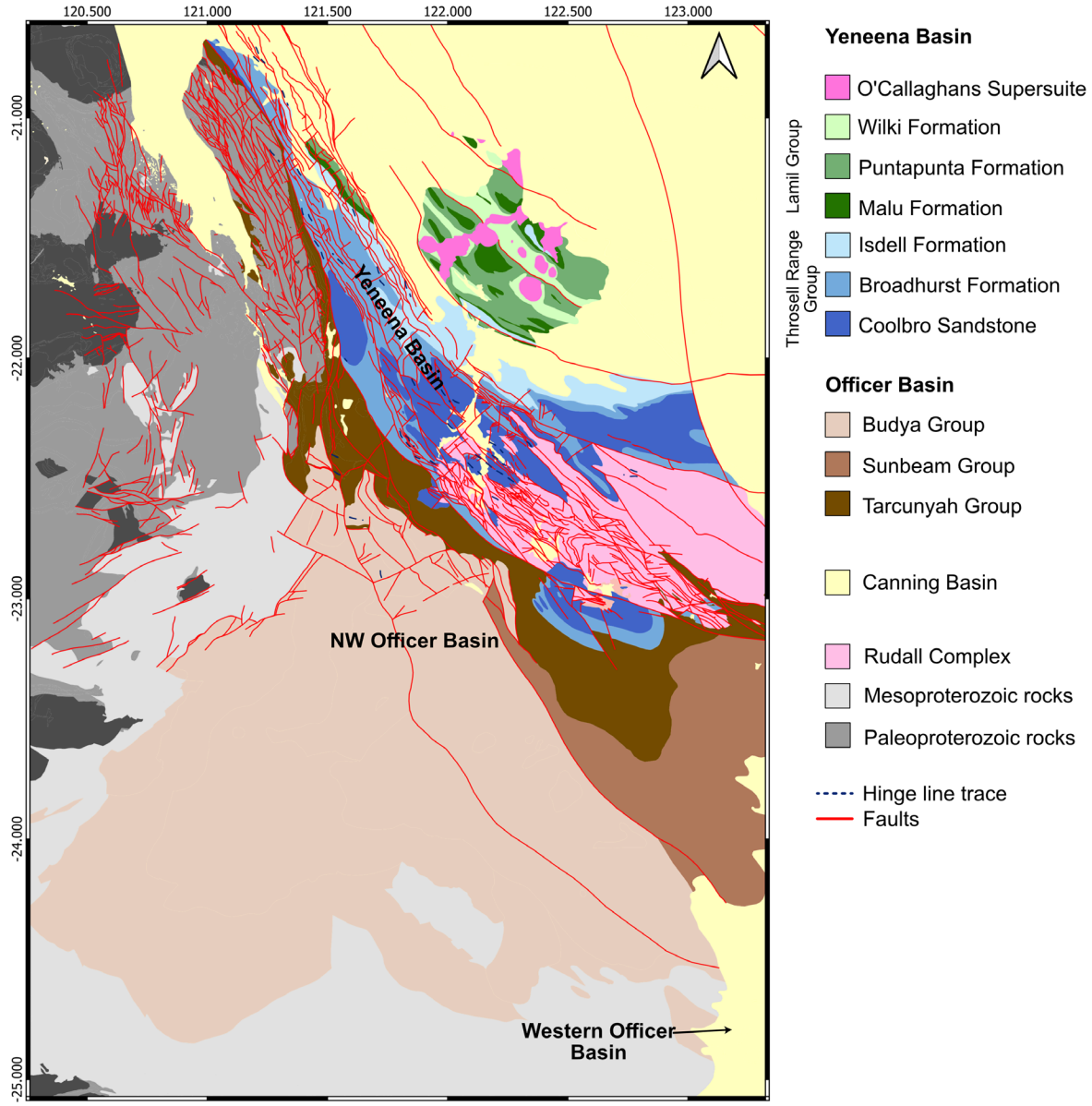

Figure 2. Geological map of the Yeneena Basin and the adjacent geological regions at 1:500000 scale (https://geoview.dmp.wa.gov.au/geoview/).

The Throssell Range Group comprises three stratigraphic units: the Coolbro Sandstone, Broadhurst Formation, and Isdell Formation (Figure 2). At the base lies the Coolbro Sandstone, which averages ~2 km in thickness but locally attains up to ~4 km (Czarnota et al. 2009; Hickman and Clarke 1993; Kohanpour et al. 2024). The sediments were deposited in a fluvial and fluvial-deltaic depositional environment and this unit is characterised by polymictic conglomerate, sandstone, siltstone, and shale. Detrital zircon U–Pb analyses indicate maximum depositional ages of ~980 Ma (Maidment et al. 2008), as well as ~923 ± 9 Ma and ~911 ± 23 Ma (Clark et al. 2023). Conformably overlying this succession is the Broadhurst Formation, around 1 km thick (Czarnota et al. 2009; Hickman and Clarke 1993; Kohanpour et al. 2024). It represents a marine environment and includes organic-rich shale, siltstone, dolostone, and limestone (Grey et al. 2005; Hickman and Clarke 1993). Detrital zircon geochronology constrains deposition to younger than ~960 ± 21 Ma (Kohanpour et al.

2024). This formation hosts the Nifty Cu deposit as well as other sedimentary-hosted Cu mineralisation within the basin. The uppermost unit, the Isdell Formation, also ~1 km thick, rests conformably above the Broadhurst Formation (Hickman and Clarke 1993). It mainly consists of marine dolomitic limestone and dolostone, with minor shale. Carbonate Pb–Pb isochron dating suggests a diagenetic age of ~858 ± 29 Ma (Maidment et al. 2008), and U–Pb zircon ages from a mafic sill intruding the formation yield ~837 ± 6 Ma, placing a lower limit on the depositional age (Maidment et al. 2008).

The Lamil Group conformably overlies the Throssell Range Group and is subdivided into the Malu, Puntapunta, and Wilki formations (Bagas 2000). The Malu Formation is ~1.2 km thick and dominated by shallow-marine sandstone interbedded with minor siltstone and shale (Bagas 2000). U-Pb detrital zircon dating constrains the maximum depositional age to ~920–915 Ma (Maidment et al. 2008), or 927±9 Ma and ~855±19 Ma (Kohanpour et al. 2024). The Telfer and Winu Au-Cu deposits are hosted within this unit (Figure 2; Dalstra et al., 2023; Schindler et al., 2016). The Puntapunta Formation conformably overlies the Malu Formation and is ~1 km thick (Bagas 2000). It mainly comprises shallow-marine dolomitic sandstone, siltstone, shale, limestone, and dolorudite (Bagas 2000). U-Pb detrital zircon ages indicate maximum depositional ages of ~845 Ma (Maidment et al., 2008), ~898±20 Ma (Clark et al. 2023), and 889±27 to ~825±33 Ma (Kohanpour et al. 2024). A monzonite intrusion provides a minimum depositional age of ~835±4 Ma (Maidment et al. 2008). The Wilki Formation conformably overlies the Puntapunta Formation and is ~1.4 km thick (Bagas 2000). It consists of organic-rich shale, siltstone, and sandstone (Bagas 2000). While the upper age limit of the Yeneena Basin stratigraphy remains poorly-constrained, these sedimentary units are part of Supersequence 1 of the Centralian Superbasin (Grey et al. 2005). This broader regional correlation provides an approximate upper age limit of 720 Ma (Munday et al. 2022), implying that sedimentation in the Yeneena Basin may have ceased by that time.

3.2.2 Officer Basin

In the Officer Basin, the Tonian succession is subdivided differently between the western and northwestern regions (Grey et al. 2005). We briefly summarise them here.

3.2.2.1 Western Officer Basin

The Western Officer Basin lies beneath the Phanerozoic Canning Basin (Figure 2). In the western Officer Basin, Tonian-age strata include the Townsend Quartzite, Lefroy, Browne, Hussar, Kanpa, and Steptoe formations (Figure 2; Grey et al. 2005). While detailed lithostratigraphic descriptions of these units are provided in (Grey et al. 2005), the Browne Formation is particularly relevant to this study due to its evaporitic components. This formation has a maximum thickness of ~2.3 km, with local accumulations as great as ~4 km (Apak et al. 2000; Apak and Moors 2000). It comprises of fine-grained siliciclastic rocks (siltstone and shale), carbonates (dolostone and dolomitic limestone), and evaporites (anhydrite, gypsum, halite), reflecting a range of depositional environments from shallow marine and peritidal to more terrestrial settings (Apak et al. 2000; Apak and Moors 2000; Grey et al. 2005).

3.2.2.2 Northwest Officer Basin

The Tarcunyah Group in the northwestern Officer Basin comprises the Googhenama, Brownrigg Sandstone, Yandanunyah, Wongarlong, and Nooloo formations (Grey et al. 2005). While detailed lithostratigraphic descriptions are provided by Grey et al. (2005), we summarise their depositional environments here due to their relevance for forward stratigraphic modelling.

The basal Googhenama Formation comprises fluvial sandstones and conglomerates, in places fining upward into wacke and shale, and represents deposition in alluvial to river-dominated systems (Grey et al. 2005). The Brownrigg Sandstone records shallow marine sedimentation in cross-bedded quartz-rich sandstones (Grey et al. 2005). At the same time, the Yandanunyah and Wongarlong formations reflect continued shallow marine deposition, with gypsum pseudomorphs and silicified horizons pointing to episodes of subaerial exposure and evaporite formation (Grey et al. 2005). The Nooloo Formation, which includes dolostone, limestone, and siliciclastic facies deposited in a marine environment, with ripple marks indicating northeast-directed paleoflow (Grey et al. 2005).

Overall, the Tarcunyah Group records repeated alternations between fluvial systems and shallow marine environments, with local evidence for tidal influence, evaporitic conditions, and subaerial emergence.

3.3 Mineralisation

Deposit-scale studies focusing on the ore genesis and timing of mineralisation at Nifty (Anderson et al. 2001; Haynes and Mazzoni 1993; Raye et al. 2025; Ribeiro et al. 2023), Rainbow (Haynes and Mazzoni 1993), and Maroochydore (Reed et al. 1995) demonstrated that Cu mineralisation is multi-genetic and multi-stage. Based on Sm-Nd and U-Pb apatite ages (Huston et al. 2020; Ribeiro et al. 2023), Pb-Pb apatite and galena ages (Huston et al. 2020), U-Pb monazite ages (Ribeiro et al. 2023), and Re-Os pyrite ages (Raye et al. 2025), the Cu mineralisation at Nifty occurred in three stages: 840-810 Ma, ~747-717 Ma, and ~675-619 Ma. These ages indicate that mineralisation took place prior to and during basin inversion. Although disseminated pre-deformation stratiform chalcopyrite mineralisation occurs at Nifty (Raye et al. 2025) and Rainbow (Haynes and Mazzoni 1993), the main Cu mineralisation at Nifty and Maroochydore is structurally controlled, vein-hosted and breccia-hosted in the hinge zone of a fold that developed syn-compression (Anderson et al. 2001; Raye et al. 2025; Reed et al. 1995).

Cu mineralisation in the Yeneena Basin is hosted within the Broadhurst Formation, which comprises of organic-rich shale, siltstone, limestone, and dolostone (section 3.2.1). These lithologies indicate a reducing depositional environment, which is a key pre-requisite for the precipitation of copper sulphides when oxidised, metal-bearing fluids migrate through the basin (Hitzman et al. 2005; Brown 2014; Hayes et al. 2015). This redox interface, where oxidised fluids meet reduced host rocks, is a fundamental control in many sedimentary-hosted Cu deposits (e.g., Hayes et al. 2015). The Broadhurst Formation's geochemical and stratigraphic characteristics make it the primary exploration target for Cu mineralisation in the region.

The Yeneena Basin also hosts other ore deposits, most notably the intrusion-related Au-Cu deposits at Telfer (Schindler et al. 2016; Wilson et al. 2020), Havieron (Hanneson and

Baxter 2022) and Winu (H. Dalstra et al., 2023; H. J. Dalstra et al., 2025; Figure 2). These deposits formed toward the end-stage of the Miles Event (~680–630 Ma; Durocher et al., 2003) and are genetically linked with the O'Callaghan Supersuite (Figure 2; Maidment et al., 2017), which intruded the basin between ~654–603 Ma (Wilson et al. 2020).

4 Module 1: Data collection and analysis to determine the present-day structural and sedimentological framework of the Yeneena Basin

The Yeneena Basin is characterised by limited rock exposure and a part of the basin is overlain by Permian Canning Basin (Czarnota et al. 2009), which poses significant challenges for direct geological observation. To address this, the region has been the focus of extensive geophysical and drilling investigations aimed at resolving its deep crustal architecture, basin–basement relationships, and mineral potential.

This chapter summarises the existing datasets, describes new data collection undertaken as part of this study, and presents interpretations of the combined datasets.

4.1 Milestone 1: Geophysical interpretation of present-day basin architecture

4.1.1 Geophysical datasets

Airborne magnetics, radiometrics and ground gravity infill were acquired in the early 2000s to support new mapping and 3D modelling of the region (Meixner et al. 2006; Costelloe et al. 2007; Czarnota et al. 2009). Regional airborne gravity gradiometry (FALCON®) and TEMPEST® airborne EM surveys (2010–2012) were flown to refine lithological boundaries, conductivity architecture and structural controls on mineralisation, particularly around Telfer (Mackey 2012; Costelloe et al. 2010; 2012; Hutchinson et al. 2010; Roach et al. 2010). In 2018, the 18GA-KB1 deep seismic reflection line with coincident gravity provided the first crustal-scale image through the region (Doublier et al. 2020). More recently, AusAEM has provided state-wide EM coverage at ~20 km spacing, while AusLAMP long-period magnetotelluric stations and GSWA's petrophysical datasets have added constraints on lithospheric resistivity and rock properties (Czarnota et al. 2022; Ley-Cooper 2020; Markoski et al. 2021; Yuan et al. 2024). 3D geoscience models and interpretations based on these datasets highlight basin geometries, basement highs, and deep crustal structures, improving understanding of basin evolution, structural geometry and exploration potential for base metals and gold.

4.1.2 Structural interpretation

The initial phase of this project focused on structural interpretation of the area of interest. Linear structures mapped in the 1:500K and 1:100K interpreted bedrock geology of Western Australia were extracted and incorporated into the baseline 3D framework. Then, the TMI and CSCBA grids were processed to assist in structural interpretation (See Geophysics for methodology and Appendix 1Project outputs for the corresponding digital deliverables). The interpretation of these datasets is described below.

4.1.2.1 Regional magnetic signature of the area

To the west, the Yeneena Basin is bounded by N-S- to NNW-trending magnetic anomalies associated with Neoarchean to Mesoproterozoic rocks of the Pilbara Craton (Figure 2 and

Figure 3). This region exhibits strong positive (> 600 nT, up to ca 2000 nT) and negative (< -200 nT, down to ca -400 nT) magnetic anomalies with steep gradients along with gravity lows reaching ~–600 mGal (Figure 3).

Eastward, rocks of the Officer Basin (Figure 2) form a narrow northern corridor that broadens southward into the main depocenter. The corridor is characterized by a low to moderate magnetic signature, while the southern depocenter shows a wider range of values (~–400 to ~700 nT; Figure 3). These variations likely reflect basement topography, intrusive bodies at varying crustal levels, and magnetic horizons within the basin fill.

The central Yeneena Basin exhibits a regional arcuate NNW to NW structural grain and a low to moderate magnetic response (~–300 to 600 nT), generally smooth in texture (Figure 3). Lower values correspond to the Coolbro Sandstone, while stippled higher values are associated with magnetic horizons in the Broadhurst and Isdell formations (Figure 2 and Figure 3). Inversion modelling (See Appendix 2 Geophysics) indicates that long-wavelength anomalies may partly originate from basement units of the Pilbara Craton and Rudall Complex at depth. Superimposed short-wavelength (1–1.5 km) positive anomalies likely correlate with shallow intrusions.

Further east, the Mount Crofton Granite (O'Callaghan Supersuite; Figure 2 and Figure 3A) generates circular positive magnetic anomalies (up to ~600 nT) with distinct zonation, intruding the low- to moderately magnetic Wilki, Malu, and Puntapunta formations (Figure 2 and Figure 3).

The regional gravity signal increases from ~–600 mGal in the WSW to ~30 mGal in the ENE (Figure 3). In the area of interest, the Phanerozoic Canning Basin partly overlies the Yeneena Basin (Figure 2). This region corresponds to negative magnetic anomalies (down to ~–200 nT) and associated gravity lows, possibly reflecting basement deepening.

In the southeast, the Rudall Complex (Figure 2) crops out and is characterised by magnetic anomalies ranging from ~–400 to 1000 nT with a stippled texture (Figure 3), together with gravity lows down to ~–400 mGal.

Superimposed linear, short-wavelength positive magnetic anomalies across the region likely mark shallow intrusives such as dykes (Figure 3).

4.1.2.2 Regional fault architecture

A set of NNW- to NW-trending faults, which either exhibit significant lateral continuity or form an anastomosing pattern by branching and merging along their strikes, has been identified in the study area (Figure 3A).

The NNW-trending, basin-bounding Vines Fault, which is partly exposed or near surface in the northwestern Yeneena Basin, and the Southwest Thrust have been identified in the L211 18GA-KB1 seismic transect (Doublier et al. 2020). These faults are characterized by NNE-oriented magnetic gradients exceeding 1000 nT/km in the central northern Yeneena Basin and generally decreasing in magnitude toward the south. These gradients allow the faults to be traced further south, where they extend under cover. West of the Vines Fault, basement rocks are extensively exposed (Figure 2). These structures not only coincide with sharp variations in the conductivity sections but also define regional domains that exhibit different broad conductivities.

Further east, a prominent NNW-trending fault coincides with a linear magnetic anomaly, characterised by NNE-directed gradients reaching up to 200 nT/km. This structure defines the boundary between the mapped Broadhurst Formation and the Isdell Formation (Figure 2 and Figure 3). The West Waukarlycarly Fault, which runs parallel to the Vines Fault and Southwest Thrust, separates a zone of moderate to high magnetic intensity to the west from a broad magnetic low associated with Canning Basin deposition to the east (Figure 2 and Figure 3).

The major NNW-trending faults are cross-cut by a set of NNE- to NE-trending shear zones, expressed in the magnetic grid as offsets of markers associated with the NNW-trending structures. In addition, highly magnetic linear to elongated bodies occur near major faults, often overprinting the geophysical signals of these structures (Figure 3A).

Overall, these NNW-trending faults - including the Vines Fault, Northwest Thrust, and West Waukarlycarly Fault - displace both magnetic horizons within the Yeneena stratigraphy and the underlying basement, strongly controlling basement topography. These faults exert a fundamental influence on basin architecture and the regional geophysical signature (see Bagas 2004; Hickman and Bagas 1999; Huston et al. 2007; Kunzmann et al. 2021).

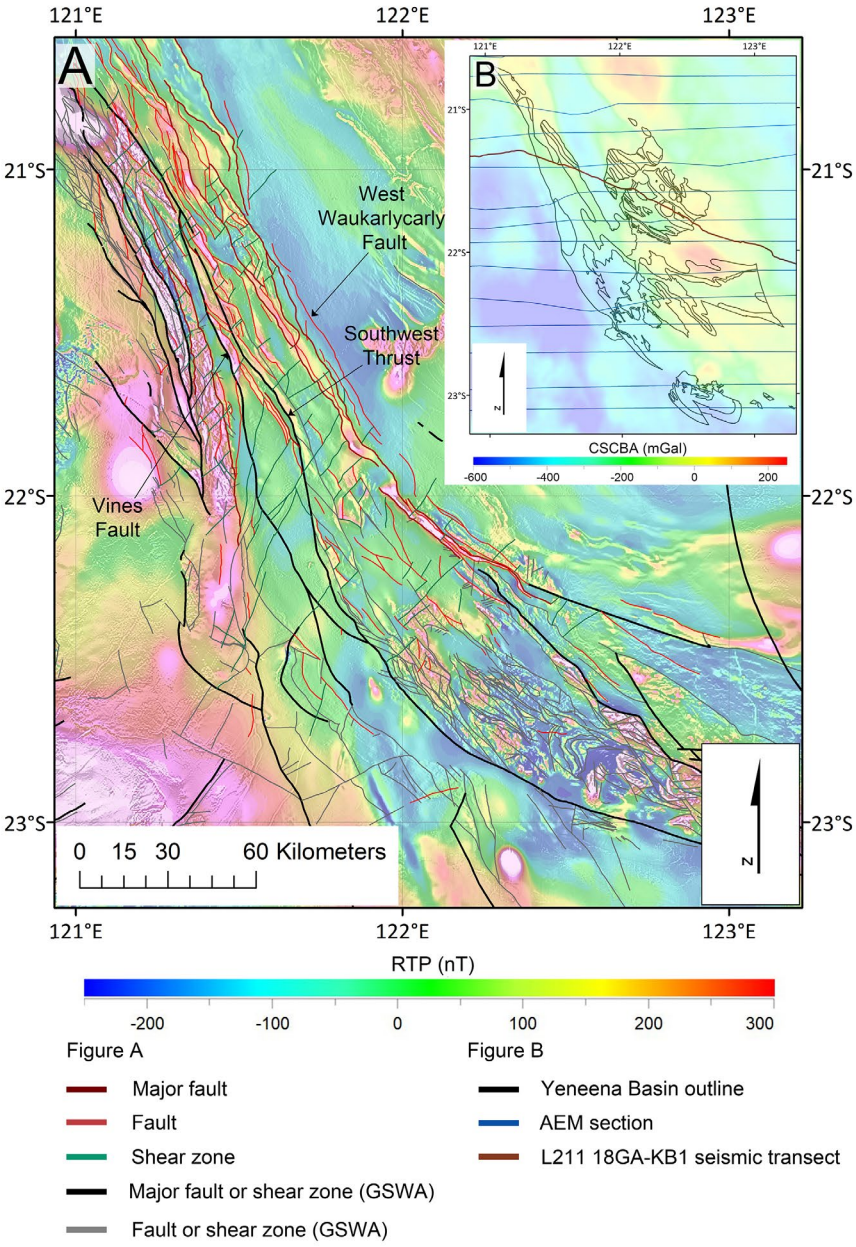

Figure 3. A) Interpreted fault architecture over a pseudo-colour map of the RTP magnetic anomalies (60% transparency) and RTP-1VD magnetic anomalies (75% transparency) of the area of study. Black lines and grey lines are mapped faults and shear zones sourced from the GSWA 1:500 000 interpreted bedrock geology of Western Australia B) location of AEM profiles and L211 18GA-KB1 seismic transect over a pseudo-colour image of the complete spherical cap Bouguer anomalies (50% transparency).

4.1.2.3 Depth to basement

Constraining 3D models (Dalmaso Spode 2020; Meixner et al. 2006) indicate that, regionally, the basement deepens toward the northeast, reaching a maximum depth of more than 8000 m below the surface east of the West Waukarlycarly Fault (Figure 3 and Figure 4). This is also reflected in the magnetic grid as a broad magnetic low surrounding the highly magnetic Mount Crofton Granite (Figure 3).

The spectral analysis highlights three main slope breaks, which might correspond to ensembles of sources at different depths. These ensembles of magnetic sources are located at approximately 7 km, 2.5 km, and 800 m below the surface (See Appendix 2 Geophysics).

The major NNW-trending faults, including the Vines Fault, Northwest Thrust, and Camel-Tabletop Fault, appear to offset the basement units, significantly influencing the present-day basement topography. West of the Vines Fault, the basement rocks extensively outcrop. The area between the Vines Fault and the Southwest Thrust is relatively shallow, with depths ranging from 0 to approximately 3000 m below the surface, and depths generally increasing towards the south (Figure 4). The basement topography in the region comprised between the Southwest Thrust and the West Waukarlycarly Fault appears to be deeper (down to approximately 3200 m below the surface) in the northern part and becomes shallower in the southern part, where rocks of the Rudall Complex eventually outcrop.

Unconstrained inversion indicates that magnetic source bodies (>0.01 SI) at variable depths in the eastern-southeastern part might represent magnetized units within the basement rocks, while magnetized units in the northeastern part correlate with the shallow granitic intrusion of the Mount Crofton Formation (See Appendix 2 Geophysics). However, this is not diagnostic of basement topography, as the rocks forming the Pilbara Craton and Rudall Complex have different compositions and are likely to exhibit a wide range of magnetic susceptibilities. This is further supported by the poor correlation between these outcropping rocks and the relative magnetic signal (Figure *5*). However, the long wavelength anomalies in the southwestern part of the area of study might indeed reflect source bodies at depth.

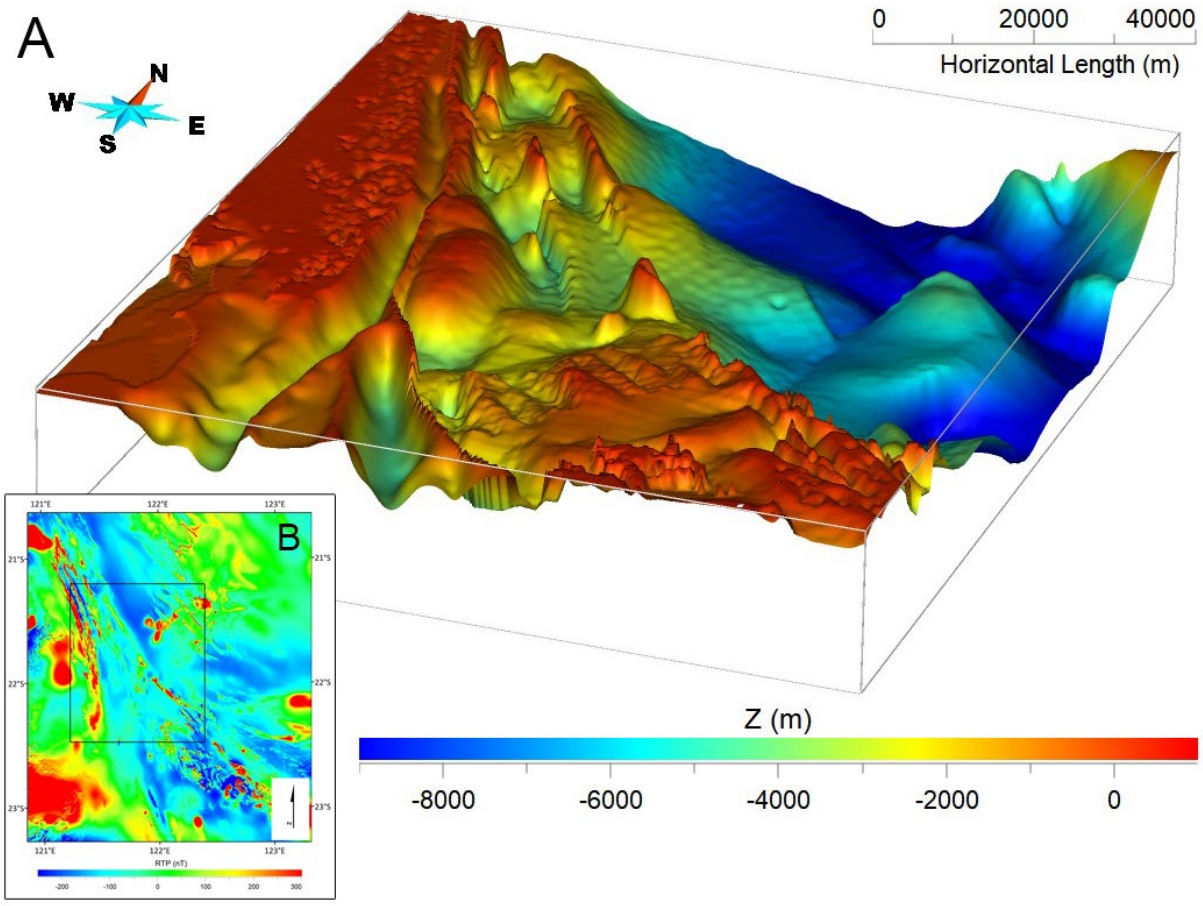

Figure 4. (A) 3D surface representing the basement topography in the area of study, which is outlined by the black polygon in the insert (B). The 3D surface has a 3 times vertical exaggeration.

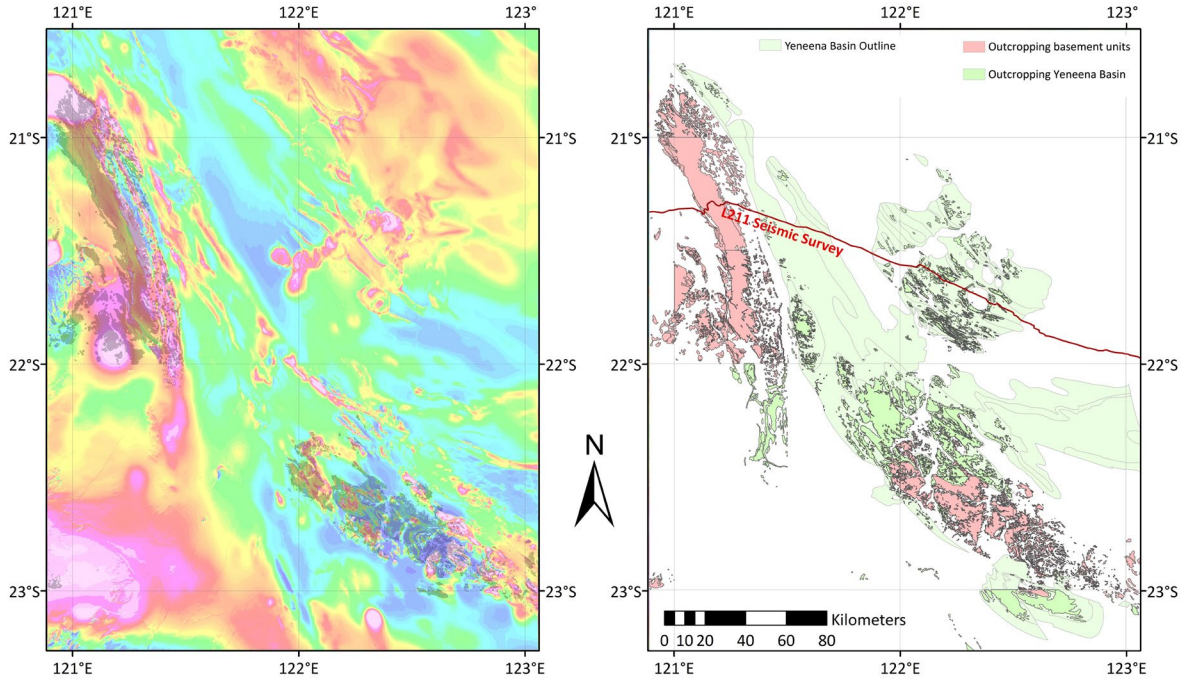

Figure 5. (A) outcropping basement rocks (greyed regions) over a RTP grid of the magnetic anomalies in the area of study; (B) outcropping basement rocks, Yeneena Basin rocks for a better comparison between the magnetic signature of the region and the outcrop occurrences.

4.2 Milestone 2: Structural logging of drill cores

4.2.1 Drill core data

More than 30 drill cores are publicly available through the Geological Survey of Western Australia (GSWA) core library. However, not all of these cores are oriented. A previous study conducted by Kunzmann et al. (2021) as part of the MRIWA M521 project structurally logged eight drill cores (Figure 6; 17FCHRCD001; EPT062, EPT1831, EPT2192, EPT2193, EPT2281, EPT2299, and EPT2300). Their analysis aimed to capture the structural architecture and kinematic evolution of the deformed rocks. The results revealed NW-SE trending antiform-synform pairs and indicated reactivation of basement normal faults as reverse faults. Additionally, they demonstrated that the Southwest South Fault exhibits NE-directed vergence.

To complement this dataset, we collected new structural data from nine additional drill cores (Figure 6; EPT2279, EPT2280A, EPT2282, EPT2283, EPT2290, EPT2294, EPT2308, EPT2309, and EPT2310). The structural orientations of various planar (bedding, cleavage, vein) and linear (mineral lineation, intersection lineation, hinge line) fabrics were measured and reported as dip, dip direction for planar fabrics, and plunge, azimuth for linear fabrics. The new structural dataset has enabled us to better constrain the present-day structural architecture of the basin, especially in areas of sparse surface structural data, and to develop more robust interpretations of its geological framework.

Published petrophysical and sedimentological data were also compiled for use in subsequent sections of the project.

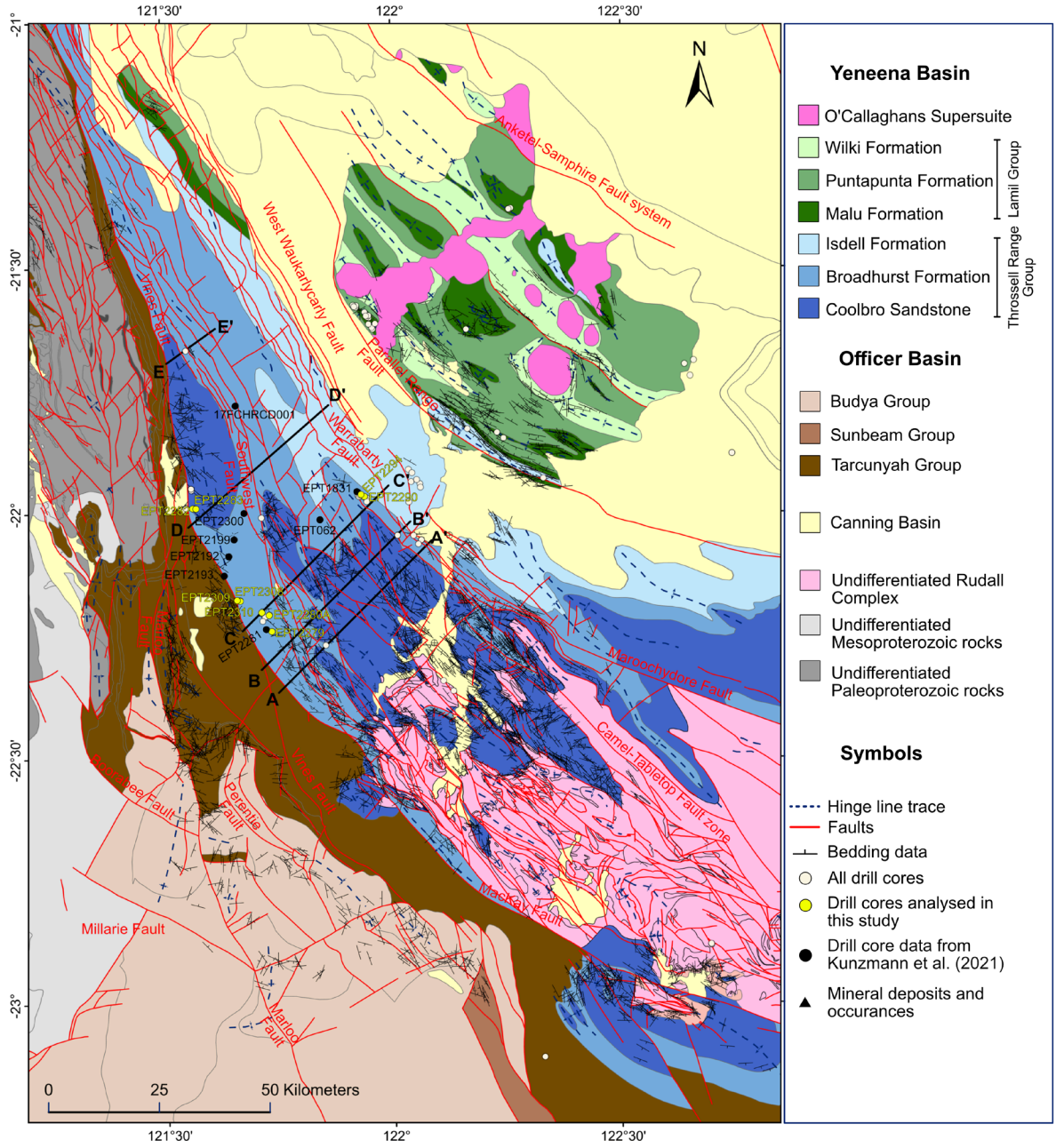

Figure 6. Geological map of the Yeneena Basin modified after Parui et al. (under review). Red lines mark the faults, based on data from the Geological Survey of Western Australia (https://geoview.dmp.wa.gov.au/geoview/) and section 4.1.2.2. AA'–DD' mark the transects of the balanced cross-sections constructed in this project. The EE' transect passes through the Nifty Cu deposit.

4.2.2 Methodology

To determine the present-day deformed geometry of the Yeneena Basin, we compiled structural datasets from surface geological mapping (1943 bedding, 796 cleavage, and 69 hinge line orientations) from the Geological Survey of Western Australia (https://geoview.dmp.wa.gov.au/geoview/) with new and previously published structural data from oriented drill cores (see section 4.2.1). The depth of the drill cores varied from 222.9 to 917.5 m. The data were plotted on stereonets to identify average orientations of structural features (Figure 7).

4.2.3 Results

Bedding orientations from surface geological mapping define a girdle distribution, indicating that the beds are folded. To calculate mean bedding orientations, a Bingham axial distribution was applied using the *Stereonet* software (Allmendinger et al. 2011). Two dominant bedding orientations are observed, with mean attitudes of 37°, 040° and 53°, 225° (Figure 7a). The beds are folded along a NW-trending hinge line, with a mean orientation of 2°, 313° (Figure 7a). Cleavage data also show folding along SE-trending hinge line, with a mean orientation of 9°, 134° (Figure 7b). Hinge line orientations of outcrop-scale folds plunge gently to steeply toward the NW and SE (Figure 7c).

In the northeast, bedding measurements from dill cores indicate folding around an N-NW-trending hinge line, with an average orientation of 15°, 339° (Figure 7d). Based on cleavage orientations, their pervasiveness, and overprinting relationships, two dominant cleavage sets were identified (Figure 8). The S_1 cleavage is parallel to bedding, with a mean orientation of 24°, 289° (Figure 7e). The S_2 cleavage shows a girdle distribution, consistent with folding about a hinge line of 10°, 002° (Figure 7e). Bedding data measured from EPT062 (Kunzmann et al. 2021) also indicate folding along a N-NW-trending hinge line, with a mean orientation of 4°, 351° (Figure 7f). The S_2 cleavage at this site is likewise folded, with a mean hinge line orientation of 4°, 347° (Figure 7g).

In the southwest, bedding measurements collected from drill core EPT2279, EPT2280A, EPT2281, EPT2308, EPT2309, and EPT2310 indicate folding around an N-NW-trending hinge line with a mean orientation of 1°, 341 (Figure 7h). The S_2 cleavage is also folded, but along a SE-trending hinge line averaging 22°, 125°. Similarly, bedding orientations collected from drill core EPT2282, EPT2283, EPT2192, EPT2193, EPT2299, and EPT2300 also suggest folding about a SE-trending hinge line with a mean orientation of 9°, 130° (Figure 7j). Within these drill cores, both S_1 and S_2 cleavages are themselves folded, with mean hinge line orientations of 17°, 339° and 8°, 324°, respectively (Figure 7k). In 17FCHRCD001 hole, the beds have a mean orientation of 31°, 269° (Figure 7l), with S_1 and S_2 cleavages dipping westward with mean orientations of 42°, 266° and 29°, 294°, respectively (Figure 7m). Compilation of core-scale fold hinge lines from Kunzmann et al. (2021) indicates that these structures plunge gently toward both the NW and SE (Figure 7n).

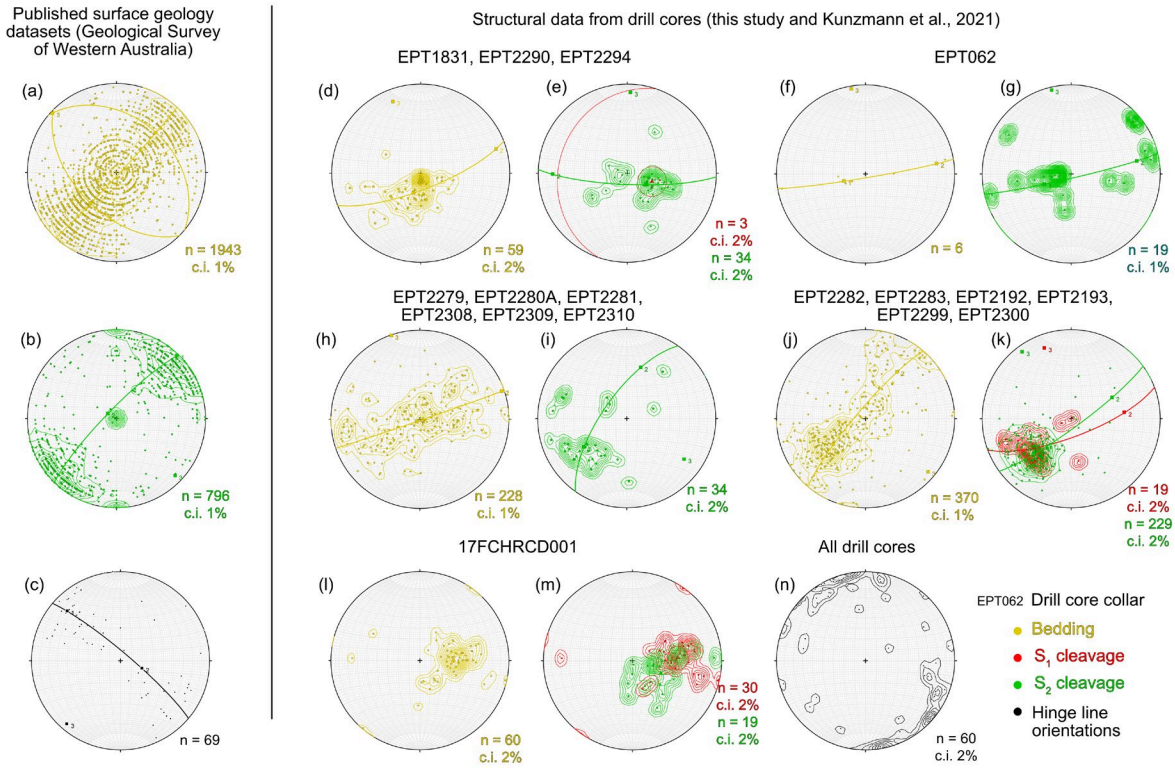

Figure 7. Equal-area, lower-hemisphere plots illustrating: (a) bedding poles, (b) cleavage poles, and (c) fold hinge line orientations derived from published surface geology data. Panels (d), (f), (h), (j), and (l) display bedding poles obtained from drill cores, while panels (e), (g), (i), (k), and (m) show cleavage poles from the same cores. Panel (n) presents hinge line orientations of folds at the core scale. c.i. denotes contour interval, and n represents the number of measurements.

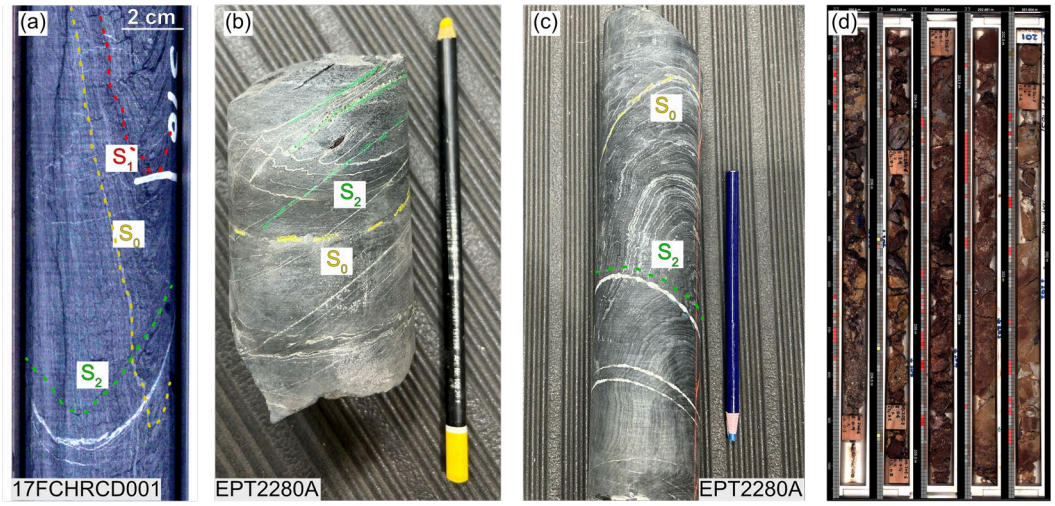

Figure 8: (a) Carbonaceous shale from the Broadhurst Formation displaying bedding (S_0), bedding-parallel dissolution cleavage (S_1), and S_2 cleavage. Sample 17FCHRCD001 at 376 m depth. (b) Carbonaceous shale illustrating an acute (~12°) angle between bedding (S_0) and S_2 cleavage. Sample EPT2280A at 78.9 m. (c) Carbonaceous shale showing an angular (~68°) relationship between bedding (S_0) and S_2 cleavage. Sample EPT2280A at 78.9 m. (d) Major fault zone encountered in drill core EPT1831 at 201 m, with evidence of hematite alteration and kaolinization.

4.2.4 Interpretations

The S_1 cleavage is bedding-parallel and stylolitic in nature (Figure 8) and is folded together with the bedding planes (Figure 7). S_1 is interpreted as a diagenetic cleavage that developed during sediment burial, prior to basin inversion. In contrast, the S_2 cleavage overprints S_1 and is characterised as an axial planar cleavage (Figure 8), indicating its formation was synchronous with folding during basin inversion. Notably, the angle between S_2 cleavage and bedding varies with structural position. For example, in drill core EPT2280A, the S_2 cleavage forms an angle of ~12° with bedding at a depth of 78.9 m (Figure 8b), increasing progressively to about ~68° at 294.8 m (Figure 8c). This drill core intersects a fold, encountering the fold limb at shallower depths and the hinge zone at greater depths. Hence, the S_2 cleavage forms an acute angle with bedding in the fold limb and makes a right angle in the hinge zone (Figure 8). This angular relationship is consistently observed in other drill cores across the basin. The systematic variation in cleavage-bedding angles relative to fold geometry suggests that folding occurred via buckling by the flexural shear mechanism (e.g., Twiss and Moores, 1992). The sedimentary succession of the Yeneena Basin comprises mechanically heterogeneous strata, with less competent shale and siltstone interbedded with more competent sandstone, dolomitic mudstones, dolostones and limestone units (Grey et al. 2005). This mechanical anisotropy likely facilitated flexural shear folding during layer-parallel shortening (buckling) associated with basin inversion.

4.3 Milestone 6: Geochronology

4.3.1 Existing data

The most comprehensive depositional ages of the sedimentary units in the Yeneena Basin were constrained by U–Pb dating of detrital zircons (Clark et al. 2023; Kohanpour et al. 2024; Maidment et al. 2008), Pb–Pb carbonate dating (Maidment et al. 2008), and U–Pb dating of mafic sills and monzonite intrusions (Maidment et al. 2008). These age datasets are discussed in detail in section 3.2.1.

Based on Sm-Nd and U-Pb apatite ages (Huston et al. 2020; Ribeiro et al. 2023), Pb-Pb apatite and galena ages (Huston et al. 2020), U-Pb monazite ages (Ribeiro et al. 2023), and Re-Os pyrite ages (Raye et al. 2025), the Cu mineralisation within the basin is constrained to three intervals at ~840-810 Ma, ~747-717 Ma, and ~675-619 Ma (Raye et al. 2025).

A recent study by (Kelsey et al. 2024) attempted to constrain the age of deformation associated with the Miles event; however, their findings were inconclusive. The best possible age estimates for this event were reported by (Durocher et al. 2003; see section 3.2.1).

4.3.2 Methodology

The geochronology component of this study aims to refine the timing of key events in the basin history through U–Pb dating of calcite and apatite in veins.

Thirteen vein samples were collected from drill cores EPT2192, EPT2193, and EPT2280A for apatite and carbonate U-Pb dating (Figure 6; Table 1 and Table 2). Mineral phase maps were obtained using a Tescan Integrated Mineral Analyzer (TIMA) in the John De Laeter Centre, Curtin University, with a 1 µm resolution for back-scattered electron (BSE) imaging, and 9 µm resolution for energy dispersive X-ray spectroscopy (EDX) dot mapping. Data

tables including the single-spot results of unknowns and reference materials are included in Appendix 3 p.134.

Table 1. Summary of the vein samples collected for the apatite and calcite U-Pb dating.

GSWA sample no.	Drill core collar	Depth (m)	Description
619054	EPT 2192	134.95	Boudinaged, bed-parallel, dolomite-quartz-chalcopyrite vein
619058	EPT 2192	165.45	Bed-parallel, dolomite vein
619062	EPT 2192	241.09	Dolomite-calcite vein oriented at a high angle to the bedding
619063	EPT 2192	266.52	Calcite-quartz vein making moderate- to high-angle to bedding
619064	EPT 2192	269.23	Bed-parallel dolomite vein
619069	EPT 2192	339.54	Boudinaged, dolomite vein makes a moderate angle to the bedding
619073	EPT 2193	184.71	Dolomite vein makes a high angle to the bedding
619076	EPT 2193	305.4	Massive dolomite-chalcopyrite vein
618916	EPT 2280A	265.31	Massive calcite-quartz vein
618919	EPT 2280A	341.47	Massive calcite-quartz vein
618920	EPT 2280A	378.95	Boudinaged, bed-parallel dolomite vein
618922	EPT 2280A	385.85	Bed-parallel calcite-chalcopyrite vein
618923	EPT 2280A	420.95	Bed-parallel dolomite-quartz vein

4.3.2.1 Apatite U-Pb

Apatite U-Pb analysis was undertaken at the GeoHistory facility, Curtin University, using a Resonetics S-155-LR 193 nm excimer laser coupled to an Agilent 8900 triple quadrupole ICP-MS. The laser spot diameter was 30 µm, with 2.3 J cm^{-2} on-sample laser fluence, a repetition rate of 5 Hz, and an ablation time of 25 s with 30 s of baseline acquisition. Measured masses included ^{202}Hg, ^{204}(Pb+Hg), ^{206}Pb, ^{207}Pb, ^{208}Pb, ^{232}Th, ^{235}U, and ^{238}U. McClure Mountain syenite apatite (523.51 ± 1.53 Ma, Schoene and Bowring 2007; Thomson et al. 2012) was used as the primary reference. MAD apatite (474.25 ± 0.41 Ma, Thomson et al. 2012) and FC1 apatite (1099.0 ± 0.6 Ma, Paces and Miller Jr 1993) were analysed as secondary reference materials, interspersed with unknowns. Secondary reference apatites reproduced their recommended ages within uncertainty: The intercept age obtained by free regression for MAD apatite was 476.8 ± 11.4 Ma (MSWD = 1.6, n = 46); the intercept age obtained for FC1 apatite by free regression was 1091.0 ± 10.4 Ma (MSWD = 1.7, n = 46).

Raw data were reduced in Iolite4 (Paton et al. 2011) using the VizualAge UComPbine data reduction scheme (Chew et al. 2014), and ages were calculated using IsoplotR (Vermeesch 2018). Apatite ages for individual samples were determined as intercept ages based on free regressions. Unless stated otherwise, all uncertainties are reported at the 95% confidence level. The uncertainties of apatite ages determined from over-dispersed populations (i.e. with MSWD >> 1) are quoted as the 95% confidence interval multiplied by a factor to account for overdispersion (for details see Vermeesch 2018).

4.3.2.2 Carbonate U-Pb

Carbonate U-Pb analysis was undertaken at the GeoHistory facility, Curtin University, using a Resonetics S-155-LR 193 nm excimer laser coupled to a Nu Plasma III multi-collector ICP-MS. The laser spot diameter was 50 µm, with 3.2 J cm-2 on-sample laser fluence, a repetition rate of 8 Hz, and an ablation time of 25 s with 30 s of baseline acquisition. Measured masses included ^{202}Hg, ^{204}(Pb+Hg), ^{206}Pb, ^{207}Pb, ^{208}Pb, and ^{238}U. Prior to U-Pb analysis, all 13 samples were screened for their uranium concentration to aid in selecting analytical targets. Only two of the 13 samples contained uranium (U) above the detection limit (Table 2). These two samples (Sample no. 619073 and 618919) were subsequently selected for analysis. The remaining 11 samples had U concentrations below the detection limit, rendering them unsuitable for U-Pb geochronology (Table 2). A data reduction protocol as described by Roberts et al. (2017) was applied, involving normalisation of isotopic ratios to standard glass NIST 614 (Jochum et al. 2011), and a subsequent matrix correction of ^{238}U/^{206}Pb using the matrix-matched calcite standard WC-1 (254.4 ± 6.4 Ma; Roberts et al. 2017). Following the data reduction protocols of (Roberts et al. 2017), an additional 3% uncertainty was propagated in quadrature to all reported ages to account for minor heterogeneity of the WC-1 reference material. Secondary reference materials, analysed interspersed with the unknowns included Ash-15 calcite (2.965 ± 0.011 Ma; Nuriel et al. 2020) and JT-1 calcite (13.797 ± 0.031Ma; Guillong et al. 2020).The ages obtained for both secondary reference calcites are within uncertainty of their accepted values: Ash-15 yielded a lower intercept age of 2.694 ± 0.11 Ma (n = 28, MSWD = 0.73), and JT-1 yielded a lower intercept age of 12.9 ± 1.2 Ma (n = 15, MSWD = 0.76).

4.3.3 Results

The ^{207}Pb-corrected apatite ages reveal at least two broad age components (Figure 9): one likely representing a detrital component and another reflecting the younger, post-depositional history of the basin. Specifically, apatite ages demonstrate both older Precambrian events (>1000 Ma) and younger Phanerozoic influences (~600 Ma and ~250 Ma), indicating multi-stage geological processes.

The ^{207}Pb/^{206}Pb$_c$ values represent the common lead (Pb) isotopic signature of the fluid present during the mineral growth. These ratios provide insights into the source and evolution of the fluids that contributed to apatite growth. Key observations include: 1) The range of ^{207}Pb/^{206}Pb$_c$ values in apatite suggests variability in the isotopic composition of the fluids during mineral growth or subsequent alteration, and 2) this variability in ^{207}Pb/^{206}Pb$_c$ likely reflects different fluid sources, aiding in the distinction between detrital components and post-depositional processes. The apatite U-Pb dates along with the corresponding ^{207}Pb/^{206}Pb$_c$ ratios provide valuable information about the provenance of the samples.

However, it is important to caution against interpreting these apatite dates as precise geologic ages due to their limited temporal resolution (see regression plots in Appendix 3 p.134). In contrast, analyses of calcite from the carbonate sample define a clearer common–radiogenic Pb mixing array. Although the regression is moderately over-dispersed relative to analytical uncertainties alone (MSWD = 7), the lower-intercept age on concordia may still be geologically meaningful, indicating that most radiogenic Pb in the calcite accumulated at 927 ± 33 Ma. This behaviour contrasts with zircon, which, owing to its typically high closure temperature and robust lattice, commonly yields a single, precise crystallisation age, whereas calcite more readily records multi-domain behaviour and open-system disturbance, producing mixing relationships that can reflect additional fluid-mediated Pb gain / loss / variable closure to Pb diffusion. The implications of this apparent carbonate age are discussed in the next section.

*Table 2: Summary of geochronology results. All uncertainties are reported at the 95% confidence level. * no apatite in thin section; ** no regression defined by U-Pb data; *** carbonate U concentration below limit of detection.*

GSWA sample No.	Apatite		Carbonate	
	Age(s)	$^{207}Pb/^{206}Pb_c$	Age	$^{207}Pb/^{206}Pb_c$
619054	- *		-***	
619058	- *		-***	
619062	- *		-***	
619063	1182 ± 26 Ma	1.07 ± 0.02	-***	
619064	1083 ± 168 Ma 684 ± 58 Ma	0.86 ± 0.03 0.82 ± 0.02	-***	
619069	- *		-***	
619073	1015 ± 232 Ma 215 ± 41 Ma	0.94 ± 0.03 0.86 ± 0.01	926.6 ± 32.8 Ma	0.806 ± 0.001
619076	526 ± 131 Ma	0.84 ± 0.01	-***	
618916	- **	c. 0.78-0.90	-***	
618919	- **	0.85 ± 0.01	-**	0.801 ± 0.001
618920	- *		-***	
618922	1051 ± 23 Ma	0.86 ± 0.01	-***	
618923	1180 ± 27 Ma 551 ± 40 Ma	0.89 ± 0.03 0.86 ± 0.02	-***	

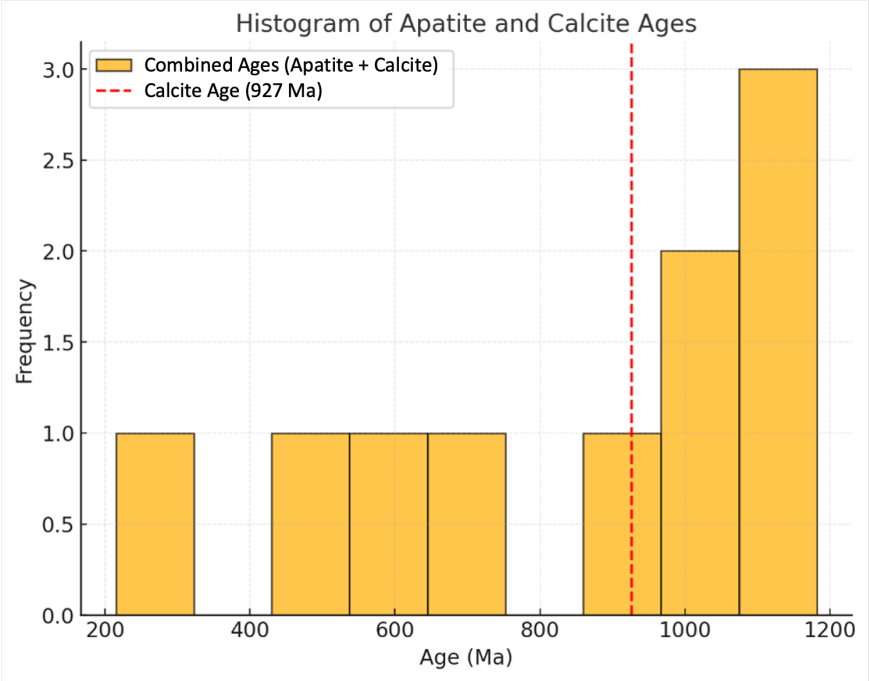

Figure 9: Histogram showing the distribution of individual ^{207}Pb-corrected apatite apparent ages and the calcite common-radiogenic regression apparent age (927 Ma, marked by a dashed red line). The apatite ages display a range interpreted to reflect a mix of detrital grains and secondary post-depositional processes. The best estimate age for the calcite is interpreted to reflect the dominant time of radiogenic-Pb accumulation in this mineral, likely approximating the time of vein formation. This visualization highlights the complex thermal and fluid history recorded in these minerals.

4.3.4 Implications

The best estimate for the apparent age of most radiogenic Pb accumulation in calcite (927 ± 33 Ma) closely aligns with the depositional ages of the surrounding sedimentary units, suggesting that vein formation could have occurred during the basin-development phase prior to basin inversion. While vein formation is commonly associated with deformation, studies have shown that veins can also form during the diagenesis of sediments (Laubach et al. 2010). The vein is hosted within the Broadhurst Formation (Figure 6). Previous detrital zircon geochronology has provided a maximum depositional age of approximately 960 ± 21 Ma for this unit (Kohanpour et al. 2024). The new U–Pb calcite age therefore offers a minimum age constraint for the Broadhurst Formation, contributing to a more refined depositional age framework for the Yeneena Basin.

5 Module 2: 4D reconstruction of the Yeneena Basin through time

The formation and evolution of sedimentary basins is dependent on spatial and temporal variations in tectonic and thermal subsidence/uplift, which are primarily controlled by deep mantle dynamics and associated plate motion (Allen and Allen 2013). The infill and sedimentary architecture of such basins, in addition to reflecting subsidence conditions, is controlled by a series of interacting factors, including the physiography of the basin itself, which impacts the strength or energy-dissipation of certain processes (e.g, waves, tides); the geology of the hinterland; and the climate and its variations, which influences eustatic sea level, the amount and distribution of precipitation, and the type of sediment precipitating or being deposited in the basin (Church and Coe 2003).

The reconstruction of sedimentary basin evolution requires a suite of datasets and methods, including various geophysical methods (e.g., reflection seismic, electromagnetic methods), borehole datasets (e.g., downhole images, petrophysics, cores), intra-basinal and analogue outcrop studies, as well as experimental and numerical simulations. This integrated approach has long been the standard in hydrocarbon exploration, especially with regards to the development of predictive models used to approximate the geology in and around the area of interest. This study applies a similar approach in the context of mineral exploration, using a range of datasets and methods to reconstruct the evolution of the Yeneena Basin to understand various aspects of its sedimentary-hosted copper mineral system. Specifically, this chapter describes the application of three methods to unravel the history of the Yeneena Basin: (1) subsidence modelling; (2) construction and restoration of cross-sections; and (3) stratigraphic forward modelling.

5.1 Milestone 3: Subsidence modelling

5.1.1 Methodology

Subsidence analysis is a fundamental tool in basin evolution studies, providing insights into the interplay between tectonic movements, sediment deposition, and burial-induced compaction. It allows to distinguish between tectonic subsidence (driven by extension-related crustal thinning, cooling, or flexural loading associated with sediment accumulation or magmatic emplacement) and subsidence associated with sediment compaction. Subsidence geometry and its controlling mechanisms vary across tectonic settings, so these patterns can be used to discriminate between such settings (Xie and Heller 2009).

Subsidence analysis was carried out by applying a back-stripping and decompaction method (Allen and Allen 2005) implemented in Python (CSIRO in-house code). Decompaction restores porosity lost due to compaction, following principles established by Athy (1930) and Hedberg (1936). The back-stripping component estimates the movement of basement through time by sequential removal of stratigraphic or sedimentary intervals at one particular place, enabling estimation of de-compacted thickness, porosity, and depth of each layer at any given time (Barton and Wood 1984; Makuluni et al. 2022; Roberts et al. 1998; Sclater and Christie 1980). The results are presented as a basement subsidence curve that shows vertical movement of the basement through time.

The input required for subsidence analysis is the age and thickness of the stratigraphic units. Due to limited constraints on these parameters in the Yeneena and surrounding basins, the subsidence modelling conducted for this project relied on average maximum and minimum depositional ages and average thicknesses of stratigraphic units reported in the published literature and well data (see Section 3.2). Average formation thicknesses from wells YNC350, 17FHCRCD001, MWD14002, EPT2300, EPT060, EPT062, EPT1702, EPT1831, 84MCDD2A, EPT2192, EPT2193, EPT2308 and EPT2281 were used to assess subsidence of the Yeneena Basin, with a total average fill thickness of ~6.9km. Additional subsidence curves were calculated for the neighbouring Tarcunyah Group using maximum thicknesses of the constituent formations (e.g., Grey et al. 2005), the NW Officer Basin using data from wells Mundajini1, Akubra1, and Boondawari1, and the Western Officer Basin using data from wells Lancer-1 and Hussar-1. The analysis was conducted for an indicative time span of 235 million years (Myr). The results should be considered first-order estimates owing to uncertainty in the average ages and thicknesses used as input.

5.1.2 Results

Subsidence analysis reveals that the highest subsidence rate in the Yeneena Basin (~65 m/Myr) occurred during deposition of the Coolbro Sandstone, followed by a moderate decline during the Broadhurst Formation, and a gradual decrease to ~18 m/Myr during deposition of the uppermost Wilki Formation (Figure 10). This variation produced a steep initial slope on the depth–time curve, transitioning to a moderate slope and eventually a long-term gentler gradient. The subsidence rates in the Yeneena Basin strongly contrast with the much lower rates observed in the contemporaneous Tarcunyah Group, the NW Officer Basin, and the Western Officer Basin. The subsidence analysis also indicates that, while the NW and Western Officer basins experienced a much slower initial subsidence rate, these two subbasins potentially experienced an increase in subsidence rate at 850 Ma. This increase occurred after the slow-down of subsidence in the Yeneena Basin, suggesting that the subsidence front migrated southward over time, from the Yeneena Basin to the Officer Basin, although limited age constraints require interpreting these subsidence results with caution. Based on the subsidence trends and tectonic setting classification framework of Xie and Heller (2009), the Yeneena Basin likely formed in an extensional context, with subsidence rates fitting the ones representing rift-stage, sag-stage profiles along passive margins, whereas the NW and Western Officer basins display subsidence trajectories more akin to Phanerozoic intracontinental basins. However, Precambrian basins were impacted by different processes than Phanerozoic ones (i.e. heat flow, tectonic, etc.; e.g., Eriksson et al. 2001), interpreting Precambrian subsidence rates as directly comparable to those of Phanerozoic passive margins should be approached with parsimony.

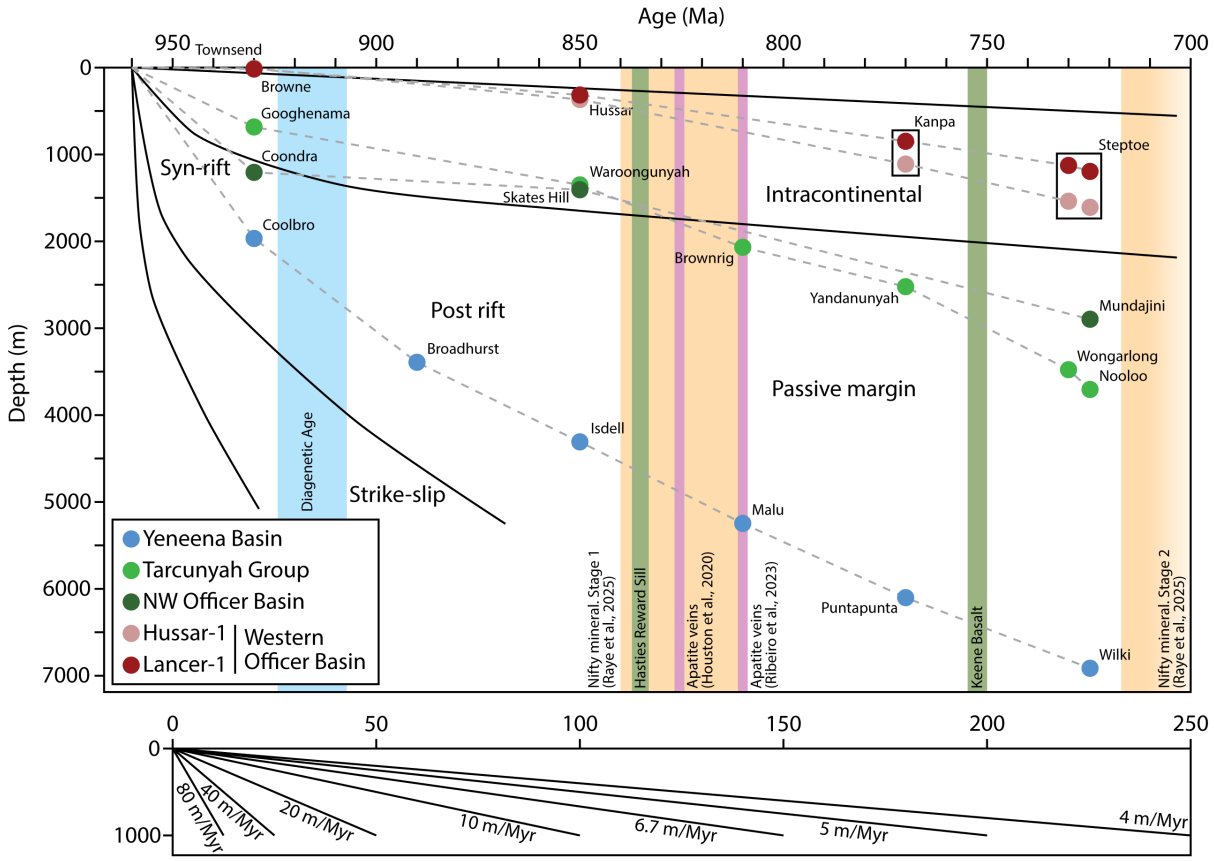

Figure 10: Subsidence plots tracking the basement for the Yeneena and Officer Basins. Control points for ages are labelled with the formation top name. Basin-type boundaries after Xie and Heller (Eriksson et al. 2001). Lower plot shows subsidence rates for different subsidence curve slopes.

5.2 Milestones 4 and 5: 2D cross sections and reconstructions

5.2.1 Present-day structural architecture

Four regional-scale cross-sections were constructed to characterise the present-day geometry of the inverted basin. These AA′, BB′, CC′, and DD′ transects span ~42-48 km between the Vines Fault in the SW to the Warrabarty Fault in the NE (Figure 6). Please note that these lines were not extended into areas exposing the Lamil Group, as these rocks were intruded by the O'Callaghans Supersuite (Figure 6). A fifth cross-section along EE′ was also constructed to provide insight into the Nifty Cu deposit within the regional structural framework (Figure 6). The EE′ transect spans ~14 km between the Vines fault and the Southwest fault system (Figure 6). Published mapped structural data, published seismic interpretations (Doublier et al. 2020), published interpretations of the lithological units, and structural measurements from drill cores (Kunzmann et al. 2021; this study) were used to construct the deformed cross-sections (Figure 11), representing the present-day geometry minus erosion.

The decisions taken in constructing these cross-sections are listed below.

(i) The deformed cross-sections were constructed at 1:500,000 scale. Outcrop- and core-scale shortening structures and penetrative strain were ignored, as they remained below the resolution at which the cross-sections were constructed.

(ii) Mapped and drill hole bedding data were projected onto the cross-sections by calculating apparent dip along the line of section, up to a normal-distance of 5 km from it, assuming there are no significant lateral structural variations within that distance.

(iii) The average dip direction of the bedding and hinge line orientations of the outcrop- and core-scale folds (Figure 7) indicates a NE-SW-oriented shortening direction. Please note that the regional shortening direction is calculated with respect to the present-day geographic reference framework.

(iv) The cross-sections only portray the structural geometry of the Yeneena Basin. No attempt was made to represent the complex deformation history of the Rudall Complex (Bagas 2004; Gardiner et al. 2018) , hence it is represented as a single undifferentiated unit.

(v) Fault trajectories were constrained using the mapped fault positions, basement offsets, drill hole intercepts and interpretations from the regional seismic profile (Doublier et al. 2020).

(vi) The seismic profile shows that the basal décollement lies at a depth of ~13-20 km beneath the cross-section. The dip of the basal décollement is ~8.5° NE (Doublier et al. 2020). The Vines fault and the NE-most reverse fault of the Southwest fault system are branching out from the basal décollement. However, it is difficult to ascertain the relationship of the other faults with the basal décollement as the seismic survey was conducted at a regional-scale (872 km long and 20 s TWT or ~60 km depth; Doublier et al. 2020).

(vii) The dip of the reverse faults on cross-sections range between ~36-79°, with most faults dipping between ~50-65° (Figure 11).

(viii) Minimum displacements were imposed on faults so that they match the mapped surface geology.

(ix) The 3D magnetic inversion was projected along the line of cross-sections to constrain the locations of basement highs.

(x) We did not include the youngest Wilki Formation in the cross sections, as the true thickness of this unit is ambiguous. However, its omission does not affect the structural geometry or interpretations presented in this study.

(xi) The EE′ transect is oriented along 055°-235°, perpendicular to the strike of regional structures in that area (Figure 6). We only portrayed the Coolbro Sandstone, Broadhurst, and Isdell formations in this cross-section (Figure 11). The geometry of the Nifty syncline was constrained from the detailed structural model of (Anderson et al. 2001) and Ferguson et al. (2005).

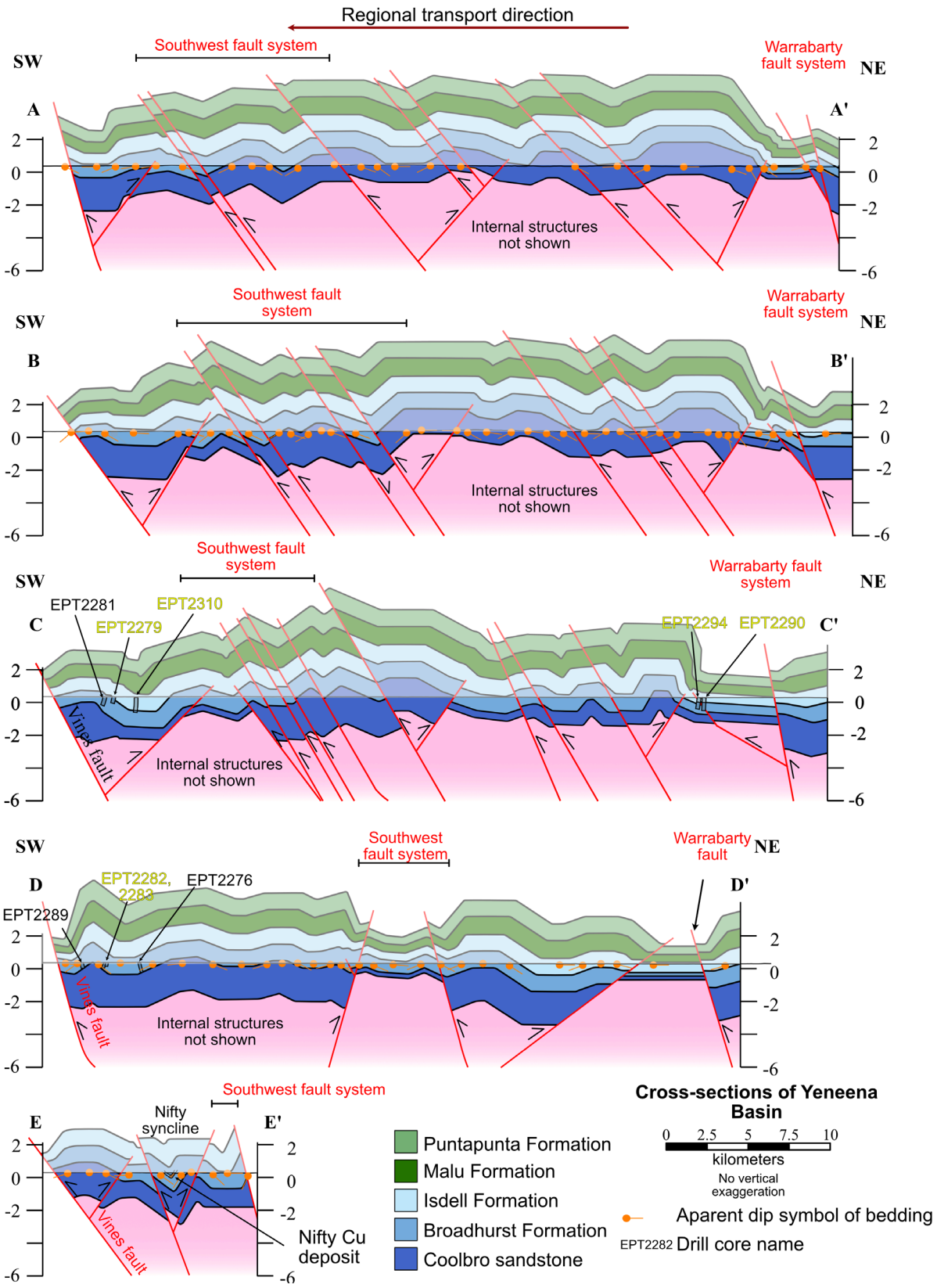

Figure 11: Present-day, regional-scale cross-sections of the Yeneena Basin along AA', BB', CC', DD', and EE' (locations shown in Figure 6). Lighter shading indicates rocks that extend above the current erosion surface.

5.2.2 Restored sections

The deformed cross-sections AA′-DD′ were restored to their undeformed state using the line-length balancing technique in the *KronosFlow* (BeicipFranlab) software (Figure 12). The EE′ cross-section was not restored, as this region recorded significant out-of-plane motion associated with strike-slip deformation during the Paterson event (Bagas 2004), violating the plane strain (in-plane motion) assumption of constructing a balanced cross-section.

Restoration of the cross-sections indicates that there are at least two basement highs in the studied region, which segmented the basin into smaller subbasins (Figure 13). Minimum shortening was calculated by subtracting the deformed length of the lithological units from their undeformed lengths (Figure 12). The total minimum shortening was calculated to be ~11 km with a shortening percentage of ~19% from the AA′ transect. The total minimum shortening progressively increases to ~17 km (~26%) at the BB′ transect and ~21 km (~31%) at the CC′ transect, then decreases to ~13 km (~23%) at the DD’ transect.

Based on the four restored cross-sections, we constructed a 3D model of the undeformed basin using *Leapfrog Geo* software (Figure 13). Within the software, fault planes and lithological boundaries were digitised as polylines. These polylines served as the foundation for generating 3D surfaces of both faults and formation boundaries, using the radial basis function algorithm implemented in *Leapfrog Geo* to interpolate between the polylines. This 3D model provided geometric input for the small-scale SFM (Section 5.3.3.5).

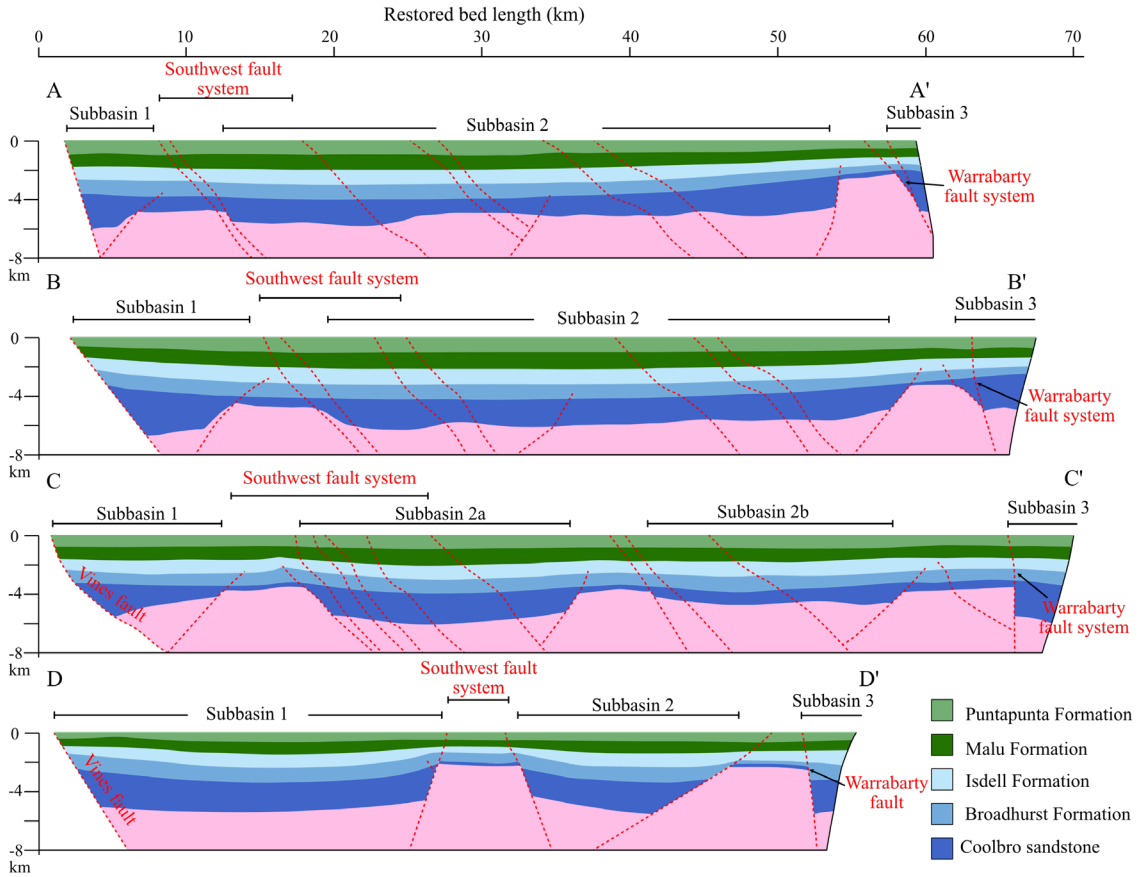

Figure 12: Restored cross-sections along AA', BB', CC', and DD' showing basement highs and subbasins that formed during deposition of the Coolbro Sandstone and Broadhurst Formation. At this stage, faults bounding the basement highs acted as normal faults but did not affect overlying younger strata. These faults were later reactivated as reverse faults during subsequent shortening, when they cut through the Isdell, Malu, and Puntapunta formations.

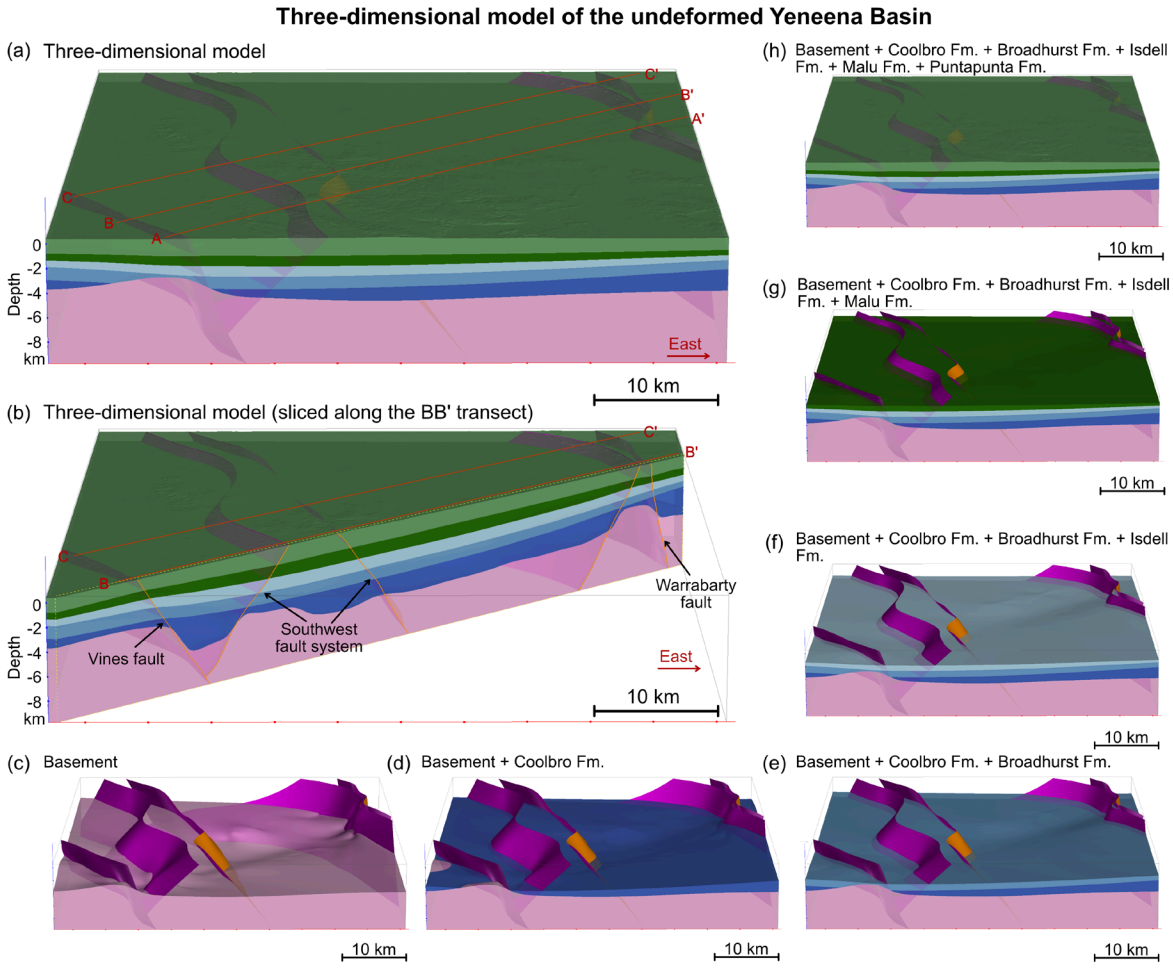

Figure 13: Three-dimensional model of the Yeneena Basin in its undeformed state, before basin inversion. The model was generated from the 2D restored sections AA'–CC' using Leapfrog Geo software.

5.2.3 2.5D reconstructions

The term 2.5D is used here to refer to 2D plus time, i.e. kinematic reconstruction based on 2D cross sections. In the absence of direct faulting age data, the kinematic sequence of structure formation remains uncertain. Therefore, we have relied on indirect lines of evidence to infer the sequence of deformation.

1) Shear fractures typically form at angles of 30°±15° relative to the maximum principal stress (σ_1; e.g., Twiss and Moores 1992). Therefore, the observed dips in the deformed- and undeformed-state sections (Figure 11, Figure 12) suggest that most of these faults did not nucleate as reverse faults during the Miles event, assuming that σ_1 was horizontal to sub-horizontal. Instead, they likely represent the reactivation of pre-existing structures. Major reverse faults, such as the Southwest and Warrabarty fault systems, are located along the margins of basement highs (Figure 11). These basement highs are restored as horsts delimited by the Southwest and Warrabarty fault systems (Figure 12). Additionally, the orientations of the reverse faults (Figure 6) are parallel to the planar structural fabrics observed in the basement rocks (Geognostics Australia Pty Ltd 2022). This geometric relationship suggests

structural inheritance, where normal faults that formed during the basin development phase (extensional) were reactivated as reverse faults during subsequent basin inversion. Sibson et al. (1988) and Sibson (1990) provided a mechanical model to explain the reactivation of normal faults as high-angle reverse faults. According to their model, faults that are favourably oriented (~30°±15° to σ_1) are more readily reactivated due to the lower stress ratios required. In contrast, faults that are unfavourably oriented require significantly higher stress ratios to reactivate, which often necessitates elevated fluid pressures to overcome the increased resistance and initiate reactivation. Drill cores (e.g., EPT1831) intersecting major fault zones exhibit kaolinization, brecciation, hematite alteration, and veining, all of which indicate the presence of fluid during faulting (Figure 8). Additionally, the presence of relatively impermeable layers, such as shale, throughout the Yeneena Basin stratigraphy may have resulted in the development of fluid overpressure during the deformation. This overpressure would have promoted the reactivation of normal faults (Sibson et al. 1988; Sibson 1990) as reverse faults during the Miles event. Subsequently, these reverse faults were reactivated again during the Paterson event as oblique-slip faults characterised by a greater strike-slip component than a dip-slip. However, the effects of this oblique-slip movement are most prominently observed NW of the DD′ transect (Williams and Bagas 1999; Bagas 2005).

2) Shortening structures do not develop simultaneously throughout a deforming region. They form progressively as the deformation front moves from one area to another. The deformation front is defined as a conceptual boundary that separates rocks undergoing deformation from those that remain undeformed during progressive deformation (e.g., Gray and Mitra 1993). In the Yeneena Basin, the shortening structures are predominantly NE-SW-trending, but they do not extend beyond the Marloo Fault, which lies to the W-SW of the Yeneena Basin, in the Officer Basin (Figure 6). Hence, the deformation front associated with the Miles event lies near the Marloo Fault. The average fold wavelength between antiform-synform pairs increases systematically toward the southwest. For example, it remains ~3.4 km in areas exposing the Lamil Group in the NE, ~4.8 km in regions exposing the Throssell Range Group in the center, and ~20.2 km in the Officer Basin in the SW (Figure 6). This spatial trend indicates that the NE part of the basin experienced more intense folding than the SW part. A similar conclusion was also reached by Kunzmann et al. (2021). Based on these observations, we interpret that the deformation front within the Yeneena Basin progressively migrated from the northeast to the southwest during basin inversion.

3) Geological mapping of the exposed part of the Rudall complex shows that the basement rocks and the Yeneena Basin rocks are folded along NW-SE-trending hinge lines (Figure 6; Hickman and Bagas 1999), indicating coupled deformation of the basement and the sedimentary cover. Additionally, the reverse faults have crosscut the hinge and limbs of these folds, with segments of the same fold exposed in both the hanging wall and footwall of the reverse faults (Figure 6). Hence, folding predates reverse faulting. The deformation initiated in the NE part of the basin, where sedimentary rocks and the underlying basement were first folded. Subsequently, the basement normal faults were reactivated as reverse faults, transecting these earlier folds. The deformation front then progressively migrated southwestward across the

basin. This progressive kinematic evolution is illustrated in Figure 14, Figure 15, Figure 16, and Figure 17.

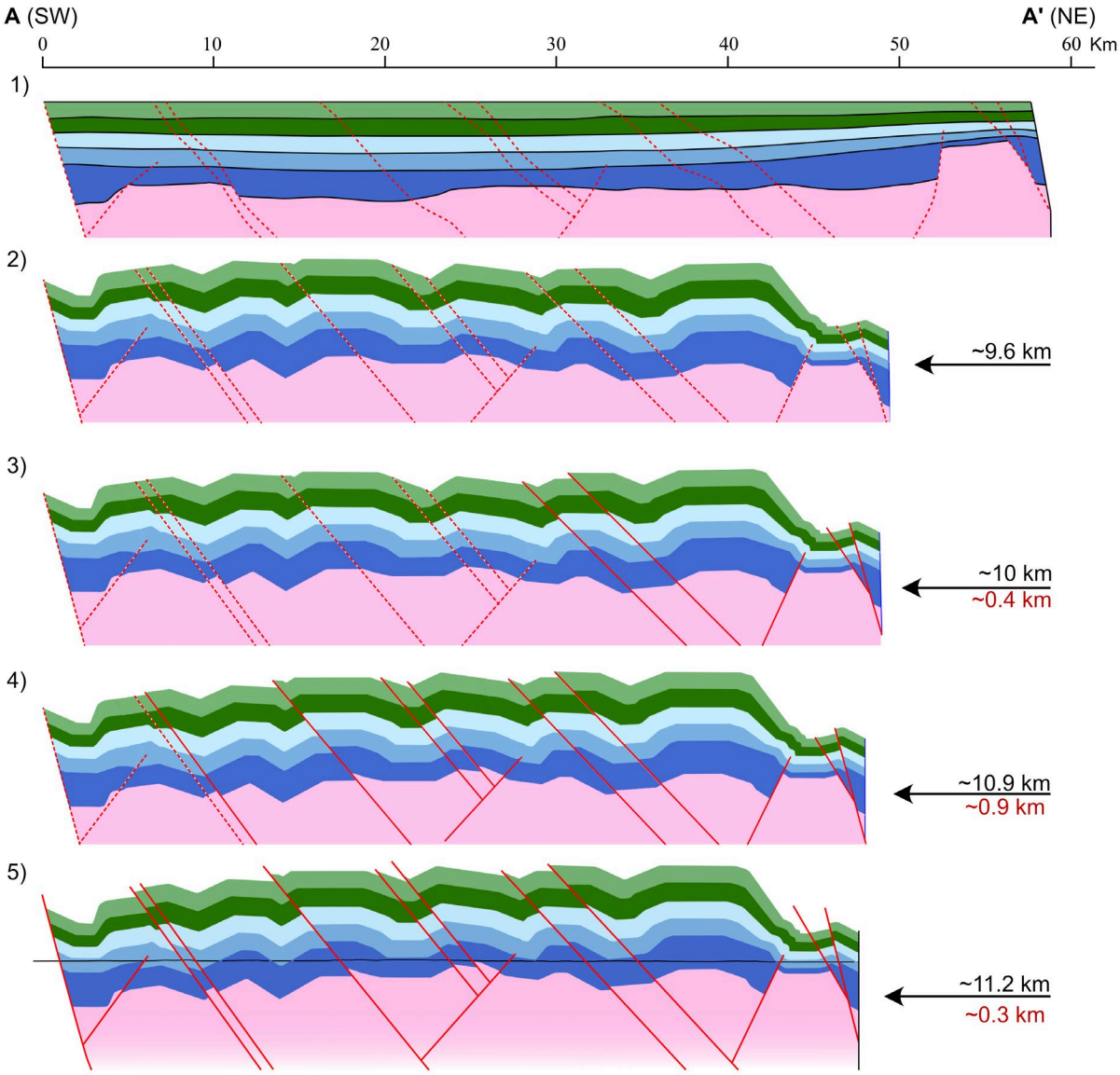

Figure 14: Stepwise kinematic evolution of the Yeneena Basin along the AA' transect. Dashed red lines indicate the locations of developing reverse faults at each stage. Total minimum shortening (black) and incremental minimum shortening (red) are shown for each step.

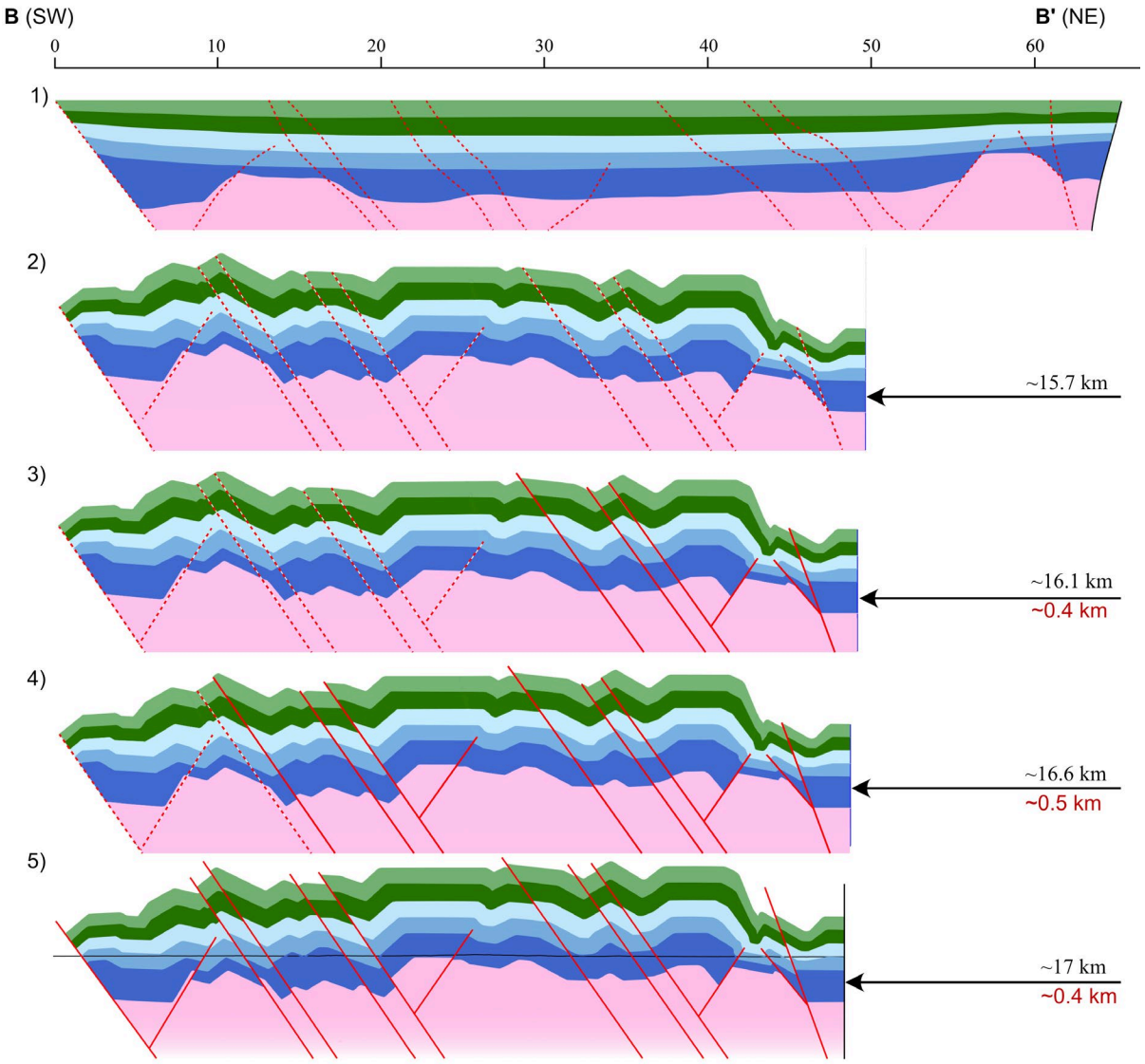

Figure 15. Stepwise kinematic evolution of the Yeneena Basin along the BB' transect. Dashed red lines indicate the locations of developing reverse faults at each stage. Total minimum shortening (black) and incremental minimum shortening (red) are shown for each step.

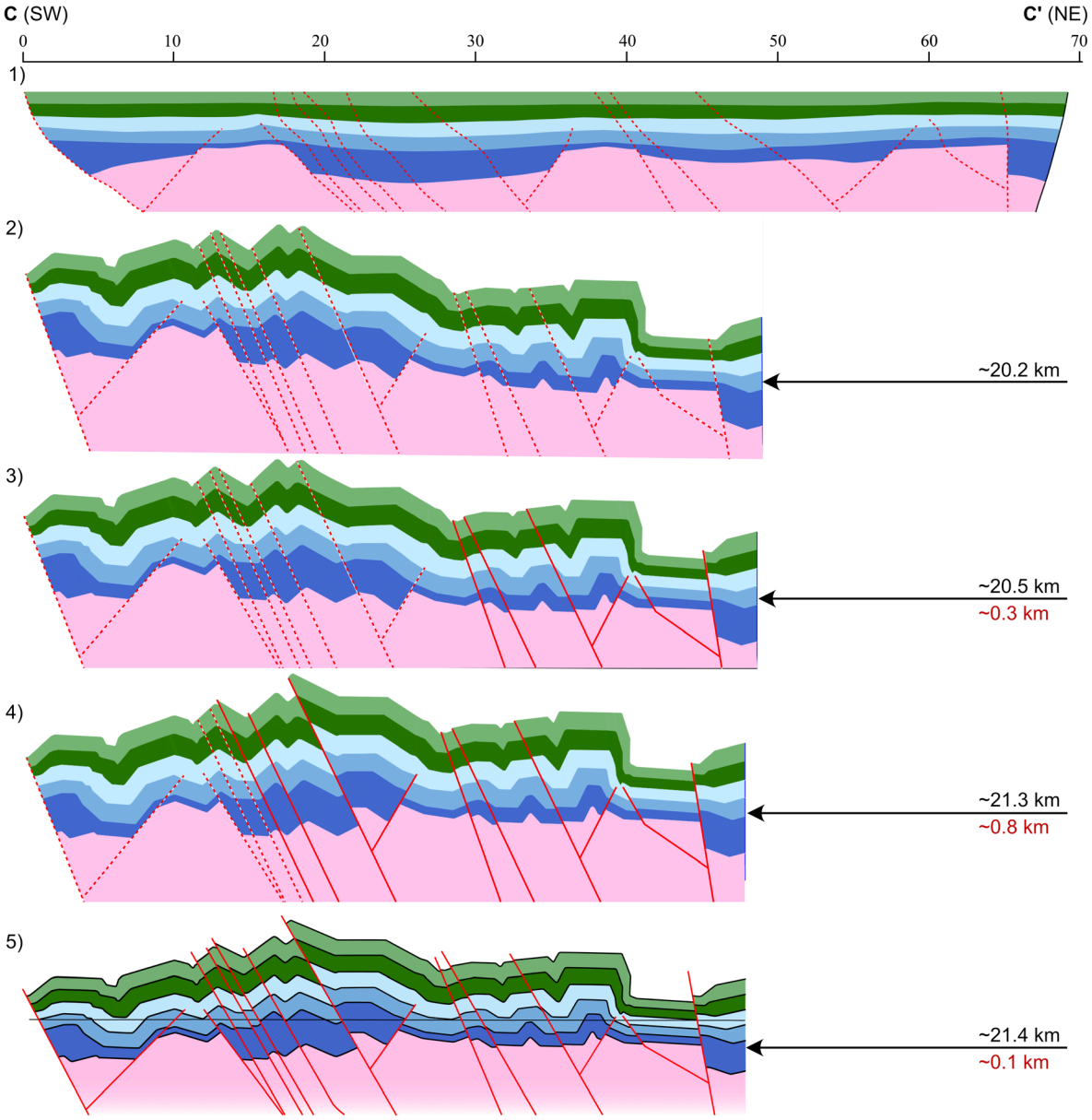

Figure 16. Stepwise kinematic evolution of the Yeneena Basin along the CC' transect. Dashed red lines indicate the locations of developing reverse faults at each stage. Total minimum shortening (black) and incremental minimum shortening (red) are shown for each step.

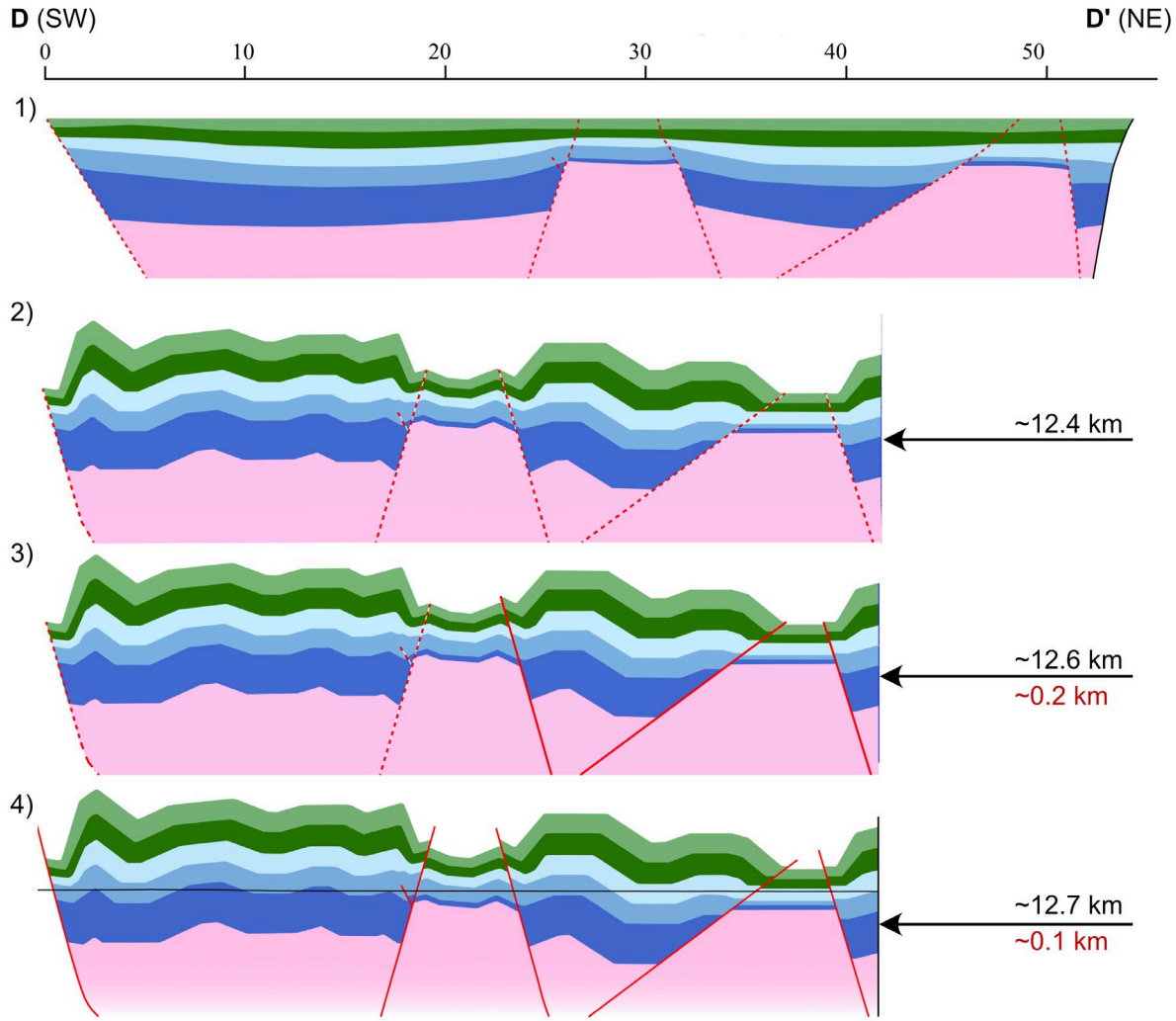

Figure 17. Stepwise kinematic evolution of the Yeneena Basin along the DD' transect. Dashed red lines indicate the locations of developing reverse faults at each stage. Total minimum shortening (black) and incremental minimum shortening (red) are shown for each step.

5.3 Milestone 7: Sedimentary facies distribution through time

5.3.1 Introduction

This step in the analysis uses Stratigraphic Forward Modelling (SFM) to generate a realistic 4D distribution of sedimentary facies in the basin prior to the onset of deformation.

From its introduction by Sloss (1962), the concept of quantitative and predictive stratigraphic modelling has been developed to simulate in 4D the evolution of sedimentary basins by integrating their structural evolution with surface processes, sediment-dispersion equations, and chemical reactions in various SFM programs (Paola 2000; Burgess et al. 2006). The power of this approach lies in its ability to generate realistic geological property distributions between and away from known control points, lines, or volumes under defined boundary conditions (e.g., Madhoo et al. 2016; Lasabuda et al. 2024) , as well as to test hypotheses and identify the influence of various parameters (e.g., subsidence rate) in areas where data are scarce (e.g., Zhang et al. 2020).

This project demonstrates an innovative application of SFM, namely restoring a tectonically-deformed sedimentary basin to its initial undeformed state in order to study its infill, as well as testing different end-member scenarios in order to evaluate whether or not this SFM approach can answer some questions that help identify and/or exclude certain parts of the basin for further mineral exploration purposes. Two models were generated for this project: a large-scale, supra-basin scale model (620 x 560 km) to test the potential for sediment-routing/source-to-sink analysis in the basin, and a high-resolution model (ca. 84 x 90 km), built to provide a framework for fluid flow modelling prior to the tectonic deformation. It is worth noting that these models are plotted in today's geographic context and were not rotated to display them in the geographic orientation that prevailed at the time of the basin's existence due to the lack of control on such parameters.

5.3.2 Methods

Several SFM programs exist, each with a range of strengths and limitations (see full discussion in Dhote and Bhan 2025). This project used the commercial software DionisosFlow by BeicipFranlab, which is built on diffusive transport processes equations (Granjeon and Joseph 1999), and the open-source software Badlands, which is designed to simulate "landform development and test source-to-sink concepts" (Salles and Hardiman 2016).

Both programs were used for the large-scale model to compare their output, whereas only DionisosFlow was used to generate the high-resolution model. Parameter values are listed in the related sub-chapters below.

5.3.3 SFM models

5.3.3.1 DionisosFlow input parameters

For the large-scale and high-resolution models, the following inputs were implemented in DionisosFlow:

- Paleogeographic maps defining the topography/bathymetry at specific time horizons;
- Sediment class definitions and associated properties such as grain size and density;
- Precipitation rates of carbonates and evaporites through time and at various depths;
- Subsidence and thickness maps for each time interval;
- Eustatic sea-level curve;
- Position of sediment sources;
- Sediment supply rate, fluvial discharge, and sediment class proportions through time for all sediment sources;
- Transport process parameters;
- Wave characteristics.

5.3.3.2 Large-scale model – DionisosFlow

The large-scale model was designed to test the sediment route from a source-to-sink perspective for 190 Myr during the deposition of the Coolbro Sandstone starting at 960 Ma to the Puntapunta Formation ending at 770 Ma. The model was centred around the Yeneena Basin, from which it expands in all directions in order to capture the surrounding terrain in a source-to-sink approach and reduce boundary effects. The SFM codes use finite boundaries that do not allow sediment to pass through, hence the boundaries tend to generate artifacts where the sediment flows interact with them. Expanding the model beyond the area of interest reduces the impact of these artifacts. Using the EPSG:7851 projection (GDA2020; MGA Zone 51), the four corners of the input datasets have the following coordinates:

- Bottom left: 217,054; 7,227,011
- Bottom right: 793,054; 7,227,011
- Top left: 217,054; 7,865,011
- Top right: 793,054: 7,865,011

defining an area extending 638 km north-south and 576 km east-west (Fig. 15). High-resolution palaeogeographical maps of this area were imported into DionisosFlow, where each grid-cell has a resolution of 20 x 20 km (which can be changed). Note that DionisosFlow can only handle a square or rectangular model domain and grid-cells. Because of the 20 x 20 km cell-size and the origin of the grid coinciding with the SW-corner of the palaeogeographical maps, the large-scale model in DionisosFlow is 620 km north-south and 560 km east-west, trimming 18 and 16 km off the northern and western sides of these maps.

Geometric input parameters such as palaeogeographic maps cannot be generated from the restored cross-sections given their very limited extent compared with the overall size of the SFM model domain (Fig. 15). Five palaeogeographic maps therefore had to be constructed manually from available data to represent the elevation/bathymetry of the “Top Basement-Base Coolbro Sandstone” at 960 Ma used to start the model; “Top Coolbro Sandstone-Base Broadhurst Formation” at 930 Ma; “Top Broadhurst Formation-Base Isdell Formation” at 890 Ma; “Top Isdell Formation-Base Malu Formation” at 850 Ma; and “Top Malu Formation-Base Puntapunta Formation” at 810 Ma (Fig. 16). These paleogeographic maps were designed in Adobe Illustrator using the “Depth to Basement” surface (see chapter 4.1.2.3), major fault traces, borehole data, and results from the subsidence modelling. As no accurate height (topographic elevation) and depth (bathymetry) values exist for these palaeogeographical maps, each of them was constrained with a maximum possible height of 250 m, and a maximum seafloor depth of 450 m. It should be noted that these paleogeographic maps are approximate in nature and subject to considerable uncertainty; nonetheless, they represent a reasonable starting point for the SFM.

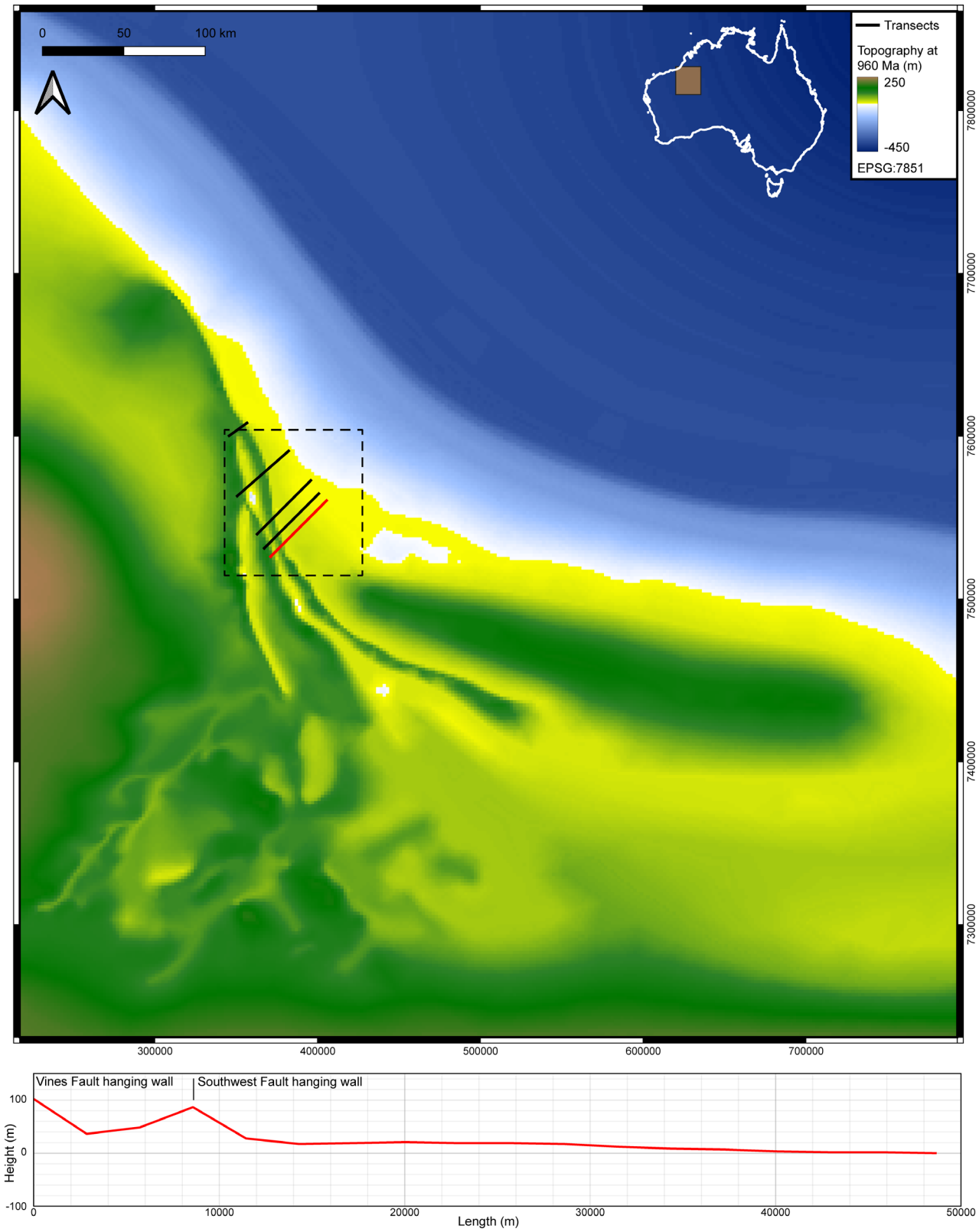

Figure 18: Palaeogeographical map at the time of the onset of Coolbro Sandstone deposition, with the trace of the cross sections for reference. The topography along the red trace of the AA' cross-section is displayed underneath the map. The dashed black rectangle indicates the extent of the high-resolution model.

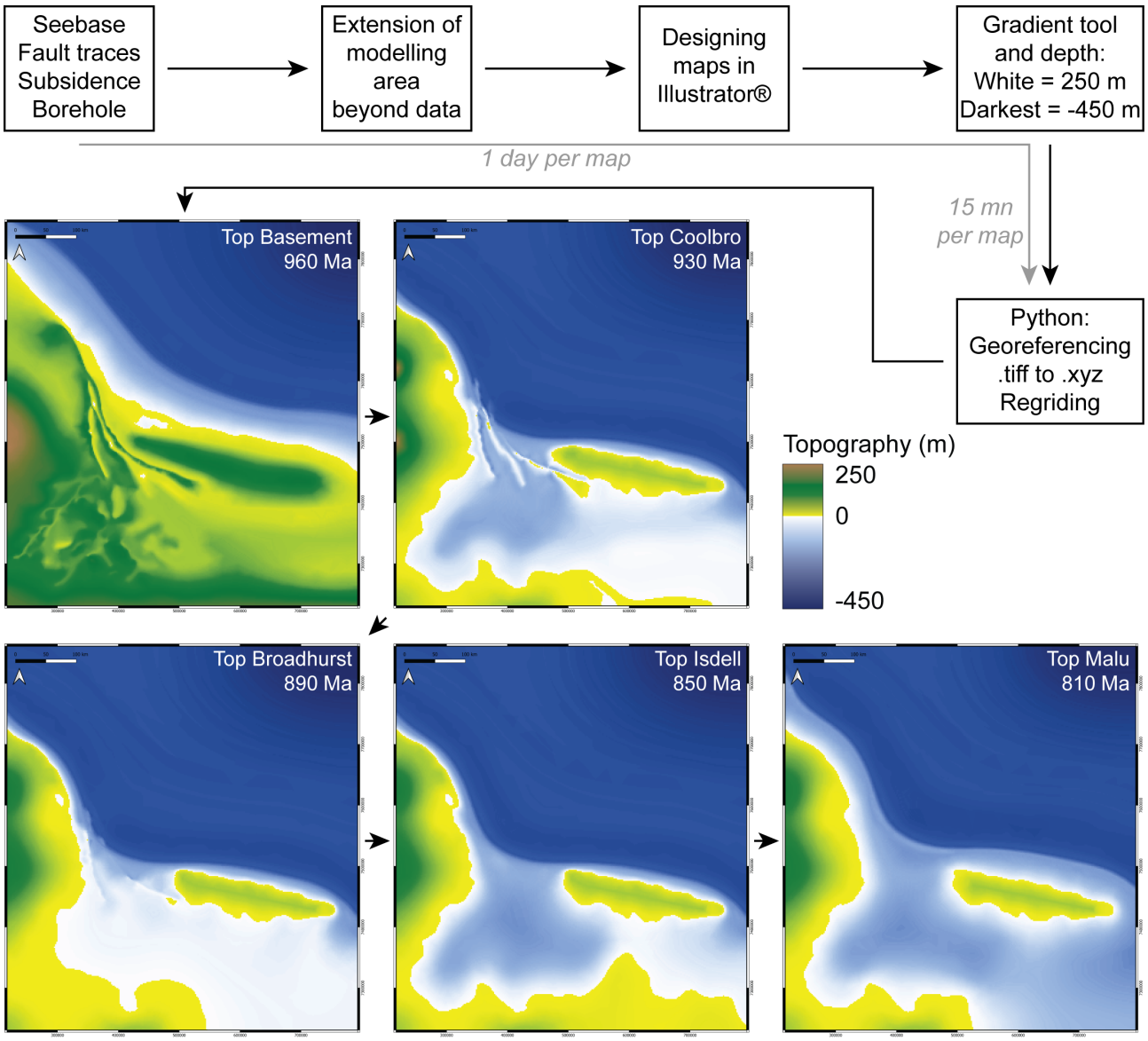

Figure 19: Workflow to design the different palaeogeographical maps used in the large-scale SFM model.

Sediment classes were defined as: gravel; sand; silt; (siliciclastic) mud; carbonate mud; carbonate (microbialites), and gypsum. These sediment classes were attributed specific values defined using some of DionisosFlow default density, hydraulic-conductivity, infiltration-capacity values, predefined compaction curves, and carbonate- and evaporite-growth rates, or generic average grain-size values (e.g., 0.4 mm for medium sand grain size; Table 3 and Table 4).

Table 3: Sediment class characteristics.

Sediment Type	Grain size (mm)	Density (km/m3; default)	Hydraulic conductivity (cm/s; default)	Infliltration capacity (mm/yr; default)	Default burial compaction curve
Gravel	4	2500	0.1	100	Yes
Sand	0.4	2630	0.1	100	Yes
Silt	0.03	2600	0.1	100	Yes
Mud	0.004	2750	0.1	100	Yes
Carbonate mud	0.01*	2710	0.1	100	Yes
Carbonate	0.5*	2710	0.1	100	Yes
Gypsum	0.01*	2500	0.1	100	Yes
	*Default				

Table 4: Carbonate- and evaporite-sediment growth and dissolution rates used for the large-scale model. Values in A for the carbonate mud and the carbonate precipitation rates were automatically generated from DionisosFlow in-built literature repository (Al-Salmi et al. 2019; Kolodka et al. 2016) , whereas the gypsum precipitation rate was derived from Ebner & Meijer (2025). Values in B and C were provided by Schmid, S. Values in D for the carbonate mud and the carbonate were automatically generated by multiplying A with B for each depth and each time-interval.

A — **Precipitatopm rate with depth**

Water Depth (m)	Carbonate mud	Carbonate	Gypsum
	Default, Al-Salmi et al., 2019	Default, Kolodka et al., 2016	Ebner & Meijer, 2025
0	1	1	0
0.5	1	0.995	1
1	1	0.99	0
5	1	0.95	0
8	0.99	0.92	0
10	0.76	0.9	0
12	0.13	0.846	0
15	0	0.765	0
20	0	0.63	0
30	0	0.52	0
40	0	0.26	0
50	0	0.18	0
60	0	0.1	0
80	0	0.02	0
100	0	0	0

B — **Precipitation rate with time**

Age (Myr)	Carbonate mud (m/Myr)	Carbonate (m/Myr)	Gypsum (m/Myr)
770	0	0	0
810	100	100	1600
850	35	35	1600
890	160	160	1600
930	35	35	1600
960	0	0	0

C — **Dissolution rate (m/Myr)**

Carbonate mud (m/Myr)	Carbonate (m/Myr)	Gypsum (m/Myr)
12	16	16

D — **Precipitation rate with time**

Depth (m)	Carbonate mud (m/Myr)					Carbonate (m/Myr)					Gypsum (m/Myr)				
	960-930 Ma	930-890 Ma	890-850 Ma	850-810 Ma	810-770 Ma	960-930 Ma	930-890 Ma	890-850 Ma	850-810 Ma	810-770 Ma	960-930 Ma	930-890 Ma	890-850 Ma	850-810 Ma	810-770 Ma
0	0	35	160	35	100	0	35	160	35	100	0	0	0	0	0
0.5	0	35	160	35	100	0	34.825	159.2	34.825	99.5	0	1600	1600	1600	1600
1	0	35	160	35	100	0	34.65	158.4	34.65	99	0	0	0	0	0
5	0	35	160	35	100	0	33.25	152	33.25	95	0	0	0	0	0
8	0	34.65	158.4	34.65	99	0	32.2	147.2	32.2	92	0	0	0	0	0
10	0	26.6	121.6	26.6	76	0	31.5	144	31.5	90	0	0	0	0	0
12	0	4.55	20.8	4.55	13	0	29.61	135.36	29.61	84.6	0	0	0	0	0
15	0	0	0	0	0	0	26.775	122.4	26.775	76.5	0	0	0	0	0
20	0	0	0	0	0	0	22.05	100.8	22.05	63	0	0	0	0	0
30	0	0	0	0	0	0	18.2	83.2	18.2	52	0	0	0	0	0
40	0	0	0	0	0	0	9.1	41.6	9.1	26	0	0	0	0	0
50	0	0	0	0	0	0	6.3	28.8	6.3	18	0	0	0	0	0
60	0	0	0	0	0	0	3.5	16	3.5	10	0	0	0	0	0
80	0	0	0	0	0	0	0.7	3.2	0.7	2	0	0	0	0	0
100	0	0	0	0	0	0	0	0	0	0	0	0	0	0	0

The next parameters to define are subsidence maps and thickness maps. Ideally, these maps are directly generated from seismic data, well data, or interpolated from various kind of horizons (see high-resolution model chapter). For this large-scale model, none of these maps can directly be generated from data. They had to be generated in DionisosFlow, using wells and restored cross-sections as tools to approximate the value each pixel should have, as well as the spatial and temporal distribution of subsidence and thickness associated with fault activity. It is worth noting that the subsidence maps display total subsidence of the lowermost surface, i.e. Top Basement, through time (Figure 17). Thickness maps display the thickness of the sediment accumulated during the time-period encapsulated by each formation and equivalent lateral lithostratigraphical units (Figure 18). Additionally, concepts such as clinoform migration and tectonostratigraphy were incorporated in the design of these

maps. Sea-level oscillations were also incorporated in the simulations, with ±40 m of eustatic sea-level cycle lasting 400 kyr.

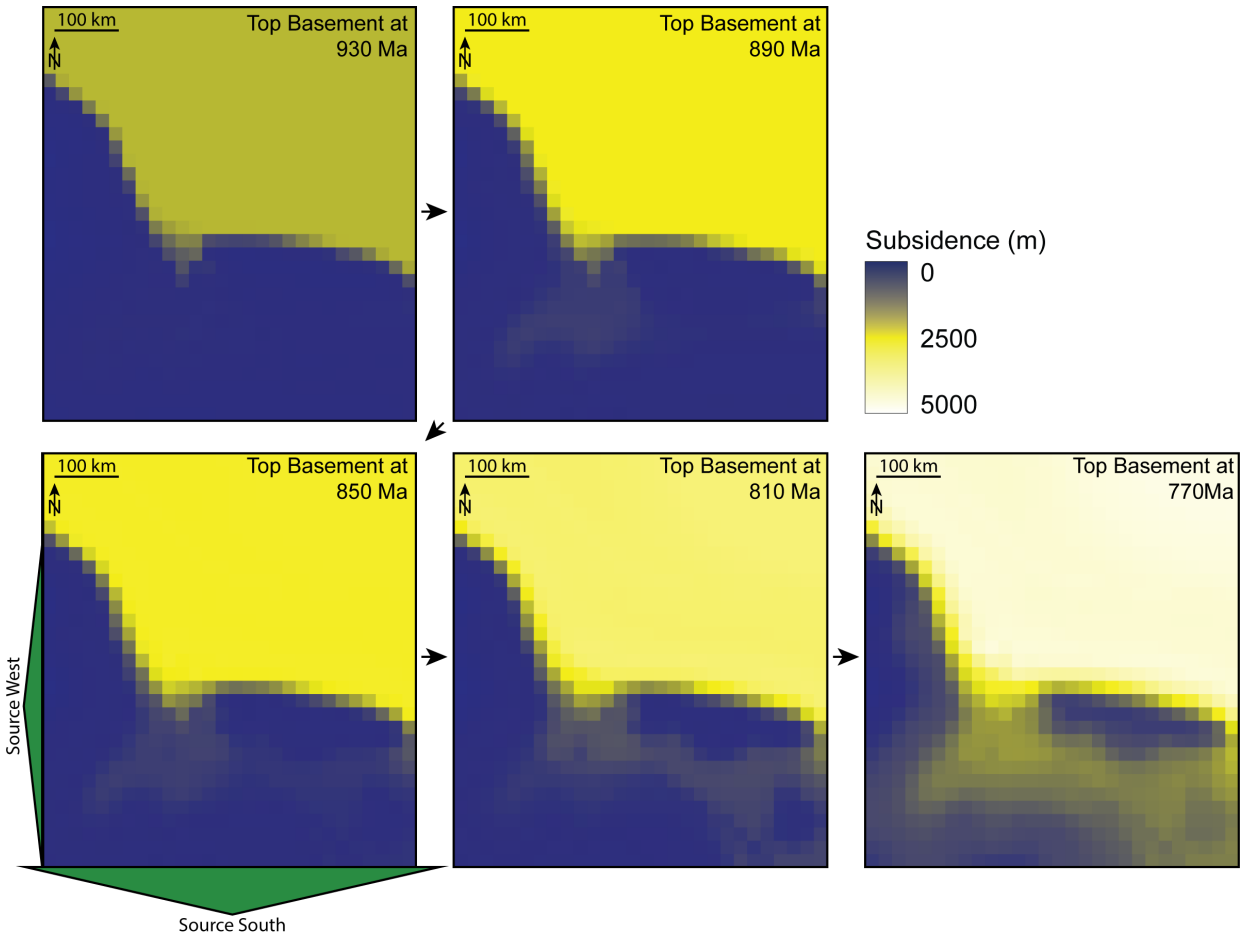

Figure 20: Subsidence maps calculated for the Top Basement surface. Note the illustrative position of the two sediment sources active throughout the simulation.

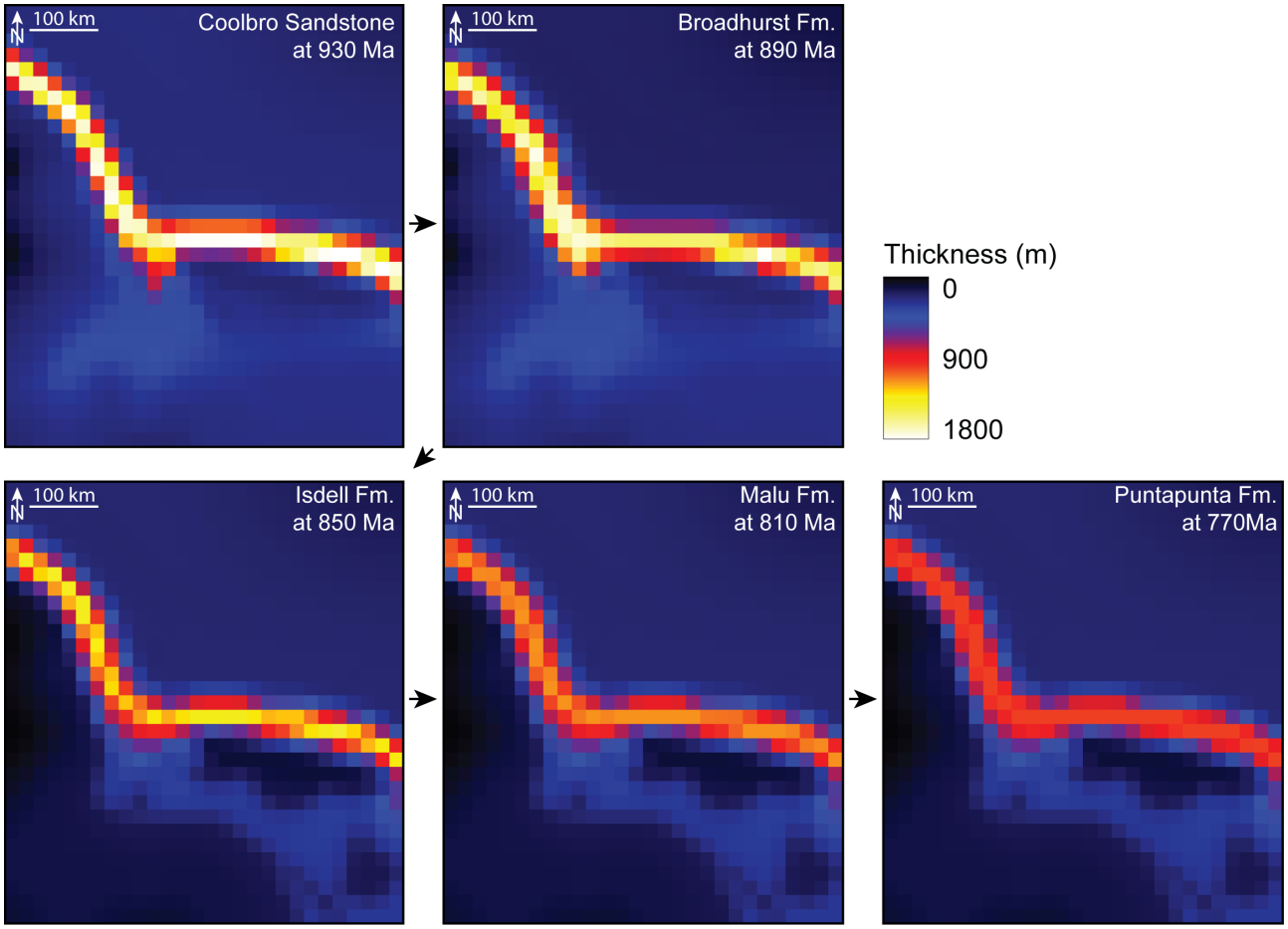

Figure 21: Distribution of the thicknesses associated with the duration of each formation, illustrating the integration of the concept of clinoform migration in the workflow.

Two sediment sources were placed on the western and southern sides of the grid, representing sediment sourced from the Pilbara Craton and from the Officer Basin, respectively (Figure 17; Kohanpour et al. 2024). The southern source is the major source of sediment, whereas the western one represents between 1/3 to 20 % of the overall sediment supply and discharge in the series of run simulations. Because the southern source is the major one and covers the entire southern edge of the grid, it was expanded beyond the edge of the grid to mitigate the interaction of source-edge and the finite-boundary of the grid itself. The sediment supply and fluvial discharge were first estimated directly from the DionisoFlow built-in estimation tool (which divides the thickness maps by the time they represent), and were updated after each simulation's error calculation to reduce the error. The sediment-supply discharge-values used in the last simulation are displayed in Table 5. Note that the 0-value for the carbonate-, carbonate-mud-, and gypsum-sediment classes mean that these did not enter the system as clastic particles through the two sediment sources; instead, these sediment classes could precipitate in-situ during the simulation. Based on available knowledge of the area, evaporation and rainfall-precipitation rates were set at 850 mm/year and 250 mm per year, respectively. These values correspond to an aridity index of 0.21, consistent with AQUASTAT of Food and Agriculture Organisation of the United Nation semi-arid classification (data.apps.fao.org).

Table 5: Sediment supply, fluvial discharge, and sediment proportion through time for both sediment sources.

Source West			Sediment proportion (%)						
Age [Ma]	Supply (km^3/Ma)	Fluvial Discharge (m^3/s	Gravel	Mud	Sand	Silt	Carbonate	Carbonate Mu	Gypsum
Average	*1341.72*	*868.01*	*10*	*30*	*40*	*20*	*0*	*0*	*0*
810-770	1111.36	718.98	10	30	40	20	0	0	0
850-810	1140.78	738.02	10	30	40	20	0	0	0
890-850	1166.56	754.69	10	30	40	20	0	0	0
930-890	1429.73	924.95	10	30	40	20	0	0	0
960-930	2033.02	1315.24	10	30	40	20	0	0	0

Source South			Sediment proportion (%)						
Age [Ma]	Supply (km^3/Ma)	Fluvial Discharge (m^3/s	Gravel	Mud	Sand	Silt	Carbonate	Carbonate Mu	Gypsum
Average	*4025.17*	*2604.04*	*10*	*30*	*40*	*20*	*0*	*0*	*0*
810-770	3334.07	2156.94	10	30	30	30	0	0	0
850-810	3422.35	2214.05	10	30	30	30	0	0	0
890-850	3499.68	2264.08	10	40	25	25	0	0	0
930-890	4289.19	2774.84	10	40	25	25	0	0	0
960-930	6099.06	3945.71	10	30	40	20	0	0	0

The transport process inputs were kept as default values (Figure 19), whereas the values associated with each sediment category were attributed using DionisosFlow in-built tool, which derives those values from the grain-size of each sediment category (Table 3).

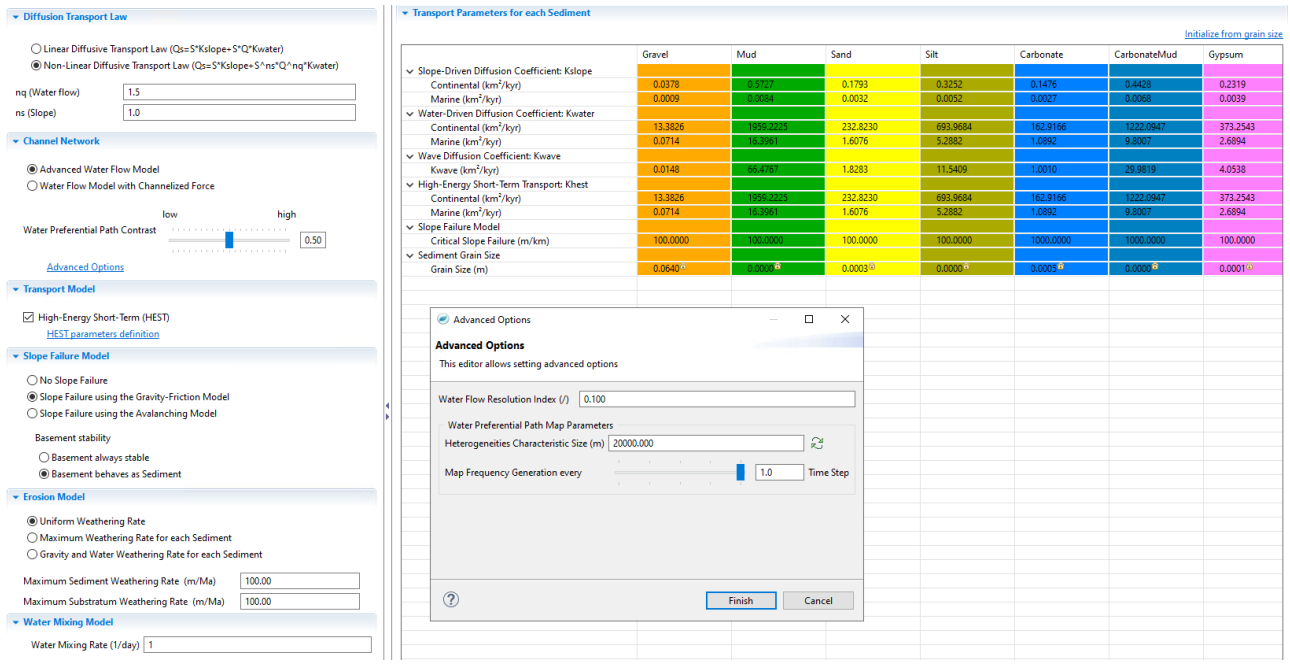

Figure 22: Capture of the transport-process window in DionisosFlow.

Two sets of wave inputs were parametrised to simulate fair-weather and storm-weather waves. Both of these propagated from the north-east to the south-west, and their energy-decrease with depth and as they propagate towards the shoreline followed DionisosFlow's in-built Snell's law equation (e.g., Holthuijsen 2007, ch. 7). All the values of wave-base depth, propagation azimuth, and frequency/year values were kept constant throughout the 960-770 Ma time-frame of the simulations (Table 6). The tidal range was set at 2 m. No

organic-matter production is incorporated in the model. Ocean salinity and temperature were kept at their default value of 35g/L and 20 °C, respectively.

Table 6: Fair- and storm-weather waves parameters.

	Age (Ma)	960	930	890	850	810	770	
Fair-weather wave	Wave base (m)	7.00	7.00	7.00	7.00	7.00	7.00	Automatically generated
	Wave propagation azimuth (°)	225.00	225.00	225.00	225.00	225.00	225.00	
	Frequency/year	52.00	52.00	52.00	52.00	52.00	52.00	
	Wave energy (kW/m)	1023.74	1023.74	1023.74	1023.74	1023.74	1023.74	
	Wind speed (m/s)	941.64	941.64	941.64	941.64	941.64	941.64	
	Wave period (s)	4.01	4.01	4.01	4.01	4.01	4.01	
	Wave height (m)	2.51	2.51	2.51	2.51	2.51	2.51	
Storm weather wave	Wave base (m)	40.00	40.00	40.00	40.00	40.00	40.00	Automatically generated
	Wave propagation azimuth (°)	225.00	225.00	225.00	225.00	225.00	225.00	
	Frequency/year	0.50	0.50	0.50	0.50	0.50	0.50	
	Wave energy (kW/m)	650.16	650.16	650.16	650.16	650.16	650.16	
	Wind speed (m/s)	2732.15	2732.15	2732.15	2732.15	2732.15	2732.15	
	Wave period (s)	9.59	9.59	9.59	9.59	9.59	9.59	
	Wave height (m)	14.36	14.36	14.36	14.36	14.36	14.36	

5.3.3.3 Example of results from the large-scale SFM

Once the simulation has finished running, the proportions of the different sediment classes and associated properties (e.g., porosity), and environmental properties (e.g., wave energy, turbidity level), are plotted on a 4 dimensional grid (Figure 20). Several properties can be grouped together to define so-called “facies”. Note that this concept of facies is rather loose and does not correspond to the sedimentological definition of a process-based facies (Posamentier and Walker 2006), but rather comprises properties such as depositional depth, sediment proportion, distance to shore, or turbidity level (among others), which the user can tweak. Given the subjective aspect of it, this project has refrained from defining such features in DionisosFlow as they are not required for fluid-flow studies but are rather an unnecessary categorisation of the data for the purpose of this project.

Simulation results showed that, to the best of the available knowledge incorporated in the input parameters, the sediments could have transited through the Western and NW Officer Basin before reaching the Yeneena Basin.

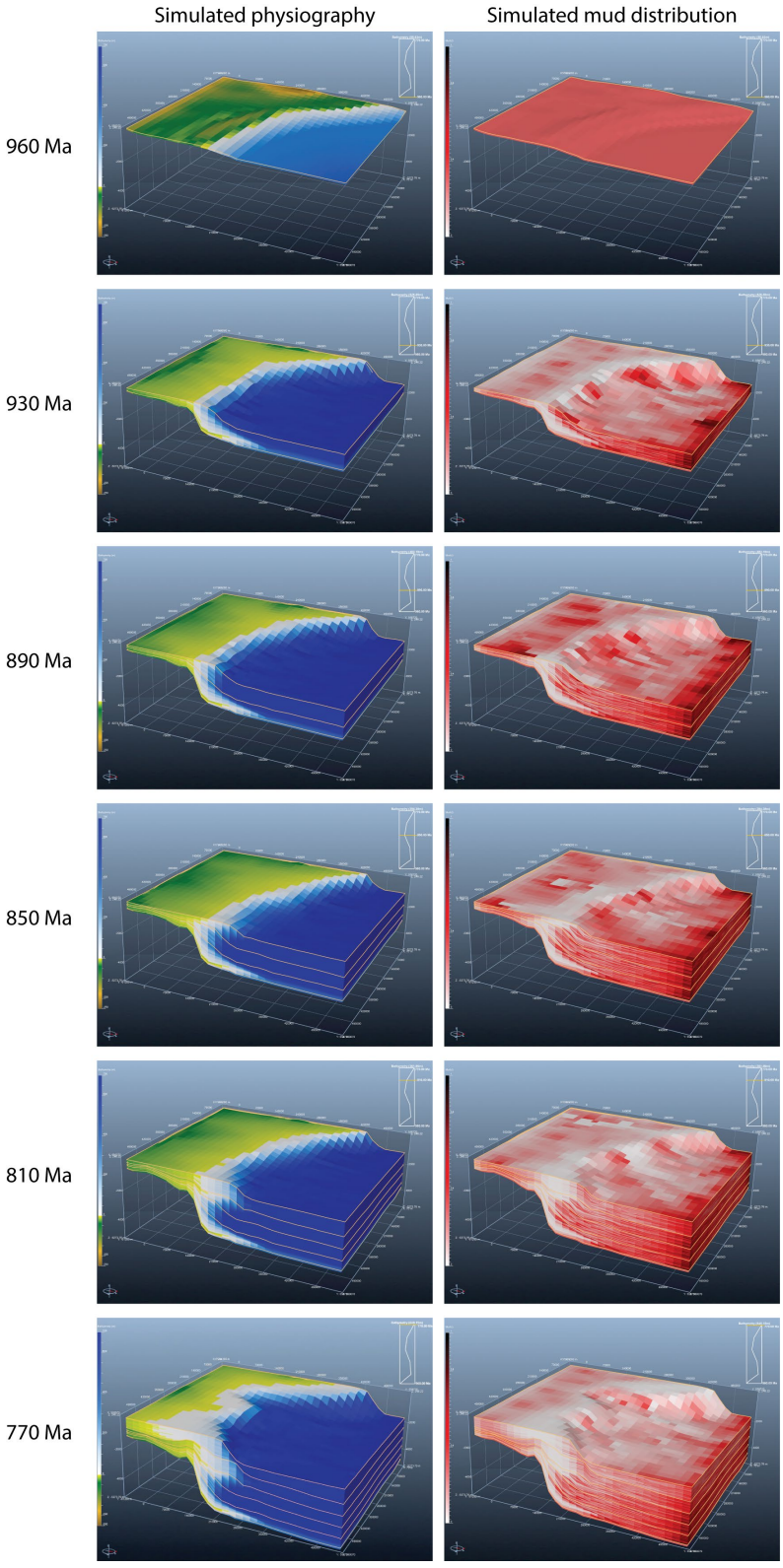

Figure 23: Example of simulation results plotted on a four-dimensional grid. This figure displays the evolution of the physiography through time, and the associated mud distribution. The shoreline is marked by the contact of the white (marine) and yellow colours (continent). The higher the mud concentration, the redder the grid cell. Note that north is to the right side of the image.

5.3.3.4 Large-scale model – Badlands

In addition to fundamental design differences between DionisosFlow and Badlands (Granjeon and Joseph 1999; Salles and Hardiman 2016), one of the main differences is that Badlands is python-based, with all input parameters set in one .xml file that the program then reads. The detail of that .xml file is available as Appendix A1.3 p.128. Badlands used the same initial grid of the Top Basement surface, wave-propagation direction, as well as the same eustatic sea-level curve as used in the DionisosFlow model. Note that Badlands was not run for the 190 Ma covered by the targeted stratigraphy, but was rather used to test sediment-routing hypotheses during the time the Coolbro Sandstone was being deposited during the main extensional phase of the Basin (Figure 21). One river source was forced from the edge of the Officer Basin to simulate a sediment-entry point to the south of the Yeneena Basin.

Bandlads simulation results suggested that most of the fault-controlled subbasins in the NW Officer Basin and Yeenena Basin were initially filled by sediments sourced from adjacent highs. When the relief was healed, the sediment transport-distance could have then increased. Prominent river systems could have accelerated this relief-healing process, meaning that river-derived sediments could have entered the Yeneena Basin after passing through the NW Officer Basin at a very early stage of the basin development.

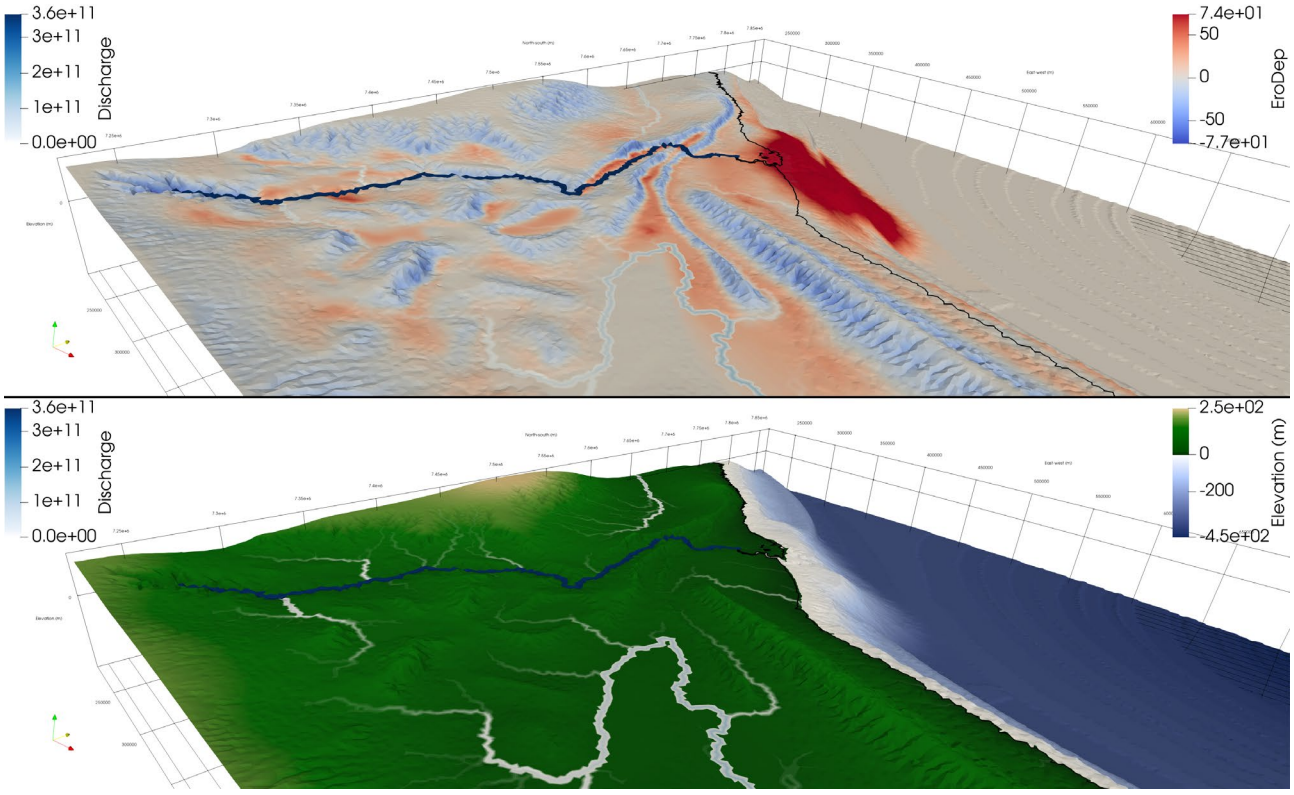

Figure 24: Large-scale model run in Badlands, illustrating a potential physiography during the early Coolbro-time. Top: Erosion/deposition, showing infill (red) of local depressions by sediment eroded from adjacent highs (blue). Bottom: Elevation/bathymetry. Vertical exaggeration: 100 x.

5.3.3.5 High-resolution model – DionisosFlow

Using all available drill-core data and results from the structural restoration, this step aims at generating a geologically realistic 4D distribution of the sedimentary facies in part of the

basin prior to deformation. Ultimately, this step results in a 4D distribution of porosities, which are later converted into permeabilities for fluid flow modelling (Section 6.1.3). Although using the same sediment properties (with the exception of gypsum precipitation rates; Table 7), sediment transport parameters (Figure 19), eustasy, and wave setup (Table 6) as the large-scale model, this high-resolution model differs from the large-scale model because its smaller scale enables used of inter- and extrapolated surfaces from the structural reconstructions to create subsidence and thickness maps. Fault surfaces were also useful to illustrate the development of syn-sedimentary growth packages in the Coolbro Sandstone (Figure 22).

Table 7: Carbonate- and evaporite-sediment growth and dissolution rates used for the high-resolution model. Values in A for the carbonate mud and the carbonate precipitation rates were automatically generated from DionisosFlow in-built literature repository (Al-Salmi et al. 2019; Kolodka et al. 2016), whereas the gypsum precipitation rate was derived from Ebner and Meijer (2025). Values in B and C were provided by Schmid, S. Values in D the carbonate mud and the carbonate mud were automatically generated by multiplying A with B for each depth and each time-interval.

A — **Precipitatopm rate with depth**

Water Depth (m)	Carbonate mud (m/Myr)	Carbonate (m/Myr)	Gypsum (m/Myr)
	Default, Al-Salmi et al., 2019	Default, Kolodka et al., 2016	Ebner & Meijer, 2025
0	1	1	0
0.5	1	0.995	1
1	1	0.99	0
5	1	0.95	0
8	0.99	0.92	0
10	0.76	0.9	0
12	0.13	0.846	0
15	0	0.765	0
20	0	0.63	0
30	0	0.52	0
40	0	0.26	0
50	0	0.18	0
60	0	0.1	0
80	0	0.02	0
100	0	0	0

B — **Precipitation rate with time**

Age (Myr)	Carbonate mud (m/Myr)	Carbonate (m/Myr)	Gypsum (m/Myr)
770	0	0	0
810	160	160	0
850	35	35	0
890	160	160	0
930	35	35	0
960	0	0	0

C — **Dissolution rate (m/Myr)**

Carbonate mud (m/Myr)	Carbonate (m/Myr)	Gypsum (m/Myr)
12	16	16

D — **Precipitation rate with time**

Depth (m)	Carbonate mud (m/Myr)					Carbonate (m/Myr)					Gypsum (m/Myr)				
	960-930 Ma	930-890 Ma	890-850 Ma	850-810 Ma	810-770 Ma	960-930 Ma	930-890 Ma	890-850 Ma	850-810 Ma	810-770 Ma	960-930 Ma	930-890 Ma	890-850 Ma	850-810 Ma	810-770 Ma
0	0	35	160	35	100	0	35	160	35	100	0	0	0	0	0
0.5	0	35	160	35	100	0	34.825	159.2	34.825	99.5	0	0	0	0	0
1	0	35	160	35	100	0	34.65	158.4	34.65	99	0	0	0	0	0
5	0	35	160	35	100	0	33.25	152	33.25	95	0	0	0	0	0
8	0	34.65	158.4	34.65	99	0	32.2	147.2	32.2	92	0	0	0	0	0
10	0	26.6	121.6	26.6	76	0	31.5	144	31.5	90	0	0	0	0	0
12	0	4.55	20.8	4.55	13	0	29.61	135.36	29.61	84.6	0	0	0	0	0
15	0	0	0	0	0	0	26.775	122.4	26.775	76.5	0	0	0	0	0
20	0	0	0	0	0	0	22.05	100.8	22.05	63	0	0	0	0	0
30	0	0	0	0	0	0	18.2	83.2	18.2	52	0	0	0	0	0
40	0	0	0	0	0	0	9.1	41.6	9.1	26	0	0	0	0	0
50	0	0	0	0	0	0	6.3	28.8	6.3	18	0	0	0	0	0
60	0	0	0	0	0	0	3.5	16	3.5	10	0	0	0	0	0
80	0	0	0	0	0	0	0.7	3.2	0.7	2	0	0	0	0	0
100	0	0	0	0	0	0	0	0	0	0	0	0	0	0	0

The sediment supply, fluvial discharge, and sediment proportion through time (Table 8) had to be adjusted from the large-scale model because of the overall smaller size of this model as well as its palaeogeographical location resulting in marine conditions prevailing over continental ones. This resulted, for instance, in a much lower gravel concentration in the flows, as these sediments would have been deposited prior to reaching the targeted area.

Table 8: Sediment supply, fluvial discharge, and sediment proportion through time for both sediment sources.

Source West			Sediment proportion (%)						
Age [Ma]	Supply (km^3/Ma)	Fluvial Discharge (m^3/s)	Gravel	Mud	Sand	Silt	Carbonate	Carbonate Mud	Gypsum
Average	*40.93*	*28.80*	*4*	*16*	*20*	*16*	*29*	*16*	*0*
810-770	32.00	718.98	0	20	30	20	20	10	0
850-810	26.00	21.00	0	20	20	20	20	20	0
890-850	29.00	17.00	0	10	10	10	50	20	0
930-890	37.00	19.00	0	10	10	10	50	20	0
960-930	82.00	64.00	10	20	30	20	10	10	0

Source South			Sediment proportion (%)						
Age [Ma]	Supply (km^3/Ma)	Fluvial Discharge (m^3/s)	Gravel	Mud	Sand	Silt	Carbonate	Carbonate Mud	Gypsum
Average	*164.07*	*115.40*	*4*	*16*	*20*	*16*	*29*	*16*	*0*
810-770	130.00	2156.94	0	20	30	20	20	10	0
850-810	105.00	84.00	0	20	20	20	20	20	0
890-850	117.00	68.00	0	10	10	10	50	20	0
930-890	148.00	76.00	0	10	10	10	50	20	0
960-930	327.00	96.00	10	20	30	20	10	10	0

The thickness maps of the different sedimentary units were easily generated by calculating the depth difference between the different horizons using the following rule:

$$T_{TargetFormation} = \left| z_1 - z_2 \right| \quad (1)$$

with $T_{TargetFormation}$ being the thickness (m) of a rock formation, z_1 being the depth of top surface of this unit underlying the target formation (or the depth of the base of the target formation; m), and z_2 being the depth of top surface of the target formation unit (or the base of the overlying formation; m). Note that all thicknesses are positive, whereas depth of formation-tops have negative values. Subsidence maps required a more iterative approach, and were generated using the following equations:

$$S_{t770} = \left| z_{TopBasement} \right| \quad (2)$$

$$S_{t810} = S_{t770} + z_{TopMalu} \quad (3)$$

$$S_{t850} = S_{t810} + z_{TopIsdell} \quad (4)$$

$$S_{t890} = S_{t850} + z_{TopBroadhurst} \quad (5)$$

$$S_{t960} = S_{t890} + z_{TopCoolbro} \quad (6)$$

With S_{tx} being the subsidence at time x (m), and $z_{TopFormation}$ being the depth of the top surface of specific formation (m). Note that a positive subsidence means that accommodation is created whereas a negative subsidence implies uplift. Note also that all depth of formation-tops have negative values. Calculating subsidence maps in such a way allowed for fault-related subsidence to be implemented when and where necessary, based on the information from the structural reconstructions.

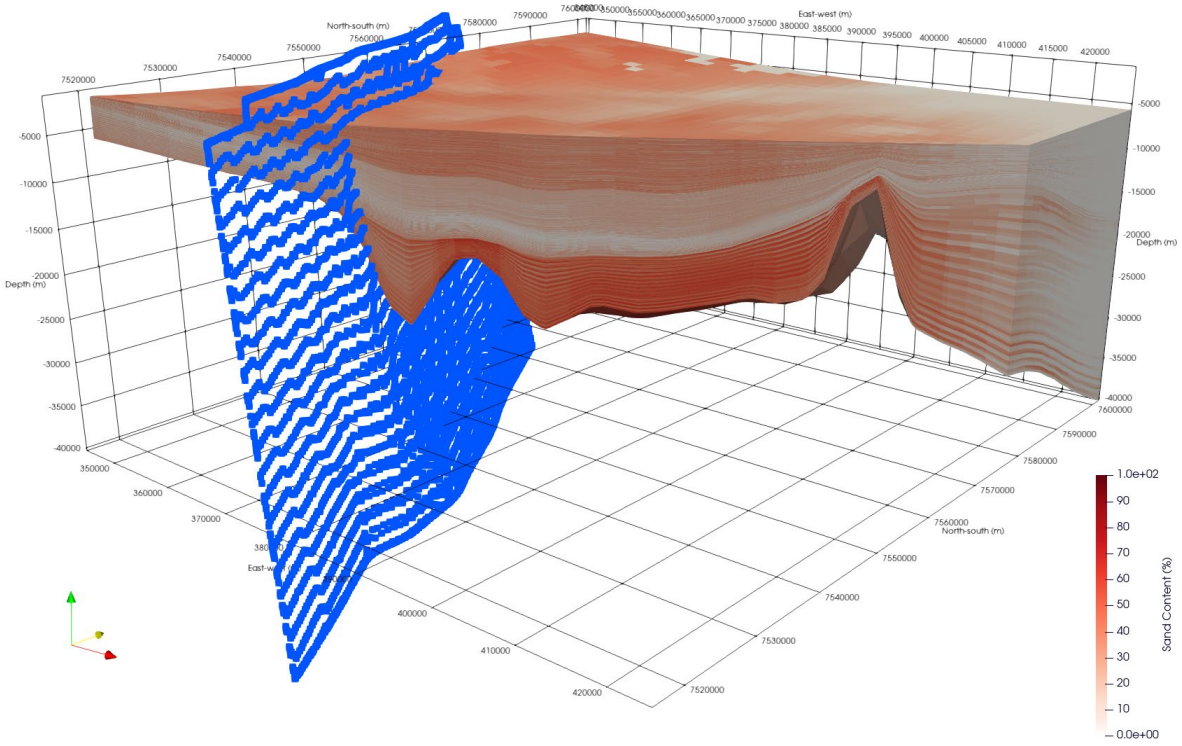

Figure 25: High-resolution model displaying the distribution of sand at 810 Ma (i.e. Top Malu time). The blue surface is the Vines Fault, which was most active during deposition of the Coolbro Sandstone, when several sub-basins were developing. Movement on this fault had largely ceased by the time the overlying Broadhurst Formation and time equivalent units were deposited, reflected in the relatively uniform thickness of the layer of low sand content across the basement high and adjacent sub-basins. The geometry of the fault displayed is the restored fault geometry prior to basin inversion. At 810 Ma, that fault did not penetrate the whole stratigraphy.

5.3.4 Lessons learned from the SFM approach

Approaching the area from different scales has highlighted some important points regarding the use of SFM on different scales.

First, applying SFM on a restored (pre-deformation) basin geometry means that geophysical data, as well as borehole and outcrop data that record today's deformed geometries, lose some of their usefulness for calibration. This, combined with a lower data-density for the large-scale model than the high-resolution model, make it difficult to constrain the inputs and calibrate outputs of the large-scale model. Concepts such as clinoform migration, as well as modern and ancient analogous areas, including the post-rift passive margin along the Sudan-Eritrea Red Sea coastline, are helpful to generate the required inputs, but are generic rather than location-specific. Consequently, the large-scale model is best suited to address conceptual and "what if" questions, for example: What if the Rudall Complex was always exposed? Or, what if the Rudall Complex was buried by sediments? Or, is it physically possible, to the best of the existing knowledge, for sediments to reach the Yeneena Basin from the South?

Secondly, approaching the problem from a source-to-sink perspective means coupling subaerial and subaqueous processes. Both DionisosFlow and Badlands can handle heterogeneous subsidence-rates, as well as different lithologies, sea-level variations, and operate on similar temporal resolutions. While Badlands integrates surface hydrology,

erosion, and river incision, which DionisosFlow does not handle as well, the latter provides more advanced diffusion- and wave-energy dissipation equations than the former. In other words, DionisosFlow is very well suited to simulate subaqueous processes, while Badlands excels at approaching the system from a holistic, source-to-sink perspective and is better able to represent the sub-aerial parts of the system. However, because of Badlands' focus on surface processes (and therefore catchment evolution), the models might need to be extended over a larger area to incorporate the source of sediments to adequately address sediment supply and river discharge to the area of interest, before the model reaches equilibrium. Badlands has highlighted, though, that continental depressions that existed at the top of the basement (i.e. graben or half-graben structures) have the potential to have been first filled from adjacent highs rather than more distant sources. Such material sourced from distant terranes, in turn, has the potential to be transported straight to the marine realm as soon as these top-basement depressions are filled. This, of course, depends on the rivers' characteristics, such as their discharge, and sediment-transport capacity of the flow as well as sediment-particle density which might have varied seasonally (typical for a semi-arid environment; Figure 21). For future work, deciding what software to use will depend on the problem that is to be addressed.

Despite the above-mentioned caveats, the results of the large-scale model confirm that the Officer Basin, where continental and shallow-marine conditions prevailed, could have co-existed with and fed the marine-dominated Yeneena Basin (Grey et al. 2005). This is important for understanding the source of brine involved in copper mineralisation. This is one of the most powerful benefits of considering neighbouring basins in a source-to-sink perspective. Indeed, some of the most popular models for sedimentary-hosted mineral systems assume all the critical components of the mineral systems to be present in one basin. A large-scale source-to-sink modelling approach allows for such an assumption to be tested. Based on results obtained in this project (e.g., section 5.1), and to the best of our knowledge, no thick evaporites could have precipitated in the Yeneena Basin as the high subsidence rate there would have been associated with marine conditions (confirmed by the SFM) unsuitable for evaporite formation. However, adjacent, shallower, and more proximal parts of this source-to-sink system, as existed in the Officer Basin, would have been suitable for evaporites to develop. This highlights that not all the critical components for the precipitation of metals in a sedimentary basin need to be as close to each other as previously thought, since they can occur in different (sub)basins.

High-resolution SFM models benefit from inputs that can be much more robustly constructed and better constrained to existing data, in comparison to regional-scale models. The purposes of high-resolution models, including the ones generated in this project, differ from large-scale ones. Indeed, they answer much more applied questions rather than conceptual ones. They provide a physically realistic distribution of sediment properties in the basin that reflect their calibrated input-parameters (as opposed to more generic, conceptual inputs used for large-scale models), which can then be used directly in fluid flow simulations for example (see Section 6.1.3).

In summary, it is crucial to be aware of the different questions that can be addressed by SFM on different scales, and their associated limitations, when planning to incorporate SFM into an exploration project.

6 Module 3: Fluid flow modelling

6.1 Milestone 8: 2D or 3D simulations of fluid flow through the stratigraphic framework and fault architecture of the basin through time

Fluid flow modelling was used in this project to test hypotheses about fluid pathways and drivers in the sedimentary-hosted copper mineral system of the Yeneena Basin. Modelling was integrated into the project from an early stage, starting with geometrically simple conceptual models designed to build understanding of fundamental processes in the mineral system (e.g., brine migration), and working towards geometrically complex models based on realistic representations of the basin architecture at different stages in the basin history. The simple conceptual models required only a general understanding of the basin architecture, while the complex models relied on outputs of other modules, including cross sections, basement surfaces, subsidence analysis and stratigraphic forward models.

The fluid flow models are summarised in Table 9. The first set of models focused on brine migration from evaporites in the Officer Basin into the Yeneena Basin, quantifying some fundamental aspects of brine migration through shallowly-dipping strata. Subsequent models focused on upward flow to transport fluid from the Coolbro Sandstone into the overlying Broadhurst Formation that hosts the known copper mineralisation. Several possible mechanisms could account for upward flow, including:

1. Fluid release from over-pressured compartments;
2. Metamorphic fluid production driven by a thermal event;
3. Thermal convection;
4. Upward flow driven by crustal shortening.

Different mechanisms would have been active at various times in the basin history. For example, gravitational compaction of sediments would enable mechanism 1 early in the basin history, whereas mechanisms 2 and 3 may have been triggered by thermal events, and mechanism 4 by the late-stage basin inversion. It is not feasible to model these processes over the entire basin history. Instead, three model scenarios were used to explore subsets of these processes at different times in the basin history. Note that faults were treated purely as regions of contrasting permeability in all fluid flow models; no attempt was made to model movement on the faults. The models are described further in the remainder of this chapter.

Model scenario	2D or 3D	Timing	Geometry	Processes simulated	Properties
1. Brine migration	2D	Before inversion	Simple conceptual representation of shelf and basin	Density-driven flow	Estimated
2. Fluid release from an over-pressured compartment	2D	Before inversion	Simple conceptual representation of sub-basin	Fluid flow driven by overpressure; salt transport	Estimated
3. Hydrothermal convection in the un-deformed basin	3D	Before inversion	Derived from SFM, restored cross sections and basement surface	Thermal convection (fluid flow + heat transport)	Derived from SFM
4. Upward flow through the deformed basin	2D	After inversion	Deformed cross section	Fluid flow driven by a deep fluid source; heat and tracer transport	Estimated from subsidence modelling

Table 9. Fluid flow models developed in this project

6.1.1 Fluid flow modelling scenario 1: Brine migration

6.1.1.1 Context

Genetic models for sedimentary-hosted copper deposits commonly invoke evaporites as sources for the brine, typically assumed to be in close proximity to (e.g., directly above) the ore deposit (Hitzman et al. 2010). In the Yeneena Basin, however, the source of salt is likely to have been in the Officer Basin, approximatively 100km from the edge of the Yeneena Basin (Figure 26). The long distance between the brine source and the Yeneena Basin implies that the slope connecting the two is particularly small, less than one degree. It is therefore of interest to test this hypothesis and investigate the characteristics of brine transport over such large distances through sedimentary strata with near-horizontal dip angles. Key questions include the duration of brine transport from its source to the edge of the Yeneena Basin; whether the brine would sink to the basement before reaching the edge of the Yeneena Basin; and what path the brine would follow once it reached the Yeneena Basin. We therefore investigated the problem of brine migration through shallowly dipping strata, starting with a general analysis from first principles. Note that the details of brine generation from the evaporites were not considered, as the timing and mechanism of brine formation has only a minor influence on its long-distance transport.

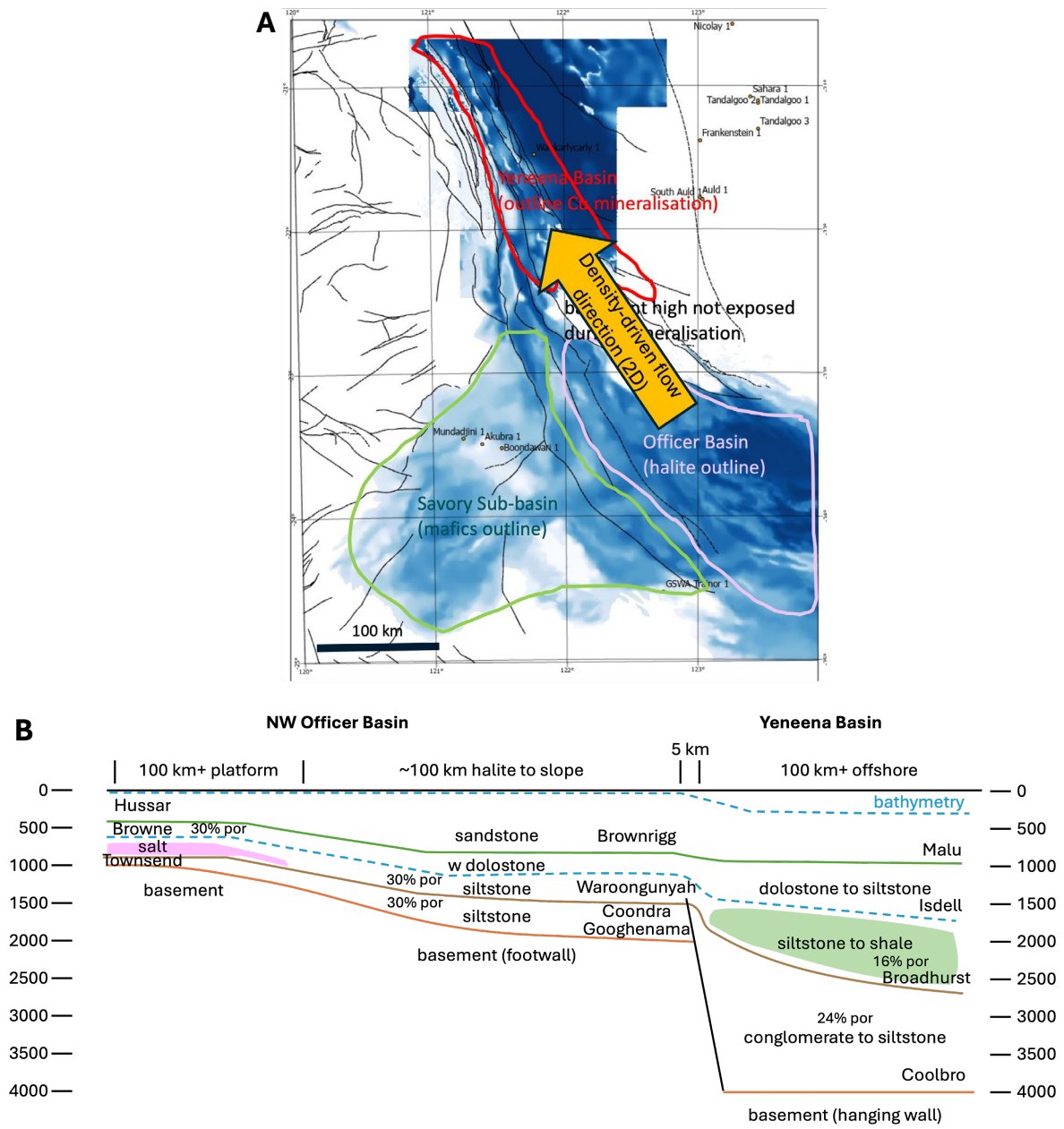

Figure 26: (A) map view of the Officer and Yeneena Basins, where the brine source and mineralisation host rocks are respectively located; (B) conceptual cross-section (along the yellow arrow in subfigure A) linking the source of salt (pink) to the rock unit hosting mineralisation (green). Geometry and thicknesses of stratigraphic units constrained from drill core data and subsidence modelling. Basement geometry constrained by 3D inversion of geophysical datasets.

6.1.1.2 Theoretical approach

From a theoretical perspective, the problem of brine migration in sedimentary basins rests on two fundamental aspects:

- density-driven flow, as brine density exceeds that of pure water and brines therefore tend to sink in porous rocks/sediments saturated with less saline pore fluid, and

- the role of permeability anisotropy, which is an important characteristic of sedimentary rocks, yet had not been explicitly considered in the context of density-driven flow.

Density-driven flow of brine, also called gravitational flow, buoyancy-driven flow, or free convection, is triggered by the negative buoyancy of the dense brine, which causes it to sink and flow along the basin floor, while less dense fluids rise. The exact pathway of the brine is controlled by the permeability and geometry of different sedimentary strata in the basin. This principle is well understood and commonly applied in modelling applications, including in the context of forming sedimentary-hosted ore deposits (e.g., Manning and Emsbo 2018). However, the brine pathway is typically modelled at the rock unit level, by using constant isotropic permeability values per rock type, and letting the geometry of less permeable stratigraphic layers (e.g., shale, basement) guide the brine migration that remains mostly confined in more permeable units (e.g., sandstone). Despite capturing an important phenomenon at the large scale – i.e. the flow-guiding role of less permeable units – this approach does not account for another important source of flow channelling: the permeability anisotropy *within* rock units. Indeed, we recently demonstrated the critical role of permeability anisotropy in sedimentary basins for the formation of supergene mimetic martite-goethite deposits (Poulet, Giraldo, et al. 2023), showcasing the importance of setting up the permeability tensor from its longitudinal k_L(along the strata) and transverse k_T (across the strata) components, instead of using horizontal and vertical values, k_H and k_V. We also quantified the error arising from this common misalignment of the permeability tensor in fluid flow models (Poulet, Sheldon, et al. 2023), and showed that a 5° discrepancy (i.e. considering the horizontal and vertical permeability components when the rock bedding is not perfectly horizontal but dips at an angle of 5°) can lead to errors of nearly two orders of magnitudes on the fluid flow velocity in thin permeable channels when the permeability anisotropy ratio $r = \frac{k_L}{k_T} = 10^4$, as can be the case at small scale where alternating layers of sand and shale easily create such contrasts. For larger scale models, e.g., at the size of a sub-basin or larger, the permeability ratio depends strongly on the rock type but typically takes values in the tens, with values up to low hundreds not uncommon (Bear 1972; Neuzil 1994; Domenico and Schwartz 1998; Ingebritsen et al. 2006). For $r = 10^2$, a 5° misalignment still leads to about one order magnitude error in the fluid flow velocity in a thin permeable layer.

In the current project we investigated the impact of permeability anisotropy on density-driven flow and published the analysis (Poulet et al. 2025). In essence, that study quantifies analytically the angle and velocity magnitude of a density-driven plume when the flow remains laminar, from the gravity component of the Darcy flow. For strata dipping at an angle θ, the expressions of the corresponding plume angle α and flow magnitude $\|\Delta\mathbf{q}\|$ are (see manuscript for details)

$$\begin{cases} \alpha = atan\left(\frac{r\,sin^2\,\theta + cos^2\,\theta}{(r-1)\,sin\,\theta\,cos\,\theta}\right) \\ \|\Delta\boldsymbol{q}\| = \Delta\rho_f g\,\frac{k_L}{\mu}\sqrt{sin^2\,\theta + r^2\,cos^2\,\theta} \end{cases} \quad (7)$$

The study showed that both the plume angle and velocity are extremely sensitive to the bedding dip angle θ when the bedding is close to horizontal, which is exactly the scenario for the brine migration pathway from the Officer Basin towards the Yeneena Basin, as well as within the Yeneena Basin itself. Figure 27 displays the evolution of the plume angle (α) as a

function of the bedding dip angle (slope θ), for three values of permeability anisotropy ratio. The steep variation of all three curves for low dip angles ($\theta \to 0$) highlight the high sensitivity of the plume angle (α) to the bedding dip angle (θ).

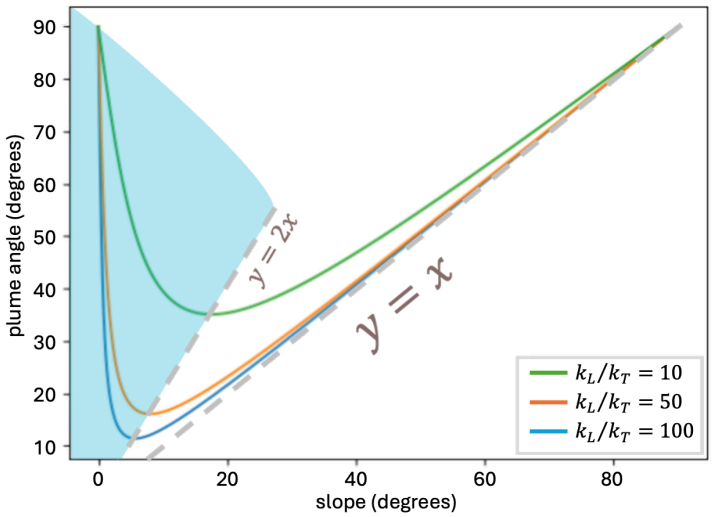

Figure 27: Evolution of the plume angle (α) as a function of the slope (θ), for three values of permeability anisotropy ratios $r \in [10, 50, 100]$.

Figure 27 shows clearly two different regimes:

- For low values of the bedding dip angle, the plume angle decreases from a maximum of 90° (vertical plume for perfectly horizontal strata). This zone, highlighted in blue in Figure 27, corresponds to cases where the strata is sufficiently close to horizontal for the plume to preserve a relatively steep angle, as gravity pulls the brine downwards.
- The rest of the curves, for higher values of the bedding dip angle, asymptotically converge towards the line $y = x$, as $\theta \to 90^o$. This regime corresponds to cases where the bedding dip angle is sufficiently pronounced for the brine to be channelled by the permeability anisotropy and therefore follow the strata orientation. The separatrix between the two regimes is the line of equation $y = 2x$.

From these results, we already draw some important conclusions:

- It is critical to account properly for the permeability anisotropy orientation locally to understand the direction and timing of brine transport, especially as the strata orientation is close to being horizontal.
- For the long transport distance involved in the Yeneena scenario (~100 km; Figure 26), any brine will inevitably sink to the basement before reaching the edge of the Yeneena Basin, since the minimum value of the plume angle for $r = 100$ is $\alpha_{min} \approx 11.4^o$ (Figure 27), which implies that the brine will drop by a height *H* within a horizontal distance of approximately *5H*. For example, if the brine source is 1 km above the basement in the Officer Basin, all of the brine will have reached the basement within 5 km laterally of the source, irrespective of the strata orientation. For lower anisotropy ratios, this distance factor reduces; it is about 1.4 for $r = 10$. The brine will then follow the slope of the basement, eventually reaching the Yeneena Basin unless it becomes trapped in a local basement low before reaching the edge of

the footwall. Note that some of the brine will permeate into the basement, which is much less permeable than the sediments but not impermeable.

- Transport time can be derived based on the average longitudinal permeability *k*. For $k_L = 10^{-13}\, m^2$ and $k_T = 10^{-15}\, m^2$, an indicative transport time over a distance of 100 km (i.e. from brine source in the Officer Basin to the edge of the Yeneena Basin) would be of the order of 1.5 million years.

For a more quantitative assessment of brine migration, a numerical approach is necessary.

6.1.1.3 Numerical approach – general simulations

We selected the *PorousFlow* module (Wilkins et al. 2021) of the *MOOSE* Finite Element simulator (Giudicelli et al. 2024) to run numerical experiments. This choice is not the result of an exhaustive comparative study and, therefore, might not be the optimal tool for the problem at hand. However, this open-source simulator provides an excellent way to ensure full control over all aspects of the code, from all the convergence parameters to the ability to implement any new feature.

That simulator has already been benchmarked against hydrogeological benchmarks in the context of isotropic permeability flow. It also contains all the required features to model density-driven flow, with equations of state for brine that account for temperature, pore-pressure, and NaCl concentration (Figure 28). This allowed us to focus solely on the issue of permeability anisotropy, to better understand any numerical limitations and subsequent requirements to ensure adequate representation and accurate results.

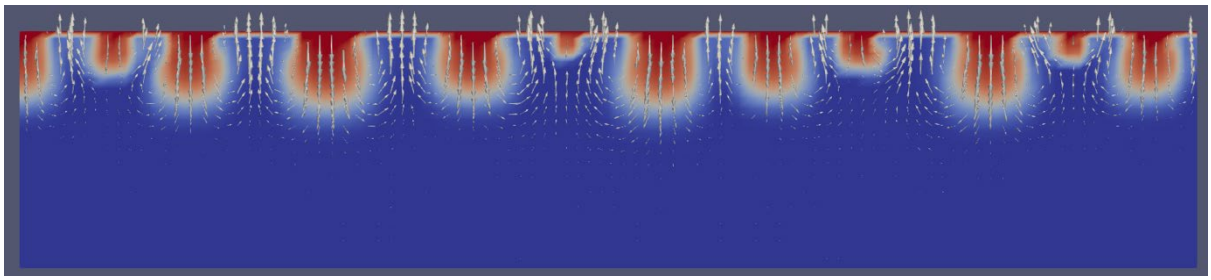

Figure 28: Illustrative example of typical density-driven flow with the MOOSE simulator, where a source of brine at the top of the model permeates downwards, with plumes creating a fingering pattern. Note this simulation uses isotropic permeability.

We ran various series of simulations with common settings. All used a localised constant source of salt in a rectangle block and were run until the resulting plume reached a distance that was deemed sufficient to be able to measure a plume angle, noting that the turbulent nature of density-driven flow limits our ability to measure that angle with absolute precision. Nonetheless, measures within 1° remain possible and sufficient for our benchmarking purposes. Figure 29 shows an example of one series of simulations performed for a constant mesh resolution, constant permeability anisotropy ratio, and varying the bedding dip angle.

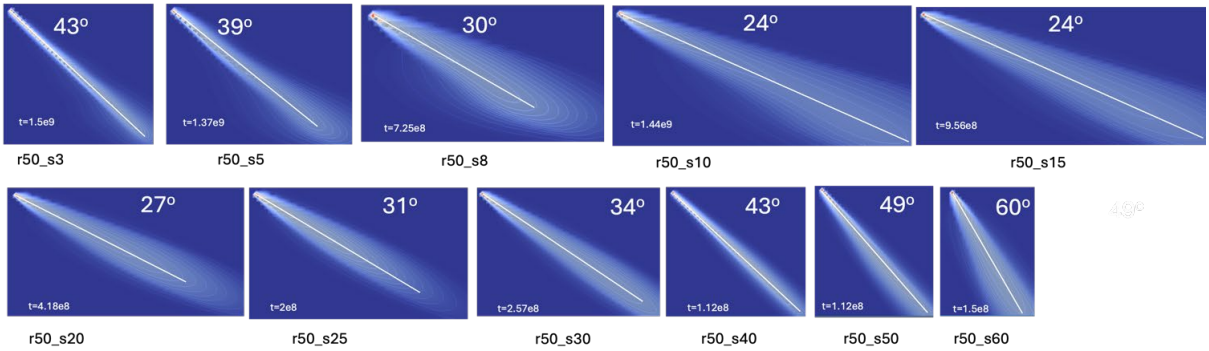

Figure 29: Example series of simulations for a constant permeability anisotropy ratio $r = 50$, where the slope (bedding dip angle) varies from $\theta = 3^o$ to $\theta = 60^o$ (labelled sXX under each sub-plot). A line is manually superimposed on the resulting plume to measure the plume angle within 1°, with that plume angle displayed on each image.

While the trend of those numerical results matches qualitatively that of the theoretical results (Figure 27), those results illustrate the need to increase the mesh resolution to improve the quality of the results, and consequently of the match with analytical results.

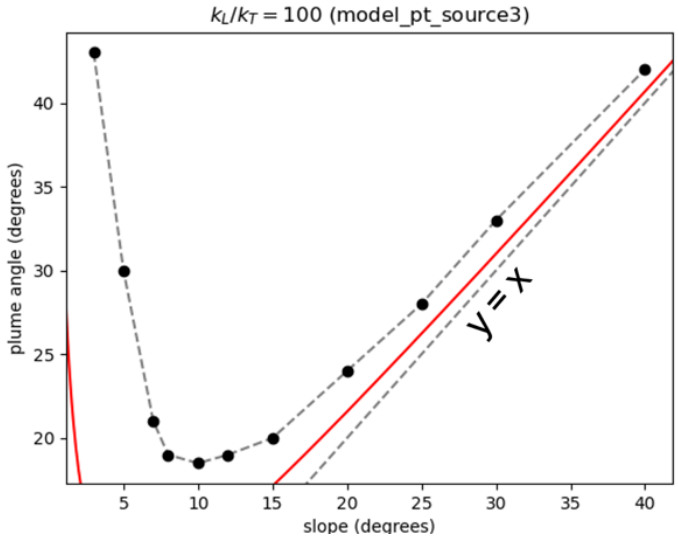

Figure 30: Comparing numerical (in black) and analytical results (in red) when varying the slope of the strata, with all parameters remaining constant, for the mesh resolution shown in Figure 29.

We then ran a mesh sensitivity analysis for a fixed value of permeability anisotropy ratio ($r = 100$) and fixed bedding dip angle (slope $s = 5^o$). The results (Figure 31) show the importance of using a mesh with sufficient resolution, as coarse meshes produce a plume angle that is far from its expected value.

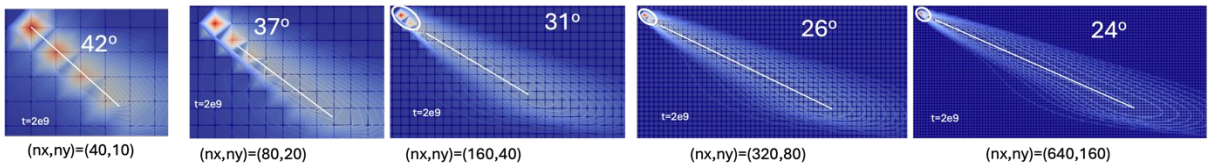

Figure 31: Mesh sensitivity analysis for a fixed value of permeability anisotropy ratio ($r = 100$) and fixed bedding dip angle (slope $s = 5^o$).

The plume angle results of Figure 31 can be plotted against the number of mesh nodes used to estimate the mesh convergence and assess how well the ultimate value matches the expected theoretical value (Figure 32).

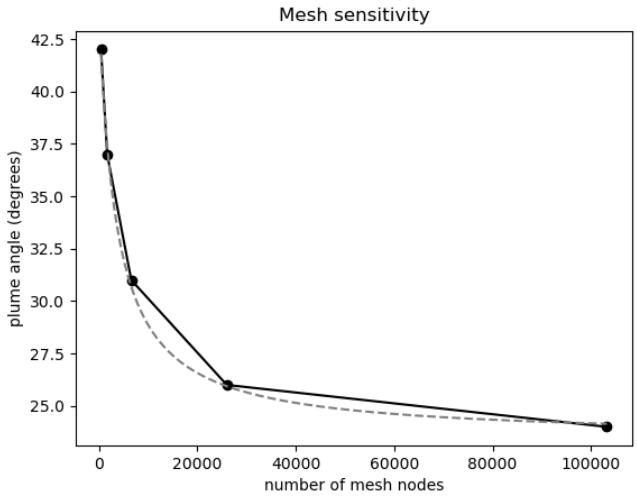

Figure 32: Matching the trend of the mesh sensitivity results from Figure 31 (black dots) with the formula $y = A + \frac{B}{x-C}$ (grey dashed line), with the parameters $A \approx 23.46, B \approx 73200, C \approx -3540$..

Such mesh sensitivity analysis reveals the numerical complexity of the density-driven flow in anisotropic permeability environment, with very fine meshes being required to approach the correct solution. We ran the series used to compare the numerical results with the analytical solution (similar to Figure 30) for a denser mesh and obtained, as expected, results that are closer to the solution (Figure 33).

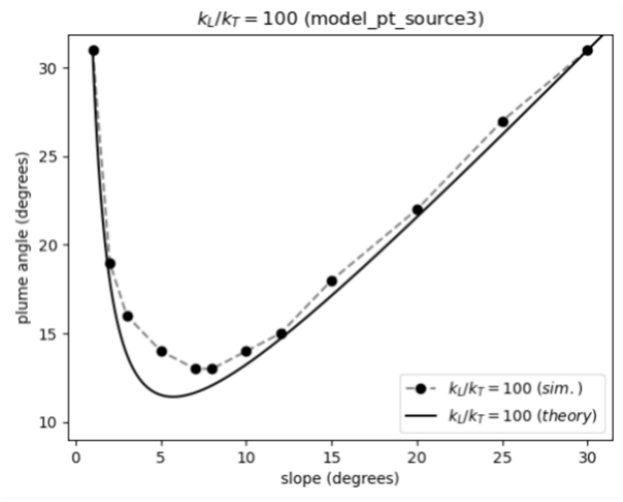

Figure 33: Comparing numerical (black dots) and analytical results (black line) when varying the slope of the strata, with all parameters remaining constant, for a higher mesh resolution than the one used to produce the results of Figure 30.

Two main conclusions can be drawn from that numerical analysis:

1. The analytical results we derived are particularly useful to assess the ability of a numerical simulator to capture the orientation and velocity of a plume in an anisotropic porous medium and we strongly recommend all numerical modellers run a similar benchmark with their selected simulator. With the benchmarking of our simulator of choice highlighting a numerical challenge much greater than expected, we warn all modellers against using what would be an adequate mesh resolution for the case of isotropic permeability, but would result in very inaccurate results for the case of anisotropic permeability.
2. The numerical cost of running an accurate brine transport simulation with anisotroic permeability over a large distance could be prohibitively expensive. We therefore recommend careful evaluation of the need for such simulations

For the Yeneena scenario (Figure 26) two transport problems should be differentiated. First, for the brine transport from its source to the edge of the Yeneena Basin (~100+ km), we established previously that the brine would fall to and then follow the top of the basement within that distance. It is therefore not necessary to consider any permeability anisotropy in that case. Second, for brine transport beyond the edge of the basement footwall, it is indeed important to account for the permeability anisotropy properly, yet not automatically necessary, as it depends on the exact question we want to answer.

6.1.1.4 Numerical approach – at the edge of the footwall

Having established that the brine will follow the basement top over the 100+ km from its source to the Yeneena Basin, the last remaining element is to understand which sub-basins the brine could reach from the edge of the footwall. A conceptual cross-section (Figure 34) illustrates the question: will all of the brine fall in the first subbasin, or can some of it flow over the horst to reach the second subbasin?

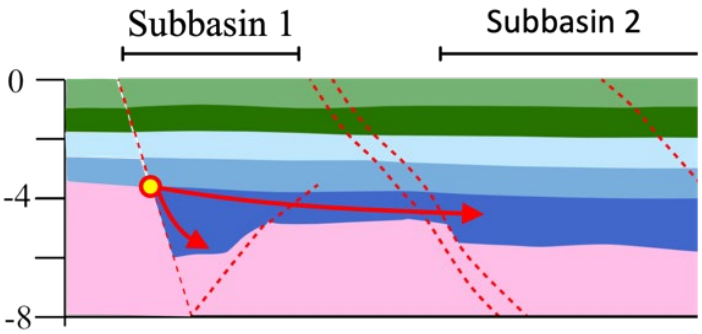

Figure 34: Conceptual cross-section illustrating the last question regarding the brine transport. After following the basement top over tens of kilometres (from the left-hand side on that model), the brine arrives at the top of the footwall (yellow dot). Will all the brine fall in the first sub-basin, or can some of it reach the second sub-basin, past the horst?

There are two main reasons for a great proportion of the brine to fall directly in the adjacent (first) subbasin. First, the fault marking the edge of the footwall is likely to possess the common feature of a damage zone on its basement side, where the rocks are more competent. This would form a permeability channel leading denser fluid directly to the first subbasin. Second, the distribution of sediments as the first subbasin forms, while that fault is active, usually sees some coarse sediments (e.g., conglomerates and sandstones) accumulate adjacent to the fault (Serck et al. 2021), which would have relatively high permeability and low anisotropy ratio. The results of Figure 27 indicate that the dip angle of a brine plume will be steeper for lower permeability anisotropy ratios (r), so some of the brine would likely descend through those coarse sediments into the first sub-basin.

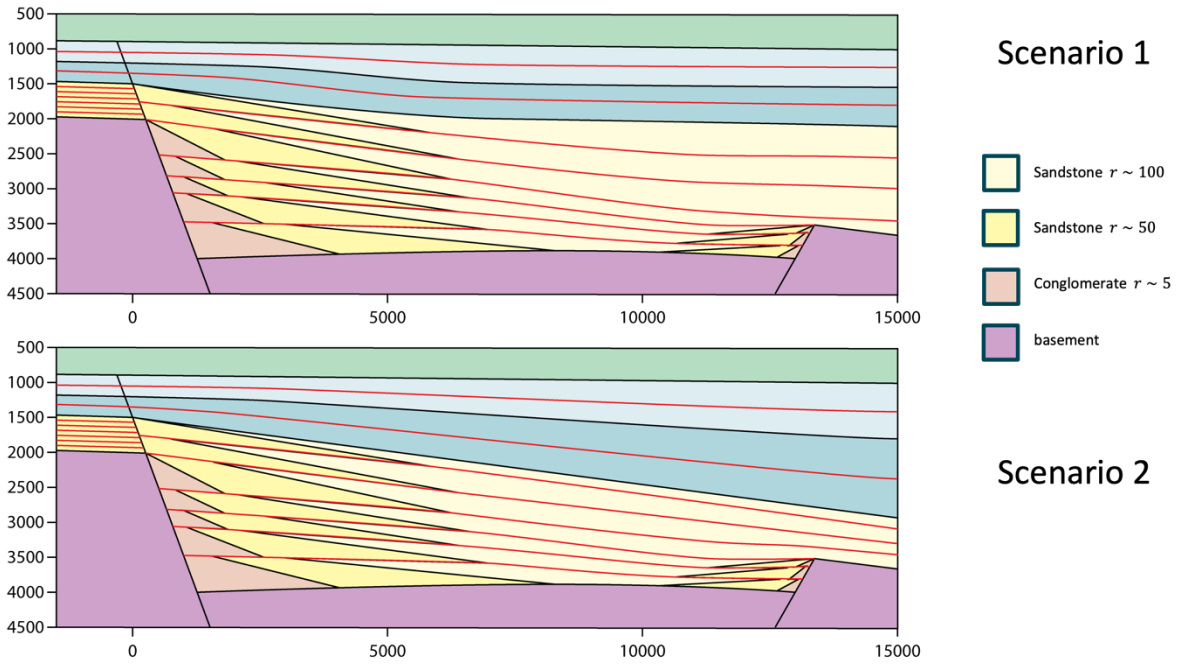

Figure 35: Two possible scenarios regarding the strata orientation in the first subbasin. Both scenarios have most features in common, including the typical distribution of sediments, with material of lower permeability anisotropy ratio closer to the faults. The only difference between the two scenarios is in the strata orientation in the top-right corner of the model, with scenario 1 presenting a flatter profile and scenario 2 a steeper inclination.

The remaining question is whether any of the brine could follow the strata past the footwall edge for sufficient distance to reach beyond the horst. This requires the brine to be transported in the more anisotropic sediments, and we therefore simplify the two scenarios of Figure 35 by ignoring the spatial distribution of permeability anisotropy. Instead, we consider the scenario whereby the basin fill has uniform permeability anisotropy but varying dip (Figure 36).

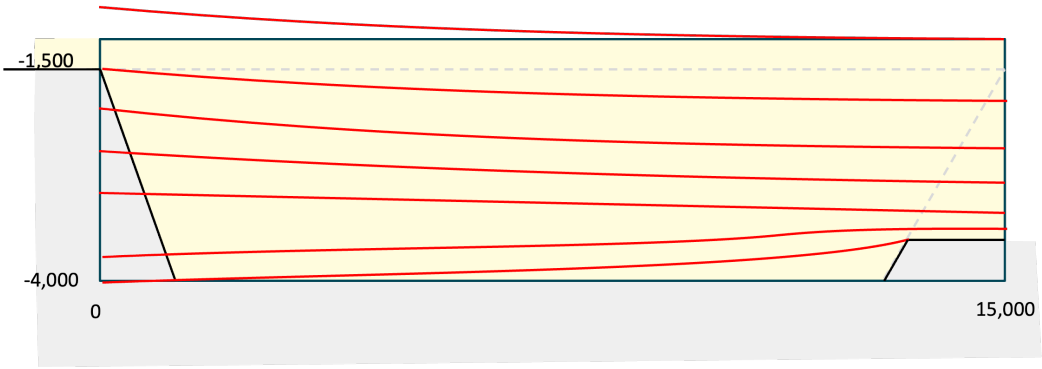

Figure 36: Simplified configuration of Figure 35, where all sediments display the highest permeability anisotropy ratio.

We then follow the implicit modelling methodology from (Poulet, Giraldo, et al. 2023) to create a corresponding mesh with values of a potential function, whose iso-values correspond to the original strata lines. The gradient of this potential field allows to determine the local orientation of the permeability tensor at any point of the mesh, from which the full permeability tensor can be determined (using user-provided longitudinal and transverse permeability values). We then integrate the Darcy flow definition over time to retrieve the trajectory of the brine. This methodology, which works equally in 3D, provides an easy and quick (nearly instant) way to assess whether any of the brine could reach beyond the first sub-basin. Results show (Figure 37) how far the brine can reach for each scenario, based on the value r of the anisotropy ratio.

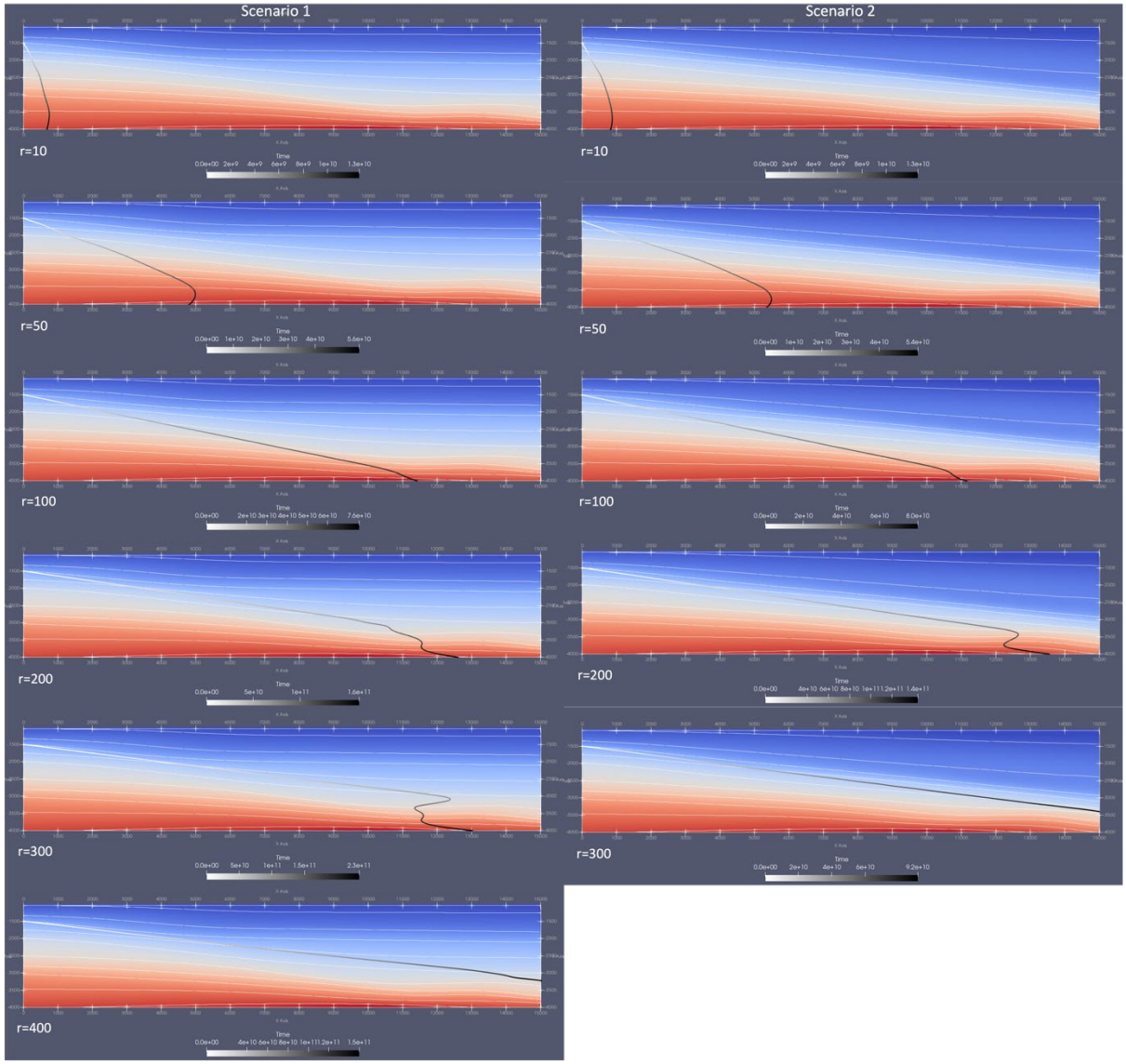

Figure 37: Brine trajectory for different values of anisotropy ratio (r), for scenario 1 (left column) and scenario 2 (right column; see Figure 35 for definition of scenarios). The trajectories are coloured by time.

While we retrieve the expected behaviour that more anisotropic rocks lead the brine further, it is interesting to note the (potentially counter-intuitive) difference between the two scenarios. Indeed, the brine passes the horst for $r = 300$ in scenario 2, which has steeper strata, but not scenario 1 (which requires $r = 400$ to see the brine pass the horst).

This example illustrates why a careful analysis must be performed that accounts for the strata orientation and permeability distribution, which could both be derived from Stratigraphic Forward Modelling simulations, to identify which subbasins the brine could reach.

6.1.1.5 Conclusions

This study on brine migration allows us to draw the following conclusions

- The theoretical analysis showed the critical importance of accounting for anisotropic permeability orientation when modelling density-driven flow in sedimentary basins. This is particularly important when the strata orientation is close to horizontal.
- For the long transport distance involved in the Yeneena scenario (~100 km), the brine will inevitably sink to the basement and follow the basement top until it reaches the Yeneena Basin. This invalidates the potential scenario of brines remaining in their original stratigraphic unit from their source to the location of the known deposits.
- Numerical simulators can capture density-driven flow accurately, but very fine mesh resolutions are likely to be required to match the expected plume angle in anisotropic media. We strongly recommend modellers test their simulators against the proposed benchmark.
- A novel solution that is numerically much more efficient was proposed to assess which subbasins the brine could potentially reach, to avoid numerically expensive simulations at the edge of the footwall.
- This analysis shows the benefits of using Stratigraphic Forward Modelling simulation results to estimate the strata orientation and permeability distribution.

We suggest this type of analysis in 3D as a mineral exploration tool, to estimate which subbasins the brine could reach, which is a necessary (but not sufficient) condition for (later) mineralisation.

6.1.2 Fluid flow modelling scenario 2: Fluid release from an over-pressured compartment

6.1.2.1 Context

Fluid release from over-pressured compartments is one possible mechanism for upward fluid flow in a sedimentary basin. Gravitational compaction can lead to formation of over-pressured compartments in sedimentary basins due to development of very low permeabilities in some units, which consequently act as seals that prevent fluid escaping from the rocks below. Seals typically form in finer-grained units such as shale or mudstone. In the Yeneena Basin this mechanism may have generated over-pressure in the Coolbro Sandstone (relatively coarse grained) due to development of a low-permeability seal in the Broadhurst Formation (relatively fine grained). Over pressure would have persisted until the seal was breached by a fault or by hydrofracturing, allowing the fluid to escape.

6.1.2.2 Model setup

In this model we explore the timing and volume of fluid release from an over-pressured compartment in the Coolbro Sandstone, using a simple 2D cross section representing a sub-basin separated from an adjacent basement high by a normal fault (Figure 38A). Porosities and permeabilities were chosen to be representative of the typical lithologies of each unit (Table 10). The lower half of the Broadhurst Formation is assumed to have low vertical permeability, thereby acting as a seal, while the upper half has higher permeability. Note there is no particular reason to assume that permeability would be lower in the lower half of the Broadhurst Formation than in the upper half; this configuration was chosen purely to

demonstrate how fluid passing through a seal could penetrate into the overlying rock, noting that penetration of fluid into the Broadhurst Formation is of particular interest as this is the unit that hosts Cu mineralisation in the Yeneena Basin. The fault was assigned a relatively high permeability, implying that the fault was reactivated at the start of the simulation. This reactivation could be due to some combination of tectonic forces and the overpressure itself; either or both could cause the fault to be reactivated and act as a fluid pathway. Note we do not simulate any movement on the fault in this model; it is treated purely as a fluid pathway.

The model was initialised with fluid pressure representing an over-pressured state in the Coolbro Sandstone, with a steep pressure gradient through the lower Broadhurst decreasing to hydrostatic pressure above (Figure 38C). A high initial salinity was specified in the bottom half of the Coolbro Sandstone, representing a halite-saturated brine that had accumulated in the sub-basin (Figure 38B) following brine migration processes described in section 6.1.1. Fluid pressure was fixed at the top of the model, representing the seafloor at 300 m water depth. All other boundaries were impermeable.

6.1.2.3 Results and implications for mineralisation

The simulation results show that fluid escapes rapidly from the over-pressured compartment, travelling up the fault and dispersing into the Broadhurst and overlying Isdell Formation (Figure 39). There is very little movement of salt; some goes up the fault and some goes down (driven by the negative buoyancy of the brine), but there is negligible impact on salinity in the Broadhurst or Isdell Formations (Figure 39).

The mineralisation potential of this fluid release event can be assessed by evaluating the volume of fluid that moves from the fault into the Broadhurst Formation, then estimating the amount of Cu that could be carried in that fluid. Estimates of Cu concentrations in ore-forming fluids range from ~10-1000 ppm (e.g., Haynes and Bloom 1987; Jowett 1986; Stoffell et al. 2008). Our model predicts approximately 7000 m^3 of fluid moving into the Broadhurst Formation per metre along strike (Figure 40A). For Cu concentrations of 10 to 1000 ppm this corresponds to ~0.07 to 7 tonnes Cu per metre along strike. For comparison, Nifty has ~1.7 Mt Cu, and large sedimentary-hosted Cu deposits can be > 20 Mt Cu. Larger fluid volumes could be achieved by assuming a larger source region for the fluid (i.e. a larger sub-basin), localised breaching of the seal along strike (i.e. the fault only breaches the seal at a few discrete locations) or repeated cycles of over-pressuring and fluid release (e.g., due to ongoing compaction and/or fluid production during diagenesis). However, none of these mechanisms could result in sufficient fluid volumes to create an economic Cu deposit. We conclude that it is not possible to make an economic Cu deposit by draining an over-pressured compartment.

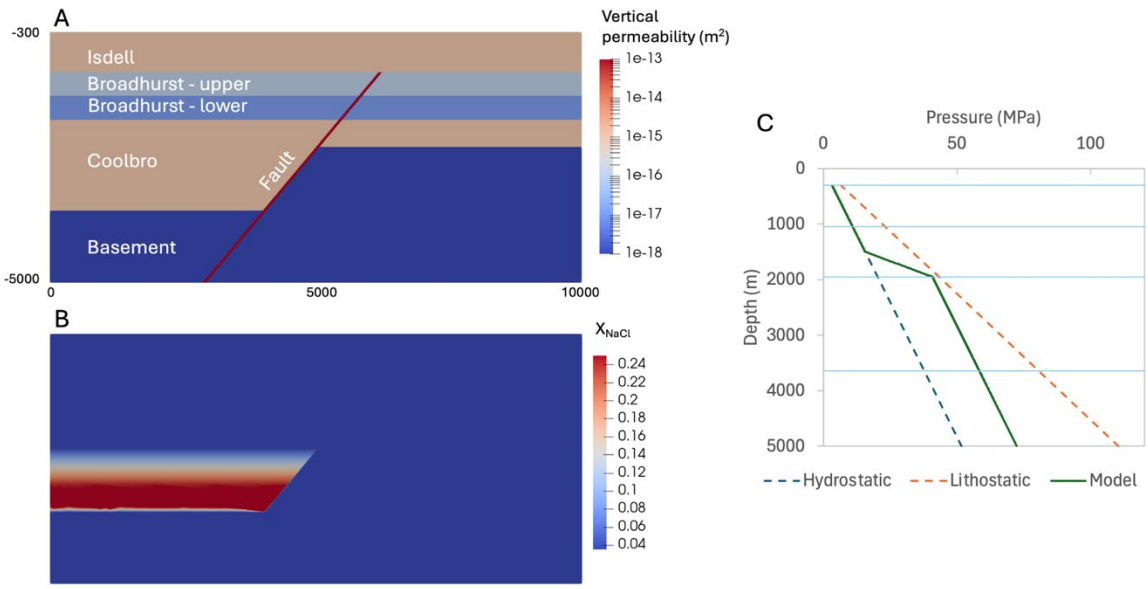

Figure 38. Model setup for fluid release from an overpressured compartment. (A) Model geometry coloured by vertical permeability (scale in m). (B) Initial salinity (mass fraction NaCl). (C) Initial fluid pressure versus depth. Dashed lines show hydrostatic and lithostatic fluid pressure gradients for comparison.

Table 10. Properties for model of fluid release from an overpressured compartment

Rock unit	Porosity (-)	Horizontal permeability (m^2)	Vertical permeability (m^2)
Isdell	0.2	10^{-15}	10^{-15}
Broadhurst: Upper	0.1	10^{-15}	10^{-16}
Broadhurst: Lower	0.05	10^{-15}	10^{-17}
Coolbro	0.1	10^{-14}	10^{-15}
Basement	0.01	10^{-18}	10^{-18}
Fault	0.1	10^{-13}	10^{-13}

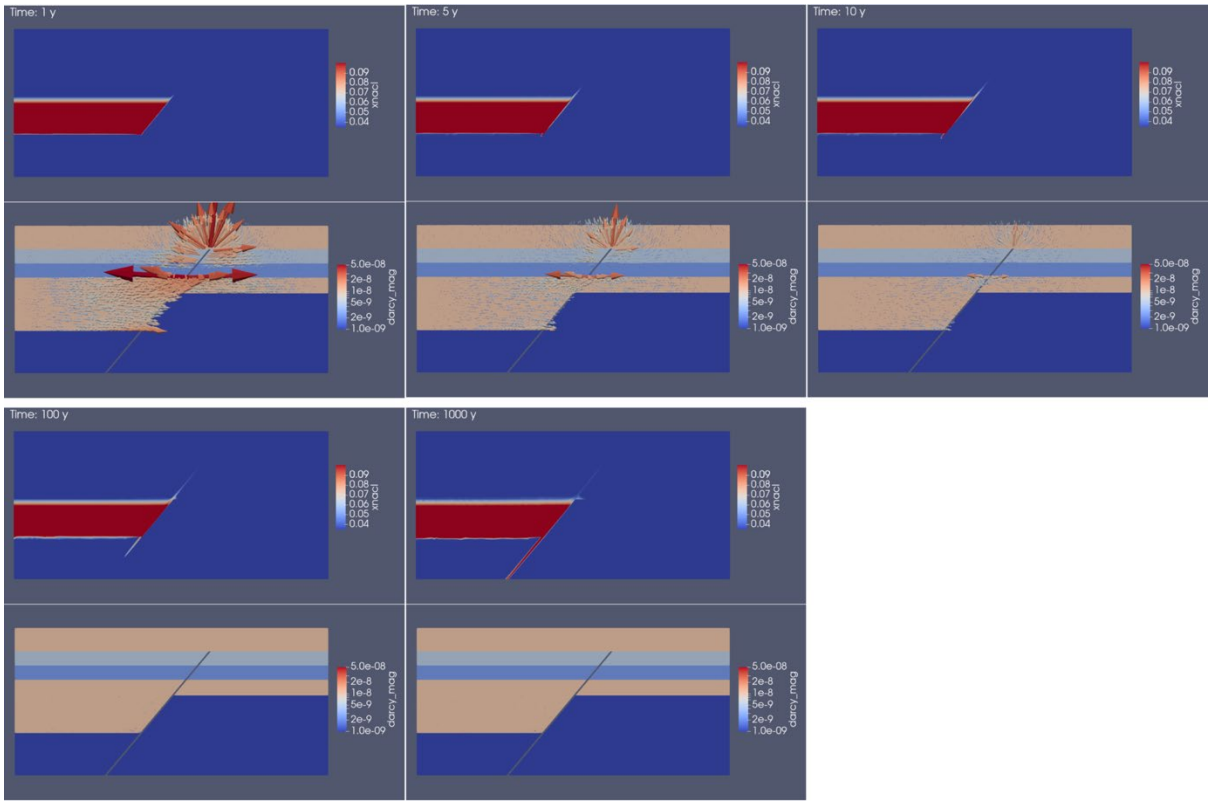

Figure 39. Salinity and fluid flow after 1, 5, 10, 100 and 1000 years since start of fluid release from an over-pressured compartment. Salinity colour scale is capped at 0.1 to emphasise the high values (c.f. Figure 38). Fluid flow vectors coloured and scaled by flow rate (m/s), superimposed on vertical permeability. Flow vectors are not shown in the fault as their size would obscure the vectors in the host rocks.

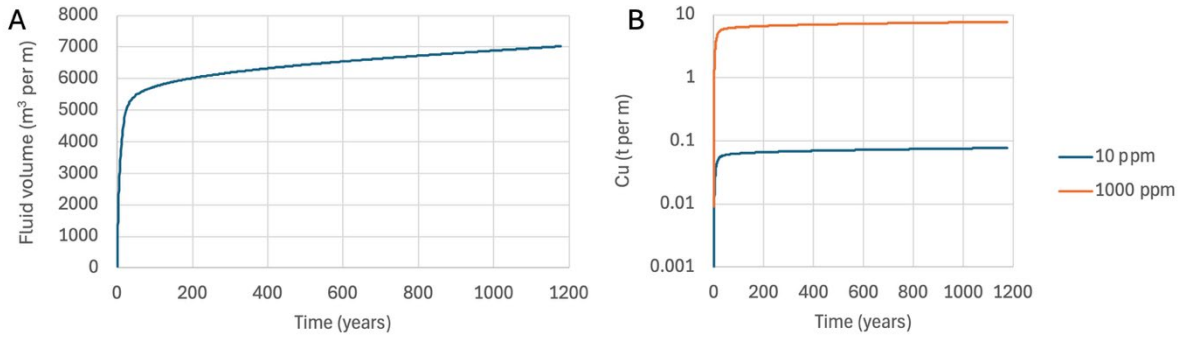

Figure 40. Fluid flux from fault into Broadhurst Formation driven by fluid release from an over-pressured compartment in the Coolbro Sandstone. (A) Fluid volume per metre along strike of the fault. (B) Tonnes of Cu per metre along strike, assuming Cu concentration of 10 or 1000 ppm in the pore fluid.

6.1.3 Fluid flow modelling scenario 3: Thermal convection in the undeformed basin

6.1.3.1 Context

This model uses the small-scale Stratigraphic Forward Model (SFM; see Section 5.3.3.5) to constrain porosity, permeability and thermal conductivity in a 3D fluid flow model, which is used to explore thermal convection as a mechanism for moving fluid within the basin. The

model represents the un-deformed state of the basin, potentially corresponding to the earliest phase of mineralisation.

Thermal convection is a spontaneous process whereby hot, low-density fluid rises and cold, higher density fluid sinks. These upwellings and downwellings create convection cells, in which fluid is continuously circulating through the system without requiring any input from external fluid sources. Over time this can result in very large fluid fluxes through the system, potentially playing an important role in mineralisation by having the same fluid repeatedly picking up metals from source rocks at depth then depositing them in host rocks at shallower levels (e.g., Schaubs et al. 2019; Li et al. 2021).

The occurrence of thermal convection and the velocity of the resulting fluid flow depend primarily on permeability and temperature gradient (both horizontal and vertical). While the vertical temperature gradient is governed by the large-scale tectono-thermal regime, local horizontal gradients can arise from variations in thermal conductivity due to lateral facies variations. Permeability is also related to sedimentary facies and can vary by orders of magnitude over small distances within sedimentary basins, as well as being strongly anisotropic. Faults may or may not be favourable pathways for convective fluid flow, depending on whether they are more or less permeable than their host rocks.

Conceptual models for the formation of sedimentary-hosted mineral deposits often invoke convection as a mechanism for concentrating metals in certain parts of the system. Such models are commonly depicted on 2D cross sections, often showing convection occurring within permeable stratigraphic horizons, with other arrows suggesting some other mechanism driving fluid upwards through faults (e.g., Hitzman et al. 2010), or faults acting as conduits linking permeable sedimentary horizons to enable convection cells to develop across strike. However, convection is inherently three-dimensional, and its complexity cannot be captured by 2D diagrams or models (see Sheldon et al. (2021) and references therein). In particular, note that convection may occur within the faults (along their strike); this aspect cannot be represented in cross sections drawn perpendicular to the strike of the faults. Further complexity arises from the heterogeneous nature of the basin fill, where alternating layers of varying grain size and mineralogy create heterogeneous and anisotropic permeability distributions.

We address these challenges by using the small-scale SFM (see section 5.3.3.5) to constrain a 3D fluid flow model with a realistic, heterogeneous and anisotropic permeability distribution in the sediments, fault permeability based on the porosity and grain size of the surrounding sediments, and thermal conductivity varying with porosity. The model represents the un-deformed state of the basin, potentially corresponding to the earliest phase of mineralisation. The model is used to explore the development of thermal convection in the faults and sediments.

The methods and workflow used in this model are described in detail in Sheldon et al. (2023) and summarised below.

6.1.3.2 Model geometry and mesh

The SFM covers an area of 80 x 86 km. For the fluid flow model a smaller area of 34 x 46 km was selected, encompassing part of the Vines Fault, Southwest South Fault and Southwest North Fault, and oriented across strike (Figure 41). The fluid flow model is based

on the SFM output at 810 Ma, corresponding to the top of the Malu Formation. The model extends beneath the base of the SFM to a horizontal surface at -8000 m, with the region between the base of the SFM and the base of the model representing the Rudall Complex (i.e. the basement).

Faults are not represented explicitly in the SFM, hence a new mesh including faults must be created for the fluid flow simulations. This was achieved by using the restored cross sections (see Section 5.2.2) to derive fault traces on top of the Malu Formation, which were then extruded downwards with an appropriate dip and dip direction (Table 11) to create 3D fault surfaces. These surfaces, along with the bounding box of the model domain, were used to construct a 3D mesh suitable for fluid flow simulation. The mesh is refined around the faults and within the basin, with a coarser grid size in the basement away from the faults (Figure 42). The resulting mesh has more than 3.5 million nodes, requiring hundreds of processors to run the fluid flow simulations.

Table 11. Fault orientations in the fluid flow model

Fault	Dip (°)	Dip direction (°)
Vines	56	045
Southwest South	54	225
Southwest North	53	045

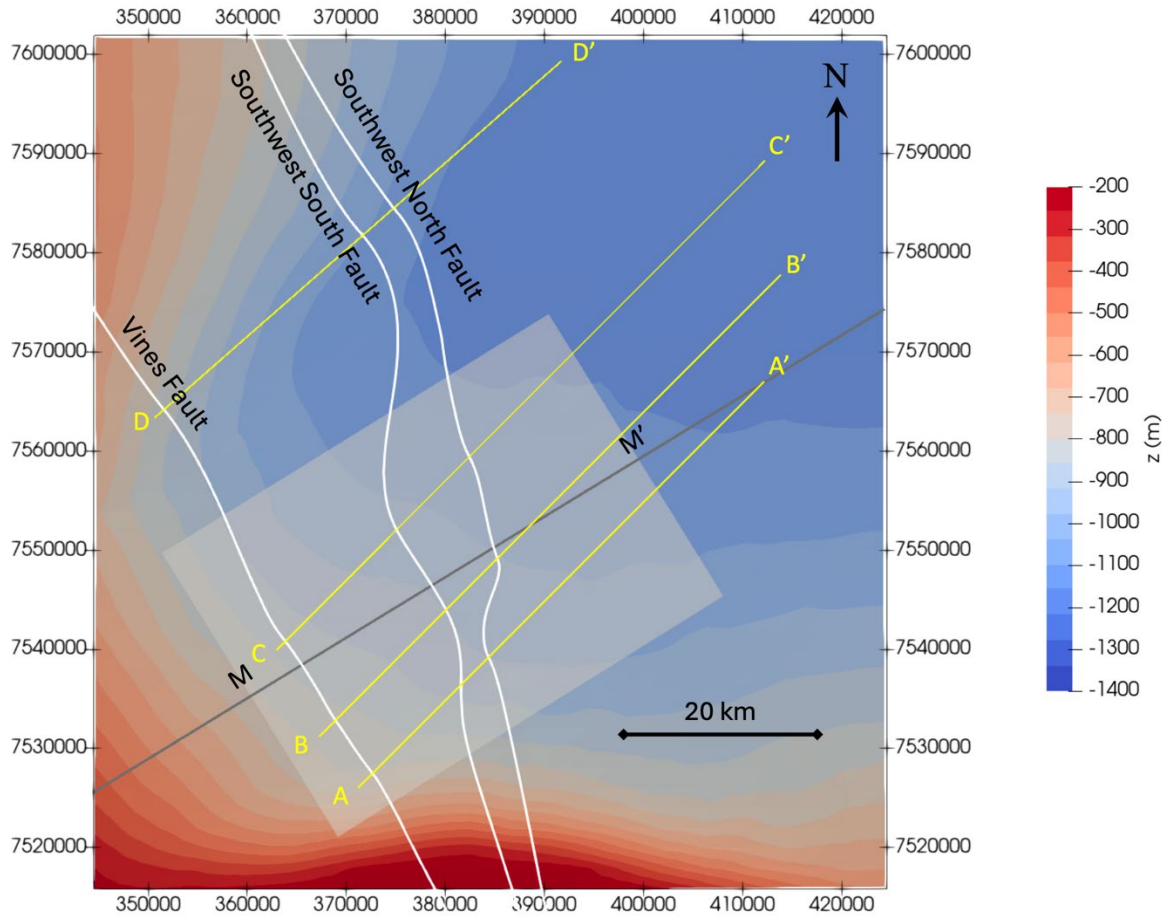

Figure 41. Relationship between SFM (large rectangle) and fluid flow model (smaller grey rectangle). Top of SFM (top Malu Formation) shaded by elevation (m). White lines are traces of faults included in fluid flow model. Heavy grey line indicates location of cross sections shown in Figure 43. Yellow lines indicate locations of restored cross sections. Grid in metres.

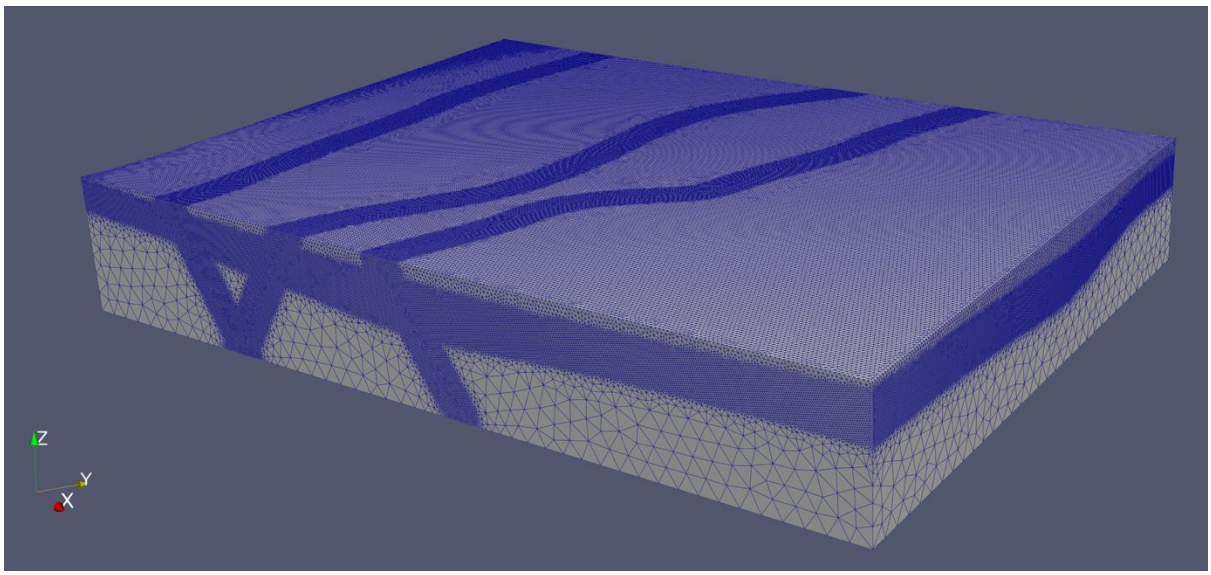

Figure 42. Finite element mesh used for fluid flow modelling, showing refinement around faults and within sediments.

6.1.3.3 Porosity-permeability distribution derived from SFM

The output of the SFM is a structured mesh, comprising stacked layers of 2 x 2 km cells with varying thickness. Each layer represents the net result of sediment deposition, erosion and compaction over a given time interval. The thickness of the layers varies over the model domain, and can be zero if no sediment was deposited or all sediment was eroded in a given cell. Each cell is characterised by its porosity and the proportion of each sediment class (gravel, sand, silt, mud, carbonate mud, carbonate and gypsum; Figure 43). The contrasting character of the 4 formations (Coolbro, Broadhurst, Isdell and Malu) is clearly visible in Figure 43, with sand/gravel dominating the Coolbro Sandstone, contrasting with the high carbonate mud content of the Broadhurst Formation. Gypsum is not shown in Figure 43 because its proportion is very low throughout the section.

The SFM does not calculate permeability, but it can be estimated from the porosity. Longitudinal permeability (k_{long}; parallel to bedding) for each sediment class in each cell of the SFM was derived from porosity (ϕ) using the following equation:

$$k_{long} = k_0 \frac{(\phi/\phi_0)^n}{((1-\phi)/(1-\phi_0))^2} \quad (8)$$

where k_0 is the permeability corresponding to porosity ϕ_0, and n is an empirical constant. Transverse permeability (perpendicular to layering) was derived from longitudinal permeability according to the relationship:

$$k_{trans} = k_{long}/\alpha \quad (9)$$

where α is the anisotropy ratio. Values of the permeability parameters for each sediment class are listed in Table 12. The basement (Rudall Complex) was assigned a uniform low permeability of 10^{-17} m^2 (isotropic) and a uniform low porosity of 1%.

The resulting longitudinal and transverse permeability values were upscaled onto a coarser mesh suitable for reading into the fluid flow simulation (Figure 43, bottom row), with the permeability of each cell on the coarser mesh being a weighted average of the sediment class permeabilities within that cell. Importantly, the upscaled permeability retains information about the orientation of the stratigraphic layers (bedding) in each cell, as well as the anisotropy that arises from the interlayering of different sediment classes with contrasting permeabilities. The end result is a heterogeneous, anisotropic permeability field in which the principal directions of permeability are parallel and perpendicular to the sedimentary layers.

Note the low transverse permeability of the Broadhurst Formation (Figure 43, bottom right), which will inhibit upward flow. However, its horizontal permeability (Figure 43, bottom left) is only slightly smaller than that of the underlying Coolbro Sandstone. This contrast between longitudinal and transverse permeability is due to alternating layers of fine-grained (mud and carbonate mud) and coarse-grained (sand and carbonate) sediments in the Broadhurst formation (Figure 44, left). The relatively high permeability of the coarse-grained layers dominates the upscaled longitudinal permeability of the Broadhurst formation, whereas the low permeability of the fine-grained layers dominates the upscaled transverse permeability (Figure 44, right). These alternating layers are resolved on a scale of 10's of metres in the SFM, but their effect on permeability is captured on a coarser scale in the upscaled SFM and in the fluid flow model. Upscaling the permeability enables us to account for the effect of relatively thin sedimentary layers in the fluid flow simulations without resolving the fine details of those layers.

Table 12. Parameters for deriving permeability from porosity

Parameter	Mud, Carbonate Mud, Gypsum	Silt	Sand, Gravel, Carbonate
k_0 (m^2)	10^{-19}	10^{-17}	10^{-14}
ϕ_0	0.1	0.1	0.1
n	3	3	3
α	30	10	1

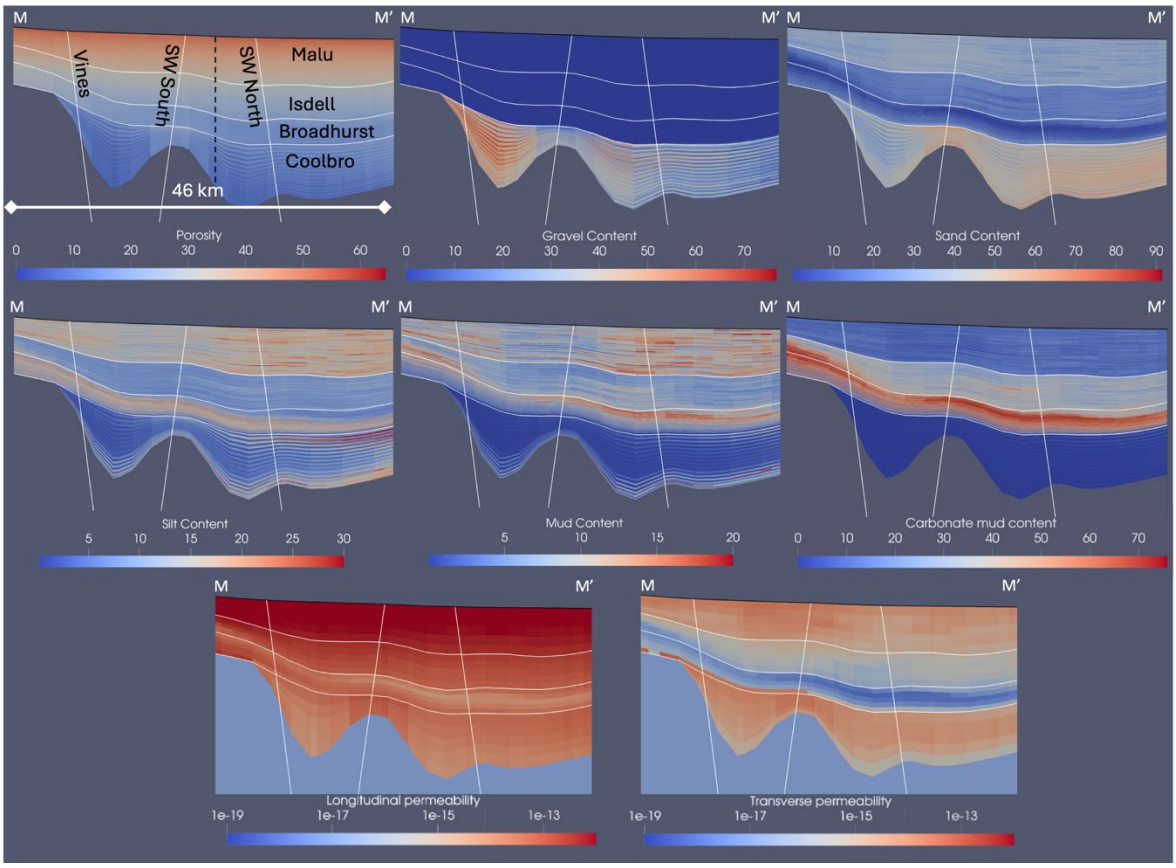

Figure 43. Cross section through the SFM used in the fluid flow model (vertical exaggeration x 5), showing porosity and sediment class fractions (percent) in the SFM, and longitudinal/transverse permeability on the upscaled grid (m^2). The section has been cropped to the edges of the fluid flow model (see Figure 41). Steep white lines indicate faults included in the fluid flow model, although faults do not exist explicitly in the SFM. Shallow white lines indicate chronostratigraphic boundaries at 60 Ma (top Coolbro), 140 Ma (top Broadhurst) and 220 Ma (top Isdell). Black dashed line indicates location of profile shown in Figure 44.

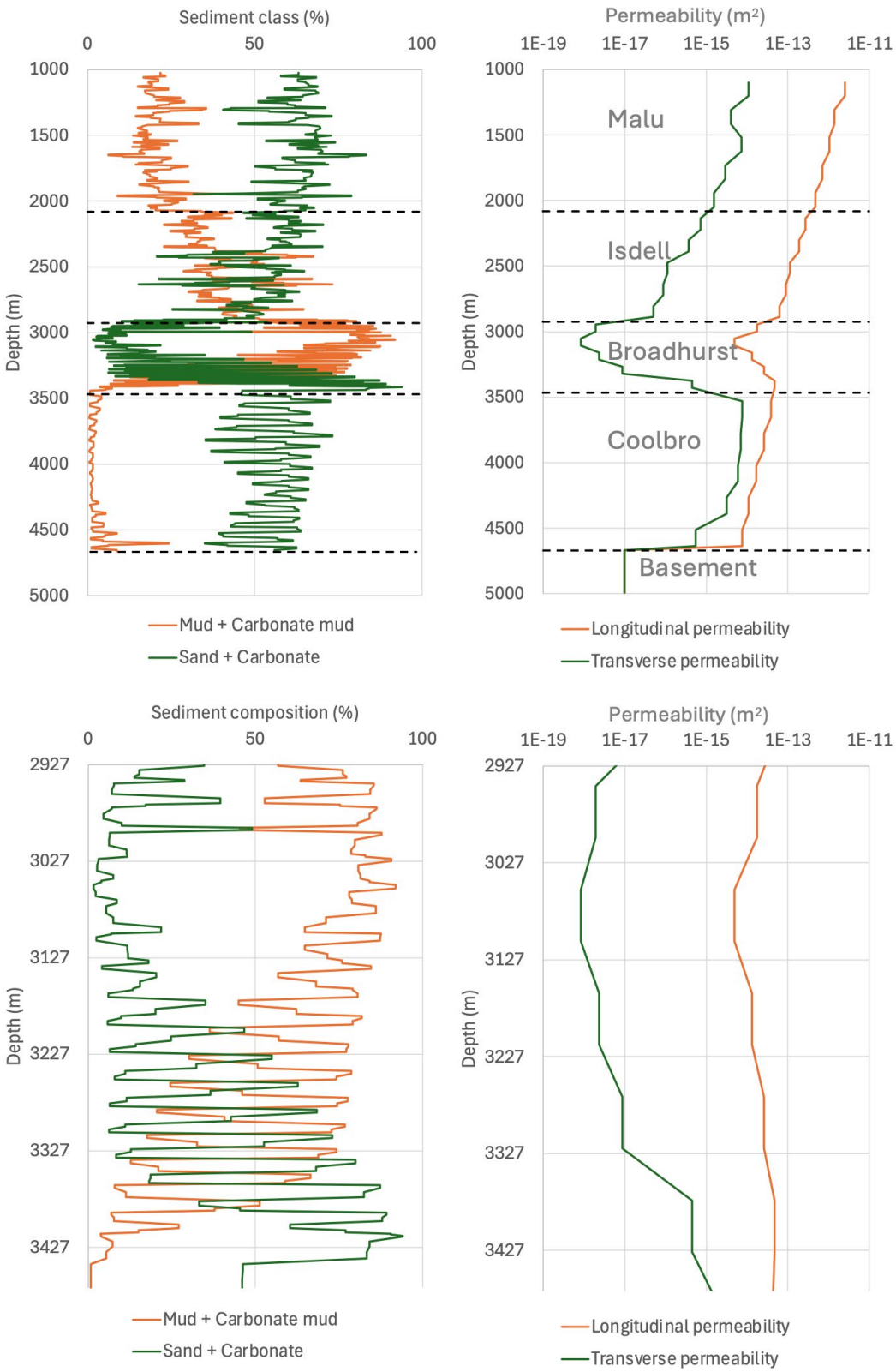

Figure 44. Vertical profile through the basin showing alternating layers of coarse and fine-grained sediments (left), with corresponding permeability profiles from the upscaled model (right). Top: Full thickness of sediments. Bottom: Detail of Broadhurst Formation. See dashed black line in Figure 43 for location of profile.

6.1.3.4 Fault permeability

Faults in sedimentary basins can be either more or less permeable than their host rocks/sediments, depending on porosity, mineralogy, grain size and degree of cementation. Shearing of porous, relatively unconsolidated sediments tends to result in permeability reduction, especially when there is a high fraction of sheet silicates (clays and micas) that tend to be smeared along the fault. Conversely, shearing of a consolidated sandstone with relatively low porosity can result in permeability enhancement. We account for these variations by calculating fault permeability (k_{fault}) from the following equation:

$$k_{fault} = k_{long} 10^{a} \quad (10a)$$

$$a = \frac{min(f_{mud}+\phi, f_{max})}{f_{max}} (R_{min} - R_{max}) + R_{max} \quad (10b)$$

where k_{long} is the longitudinal permeability of the surrounding rock/sediment, R_{min} and R_{max} are the minimum and maximum values of the exponent a, f_{mud} is the fraction of mud plus carbonate mud in the surrounding rock/sediment, ϕ is porosity of the surrounding rock/sediment and f_{max} is a cut-off value of $f_{shale} + \phi$. We used R_{min} = -2, R_{max} = 2 and f_{max} = 0.4, such that k_{fault} ranges from ~$100 \times k_{long}$ for a low porosity rock with zero mud content, to $0.01 \times k_{long}$ for a rock with high porosity and/or high mud content. This fault permeability function has not been validated against field or lab data, but it captures important aspects of fault permeability in sedimentary basins.

In the basement the faults were assigned a uniform high permeability, consistent with the fluid flow characteristics of faults in low-porosity metamorphic rocks. The resulting fault permeability distributions are illustrated in Figure 45. The Southwest South and Southwest North faults were terminated at the top of the Coolbro Sandstone, as the depositional patterns in the basin suggest that these faults were inactive during deposition of the Broadhurst and overlying units (Figure 12). The Vines Fault was continued to the top of the model, consistent with its status as a major basin-bounding fault; however, the high mud content of sediments above the Coolbro Sandstone (Figure 43) results in low fault permeability there (Figure 45).

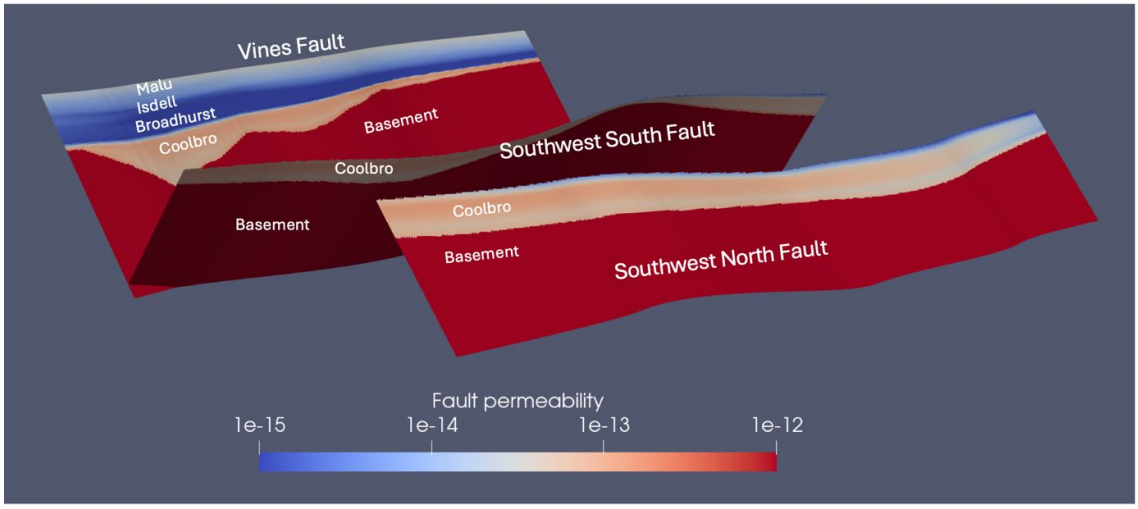

Figure 45. Fault permeability (m^2) in the thermal convection model. The Southwest South and Southwest North Faults are truncated at the top of the Coolbro Sandstone, whereas the Vines Fault continues to the top of the model. Note low permeabilities in the Vines fault where it intersects host rocks with relatively high porosity and mud content (Broadhurst, Isdell and Malu Formations), contrasting with high permeability where it intersects the basement and the Coolbro Sandstone.

6.1.3.5 Thermal properties, initial and boundary conditions

Ideally the fluid flow simulation should account for variations in thermal conductivity and specific heat capacity with lithology and temperature (e.g., Schön 2015), however to incorporate such variations in the model would have required modifications to the upscaling and simulation codes that were out of scope for this project. Consequently, representative values of 3 W/m/K and 800 J/kg/K were used throughout the model for the thermal conductivity and specific heat capacity of the solid rock, respectively. The bulk thermal conductivity of the fluid-saturated rock was calculated from the porosity as follows:

$$\lambda = \lambda_s(1 - \phi) + \lambda_f \phi \quad (11)$$

where λ, λ_s and λ_f are the thermal conductivities of the bulk rock, solid and pore fluid, respectively. This results in non-uniform bulk thermal conductivity due to porosity variations. In particular, the sediments have a lower bulk thermal conductivity than the basement due to their higher porosity, creating an insulating effect.

A heat flux of 85 mW/m^2 was applied at the bottom boundary, representing an intermediate value for a subsiding basin (see Sheldon et al. (2021) for discussion). The bottom and sides of the model were impermeable to fluid flow, and the sides were thermally insulated. The top of the model, representing the seafloor, was subject to a fixed temperature of 4 °C and fluid pressure consistent with the depth of the seafloor, which varied across the model domain (see colour shading in Figure 41).

The model was initialised with a conductive thermal steady state (no fluid flow) and hydrostatic fluid pressure consistent with the boundary conditions. The simulation was then run for sufficient time to establish thermal convection (430,000 years; this duration has no geological significance). The simulation took 40 hours to run using 640 processors on CSIRO's Petrichor cluster.

Note that salinity was not considered explicitly in this model; effectively this means the model represents a state of uniform salinity. Different results could be expected with a salinity distribution more similar to that used in the model of fluid release from an overpressured compartment (i.e. high salinity at the base of the Coolbro and low salinity elsewhere; see section 6.1.2). Consideration of salinity as another variable in the model would result in a considerable increase in computational complexity and simulation time, which could not be justified given the lack of data on likely salinity distribution in the basin at this time.

6.1.3.6 Results and discussion

The results illustrate the development of complex 3D convection cells within both the sediments and the faults (Figure 46, Figure 47, Figure 48). Within the sediments convection is most vigorous in the Coolbro Sandstone (Figure 48), owing to its relatively high longitudinal and transverse permeability (Figure 43, Figure 48). There is some fluid movement in the Broadhurst Formation above the convective upwellings (Figure 46, Figure 47), suggesting that some of the hot upwelling fluid from the Coolbro Sandstone does in fact penetrate into Broadhurst Formation, despite its low transverse permeability (Figure 43, Figure 44).

The highest flow rates in the model occur within the faults where they have relatively high permeability (Figure 46, Figure 47; see Figure 45 for fault permeabilities). Some of the hot upwelling fluid moves out of the faults and into the surrounding sediments, but note that the faults either stop at the top of the Coolbro Sandstone or have relatively low permeability above the Coolbro Sandstone, so their ability to transport fluid into the Broadhurst Formation is limited.

These results demonstrate the potential for thermal convection to circulate fluid within the undeformed basin, potentially transferring metal-bearing fluid from depth in the Coolbro Sandstone into the overlying Broadhurst Formation. Faults may have played a role in enhancing this circulation, but it is interesting to note that convective upwellings are not always associated with faults (e.g., the long ridge of convective upwelling in the Coolbro Sandstone in Figure 48). Quantifying the amount of fluid moving from the Coolbro into the Broadhurst Formation would reveal the significance of this fluid transfer mechanism for mineralisation but was out of scope for the present study owing to the complex 3D geometry of the model.

Many further questions could be addressed, either by further analysis of the results presented here, or by modifications of the model. For example:

- How much fluid moves from the Coolbro Sandstone into the Broadhurst Formation in the convective upwellings? Is it sufficient to account for economic mineralisation? Is this process enhanced by faults?
- How does the system evolve over longer timescales? Does it reach a steady state or is it a transient system in which the convective upwellings are mobile?
- Are convective upwellings favoured by certain geometric or stratigraphic features, e.g., basement highs or fault bends?
- How does the behaviour change with different porosity-permeability relationships, fault permeability models, or changes in the SFM?
- To what extent is the model influenced by boundary effects?

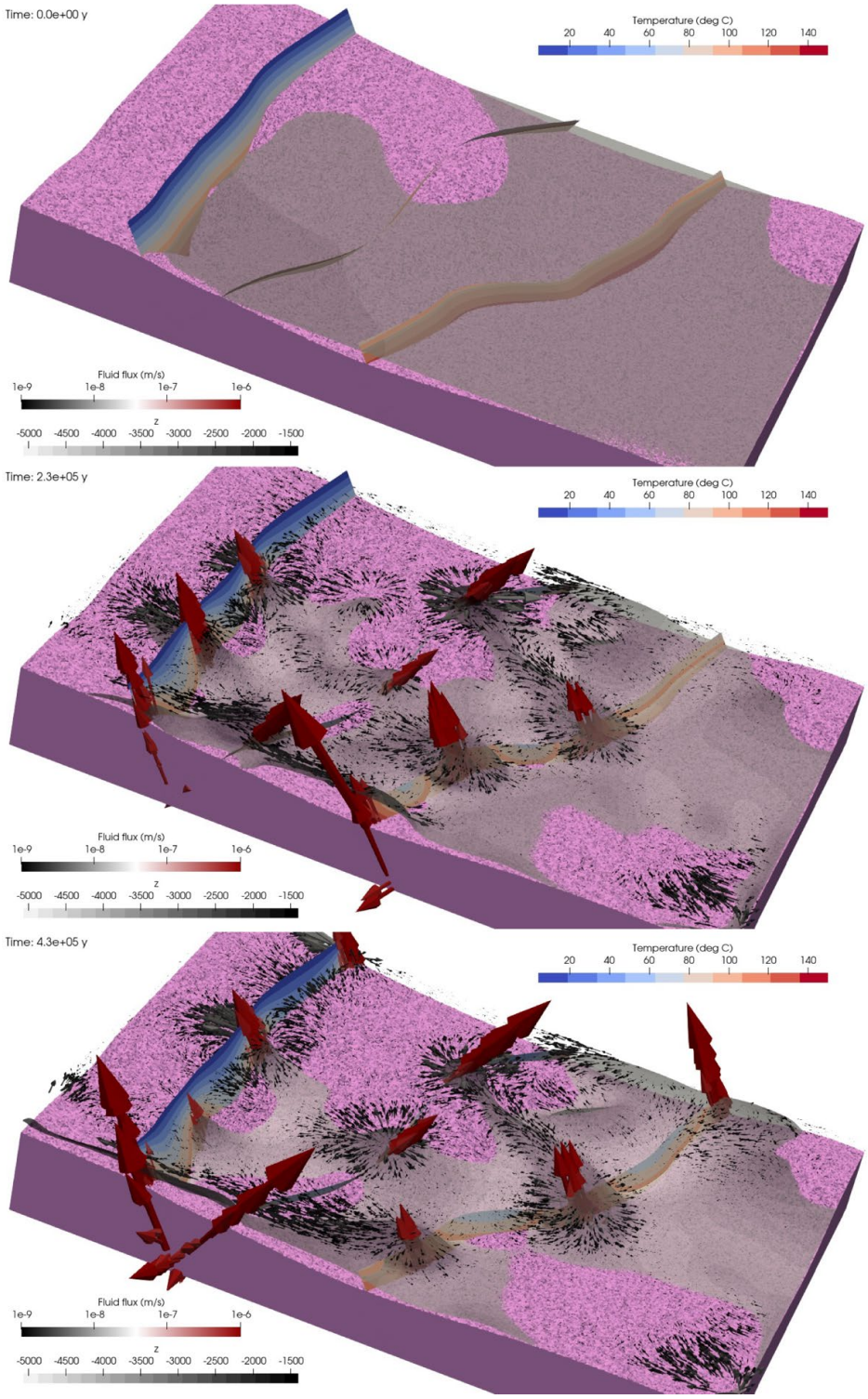

Figure 46. Development of thermal convection in faults and mud-rich layer (mud + carbonate mud > 50%) approximating the Broadhurst Formation. Faults coloured by temperature. Fluid flow vectors in faults (red) and mud-rich layer (grey-black) coloured and scaled by fluid flow rate. 100°C isosurface (grey-white) coloured by depth. Pink = basement. Top: Start of simulation. Middle: 230,000 years. Bottom: 430,000 years.

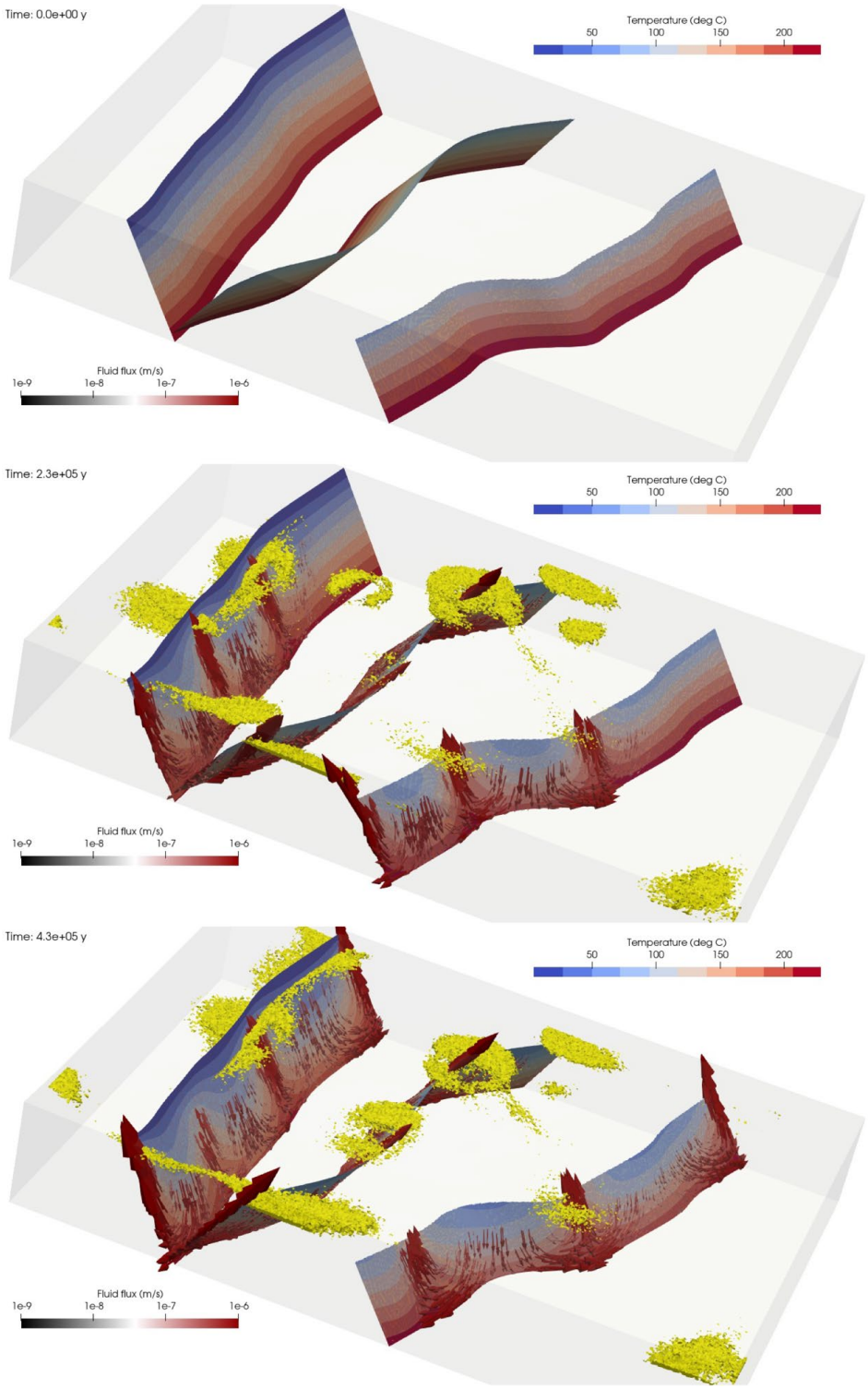

Figure 47. Development of thermal convection in faults and mud-rich layer (mud + carbonate mud > 50%) approximating the Broadhurst Formation. Faults coloured by temperature. Fluid flow vectors in faults coloured and scaled by fluid flow rate. Yellow regions indicate high fluid flux in mud-rich layer. Top: Start of simulation. Middle: 230,000 years. Bottom: 430,000 years.

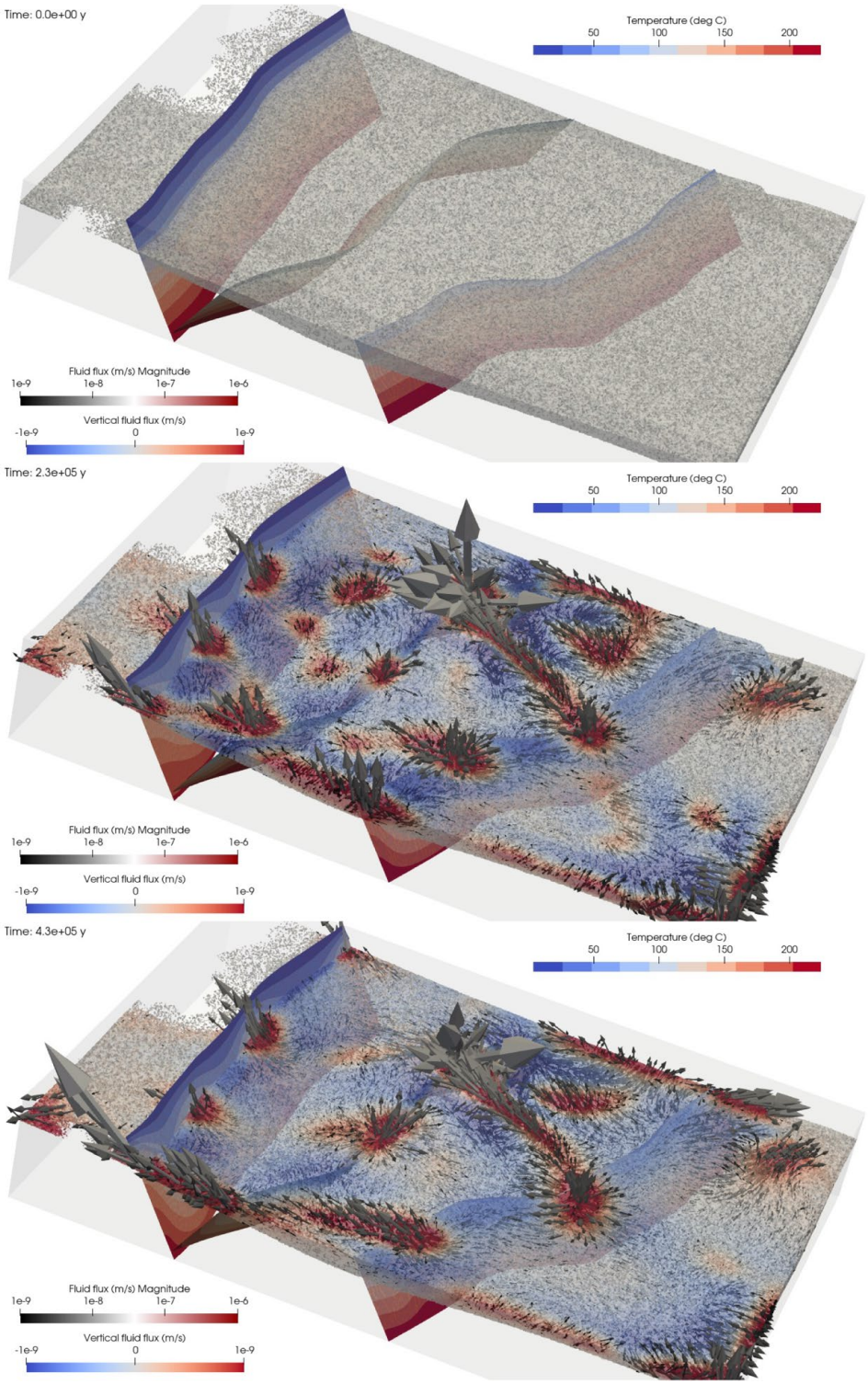

Figure 48. Development of thermal convection in faults and mud-poor layer (mud + carbonate mud < 10%) approximating the Coolbro Sandstone (semi-transparent region coloured by vertical fluid flux). Faults coloured by temperature. Fluid flow vectors in Coolbro Sandstone coloured and scaled by fluid flow rate. Top: Start of simulation. Middle: 230,000 years. Bottom: 430,000 years.

6.1.4 Fluid flow modelling scenario 4: Fluid pathways through the deformed basin

6.1.4.1 Context

The last stage of Cu mineralisation in the Yeneena Basin occurred during or after basin inversion (Miles event), hence it is of interest to explore fluid pathways through the basin in its deformed state. In this model, we simulated fluid flow and heat transport in a 2D geometry based on cross section B-B' (see section 5.2.1), with upward flow assumed to be driven by some larger-scale process (e.g., metamorphic fluid production, or deformation-driven flow associated with crustal shortening). This larger-scale process was represented by "injecting" fluid where the faults intersected the base of the model. As in previous model scenarios the faults were treated purely as regions of contrasting permeability; no attempt was made to simulate deformation or movement on the faults.

6.1.4.2 Geometry, properties and boundary conditions

The model geometry is shown in Figure 49. The cross section was truncated at -6000 m due to uncertainty about the structures at greater depth. A reasonable topographic surface was defined for the top boundary, with everything between the topographic surface and the top of the cross section (top of the Puntapunta Formation) being assigned to the Wilki Formation. Fluid pressure was fixed at atmospheric and temperature at 20 °C on the top boundary. A heat flux of 85 mW/m^2 was applied at the base of the model. Temperature and fluid pressure were fixed where the faults intersected the base of the model, with the fluid pressure being elevated at 10% above hydrostatic to drive upward flow in the faults. The temperature of the incoming fluid was fixed at 417 °C, this being broadly consistent with the temperature at the base of the model in the absence of fluid flow. There was no transfer of heat or fluid across the sides of the model. An inert tracer was added to the incoming fluid at the base of the faults to assist with visualising fluid pathways through the model.

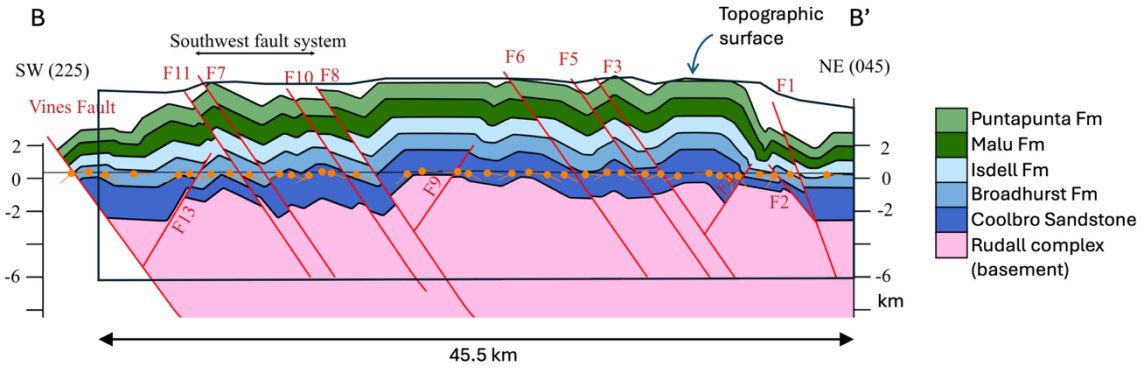

Figure 49. Model geometry based on cross section B-B'. Black outline indicates the boundaries of the model. The area between the topographic surface and the top of the Puntpunta Formation is assumed to be occupied by the Wilki Formation.

Porosity, permeability and thermal properties used in the model are listed in Table 13. Porosities derived from subsidence modelling were modified for lower Greenschist facies conditions, reflecting the burial and deformation history of the basin at this time. Horizontal permeability (k_h) was derived from porosity (ϕ) using Equation 1 (see section 6.1.3.3). We

chose $\phi_0 = 0.1$ and $k_0 = 10^{-14}$ m^2 for all model units except the faults, where $k_0 = 10^{-13}$ m^2. Vertical permeability was derived from horizontal permeability using Equation 2, with the anisotropy ratios listed in Table 13. Due to project time constraints we did not attempt to rotate the permeability tensor to follow the dip of the stratigraphic horizons (c.f. the thermal convection model, where the permeability tensor follows the stratigraphic layering derived from the SFM). Note the low permeability of the Broadhurst Formation, which has interesting implications for fluid flow and mineralisation that are discussed further below. The faults were assumed to act as high-permeability fluid pathways throughout the model, consistent with the behaviour of faults in consolidated rocks. This contrasts with the thermal convection model, which represented an earlier stage in the basin history when the sediments were not fully consolidated, hence fault permeability could be either higher or lower than that of the surrounding sediments depending on their porosity and mud content (see section 6.1.3.4).

Thermal conductivity, specific heat capacity and grain density are mean values for representative rock types from the Global Petrophysical Database (H. Sheldon et al. 2023), with the exception of the faults where generic rock values were assumed.

Table 13. Properties for fluid flow model on deformed cross section

Rock unit	Lithology	Porosity	Horizontal Permeability (m^2)	Permeability Anisotropy (k_h/k_v)	Thermal conductivity bulk rock (dry) (W/m/K)	Specific heat capacity (J/kg/K)	Grain density (kg/m^3)
Wilki	Dolomitic siltstone	0.12	1.8×10^{-14}	10	2.4	820	2580
Puntapunta	Dolomitic siltstone	0.12	1.8×10^{-14}	10	2.4	820	2580
Malu	Dolomitic siltstone	0.12	1.8×10^{-14}	10	2.4	820	2580
Isdell	Dolostone and Siltstone	0.045	8.1×10^{-16}	10	2.4	820	2580
Broadhurst	organic-rich shale, siltstone, limestone, and dolostone	0.0047	8.5×10^{-19}	100	1.7	660	2660
Coolbro	Sandstone	0.059	1.9×10^{-15}	1	2.7	790	2620
Rudall	Meta-sediments	0.02	6.7×10^{-17}	1	2.7	620	2670
Faults	NA	0.1	1.0×10^{-13}	1	2.5	800	2500

6.1.4.3 Results

Fluid flow pathways predicted by the model are illustrated in Figure 50 and Figure 51. Flow rates are much higher in faults than in the host rocks due to high permeability in the faults.

The highest flow rates occur in faults that span the whole height of the model (the penetrating faults), with much lower flow rates in the blind faults (i.e. those that terminate within the model) and in the fault that terminates on the left boundary (the Vines Fault; see Figure 49). Fault F1 (on the far right of the model) has the highest flow rate of all the faults; this is due to (i) the slightly lower topographic elevation where this fault intersects the top boundary; and (ii) the steeper dip of this fault when compared with the other penetrating faults. Both factors result in this fault being shorter than the other penetrating faults, which in turn results in a steeper fluid pressure gradient from bottom to top of this fault (noting that the fluid pressure is the same at the base of all faults). It is important to understand that the higher fluid flux in this fault is a consequence of the boundary condition that was chosen for the bottom of the faults, i.e. a fixed fluid pressure. If the boundary condition had instead been a fixed fluid flux, then the fluid flux would have been similar in all penetrating faults. Whether a fixed flux or a fixed pressure is more realistic is a question that cannot be easily resolved without resorting to a larger-scale model to explore the larger-scale processes that were assumed to be driving upward flow in this model.

Similarly, the low flow rate in the Vines fault (the fault that intersects the left boundary) is a consequence of the impermeable side boundary condition. This is unlikely to be realistic; in fact, as the Vines Fault is a major structure it is likely that it would have carried more fluid than the other faults, not less. These examples demonstrate the importance of interpreting model results with care, paying attention to the assumptions that were made when setting up the model and assigning its properties and boundary conditions.

Blind faults are less favourable than penetrating faults as pathways for fluid to travel through the crust, as they terminate in rocks that have lower permeability than the faults. The fate of fluid travelling through these blind faults can be seen in Figure 50B and in more detail in Figure 51. Fluid deviates out of the blind faults into the Coolbro Sandstone, which provides a pathway linking the blind faults to the penetrating faults, thus allowing fluid to escape to the surface. For faults that terminate in the Isdell Formation some fluid escapes through the Isdell Formation into the overlying higher permeability formations. There is negligible flow from blind faults into the Broadhurst Formation due to its very low permeability.

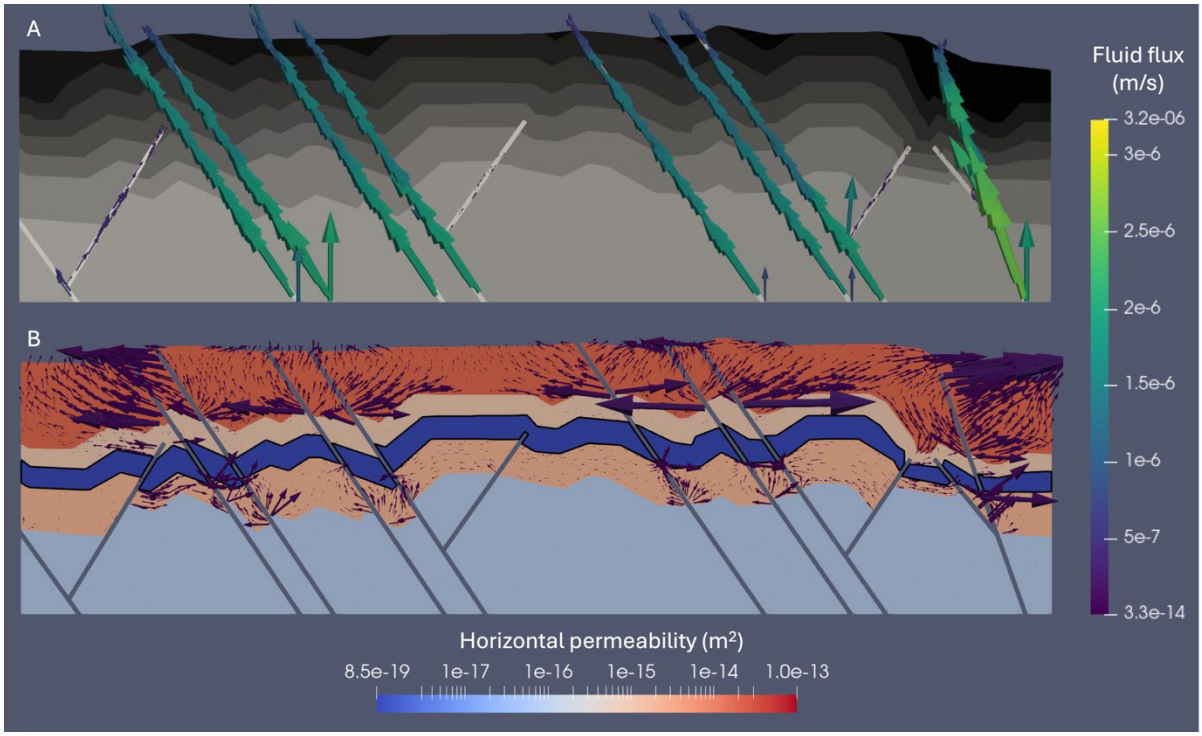

Figure 50. Fluid flow in the deformed cross section. Flow vectors are shown in (A) faults and (B) host rocks. Vectors coloured and sized by fluid flow rate. Black outline in (B) indicates the Broadhurst Formation.

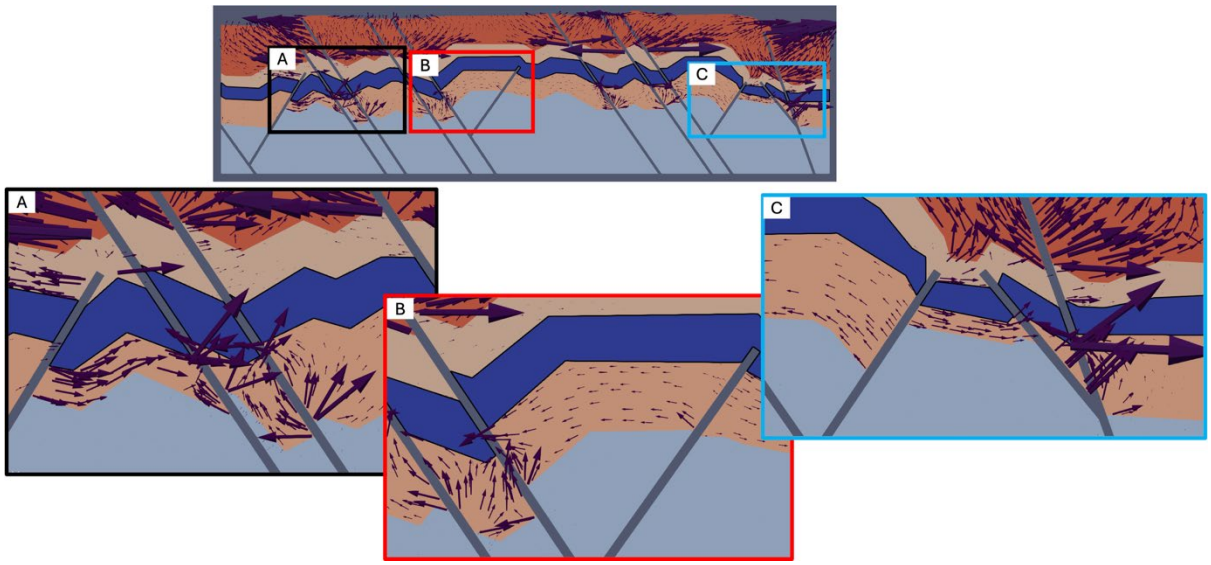

Figure 51. Details of fluid flow between faults in the deformed cross section (see Figure 50B for colour legend). Black outline indicates the Broadhurst Formation.

These fluid pathways are further illustrated in Figure 52A, which shows the distribution of an inert tracer coming from the bottom of each fault. High concentrations of tracer in the faults and the more permeable formations contrast with the absence of tracer in the Broadhurst Formation. This raises an interesting question: How can we explain mineralisation in the Broadhurst Formation, if its permeability is too low to allow fluid to enter? One possibility is localised permeability enhancement associated with fracturing in fault damage zones, consistent with the vein-hosted characteristic of late-stage mineralisation in the Yeneena

Basin. The effect of a high-permeability damage zone around the tip of blind fault F9 is illustrated in Figure 52B. The damage zone allows localised entry of fluid into the Broadhurst Formation. Alternatively, the permeability of the Broadhurst Formation may have been higher than suggested in Table 13, perhaps due to secondary porosity creation associated with carbonate replacement, or thin sandy layers within the Broadhurst Formation creating higher permeability on a small scale. Indeed, the existence of such sandy layers is indicated by the SFM (see Figure 44), but is difficult to capture on the scale of this model. The effect of higher permeability in the Broadhurst Formation is illustrated in in Figure 52C, where the permeability of the Broadhurst Formation has been increased 1000 times. This results in significant flow through the Broadhurst Formation, especially in the vicinity of the blind faults where the Broadhurst Formation now acts as a pathway linking blind faults to penetrating faults.

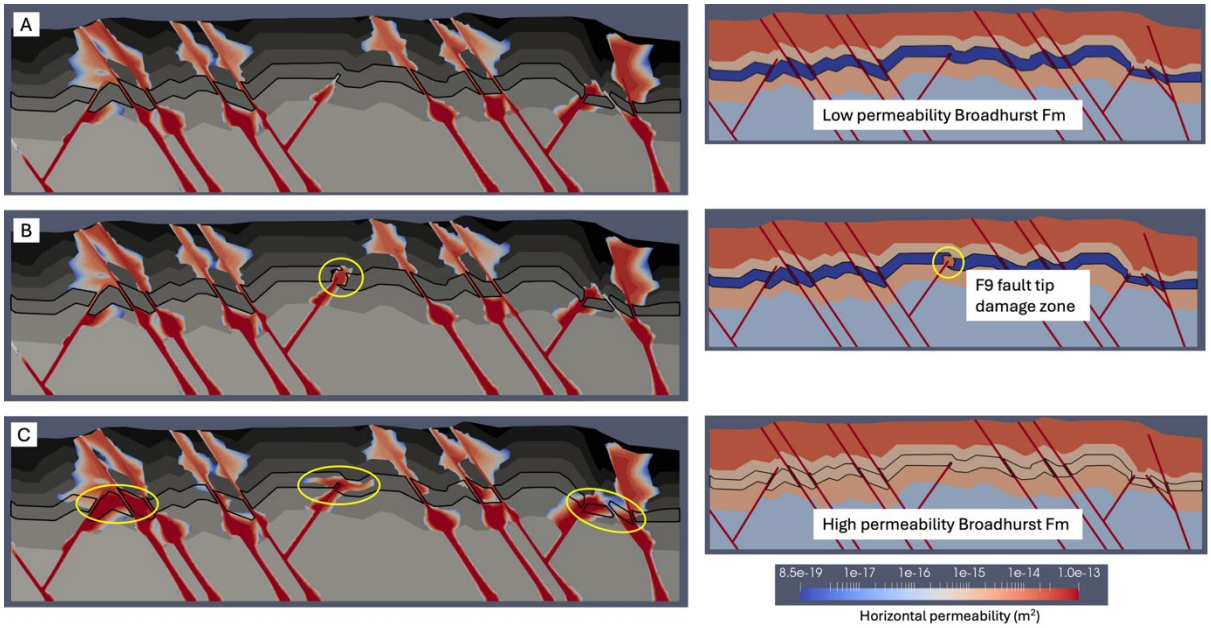

Figure 52. Tracer distribution (left) after 200 years of flow in the deformed cross section for different permeability scenarios (right). (A) Low permeability in Broadhurst Formation (see Table 13). (B) Damage zone around tip of fault F9. (C) High permeability (x1000) in Broadhurst Formation. Black outline indicates the Broadhurst Formation. Yellow ovals highlight areas of fluid flow into the Broadhurst Formation.

Technical difficulties prevented simulation of the temperature evolution over the same duration as the tracer, however the early stages of heat transport can be seen in Figure 53. At this early stage there is negligible heating of the host rocks, with elevated temperatures being largely confined to the faults. The white line represents the 300 °C temperature contour, corresponding to a recent temperature estimate for mineralisation at Nifty (Polito & Raye, 2025). At this early time the 300 °C contour barely reaches the Broadhurst Formation, but would certainly do so if the simulation could be continued, confirming that such temperatures are plausible.

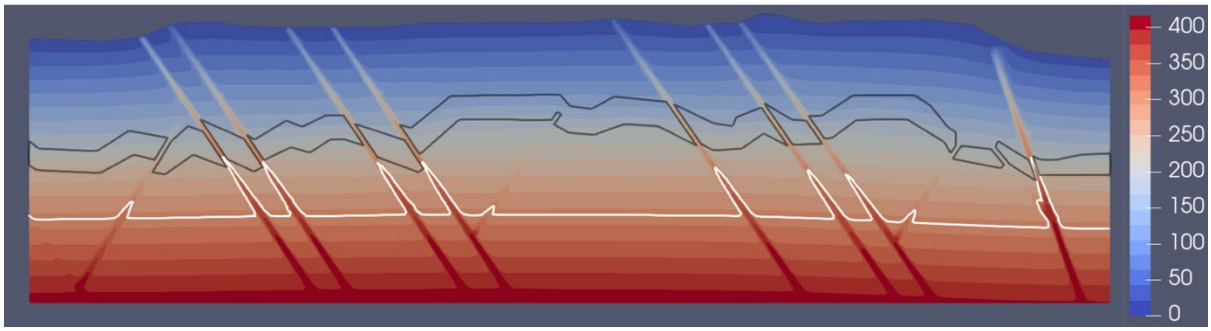

Figure 53. Temperature (°C) after 30 years of flow in the deformed cross section. Black outline indicates the Broadhurst Formation. White line = 300 °C contour.

6.1.4.4 Discussion

Stratabound base metal deposits typically occur in fine-grained sedimentary rocks (such as the Broadhurst Formation) because the mineralogy of these rocks provides the necessary geochemical conditions for base metal precipitation. Yet these fine-grained rocks tend to have very low permeability, hence there is a paradox: How did the mineralising fluid penetrate these low-permeability rocks? The fluid flow model scenarios presented in this report suggest some answers, depending on the timing of mineralisation.

For mineralisation that occurs early in the basin history, while the sediments are still relatively unconsolidated and before deformation or metamorphism, fluids ascending through faults will reach a point where the fault switches from high to low permeability. This is likely to occur in fine-grained strata, where various mechanisms (e.g., clay smear, shear-enhanced compaction) result in permeability reduction in fault zones (Barnicoat et al. 2009). At this point the fluid will deviate out of the fault and follow the path of least resistance through the sediments. This is illustrated in the thermal convection model (section 6.1.3.6), where hot upwelling fluid in convection cells within the faults deviates out into the surrounding sediments where the fault permeability switches from high to low. Thin layers of slightly coarser-grained sediment within fine-grained units (such as the Broadhurst Formation) may be critical in ensuring penetration of fluids into the host rocks.

For late-stage mineralisation the rocks are already consolidated, and faults tend to have high permeability regardless of their host rocks (Zhang et al. 2008). The model of fluid flow on a deformed cross section (section 6.1.4) suggests two factors that may have been critical in enabling fluid penetration into the Broadhurst Formation at this stage in the basin history:

1. (Localised) permeability enhancement in the Broadhurst Formation, e.g., due to fracturing in a fault damage zone, secondary porosity generation or thin sandy layers; and
2. The existence of blind faults that terminated in (or a little above or below) the Broadhurst Formation.

Cross sections through the Nifty deposit typically depict one or more blind faults (Figure 54). We postulate that these blind faults may have been critical in enabling mineralisation to occur there, as they enabled ascending fluid to penetrate into the host rock rather than escaping to the surface.

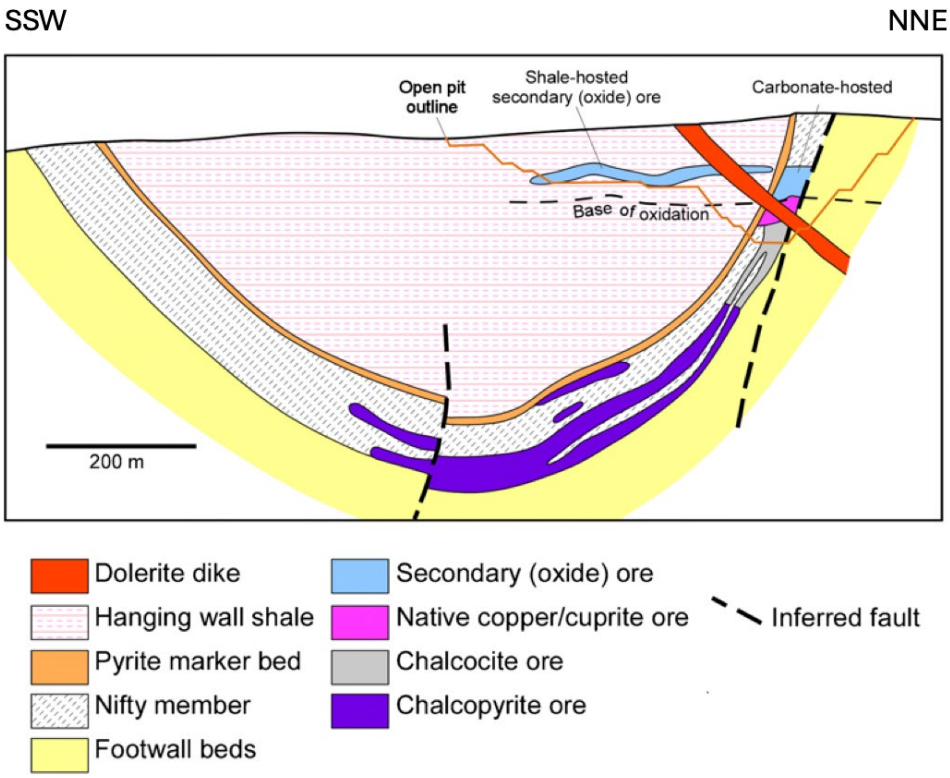

Figure 54. Cross section through the Nifty deposit, after Huston et al. (2020). Blind faults may have been critical to the formation of this deposit.

7 Discussion

The Yeneena Basin and Paterson Orogen have been the subject of several research projects in recent years (e.g., MRIWA M521, Minex CRC, GSWA projects, Geoscience Australia EFTF2), which have provided a substantial body of new geophysical, geochemical and geochronological data. These projects, combined with work undertaken by industry, have led to multiple interpretations of the present-day large-scale geological and structural framework (e.g., Bagas 2004; Grey et al. 2005; Kohanpour et al. 2024), but less attention was paid to the nature of fluid migration pathways during basin evolution. This study has addressed these gaps through a multi-disciplinary mineral systems approach, including evaluation of existing data (e.g., drill core data and geophysics), collection of new data (e.g., structural data from drill cores and geochronology), construction and restoration of cross sections, stratigraphic forward modelling to constrain the 4D distribution of sediment properties, and fluid flow modelling to test hypotheses regarding fluid sources, drivers and pathways in the Yeneena Basin sedimentary-hosted copper mineral system.

7.1 An integrated workflow for analysis of sedimentary-hosted copper

A primary aim of this project was to demonstrate a mineral systems analysis workflow for sedimentary-hosted Cu. This multi-disciplinary approach emphasises the integration of diverse datasets and methods across temporal and spatial scales to generate holistic insights into the ore-forming system.

The workflow combines well-established basin reconstruction tools (e.g., structural restoration, subsidence modelling) that are used extensively in petroleum exploration with techniques more commonly used in mineral exploration (e.g., geophysical inversion, geochronology) and modelling tools (stratigraphic forward modelling and fluid flow modelling).

Some aspects of the workflow are sequential, with the output of one method providing input to the next. For example, structural analysis combined with depth to basement determined from geophysical inversion enables construction of cross sections, which can then be restored to their undeformed state. The basement surface, fault traces, subsidence modelling and geochronology provide input for stratigraphic forward modelling, which in turn informs the porosity-permeability distribution for fluid flow modelling.

Importantly, this sequential approach is iterative. For instance, the first attempt at constructing a SFM used three restored cross-sections to constrain the 3D surfaces of key stratigraphic horizons. Early results highlighted the need for additional anchor-points to better constrain certain areas of the SFM. Consequently, one more cross-section was restored, which then allowed for the generation of more robust stratigraphic horizons, which were fed back into the SFM. Another example of such iterative work happened when project partners provided the new estimated age of 927 ± 33 Ma from vein calcite (see section 4.3.3), which implied an increase in the previously assumed duration of sedimentation in the basin, and a corresponding decrease in sedimentation rate. This in turn affected some of the architectural characteristics of the SFM results (thinner beds).

Some of the greatest insights arose from conducting different aspects of the workflow in parallel. In particular, fluid flow modelling was integrated into the project from an early stage, enabling researchers to share insights from modelling with project sponsors throughout the project. This in turn enabled the sponsors to engage with the process and pose questions that could be addressed later in the project, or recorded as avenues for further research.

Early discussions within the project team identified brine migration as a key component of the mineral system, which could be explored on a conceptual level without requiring a detailed understanding of the basin architecture (hence investigation could commence prior to structural restoration being complete). Brine migration was shown to be highly sensitive to dip angle in sub-horizontal strata. Therefore, understanding early brine migration pathways requires knowledge of sub-basin architecture (from structural restoration), sediment property distributions (from SFM), and associated anisotropic permeabilities. From this early work it became apparent that brine sourced from the Officer Basin would tend to accumulate at depth in the sub-basins, hence an alternative mechanism was required to drive upward flow into the Broadhurst Formation (the mineralisation host unit). This led to further modelling scenarios being identified to explore aspects of upward flow. Modelling conducted in later stages of the project relied on the outputs of other modules, such as cross sections, basement surfaces, subsidence analysis and stratigraphic forward models. This integrated approach resulted in a much greater understanding of the mineral system than would have been achieved if the fluid flow modelling had been undertaken as a separate exercise or left until the end of the project.

7.2 Improvements to regional geological understanding

The geophysical data interpretation conducted in this project provides new insights into the architecture of the Yeneena Basin. Integrated interpretation of the magnetic, gravity, and depth-to-basement data highlight a strong structural and geophysical partitioning of the region. Basement depth increases markedly toward the northeast, exceeding 8 km east of the West Waukarlycarly Fault, while remaining relatively shallow between the Vines Fault and the Southwest Thrust (Figure 4). Within the Yeneena Basin, arcuate NNW–NW trends reflect basin-scale structures, while localised circular anomalies such as those over the Mount Crofton Granite record intrusive events. Superimposed short-wavelength anomalies are best explained by shallow intrusives, including dykes. The NNW-trending Vines Fault, Southwest Thrust, and West Waukarlycarly Fault offset basement and stratigraphic horizons, exerting first-order control on depth-to-basement variations and domain boundaries. Cross-cutting NNE–NE trending shear zones further fragment these structures, locally displacing magnetic markers. Together, these structural systems compartmentalise the basin, influence sediment distribution, and govern the observed magnetic and gravity patterns.

Spectral analysis further indicates that magnetic sources are distributed at multiple crustal levels (~7 km, 2.5 km, and 0.8 km), consistent with a combination of deep basement heterogeneities, mid-crustal intrusives, and shallow magnetic horizons.

The expanded structural dataset (obtained from drill cores) combined with the depth to basement (interpreted from geophysics) enabled construction of detailed cross sections that reveal the post-inversion architecture of the basin. Restoration and kinematic analysis of these cross sections showed that crustal shortening during basin inversion was predominantly accommodated by folding (~86–98% of the total minimum shortening), with a

much smaller contribution from reverse faulting (~2–14% of the total minimum shortening). Normal faults formed during the basin's extensional phase were reactivated as reverse faults during basin inversion, demonstrating the importance of pre-existing mechanical weaknesses during the Miles and Paterson events.

A new age constraint from U-Pb dating of vein carbonate places the onset of sedimentation prior to 927 ± 33 Ma. Subsidence modelling confirms that the Yeneena Basin likely formed in an extensional context, with subsidence waning over time. In the Yeneena Basin, extension and associated subsidence peaked during its early stage of the basin formation when the Coolbro Sandstone and time-equivalent units were deposited in fault-controlled subbasins, after which the subsidence rate gradually slowed down. The genetic link between the NW and Western Officer basins and the Yeneena Basin was confirmed by the large-scale SFM models, which showed that sediments could have been transported into the Yeneena Basin from the south over long distances, as suggested by Grey et al. (2005) and Kunzmann et al. (2021). Additionally, Badlands simulation results suggested that most of the fault-controlled subbasins in the NW Officer Basin and Yeenena Basin were initially filled by sediments sourced from adjacent highs. When the relief was healed, the sediment transport-distance could have then increased. Prominent river systems could have accelerated this relief-healing process, meaning that river-derived sediments could have entered the Yeneena Basin after passing through the NW Officer Basin at a very early stage of the basin development.

7.3 Improved understanding of sedimentary-hosted copper mineral systems in the Yeneena Basin and beyond

Recent research (Raye et al. 2025) has shown that Cu mineralisation in the Yeneena Basin occurred in multiple stages. Two mineralisation phases predated basin inversion, while a third phase was associated with the Miles tectonic event. The geophysical interpretation, structural analysis, SFM and fluid-flow modelling provide insights into the basin's architecture and fluid flow pathways during each of these mineralisation phases.

The mineral system in the Yeneena Basin suggests a potential source of Cu in the Coolbro Sandstone, with documented Cu occurrences in the BroadhurstFormation, thought to be associated with the circulation of brines acting as the primary fluid for metal leaching and transport.

Regarding the source of the brine, SFM informed by subsidence modelling showed that evaporites would not have formed in the Yeneena Basin owing to the high subsidence rate and an overall marine depositional environment, but instead would have formed in the contemporaneous Officer Basin where subsidence rates were lower, and the depositional environment was prone to evaporites precipitation. Evaporites in the Officer Basin are therefore postulated as the source of the brines for sedimentary-hosted Cu mineralisation in the Yeneena Basin. This finding challenges prominent sedimentary-hosted mineral-system models by showing that critical components can be laterally displaced instead of vertically stacked, which broadens the exploration search space.

Structural restoration revealed the presence of horsts that formed during basin development, segmenting the basin into smaller sub-basins. One of these sub-basins hosts the Nifty Cu deposit. The geometry and location of these sub-basins relative to the postulated brine

source in the Officer Basin may have been critical in determining the location of mineralisation, because the sub-basins and the distribution of sedimentary facies within them (especially their dip and permeability anisotropy) dictated the fate of brine entering the Yeneena Basin.

Brine migration analysis through conceptual numerical modelling showed that brine would sink from its evaporitic source in the Officer Basin, travelling along the basement until it reached the edge of the Yeneena Basin. From there its path was strongly influenced by the dip and permeability anisotropy of the sedimentary strata, most likely accumulating in the closest sub-basin but potentially reaching more distant sub-basins depending on the dip and permeability anisotropy of the sediments. Importantly, it was shown that brine would accumulate at depth in the Coolbro Sandstone; there is no plausible scenario in which the brine could flow directly from its source into the Broadhurst Formation. Hence, some other mechanism is required to mobilise the fluid upwards from the Coolbro Sandstone into the overlying Broadhurst Formation, to account for mineralisation there.

The mechanism for upward brine migration was investigated numerically, noting that low to moderate concentration of copper in the fluid required large fluid volumes for mineralisation. Fluid flow modelling showed that fluid release from over-pressured compartments is unlikely to have been a viable mechanism for driving significant upward flow in this mineral system, whereas thermal convection could potentially account for the required fluid volumes due to the repeated cycling of fluid through the system. Thermal convection was shown to be strongly three-dimensional and controlled by the heterogeneous porosity-permeability distribution of the sediments and faults, emphasising the need for realistic 3D models for predicting fluid migration pathways.

Faults likely acted as important fluid pathways both before and after basin inversion. However, subsidence analysis and structural restoration indicate that most of the faults terminated at the top of the Coolbro Sandstone in the extensional phase of basin evolution; they did not penetrate far (if at all) into the Broadhurst or younger formations, except major structures such as the Vines Fault. Furthermore, faults in poorly-consolidated sediments tend to have low permeability and act as barriers to flow, especially in fine-grained sediments. This implies that fluid ascending through the faults prior to basin inversion would have deviated out into the sediments once it reached the top of the Coolbro Sandstone, potentially leading to some early-stage mineralisation. This contrasts with the situation during and after basin inversion, where most faults likely acted as fluid pathways all the way to the surface as the sediments were fully consolidated at that time.

Sedimentary-hosted copper and other base metals often occur in fine-grained sedimentary strata (e.g., the Broadhurst Formation) due to their favourable geochemistry and mineralogy. This presents a puzzle, as such units are typically assumed to have low average permeability, making it difficult to account for sufficient fluid flow to explain economic mineralisation. Modelling of fluid flow in the post-inversion (present day) geometry showed that localised permeability enhancement (e.g., due to carbonate replacement, fracturing or localised higher porosity-higher permeability layers) would be required to enable fluid to penetrate the Broadhurst Formation, and that blind faults terminating within (or perhaps just above or below) the Broadhurst Formation may have been critical, as trap mechanisms, to enable the fluid to penetrate the host rock, rather than by-passing it to escape at the surface. This is consistent with fault geometries at Nifty, as well as the vein-hosted character of late-stage mineralisation there.

7.4 Key Implications for mineral exploration

The results discussed above from provide several important insights into sedimentary-hosted Cu mineral systems that have direct implications for exploration in the Yeneena Basin and similar basins globally.

Brine source displacement
We investigated evaporites in the Officer Basin as a potential source of brines for Cu mineralisation in the Yeneena Basin. Our results suggest that brines are capable of migrating long distances between basins, indicating that critical components of the mineral system can be laterally distributed rather than vertically stacked. This finding challenges traditional models and provides valuable insights for early-stage exploration, particularly during basin screening process.

Fluid flow mechanisms and upward migration
Fluid flow modelling confirms that brine migration into the Yeneena Basin was strongly controlled by basin architecture, dip, and permeability anisotropy. Brines likely accumulated in the Coolbro Sandstone at depth, requiring an additional mechanism, such as thermal convection and/or structural reactivation during the Miles event, to mobilise fluids upward into the Broadhurst Formation. This highlights the importance of understanding both early and late-stage fluid movement when targeting mineralisation.

Both gravity-driven, downward brine-migration and upward mobilisation stages also occur on different time scales, with the former flowing at much slower rates than the upward mobilisation phase. Despite not having constrained the timing of that second phase, we suggest that shorter timescales should not be overlooked by mineral explorers, as essential components of the mineral system could have occurred very quickly.

Structural controls: faults as friends and foes
Structures exert a dual influence on fluid migration, with faults acting as barriers or conduits in complex manners, both in space and time. Faults often act as a conduit for fluid flow, localising flow within the fault gouge and its surrounding damage zone. However, in some instances (e.g., clay smearing, across-fault juxtaposition of low-permeability intervals to high-permeability rocks) one can observe lower permeability in the fault gouge despite higher permeability in the damage zone, leading to a strongly anisotropic behaviour with such faults acting as barriers transversally (across the fault gouge, leading to compartmentalisation) while simultaneously behaving as conduits longitudinally (with fluid flowing in the damage zone). On top of those spatial considerations, the (anisotropic) nature of a fault can evolve in time, based on changes of conditions (e.g., regional stress change, overpressure buildup, burial, exhumation) leading to variations in fault activity (e.g., deformation rate, inactivity, reactivation). After the extensional phase of the basin, faults terminating near the top of the Coolbro Sandstone, or within the overlying Broadhurst and Isdell formations acted as barriers to upward flow. Post-inversion, these same structures became effective conduits (at least episodically), enabling fluid ascent to near-surface environments. Blind faults terminating near the Broadhurst Formation likely played a critical role in localising mineralisation in such tight interval, as seen at Nifty.

The permeability structure of both sedimentary layers and faults – and how these properties evolve through space and time – is a critical control on fluid migration and mineralisation.

Explorers should prioritise understanding not only present-day permeability but also its dynamic changes during basin development and inversion.

7.5 Technology readiness level

It is difficult to apply the concept of Technology Readiness Level (TRL) to the workflow used in this project, as the workflow relies as much (if not more) on human expertise and communication as it does on technology. It could be argued that the workflow is at TRL 3 (experimental proof of concept). This will increase in future as the workflow is applied to more basins and mineral systems.

8 Conclusions

This study has demonstrated a comprehensive mineral systems analysis workflow for sedimentary-hosted Cu, using the Yeneena Basin as a case study. The workflow integrates a range of methods, including geophysical inversion, structural analysis, geochronology, subsidence modelling, construction and restoration of cross sections, stratigraphic forward modelling (SFM) and fluid flow modelling. The methods were integrated both sequentially (i.e. the output of one method provided input for another) and iteratively (i.e. new insights gained during the project were fed back into earlier models to improve their outputs).

Integrated interpretation of geophysical datasets constrained the present-day basement surface and fault architecture on a large scale. This information, combined with a comprehensive structural data set, was used to construct cross sections. Analysis and restoration of these cross sections provided insights into the spatial relationship between mineralisation, basin geometry, and ore-forming fluid migration pathways at different stages in the basin's history. SFM informed by the structural analysis, geochronology and subsidence modelling was shown to be useful both on a large scale, to address key conceptual questions (e.g., sediment source-to-sink pathways and the location of evaporites), and on a smaller scale, to provide detailed location-specific information that could then be fed into fluid flow models. provided Fluid flow modelling informed by the outputs of other methods enabled the researchers to test hypotheses about the Yeneena Basin mineral system, such as brine migration pathways and mechanisms for upward flow.

Subsidence modelling suggests that the Yeneena Basin formed in an extensional setting, possibly on a passive margin. U-Pb dating of vein carbonate provides a minimum depositional age of 927 ± 33 Ma for the Broadhurst Formation. Structural restoration revealed the existence of basement highs bounded by normal faults in the early stages of basin evolution. These basement highs defined a series of sub-basins, one of which contains the Nifty Cu deposit. The thicknesses of stratigraphic units on the restored cross sections indicate that the normal faults were most active during deposition of the Coolbro Sandstone, with little if any movement during deposition of the Broadhurst Formation and overlying units, suggesting that active extension had ceased by that time.

Based on the large-scale SFM, evaporites in the Officer Basin are postulated as a source of brine for sedimentary-hosted Cu mineralisation in the Yeneena Basin. Brine migration modelling showed that brine originating from evaporites in the Officer Basin would have descended to the basement and reached the Yeneena Basin within a relatively short time. Its path after that would have been strongly influenced by the dip, permeability and anisotropy of the basin fill; it is most likely that it would have accumulated at the bottom of the closest sub-basin but could potentially reach the next sub-basin depending on geometry and permeability. Accurate prediction of brine migration pathways using numerical modelling was shown to be very challenging, but an alternative approach based on an analytical solution provides a promising alternative, which could be used for a rapid first-pass assessment of potential brine pooling locations that may have been a pre-requisite for mineralisation.

Having accumulated in a sub-basin, the brine would need to be mobilised upwards to account for mineralisation in the Broadhurst Formation. Fluid flow modelling showed that fluid release from an over-pressured compartment could not generate significant upward

flow. Thermal convection may have been a viable mechanism, with convective upwellings creating regions of fluid penetration into the Broadhurst Formation.

Structural analysis of surface and drill core data suggests a NE-SW shortening direction during the Miles tectonic event, with shortening accommodated first by folding and later by reverse reactivation of the existing normal faults. Upward fluid flow driven by crustal shortening, thermal effects or metamorphic fluid production could explain late-stage mineralisation in the deformed basin. Blind faults and localised permeability enhancement in the Broadhurst Formation may have been critical in ensuring that fluid penetrated the host rock rather than bypassing it and continuing to the surface.

Specific outcomes of this project that may help to reduce the exploration search space in the Yeneena Basin (and in similar basins elsewhere) include:

1. Understanding of the role and location of basement highs and associated sub-basins; when combined with the new approach for assessing brine migration pathways, this knowledge could be used to identify locations where brine may have accumulated in sub-basins, which in turn could be a pre-requisite for mineralisation.
2. The role of blind faults terminating within (or close to) the Broadhurst Formation, which may have been critical to enable fluid to penetrate into the host rock during late-stage mineralisation.

In conclusion, the workflow demonstrated in this project has led to a significant increase in understanding of the Yeneena Basin sedimentary-hosted copper mineral system, and shows great promise to assist explorers in similar basins elsewhere.

9 Recommendations for further work

There are several avenues for further work that could improve either the workflow or understanding of the Yeneena Basin.

9.1 Mapping SFM output onto the deformed geometry

SFM provides a 4D distribution of sediment classes and their corresponding properties in the undeformed basin, which can be used to understand aspects of the mineral system prior to deformation. Future work should aim at developing the technology to map the SFM output onto the deformed geometry, to enable a better understanding of the mineral system at a later stage of the basin history (e.g., understanding the present-day distribution of source/host rocks and fluid pathways). This could be achieved in 2D using cross sections and assuming plane-strain deformation, but would be more challenging in 3D.

9.2 Improvement of SFM code

The SFM undertaken in this study utilised a combination of commercial and open-source codes, each with their own strengths and weaknesses. DionisosFlow (commercial) is well suited to modelling sub-aqueous processes but is expensive. Badlands (open-source) is better suited to modelling sub-aerial processes and provides flexibility to adapt the code as needed, but has limited capability for sub-aqueous processes. Therefore, a useful direction for future work would be to better implement sub-aqueous processes and evaporite deposition in Badlands, and/or to implement efficient coupling of Badlands to DionisosFlow. Additionally, future work should also aim at developing a particle-tracker to map the trajectory and residence time of individual sediment grains, which can be used to better track source-rock potential.

9.3 Geomechanical fault modelling for upward fluid migration

Late-stage fluid mobilisation was evaluated using fluid flow modelling under a thermal convection scenario. While this mechanism appears plausible, no definitive geological evidence was found to confirm that convection is the sole – or even the dominant – driver of fluid movement. Other theoretical processes remain possible which require investigation. We propose a geomechanical modelling study to investigate compressional regimes (e.g., during the Miles tectonic event) and identify the conditions that could lead to episodic fault reactivation associated with massive pore over-pressure, leading to short and fast upward pulses of hot fluids. This mechanism could lead to stronger thermal and pressurisation effects, enhancing the thermal convection responsible for the copper leaching and producing larger temperature and pressure gradient, therefore also enhancing deposition and mineralisation.

9.4 Methods to approximate brine migration

This study showed that numerical modelling of brine migration is very challenging, requiring extreme mesh refinement that is impractical on the scale of interest. Hence an alternative approach was proposed, which approximates the brine migration pathway incrementally based on an analytical solution (Section 6.1.1.4). This method could be implemented in 3D in a visualisation software like Paraview to provide rapid visualisation of potential brine migration pathways through a basin, revealing locations where brine may have accumulated.

That method could also be integrated within Badlands (SFM code) to model the flow of dense particles over the basement surface while accounting for the effects of heterogeneity and anisotropy in the basin fill. It would then provide an efficient first-order indication of potential brine pooling locations.

It should be noted that the accuracy of any brine migration analysis will depend on the accuracy of the basement surface, which itself must be restored to its pre-deformation state.

9.5 Parameter sensitivity studies

All models (whether fluid flow, stratigraphic, geophysical inversion or structural restoration) are sensitive to their inputs. Parameter sensitivity analysis (i.e. running models with different inputs/assumptions) can reveal the range of possible solutions, and/or identify which parameters have most influence on the outputs. This in turn can guide further data collection in order to better constrain the models.

Examples of parameter sensitivity analysis that could be useful in the context of this study include:

- Running the SFM (both large and small-scale) with different assumptions about subsidence rate, sediment sources, basement geometry
- Running fluid flow simulations with different permeabilities (or different porosity-permeability relationships)

9.6 Mesh generation

Fluid flow models require a suitable mesh to represent the faults and their host rocks. Mesh generation often is a bottleneck in the workflow, especially for complex 3D geometries with non-planar intersecting faults and discontinuous stratigraphic horizons. While some aspects of this challenge have been addressed by correctly mapping the anisotropic permeability orientation from the SFM onto an arbitrary mesh (H. A. Sheldon et al. 2023), appropriate representation of faults remains a challenging task. The most efficient approach is to represent faults as “lower dimensional features” (i.e. 2D surfaces within the 3D mesh, as in the 3D thermal convection model of Section 6.1.3); while this approach has been implemented successfully in MOOSE, further work is required to generalise it to different fault apertures and to ensure correct representation of fluid exchange between the 2D and 3D elements of the mesh.

9.7 Quantifying fluid fluxes

Quantifying fluid fluxes across key interfaces in fluid flow models (e.g., from faults into specific stratigraphic units, or from one stratigraphic unit to another) is useful for assessing the mineralisation potential of a simulated fluid flow pathway. This becomes quite challenging in 3D with complex geometries, as in the 3D thermal convection model based on the SFM (Section 6.1.3). An automated approach could be implemented in a 3D visualisation code such as Paraview to facilitate this analysis.

9.8 Data collection

Every modelling technique used in the workflow would benefit from additional constraints/data. Modelling never gives us “the answer” – instead it is part of a cycle, whereby data and observations lead to generation of hypotheses, which can be tested through modelling. The models lead to new insights, which in turn guide further data collection, and the cycle continues.

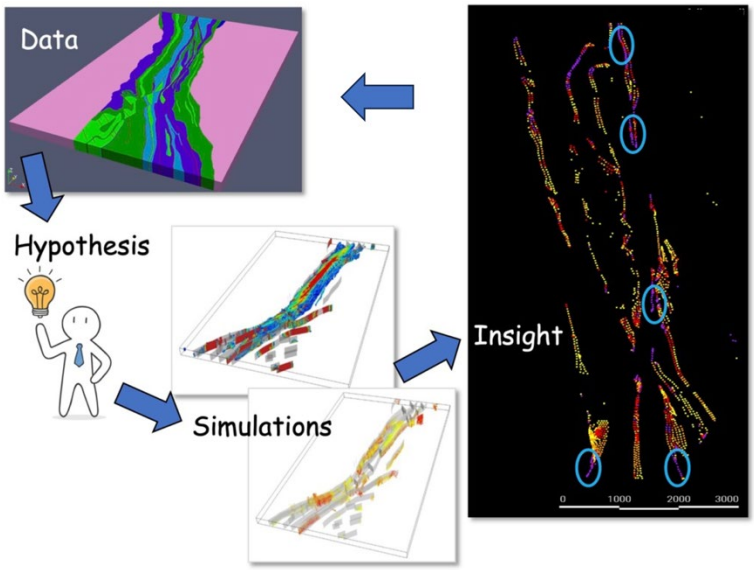

Figure 55. The role of modelling (simulations) in hypothesis testing. Data collection and modelling are part of a continuous cycle.

Here are some examples of additional data that could improve the models in this study, leading to improved understanding of the Yeneena Basin copper mineral system:

- **High-resolution gravity and magnetic data**, combined with advanced processing techniques (e.g., 3D inversion, analytic signal analysis, Euler deconvolution), can significantly enhance understanding of the structural and lithological controls on copper mineralisation. These methods help test existing geological models and delineate subsurface geometries. Incorporating **petrophysical measurements** (e.g., magnetic susceptibility, remanence, density, conductivity) from key units and faults would reduce uncertainty in 3D modelling and improve inversion accuracy, particularly for the Broadhurst Formation and associated fault systems.
- **Seismic reflection data and deep stratigraphic drill holes** are critical for constraining subsurface architecture, especially in areas with sparse surface data.

These datasets provide direct insights into deeper structural geometries, improving the reliability of structural models and reducing dependence on surface-based assumptions.

- **Accurate fault geometry** is essential for predictive fluid flow modelling. In the Yeneena Basin, limited surface exposure hampers direct mapping of fault zones. While regional seismic profiles can identify major structures, smaller faults often remain unresolved. Integrating geophysical methods capable of detecting and constraining fault geometries – such as targeted seismic surveys or potential field modelling – would enhance model fidelity.
- **Systematic acquisition of high-resolution seismic data** would support calibration of SFM simulations for mineral exploration. Unlike the energy sector, which benefits from extensive subsurface datasets, mineral exploration in metamorphosed and deformed basins lacks such data. Seismic sections, cubes, and downhole petrophysical logs would enable better parameterisation and calibration of simulation inputs.
- **Fluid flow modelling** would further benefit from additional constraints on physical and geological processes, including fluid composition, temperature, timing, and episodicity, as well as basin geometry and material properties (especially permeability) at the time of mineralisation.

9.9 Copper source rock analysis

A logical next step in understanding the Yeneena Basin sedimentary-hosted Cu mineral system (or indeed similar systems in other basins) would be a more in-depth consideration of potential copper source rocks. SFM provides some insights into the distribution of potential source rocks within the basin. However, the source rocks may be located outside the Yeneena Basin, requiring a broader study to identify likely candidates, determine their spatial distribution relative to suitable fluid flow pathways and host rocks in the Yeneena Basin, and establish their reactivity/ability to release copper into a carrier fluid. Studying modern analogues of such deposits could help assess the expected quality and architecture of ancient source rock.

References

Aitken, Alan RA, and Peter G. Betts. 2009. “Multi-Scale Integrated Structural and Aeromagnetic Analysis to Guide Tectonic Models: An Example from the Eastern Musgrave Province, Central Australia.” *Tectonophysics* 476 (3–4): 418–35.

Allen, P., and J. Allen. 2005. “Subsidence and Thermal History, Basin Analysis: Principles and Applications.” Oxford, United Kingdom, Blackwell Science Ltd.

Allen, Philip A., and John R. Allen. 2013. *Basin Analysis: Principles and Applications to Petroleum Play Assessment*. 3. ed. Wiley-Blackwell.

Allmendinger, Richard W., Nestor Cardozo, and Donald M. Fisher. 2011. *Structural Geology Algorithms: Vectors and Tensors*. Cambridge University Press.

Al-Salmi, Marya, Cédric M. John, and Nicolas Hawie. 2019. “Quantitative Controls on the Regional Geometries and Heterogeneities of the Rayda to Shu’aiba Formations (Northern Oman) Using Forward Stratigraphic Modelling.” *Marine and Petroleum Geology* 99 (January): 45–60. https://doi.org/10.1016/j.marpetgeo.2018.09.030.

Anderson, B. R., J. B. Gemmell, and R. F. Berry. 2001. “The Geology of the Nifty Copper Deposit, Throssell Group, Western Australia: Implications for Ore Genesis.” *Economic Geology* 96 (7): 1535–65. https://doi.org/10.2113/gsecongeo.96.7.1535.

Apak, S. N., and H. T. Moors. 2000. “A Sequence Stratigraphic Depositional Model of Neoproterozoic Strata, Yowalga Area, Officer Basin, Western Australia.” *The APPEA Journal* 40 (1): 15–25.

Apak, Sukru Nail, Henry Theodore Moors, and K. A. R. Ghori. 2000. *Basin Development and Petroleum Exploration Potential of the Yowalga Area, Officer Basin, Western Australia*. no. 76. Geological Survey of Western Australia.

Athy, Lawrence Ferdinand. 1930. “Density, Porosity, and Compaction of Sedimentary Rocks.” *AAPG Bulletin* 14 (1): 1–24.

Bagas, L. 2000. *Geology of the Paterson 1:100 000 Sheet*. Explanatory Notes. Geological Survey of Western Australia.

Bagas, L. 2004. “Proterozoic Evolution and Tectonic Setting of the Northwest Paterson Orogen, Western Australia.” *Precambrian Research* 128 (3–4): 475–96. https://doi.org/10.1016/j.precamres.2003.09.011.

Bagas, Leon. 2005. *Geology of the Lamil 1:100 000 Sheet*. 1:100 000 Geological Series Explanatory Notes. Western Australia Geological Survey.

Barnicoat, A. C., H. A. Sheldon, and A. Ord. 2009. “Faulting and Fluid Flow in Porous Rocks and Sediments: Implications for Mineralisation and Other Processes.” *Mineralium Deposita* 44 (6): 705–18. https://doi.org/10.1007/s00126-009-0236-4.

Barton, Penny, and Rosy Wood. 1984. “Tectonic Evolution of the North Sea Basin: Crustal Stretching and Subsidence.” *Geophysical Journal International* 79 (3): 987–1022.

Bear, Jacob. 1972. *Dynamics of Fluids in Porous Media*. Environmental Science Series. American Elsevier.

Behnam, Shekar, and Hamidreza Ramazi. 2019. “Interpretation of Geomagnetic Data Using Power Spectrum and 3D Modeling of Gol-e-Gohar Magnetic Anomaly.” *Journal of Applied Geophysics* 171 (December): 103829. https://doi.org/10.1016/j.jappgeo.2019.103829.

Betts, Peter G., David Moore, Alan Aitken, et al. 2024. “Geology from Aeromagnetic Data.” *Earth-Science Reviews* 258: 104958.

Betts, Peter G., Rick K. Valenta, and Jim Finlay. 2003. “Evolution of the Mount Woods Inlier, Northern Gawler Craton, Southern Australia: An Integrated Structural and Aeromagnetic Analysis.” *Tectonophysics* 366 (1–2): 83–111. https://doi.org/10.1016/S0040-1951(03)00062-3.

Betts, Peter Graham, David Giles, and G. S. Lister. 2004. “Aeromagnetic Patterns of Half-Graben and Basin Inversion: Implications for Sediment-Hosted Massive Sulfide Pb–Zn–Ag Exploration.” *Journal of Structural Geology* 26 (6–7): 1137–56.

Brown, A.C. 2014. “Low-Temperature Sediment-Hosted Copper Deposits.” In *Treatise on Geochemistry (Second Edition)*, edited by Heinrich D. Holland and Karl K. Turekian. Elsevier. https://doi.org/10.1016/B978-0-08-095975-7.01110-4.

Burgess, Peter M., Henne Lammers, Cees Van Oosterhout, and Didier Granjeon. 2006. “Multivariate Sequence Stratigraphy: Tackling Complexity and Uncertainty with Stratigraphic Forward Modeling, Multiple Scenarios, and Conditional Frequency Maps.” *AAPG Bulletin* 90 (12): 1883–901. https://doi.org/10.1306/06260605081.

Cawood, P. A., and R. J. Korsch. 2008. “Assembling Australia: Proterozoic Building of a Continent.” *Precambrian Research* 166 (1–4): 1–35. https://doi.org/10.1016/j.precamres.2008.08.006.

Chew, D. M., J. A. Petrus, and B. S. Kamber. 2014. “U–Pb LA–ICPMS Dating Using Accessory Mineral Standards with Variable Common Pb.” *Chemical Geology* 363: 185–99.

Chew, David M., and Richard A. Spikings. 2015. “Geochronology and Thermochronology Using Apatite: Time and Temperature, Lower Crust to Surface.” *Elements* 11 (3): 189–94.

Church, K. D., and A. L. Coe. 2003. “Chapter 5: Processes Controlling Relative Sea-Level Change and Sediment Supply.” In *The Sedimentary Record of Sea-Level Change*. The University of Cambridge. https://doi.org/10.2277/0521831113.

Clark, C., D. E. Kelsey, F. Kohanpour, C. L. Kirkland, K. Rankenburg, and S. Makin. 2023. “A Comparison of Fast Pulse and Conventional LA-ICP-MS Detrital Zircon Geochronology: A Large n Detrital Zircon Study from the Centralian Superbasin, Northwestern Australia.” *Precambrian Research* 393. https://doi.org/10.1016/j.precamres.2023.107103.

Costelloe, Marina, Ian Roach, and David Hutchinson. 2010. “Paterson AEM Survey Directly Detects Major Unconformity near Kintyre, WA.” *Preview* 145 (April): 2010.

Costelloe, Marina, Alan Whitaker, Ross Brodie, Adrian Fisher, and Camilla Sorensen. 2007. “Paterson Airborne Electromagnetic Survey, Onshore Energy and Minerals, Geoscience Australia.” *ASEG Extended Abstracts* 2007 (1): 1–4. https://doi.org/10.1071/ASEG2007ab183.

Costelloe, M.T., A. Fitzpatrick, I.C. Roach, and D.K. Hutchinson. 2012. “Paterson AEM Survey EM Vision 3D Inversion Data and Release Notes: Kintyre Area.”

https://pid.geoscience.gov.au/dataset/ga/74853, https://researchdata.edu.au/paterson-aem-survey-kintyre-area.

Czarnota, K., E. Gerner, D. W. Maidment, A. J. Meixner, and L. Bagas. 2009. “Paterson Area 1: 250 000 Scale Solid Geology Interpretation and Depth to Basement Model.” *Geoscience Australia Rec* 16.

Czarnota, K., K. Gessner, Y. LeyCooper, A. Ray, S. Wong, and N. Symington. 2022. *Exploring for the Future AEM Workshop: Perth, 2022*. Version 2.0, September 2018. https://doi.org/10.26186/147427.

Dalmaso Spode, F. 2020. “3D Prospectivity Modelling of Sedimentary-Hosted Base Metals Deposits of Yeneena Basin in Paterson Area - Western Australia.” Master of geoscience research thesis, University of Western Australia.

Dalstra, H. J., B. Rochat, C. Couper, and L. Glasser. 2025. “Au–Cu and Cu–Au Mineralisation in the Northern Paterson Province, Western Australia; New Insights into an Important Intrusion-Related Gold District.” *Australian Journal of Earth Sciences*, 1–32. https://doi.org/10.1080/08120099.2025.2514704.

Dalstra, Hilke, Adam Black, and Inna Mudrovska. 2023. “Geology of Winu-Ngapakarra, Great Sandy Desert of Western Australia, a Recently Discovered Intrusion-Related Cu-Au Deposit.” *Economic Geology* 118 (5): 967–98. https://doi.org/10.5382/econgeo.5005.

Dhote, Prashant, and Uday Bhan. 2025. “Advances in Simulation of Stratigraphic-Structural Evolution of Basin Fill: A Retrospective to Guide Future Progress.” *International Journal of Geophysics* 2025 (1): 2790962. https://doi.org/10.1155/ijge/2790962.

Domenico, Patrick A., and Franklin W. Schwartz. 1998. *Physical and Chemical Hydrogeology*. 2. ed., Paperback. Wiley.

Doublier, M. P., Brian Leslie Norman Kennett, T. Fomin, et al. 2020. *Basement Architecture from the Pilbara Craton to the Aileron Province: New Insights from Deep Seismic Reflection Line 18GA-KB1*. Geoscience Australia.

Durocher, K. E., T. K. Kyser, J. Marlatt, and A. Hanly. 2003. “New40Ar/39Ar Ages from the Central Paterson Orogen, Western Australia.” *Australian Journal of Earth Sciences* 50 (4): 601–10. https://doi.org/10.1046/j.1440-0952.2003.01011.x.

Ebner, Ronja M., and Paul T. Meijer. 2025. “A Question of Time and Space: A Model Approach to the Synchronous Precipitation of Gypsum and Halite during the Messinian Salinity Crisis.” *Climate of the Past* 21 (3): 705–18. https://doi.org/10.5194/cp-21-705-2025.

Elllis, Robert G., Barrry De Wet, and Ian N. Macleod. 2012. “Inversion of Magnetic Data from Remanent and Induced Sources.” *ASEG Extended Abstracts* 2012 (1): 1–4. https://doi.org/10.1071/ASEG2012ab117.

Eriksson, P.G, M.A Martins-Neto, D.R Nelson, et al. 2001. “An Introduction to Precambrian Basins: Their Characteristics and Genesis.” *Sedimentary Geology* 141–142 (June): 1–35. https://doi.org/10.1016/S0037-0738(01)00066-5.

Fedi, Maurizio, and Simona Mastro. 2018. “Bounded-Region Wavelet Spectrum: A New Tool for Depth Estimation of Gravity and Magnetic Data.” *SEG Technical Program Expanded Abstracts 2018*, August 27, 1425–29. https://doi.org/10.1190/segam2018-2998315.1.

Ferguson, K. M., Leon Bagas, and Ian Ruddock. 2005. *Mineral Occurrences and Exploration Potential of the Paterson Area*. Geological Survey of Western Australia.

Fullagar, P., and G. Pears. 2007. “Towards Geologically Realistic Inversion.” In *Proceedings of Exploration 07: Fifth Decennial International Conference on Mineral Exploration*, edited by B. Milkereit, vol. 28. Advances in Geophysical Inversion Modeling. https://www.911metallurgist.com/wp-content/uploads/2015/10/Towards-Geologically-Realistic-Inversion.pdf.

Fullagar, Peter K., and Glenn A. Pears. 2015. “Remanent Magnetisation Inversion.” *ASEG Extended Abstracts* 2015 (1): 1–4. https://doi.org/10.1071/ASEG2015ab188.

Gardiner, N. J., D. W. Maidment, C. L. Kirkland, S. Bodorkos, R. H. Smithies, and H. Jeon. 2018. “Isotopic Insight into the Proterozoic Crustal Evolution of the Rudall Province, Western Australia.” *Precambrian Research* 313: 31–50. https://doi.org/10.1016/j.precamres.2018.05.003.

Geognostics Australia Pty Ltd. 2022. *Western Officer Basin SEEBASE Structural Study and GIS*. No. 235. Geological Survey of Western Australia.

Giudicelli, Guillaume, Alexander Lindsay, Logan Harbour, et al. 2024. “3.0 - MOOSE: Enabling Massively Parallel Multiphysics Simulations.” *SoftwareX* 26 (May): 101690. https://doi.org/10.1016/j.softx.2024.101690.

Gorczyk, Weronika, Ian Tyler, and Fariba Kohanpour. 2025. *Lithospheric and Crustal-Scale Controls on Multi-Stage Basin Evolution: Impacts on Mineralising Systems*. No. 521. Perth.

Granjeon, D., and Phillip Joseph. 1999. “Concepts and Applications of A 3-D Multiple Lithology, Diffusive Model in Stratigraphic Modeling.” In *Numerical Experiments in Stratigraphy<subtitle>Recent Advances in Stratigraphic and Sedimentologic Computer Simulations</Subtitle>*, by John W. Harbaugh, W. Lynn Watney, Eugene C. Rankey, Rudy Slingerland, Robert H. Goldstein, and Evan K. Franseen. SEPM Society for Sedimentary Geology. https://doi.org/10.2110/pec.99.62.0197.

Gray, Mary Beth, and Gautam Mitra. 1993. “Migration of Deformation Fronts during Progressive Deformation: Evidence from Detailed Structural Studies in the Pennsylvania Anthracite Region, USA.” *Journal of Structural Geology* 15 (3–5): 435–49.

Grey, K., R. M. Hocking, M. K. Stevens, et al. 2005. *Lithostratigraphic Nomenclature of the Officer Basin and Correlative Parts of the Paterson Orogen, Western Australia*. No. 93.

Guillong, Marcel, Jörn-Frederik Wotzlaw, Nathan Looser, and Oscar Laurent. 2020. “Evaluating the Reliability of U–Pb Laser Ablation Inductively Coupled Plasma Mass Spectrometry (LA-ICP-MS) Carbonate Geochronology: Matrix Issues and a Potential Calcite Validation Reference Material.” *Geochronology* 2 (1): 155–67.

Guj, Pietro, and Richard Schodde. 2025. “Will Future Copper Resources and Supply Be Adequate to Meet the Net Zero Emission Goal?” *Geosystems and Geoenvironment* 4 (1): 100320.

Hagemann, S.G., V.A. Lisitsin, and D.L. Huston. 2016. “Mineral System Analysis: Quo Vadis.” *Ore Geology Reviews* 76 (July): 504–22. https://doi.org/10.1016/j.oregeorev.2015.12.012.

Hahn, A., E. G. Kind, and D. C. Mishra. 1976. “Depth Estimation of Magnetic Sources by Means of Fourier Amplitude Spectra.” *Geophysical Prospecting* 24 (2): 287–306. https://doi.org/10.1111/j.1365-2478.1976.tb00926.x.

Hanneson, James E., and Callum N. Baxter. 2022. “Discovery of the Havieron Gold-Copper Deposit, WA.” *Preview* 2022 (219): 42–47. https://doi.org/10.1080/14432471.2022.2103941.

Hayes, Timothy S., Dennis P. Cox, James D. Bliss, Nadine M. Piatak, and Robert R. Seal II. 2015. *Sediment-Hosted Stratabound Copper Deposit Model*. US Geological Survey.

Haynes, D. W., and P. P. Mazzoni. 1993. “Application of Conceptual Models for Sediment-Hosted Ore Deposits in the Discovery of the Nifty Copper and Adjacent Zinc-Lead Deposits, Yeneena Basin, Western Australia.” *Geological Association of Canada Special Paper* 40: 75–88.

Haynes, Douglas W., and Mark S. Bloom. 1987. “Stratiform Copper Deposits Hosted by Low-Energy Sediments; III, Aspects of Metal Transport.” *Economic Geology* 82 (3): 635–48. https://doi.org/10.2113/gsecongeo.82.3.635.

Heather A. Sheldon, Peter M. Schaubs, Teagan N. Blaikie, Marcus Kunzmann, Thomas Poulet, and Samuel C. Spinks. 2021. “3D Thermal Convection in the Proterozoic McArthur River Zn-Pb-Ag Mineral System, Northern Australia.” *Ore Geology Reviews* 133 (June): 104093. https://doi.org/10.1016/j.oregeorev.2021.104093.

Hedberg, Hollis Dow. 1936. “Gravitational Compaction of Clays and Shales.” *American Journal of Science* 5 (184): 241–87.

Hickman, Arthur Hugh, and Leon Bagas. 1999. *Geological Evolution of the Palaeoproterozoic Talbot Terrane, and Adjacent Meso-and Neoproterozoic Successions, Paterson Orogen, Western Australia*. Vol. 71. Geological Survey of Western Australia.

Hickman, Arthur Hugh, and Geoffrey L. Clarke. 1993. *Geology of the Broadhurst 1: 100 000 Sheet Western Australia*. Geological Survey of Western Australia.

Hitzman, M. W., D. Selley, and S. Bull. 2010. “Formation of Sedimentary Rock-Hosted Stratiform Copper Deposits through Earth History.” *Economic Geology* 105 (3): 627–39. https://doi.org/10.2113/gsecongeo.105.3.627.

Hitzman, Murray, Rodney Kirkham, David Broughton, Jon Thorson, and David Selley. 2005. *The Sediment-Hosted Stratiform Copper Ore System*.

Holthuijsen, Leo H. 2007. *Waves in Oceanic and Coastal Waters*. 1st ed. Cambridge University Press. https://doi.org/10.1017/CBO9780511618536.

Huston, D. L., R. Maas, and K. Czarnota. 2007. *The Age and Genesis of the Nifty Copper Deposit: Back to the Future*. Professional Opinion No. 2007/03. Geoscience Australia. https://www.ga.gov.au/bigobj/GA11121.pdf.

Huston, David L., Roland Maas, and Karol Czarnota. 2020. “The Age, Metal Source and Genesis of the Nifty Copper Deposit in the Context of the Geological Evolution of the Paterson Province, Western Australia.” *Mineralium Deposita* 55 (1): 147–62. https://doi.org/10.1007/s00126-019-00881-9.

Hutchinson, D. K., M. T. Costello, C. Sorensen, and I. C. Roach. 2010. *Paterson TEMPEST AEM Survey, Western Australia, 2010 Final Inversion Data and Conductivity Models*. https://pid.geoscience.gov.au/dataset/ga/70297.

Ingebritsen, Steven E., Ward E. Sanford, and Christopher E. Neuzil. 2006. *Groundwater in Geologic Processes*. 2nd ed. Cambridge University Press. https://doi.org/10.1017/9780511807855.

Jochum, Klaus Peter, Ulrike Weis, Brigitte Stoll, et al. 2011. “Determination of Reference Values for NIST SRM 610–617 Glasses Following ISO Guidelines.” *Geostandards and Geoanalytical Research* 35 (4): 397–429.

Jowett, E. Craig. 1986. “Genesis of Kupferschiefer Cu-Ag Deposits by Convective Flow of Rotliegendes Brines during Triassic Rifting.” *Economic Geology* 81 (8): 1823–37. https://doi.org/10.2113/gsecongeo.81.8.1823.

Kelemework, Y., M. Fedi, and M. Milano. 2021. “A Review of Spectral Analysis of Magnetic Data for Depth Estimation.” *GEOPHYSICS* 86 (6): J33–58. https://doi.org/10.1190/geo2020-0268.1.

Kelsey, D. E., B. V. Ribeiro, and C. L. Kirkland. 2024. *In Situ Mica Rb–Sr Geochronology from the Rudall Province: Searching for Miles*. No. 250.

Kohanpour, Fariba, Ian Tyler, Weronika Gorczyk, David Kelsey, Chris Fisher, and Anthony Kemp. 2024. “Early-Stage Intracontinental Rifting in the Neoproterozoic Centralian Superbasin: Systematic U–Pb and Lu–Hf Isotopes in Detrital and Inherited Zircons from the Yeneena Basin, Northwest Australia.” *Precambrian Research* 411 (September): 107524. https://doi.org/10.1016/j.precamres.2024.107524.

Kolodka, Christophe, Emmanuelle Vennin, Raphael Bourillot, Didier Granjeon, and Guy Desaubliaux. 2016. “Stratigraphic Modelling of Platform Architecture and Carbonate Production: A Messinian Case Study (Sorbas Basin, SE Spain).” *Basin Research* 28 (5): 658–84. https://doi.org/10.1111/bre.12125.

Kunzmann, Marcus, Helen McFarlane, and Susanne Schmid. 2021. *Stratigraphic and Structural Evolution of Tonian Strata in the Northwestern Officer Basin and Yeneena Basin, Paterson Orogen, WA*. Nos. EP2021-0424. CSIRO. https://doi.org/10.25919/j4mg-v783.

Lasabuda, Amando P. E., Domenico Chiarella, Tor O. Sømme, et al. 2024. “Unravelling Controls on Multi-source-to-sink Systems: A Stratigraphic Forward Model of the Early–Middle Cenozoic of the SW Barents Sea.” *Basin Research* 36 (4): e12883. https://doi.org/10.1111/bre.12883.

Laubach, Stephen E., P. Eichhubl, C. Hilgers, and R. H. Lander. 2010. “Structural Diagenesis.” *Journal of Structural Geology* 32 (12): 1866–72.

Lelièvre, Peter G., and Douglas W. Oldenburg. 2009. “A 3D Total Magnetization Inversion Applicable When Significant, Complicated Remanence Is Present.” *GEOPHYSICS* 74 (3): L21–30. https://doi.org/10.1190/1.3103249.

Ley-Cooper, AY. 2020. *AusAEM 02 WA/NT, 2019-20 Airborne Electromagnetic Survey: TEMPEST(R) Airborne Electromagnetic Data and Conductivity Estimates*. Airborne Magnetic and Radiometric Survey. Geoscience Australia. https://geoscience.nt.gov.au/gemis/ntgsjspui/handle/1/90546.

Li, Yaoguo, and Douglas W. Oldenburg. 1996. “3-D Inversion of Magnetic Data.” *GEOPHYSICS* 61 (2): 394–408. https://doi.org/10.1190/1.1443968.

Li, Zenghua, Guoxiang Chi, Kathryn M. Bethune, et al. 2021. “Interplay between Thermal Convection and Compressional Fault Reactivation in the Formation of Unconformity-Related Uranium Deposits.” *Mineralium Deposita* 56 (7): 1389–404. https://doi.org/10.1007/s00126-020-01011-6.

Mackey, Campbell. 2012. “Telfer Region FALCON Airborne Survey, Western Australia.” *ASEG Extended Abstracts* 2012 (1): 1–2. https://doi.org/10.1071/ASEG2012ab206.

Madhoo, H.A., A. Acevedo, D. Tetzlaff, and J. Tveiten. 2016. “Combining Forward Stratigraphic Modelling with Seismic Reconstruction to Improve Reservoir Characterization.” Paper presented at Second Conference on Forward Modelling of Sedimentary Systems, Trondheim, Norway. April 25. https://doi.org/10.3997/2214-4609.201600382.

Maidment, D. W., D. L. Huston, and T. Beardsmore. 2017. *Paterson Orogen Geology and Metallogeny*. No. 32.

Maidment, D. W., D. L. Huston, R. Maas, et al. 2008. *The Nifty–Kintyre–Duke Cu–U–Pb–Zn Mineralizing Events: Links to the Evolution of the Yeneena Basin, Northwest Paterson Orogen*.

Makuluni, Patrick, Juerg Hauser, and Stuart Clark. 2022. “Tilting of the Australian Continent: New Evidence from the Subsidence and Deposition History of the Northern Carnarvon Basin.” *Marine and Petroleum Geology* 137 (March): 105483. https://doi.org/10.1016/j.marpetgeo.2021.105483.

Manning, Andrew H., and Poul Emsbo. 2018. “Testing the Potential Role of Brine Reflux in the Formation of Sedimentary Exhalative (Sedex) Ore Deposits.” *Ore Geology Reviews* 102 (November): 862–74. https://doi.org/10.1016/j.oregeorev.2018.10.003.

Markoski, M., J. Trunfull, and B. Bourne. 2021. *Regional Petrophysics: Paterson Orogen 2020-21*. Geological Survey of Western Australia.

Martin, Erin L., William J. Collins, and Christopher L. Kirkland. 2017. “An Australian Source for Pacific-Gondwanan Zircons: Implications for the Assembly of Northeastern Gondwana.” *Geology*, ahead of print. https://doi.org/10.1130/g39152.1.

McCuaig, T. Campbell, Steve Beresford, and Jon Hronsky. 2010. “Translating the Mineral Systems Approach into an Effective Exploration Targeting System.” *Ore Geology Reviews* 38 (3): 128–38. https://doi.org/10.1016/j.oregeorev.2010.05.008.

McCuaig, T. Campbell, Sonia Scarselli, Timothy O’Connor, Stephen Busuttil, and Niall McCormack. 2018. *The Power of a Systems Approach to Mineral and Petroleum Exploration in Sedimentary Basins*.

Meixner, A. J., R. J. L. Lane, K. Czarnota, E. Gerner, and A. McIntyre. 2006. *The Paterson 3D VRML Model*. https://pid.geoscience.gov.au/dataset/ga/64787.

Metals X Limited. 2017. “Annual Report 2017.” Metals X Limited. https://www.metalsx.com.au/asx/annual-report-2017/.

Mudd, Gavin M., and Simon M. Jowitt. 2018. “Growing Global Copper Resources, Reserves and Production: Discovery Is Not the Only Control on Supply.” *Economic Geology* 113 (6): 1235–67.

Munday, S., D. S. Edwards, J. Chandra, et al. 2022. *Defining a Chemostratigraphic Framework for the Officer Basin. Inorganic and Stable Isotopic Analyses of Ten Petroleum Wells from Western Australia and South Australia*. No. 2022/007.

Naidu, Prabhakas S. 1972. “Maximum Likelihood (ML) Estimation of Depth from the Spectrum of Aeromagnetic Fields.” *Pure and Applied Geophysics* 95 (1): 141–49. https://doi.org/10.1007/BF00878862.

Neuzil, C. E. 1994. “How Permeable Are Clays and Shales?” *Water Resources Research* 30 (2): 145–50. https://doi.org/10.1029/93WR02930.

Nuriel, Perach, Jörn-Frederik Wotzlaw, Maria Ovtcharova, et al. 2020. “The Use of ASH-15 Flowstone as a Matrix-Matched Reference Material for Laser-Ablation U-Pb Geochronology of Calcite.” *Geochronology Discussions* 2020: 1–26.

Paces, James B., and James D. Miller Jr. 1993. “Precise U-Pb Ages of Duluth Complex and Related Mafic Intrusions, Northeastern Minnesota: Geochronological Insights to Physical, Petrogenetic, Paleomagnetic, and Tectonomagmatic Processes Associated with the 1.1 Ga Midcontinent Rift System.” *Journal of Geophysical Research: Solid Earth* 98 (B8): 13997–4013.

Paola, Chris. 2000. “Quantitative Models of Sedimentary Basin Filling.” *Sedimentology* 47 (s1): 121–78. https://doi.org/10.1046/j.1365-3091.2000.00006.x.

Parui, Chirantan, Susanne Schmid, Giovanni Spampinato, et al. under review. “Linking Basin Evolution to Sedimentary-Hosted Copper Systems: Insights from the Neoproterozoic Yeneena Basin, Australia.” Unpublished manuscript.

Paton, Chad, John Hellstrom, Bence Paul, Jon Woodhead, and Janet Hergt. 2011. “Iolite: Freeware for the Visualisation and Processing of Mass Spectrometric Data.” *Journal of Analytical Atomic Spectrometry* 26 (12): 2508–18.

Posamentier, Henry W., and Roger G. Walker, eds. 2006. *Facies Models Revisited*. SEPM (Society for Sedimentary Geology). https://doi.org/10.2110/pec.06.84.

Poulet, Thomas, Juan Felipe Giraldo, Erick Ramanaidou, Agnieszka Piechocka, and Victor M. Calo. 2023. “Paleo-stratigraphic Permeability Anisotropy Controls Supergene Mimetic Martite Goethite Deposits.” *Basin Research* 35 (2): 572–91. https://doi.org/10.1111/bre.12723.

Poulet, Thomas, Heather A. Sheldon, Ulrich Kelka, and Pouria Behnoudfar. 2023. “Impact of Permeability Anisotropy Misalignment on Flow Rates Predicted by Hydrogeological Models.” *Hydrogeology Journal* 31 (8): 2129–37. https://doi.org/10.1007/s10040-023-02708-4.

Poulet, Thomas, Heather A. Sheldon, Valentin Zuchuat, and Susanne Schmid. 2025. “Small Dip, Big Impact: How 1° Strata Inclination Affects Density-Driven Flow in Anisotropic Rocks.” *Geology*, ahead of print, September 17. https://doi.org/10.1130/G53888.1.

Raye, Urmidola, Paul Polito, Peir K. Pufahl, et al. 2025. “Reinterpretation of the Geodynamic Evolution and Multistage Mineralization Events of the Nifty Copper Deposit, Paterson Province, Western Australia through Age, Textural and Geochemical Data.” *Ore Geology Reviews* 185. https://doi.org/10.1016/j.oregeorev.2025.106801.

Reed, A. R., J. R. Vearncombe, and D. I. Groves. 1995. “Timing of Copper Mineralization at Maroochydore, Paterson Orogen, Western Australia: Implications for the Genesis of

Sediment-Hosted Copper Deposits.” Mineral Deposits: From Their Origin to Their Environmental Impact, edited by J. Pasava, B. Kribek, and K. Zak.

Ribeiro, B. V., C. L. Kirkland, M. I. H. Hartnady, E. L. Martin, E. West, and P. Polito. 2023. “Multi-Stage Alteration at Nifty Copper Deposit Resolved via Accessory Mineral Dating and Trace Elements.” *Precambrian Research* 388. https://doi.org/10.1016/j.precamres.2023.107018.

Roach, I. C., K. F. Cassidy, M. T. Costello, et al. 2010. “Geological and Energy Implications of the Paterson Province Airborne Electromagnetic (AEM) Survey, Western Australia.” *Geoscience Australia Record* 12: 318.

Roberts, Alan M., Nick J. Kusznir, Graham Yielding, and Peter Styles. 1998. “2D Flexural Backstripping of Extensional Basins; the Need for a Sideways Glance.” *Petroleum Geoscience* 4 (4): 327–38. https://doi.org/10.1144/petgeo.4.4.327.

Roberts, Nick MW, E. Troy Rasbury, Randall R. Parrish, Christopher J. Smith, Matthew SA Horstwood, and Daniel J. Condon. 2017. “A Calcite Reference Material for LA-ICP-MS U-Pb Geochronology.” *Geochemistry, Geophysics, Geosystems* 18 (7): 2807–14.

Salles, T., and L. Hardiman. 2016. “Badlands: An Open-Source, Flexible and Parallel Framework to Study Landscape Dynamics.” *Computers & Geosciences* 91 (June): 77–89. https://doi.org/10.1016/j.cageo.2016.03.011.

Schaubs, Peter, Heather Sheldon, Teagan Blaikie, Marcus Kunzmann, Susanne Schmid, and Sam Spinks. 2019. “Basin-Scale Fluid-Flow Models of the McArthur River Mineral System: Constraints from Geochemistry, Geophysics and Sequence Stratigraphy.” *ASEG Extended Abstracts* 2019 (1): 1–5. https://doi.org/10.1080/22020586.2019.12073198.

Schindler, C., S. G. Hagemann, D. Banks, T. Mernagh, and A. C. Harris. 2016. “Magmatic Hydrothermal Fluids at the Sedimentary Rock-Hosted, Intrusion-Related Telfer Gold-Copper Deposit, Paterson Orogen, Western Australia: Pressure-Temperature-Composition Constraints on the Ore-Forming Fluids.” *Economic Geology* 111 (5): 1099–126. https://doi.org/DOI%252010.2113/econgeo.111.5.1099.

Schmid, Susanne. 2022. “Copper Exploration in Sedimentary Basins, Reducing the Search Space.” MEGWA monthly meeting, October.

Schoene, Blair, and Samuel A. Bowring. 2007. “Determining Accurate Temperature–Time Paths from U–Pb Thermochronology: An Example from the Kaapvaal Craton, Southern Africa.” *Geochimica et Cosmochimica Acta* 71 (1): 165–85.

Schön, Jürgen H. 2015. “Thermal Properties.” In *Developments in Petroleum Science*, vol. 65. Elsevier. https://doi.org/10.1016/B978-0-08-100404-3.00009-3.

Sclater, John G., and P. A. F. Christie. 1980. “Continental Stretching: An Explanation of the Post-Mid-Cretaceous Subsidence of the Central North Sea Basin.” *Journal of Geophysical Research: Solid Earth* 85 (B7): 3711–39. https://doi.org/10.1029/JB085iB07p03711.

Serck, Christopher Sæbø, Alvar Braathen, Snorre Olaussen, et al. 2021. “Supradetachment to Rift Basin Transition Recorded in Continental to Marine Deposition; Paleogene Bandar Jissah Basin, NE Oman.” *Basin Research* 33 (1): 544–69. https://doi.org/10.1111/bre.12484.

Sheldon, Heather A., Vincent Crombez, Thomas Poulet, Ulrich Kelka, Marcus Kunzmann, and Emily Kerrison. 2023. “Realistic Permeability Distributions in Faults and Sediments: The

Key to Predicting Fluid Flow in Sedimentary Basins." *Basin Research* 35 (6): 2118–39. https://doi.org/10.1111/bre.12792.

Sheldon, Heather, David Dewhurst, Matthias Raiber, Chris Turnadge, and Dirk Mallants. 2023. "Global Petrophysical Database." CSIRO. 49.20 MB. https://doi.org/10.25919/2YWZ-KZ60.

Sibson, Richard H. 1990. "Conditions for Fault-Valve Behaviour." *Geological Society, London, Special Publications* 54 (1): 15–28.

Sibson, Richard H., Francois Robert, and K. Howard Poulsen. 1988. "High-Angle Reverse Faults, Fluid-Pressure Cycling, and Mesothermal Gold-Quartz Deposits." *Geology* 16 (6): 551–55.

Singer, Donald A. 2017. "Future Copper Resources." *Ore Geology Reviews* 86: 271–79. https://doi.org/10.1016/j.oregeorev.2017.02.022.

Sloss, L. L. 1962. "Stratigraphic Models in Exploration." *AAPG Bulletin* 46. https://doi.org/10.1306/BC7438A5-16BE-11D7-8645000102C1865D.

Spampinato, G. P. T., P. G. Betts, L. Ailleres, and R. J. Armit. 2015. "Structural Architecture of the Southern Mount Isa Terrane in Queensland Inferred from Magnetic and Gravity Data." *Precambrian Research* 269: 261–80.

Spampinato, Giovanni Pietro Tommaso. 2025. "Assessing Future Exploration Potential of the Central and Southern Cobar District Using Integrated 3D Geological Modelling and Geophysical Inversion of Magnetic Data." *Exploration Geophysics*.

Spampinato, Giovanni PT, Laurent Ailleres, Peter G. Betts, and Robin J. Armit. 2015. "Imaging the Basement Architecture across the Cork Fault in Queensland Using Magnetic and Gravity Data." *Precambrian Research* 264: 63–81.

Spector, A., and F. S. Grant. 1970. "Statistical Models for Interpreting Aeromagnetic Data." *Geophysics* 35 (2): 293–302. https://doi.org/10.1190/1.1440092.

Stoffell, B., M. S. Appold, J. J. Wilkinson, N. A. McClean, and T. E. Jeffries. 2008. "Geochemistry and Evolution of Mississippi Valley-Type Mineralizing Brines from the Tri-State and Northern Arkansas Districts Determined by LA-ICP-MS Microanalysis of Fluid Inclusions." *Economic Geology* 103 (7): 1411–35. https://doi.org/10.2113/gsecongeo.103.7.1411.

Thomson, Stuart N., George E. Gehrels, Joaquin Ruiz, and Robert Buchwaldt. 2012. "Routine Low-damage Apatite U-Pb Dating Using Laser Ablation–Multicollector–ICPMS." *Geochemistry, Geophysics, Geosystems* 13 (2).

Twiss, Robert J., and Eldridge M. Moores. 1992. *Structural Geology*. Macmillan.

Vallée, Marc A., Colin G. Farquharson, William A. Morris, et al. 2019. "Comparison of Geophysical Inversion Programs Run on Aeromagnetic Data Collected over the Highland Valley Copper District, British Columbia, Canada." *Exploration Geophysics* 50 (3): 310–23. https://doi.org/10.1080/08123985.2019.1604068.

Vermeesch, Pieter. 2018. "IsoplotR: A Free and Open Toolbox for Geochronology." *Geoscience Frontiers* 9 (5): 1479–93.

Walter, M. R., J. J. Veevers, C. R. Calver, and K. Grey. 1995. “Neoproterozoic Stratigraphy of the Centralian Superbasin, Australia.” *Precambrian Research* 73 (1): 173–95. https://doi.org/10.1016/0301-9268(94)00077-5.

Wilkins, Andy, Christopher P. Green, and Jonathan Ennis-King. 2021. “An Open-Source Multiphysics Simulation Code for Coupled Problems in Porous Media.” *Computers & Geosciences* 154 (September): 104820. https://doi.org/10.1016/j.cageo.2021.104820.

Williams, H. A., P. G. Betts, Laurent Ailleres, and Andrew Burtt. 2010. “Characterization of a Proposed Palaeoproterozoic Suture in the Crust beneath the Curnamona Province, Australia.” *Tectonophysics* 485 (1–4): 122–40.

Williams, I.R., and Leon Bagas. 1999. *Geology of the Throssell 1:100 000 Sheet:* 1:100 000 Geological Series Explanatory Notes. Western Australia Geological Survey.

Wilson, Alan J., Nick Lisowiec, Cameron Switzer, Anthony C. Harris, Robert A. Creaser, and C. Mark Fanning. 2020. “Chapter 11: The Telfer Gold-Copper Deposit, Paterson Province, Western Australia.” In *Geology of the World’s Major Gold Deposits and Provinces*, edited by Richard H. Sillitoe, Richard J. Goldfarb, François Robert, and Stuart F. Simmons, vol. 23. Society of Economic Geologists.

Wyborn, L. A. I., C. A. Heinrich, and A. L. Jaques. 1994. “Australian Proterozoic Mineral Systems: Essential Ingredients and Mappable Criteria.” In *Proceedings of the 1994 AusIMM Annual Conference, Darwin, August 1994*, edited by C. P. Hallenstein. Publication Series, no. 5/94. Australasian Institute of Mining and Metallurgy. https://www.ausimm.com/publications/conference-proceedings/1994-auslmm-annual-conference-darwin-august-1994/.

Xie, Xiangyang, and Paul L. Heller. 2009. “Plate Tectonics and Basin Subsidence History.” *Geological Society of America Bulletin* 121 (1–2): 55–64.

Yuan, Huaiyu, Reza Ebrahimi, Ruth Murdie, et al. 2024. “Geological Survey of Western Australia: Programme Updates.” *Preview* 2024 (230): 23–26. https://doi.org/10.1080/14432471.2024.2395639.

Zhang, Chengcheng, Christopher A. Scholz, and Ashley D. Harris. 2020. “Sedimentary Fills and Sensitivity Analysis of Deep Lacustrine Facies in Multi-Segment Rift Basins: Insights from 3D Forward Modeling.” *Sedimentary Geology* 408 (October): 105753. https://doi.org/10.1016/j.sedgeo.2020.105753.

Zhang, Y., P. M. Schaubs, C. Zhao, A. Ord, B. E. Hobbs, and A. C. Barnicoat. 2008. “Fault-Related Dilation, Permeability Enhancement, Fluid Flow and Mineral Precipitation Patterns: Numerical Models.” *Geological Society, London, Special Publications* 299 (1): 239–55. https://doi.org/10.1144/SP299.15.

Appendix 1 Project outputs

Results from this work have been submitted as journal publications, presented at conferences, and/or provided as digital products.

A1.1 Journal publications

- Poulet, T., Sheldon, H. A., Zuchuat, V., and Schmid, S., “Small Dip, Big Impact: How 1-Degree Strata Inclination affects Density-Driven Flow in Anisotropic Rocks”, Geology, https://doi.org/10.1130/G53888.1
- Parui, C., Schmid, S., Spampinato, G., McFarlane, H., Zuchuat, V., Gessner, K., Sheldon, H. A., and Poulet, T. “Linking basin evolution to sedimentary-hosted copper systems: Insights from the Neoproterozoic Yeneena Basin, Australia”. Submitted for publication in Precambrian Research.

A1.2 Conference presentations

- Poulet, T., Sheldon, H. A., Zuchuat, V., and Schmid, S., “Buoyancy flow in anisotropic saturated rocks: theory, numerical benchmark and application to mineralising brines”, Australasian Exploration Geoscience Conference 2025, Perth, Australia, accepted for a talk.
- Zuchuat, V., Poulet, T., and Shepherd, J. “Something from nothing: where and how much apparent cyclicity appears out of autogenic processes”. International Sedimentological Congress ISC 2026, Wellington, New Zealand, accepted for a talk.
- Zuchuat, V., Parui, C., Sampinato, G., Poulet, T., Sheldon, H.A., and Schmid, S. "Restore, fill, inject. How we derisk mineral exploration in a deformed and data-deprived basin – Example from the Tonian-aged Yeneena Basin, Western Australia”. International Sedimentological Congress ISC 2026, Wellington, New Zealand, accepted for a poster.
- Zuchuat, V., Poulet, T., and Shepherd, J. “Spatial distribution of allogenic artifacts in sedimentary basins: how apparent cyclicity can appear out of autogenic processes?” Australasian Exploration Geoscience Conference 2025, Perth, Australia, accepted for a talk.
- Parui, C., Schmid, S., and Spampinato, G. “Unraveling the structural evolution of the Yeneena basin hosting Cu deposits: Preliminary results”. In: European Society for Deformation Mechanisms, Rheology and Tectonics; 09 to end of 11 Jul 2024; Barcelona, Spain. csiro; 2024. 101. csiro:EP2024-1374. http://hdl.handle.net/102.100.100/636330?index=1
- Parui, C., Schmid, S., Spampinato, G., McFarlane, H., and Zuchuat, V. “Structural reconstruction of the Yeneena Basin, Western Australia – a key for understanding sedimentary-hosted copper mineralization”. In: Specialist Group in Tectonics and Structural Geology (SGTSG) Biennial Meeting; 18 to end of 22 Nov 2024; Armidale,

New England. csiro; 2024. 110. csiro:EP2024-4218. http://hdl.handle.net/102.100.100/658846?index=1

- Parui, C., Schmid, S., Spampinato, G., McFarlane, H., and Zuchuat, V. “Structural reconstruction of sedimentary basins: A critical step to understand sediment-hosted Cu deposits”. In: Australasian Exploration Geoscience Conference; 08 to end of 11 Sep 2025; Perth. csiro; 2025. 2p.. csiro:EP2025-0943. http://hdl.handle.net/102.100.100/709883?index=1
- Parui, C., Schmid, S., Spampinato, G., McFarlane, H., and Zuchuat, V. “Basin reconstruction and dissecting vein population: Implications for exploration of sedimentary-hosted copper deposits”. Society of Economic Geologists (SEG) conference 2025

A1.3 Digital products

- Line objects representing previously mapped and newly mapped structures are included in the ArcGIS project folder and consist of map package file, geodatabase, rasters and shapefiles.
- The Yeneena depth to basement surface is included in the GOCAD project, Geoscience Analyst project, and also delivered as DXF Files.
- VTK files generated from the stratigraphic forward model software DionisosFlow.
- Badlands inputs as XML file.
- Python script to generate grids from palaeogeographical maps.
- Single spot analyses used for geochronology (Excel).

Appendix 2 Geophysics

A2.1 Data import

The following datasets were imported into the 3D modelling software SKUA-GOCAD for an integrated analysis and interpretation:

- Digital Elevation Model (DEM), sourced from Geoscience Australia's portal GADDS.
- Total magnetic intensity and complete spherical cap Bouguer anomaly (CSCBA) grids sourced from Geoscience Australia's portal GADDS.
- 1:500 000 interpreted bedrock geology of Western Australia sourced from the GSWA database.
- 1:100 000 state interpreted bedrock geology of Western Australia, partially covering the area of interest, sourced from the GSWA database.
- Interpreted L211 18GA-KB1 seismic transect (Doublier et al. 2020).
- AEM data, conductivity sections and depth slices (source: Geoscience Australia; Roach et al., 2010).
- Mineral occurrences and major deposits sourced from the GSWA database.
- 3D model of the Yeneena Basin (Dalmaso Spode 2020) and the Paterson 3D model of the Cottesloe Syncline region (Meixner et al. 2006).

A2.2 Data preparation for structural interpretation

The initial phase of this research focused on the structural interpretation of the area of interest. Faults often align with distinct aeromagnetic lineaments or are associated with steep gradients as well as truncation or offset of geophysical markers, (Betts et al. 2024). Such correlations can assist in extending mapped structures beneath cover or revealing previously unidentified structures undercover (Aitken and Betts 2009; Betts et al. 2004; G. P. Spampinato et al. 2015; G. P. T. Spampinato et al. 2015; Williams et al. 2010). Faults can also be identified through offsets in near-surface conductive layers, abrupt changes in layer thickness, or the juxtaposition of electrically conductive and resistive layers in the AEM dataset (Spampinato 2025). Faults identified through seismic interpretation may also correspond to prominent gravity and/or magnetic anomalies (Doublier et al. 2020). This integrated methodology aids in tracing the subsurface continuity of known structures, identifying unmapped faults and shear zones and constraining fault geometry and dip (Aitken and Betts 2009; Betts et al. 2003; G. P. Spampinato et al. 2015; G. P. T. Spampinato et al. 2015; Williams et al. 2010).

The TMI and CSCBA grids were imported and processed to assist in structural interpretation. Firstly, the TMI grid was reduced to the pole (RTP) in order to remove the effect of the inclined magnetic field on the anomaly shapes and centre anomalies over their source bodies. Then a series of filters have been applied to the RTP and CSCBA grids, which include the first vertical derivative, analytic signal, total horizontal derivative and tilt derivative filters, to enhance the geophysical signal at different crustal levels (Table 14).

The resulting grids, along with the shapefiles representing previously mapped and newly mapped structures are included in the ArcGIS project (see example in figures below).

Table 14: Major filters used in geophysical processing and their effect on the filtered grid. Sourced from Spampinato (2015).

Filter	***Description***	***Used for***
Reduction to the pole	Magnetic data are recalculated as if the inducing magnetic field was vertical	Centering the anomalies over their source bodies
Band-pass	Retains or reject a range of wavenumber from the spectrum	Preserving the geophysical signal at different crustal levels
Low-pass	Retains long wavelengths, low frequencies	Enhancing the signal of deeply buried source bodies
Hi-pass	Retains short wavelength, high frequencies	Enhancing the signal of shallow source bodies
Butterworth	Retains or reject a range of wavenumber from the spectrum	Preserving the signal at different crustal levels; by controlling the degree of roll-off ringing (Gibb's phenomena) can be avoided.
Downward Continuation	Brings the plane of measurement closer to the source	Enhancing the response from shallow source bodies. Use of high pass filter is recommended in order to avoid noise.
Upward Continuation	Brings the plane of measurement farther to the source	Minimising the geophysical response of shallower source bodies
Vertical Derivative	Calculates the vertical rate of change in the magnetic signal	Enhancing shallow anomalies, enhancing the shape of source bodies.
Tilt Derivative	Calculates the ratio of the vertical gradient and the total horizontal gradient irrespective of the amplitude or wavelength of the geophysical anomalies	Improving vertical contacts between the source bodies; improving the geophysical response of weak anomalies.

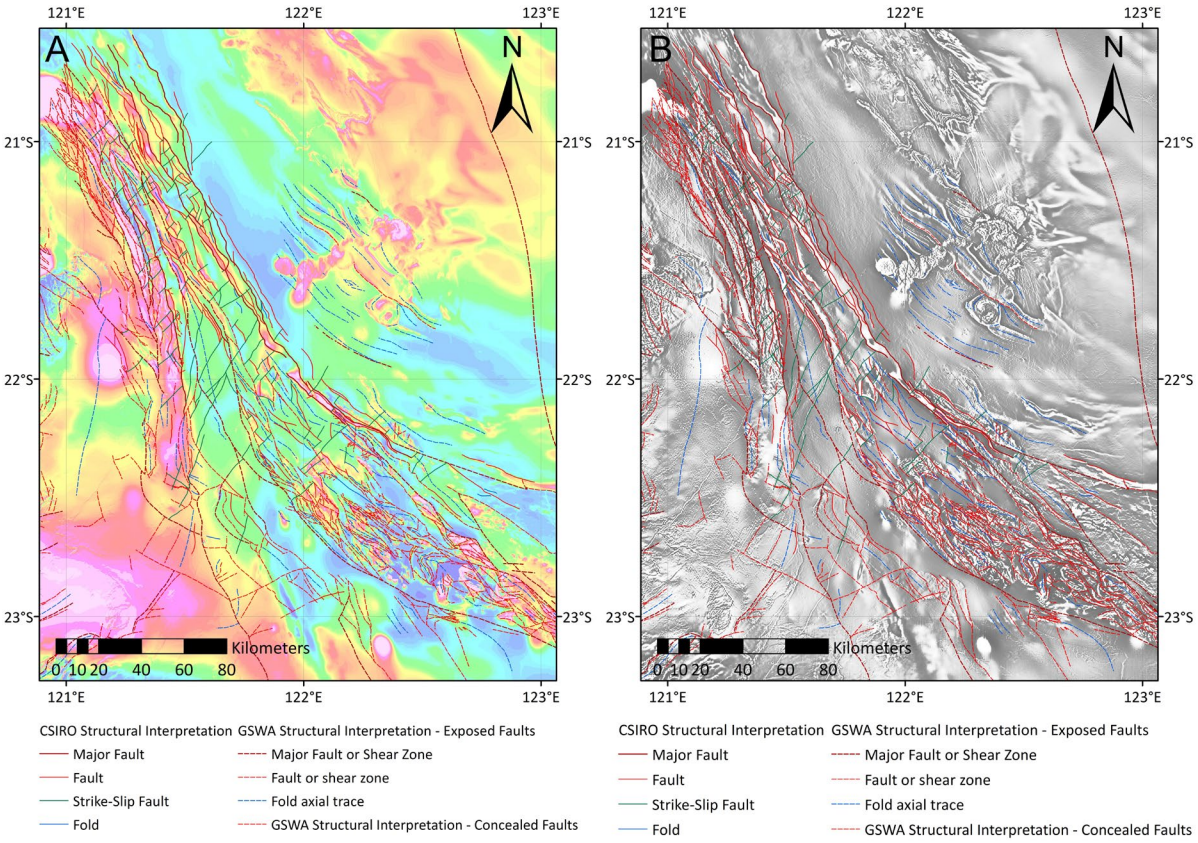

Figure 56: CSIRO and GSWA structural interpretation of the Yeneena Basin over an (A) RTP and (B) RTP-1VD grid of the magnetic anomalies.

A2.3 Estimated depth to the top of the magnetic sources

Depth estimation of the magnetic sources was conducted using the spectral analysis method. This estimation technique relies on anomaly curvature to derive source depth and provide a rough estimate of the depth to the top of magnetic source bodies (Behnam and Ramazi 2019; Fedi and Mastro 2018; Hahn et al. 1976; Kelemework et al. 2021; Naidu 1972; Spector and Grant 1970).

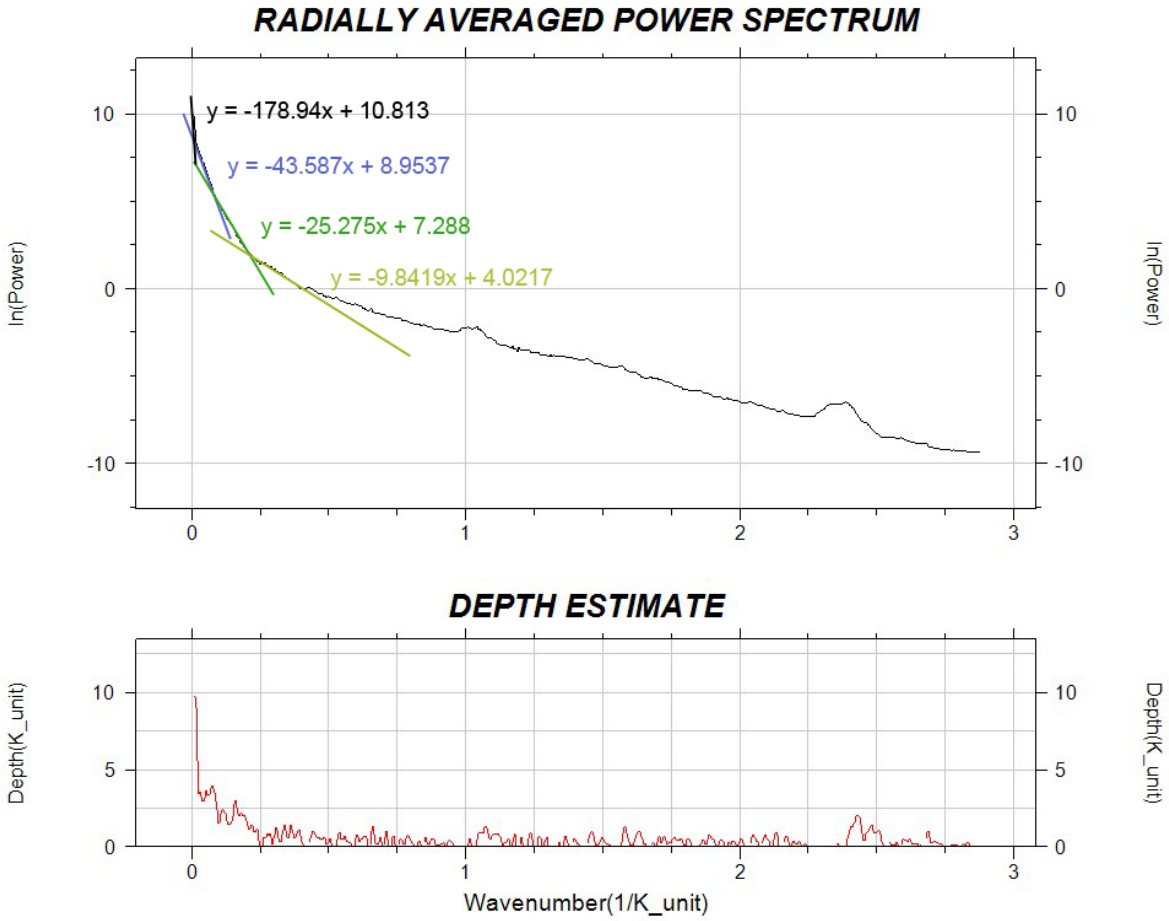

Figure 57: Power Spectrum and automatic depth estimation for the area of study. The spectral analysis highlights three main slope breaks, which might correspond to ensembles of sources at different depths. These ensembles of magnetic sources are located at approximately 7 km, 2.5 km, and 800 m below the surface.

A2.4 Unconstrained magnetic Inversion

Unconstrained 3D magnetic inversion of the region of interest was also performed to estimate the distribution and depth of magnetised units. Unconstrained geophysical inversion involves generating a best-fit model solely based on mathematical constraints, without incorporating external geological or structural information (Spampinato 2025). This computational process produces a model that satisfies the geophysical dataset alone (Fullagar and Pears 2007). During each iteration, model parameters are adjusted to minimize the misfit between the observed and calculated fields.

For this study, the inversion tool used was Mira Geoscience VP Geophysics Suite VPmg™. The magnetic dataset used in this study was the merged Total Magnetic Intensity (TMI) dataset grid of Australia (2019 – 7th edition, 80 m cell size), obtained from the Geoscience Australia GADDS portal.

Once the inverted model was produced, 3D regions having an arbitrary minimum susceptibility value were also created, to aid visualisation of magnetisation distribution (Figure 58B). 3D magnetic inversion is a useful first-pass tool for identifying the distribution of magnetised source bodies despite its inherent limitations which includes non-uniqueness and the potential influence of both induced and remanent magnetization (Elllis et al. 2012;

Fullagar and Pears 2015; 2007; Lelièvre and Oldenburg 2009; Li and Oldenburg 1996; Spampinato 2025; Vallée et al. 2019).

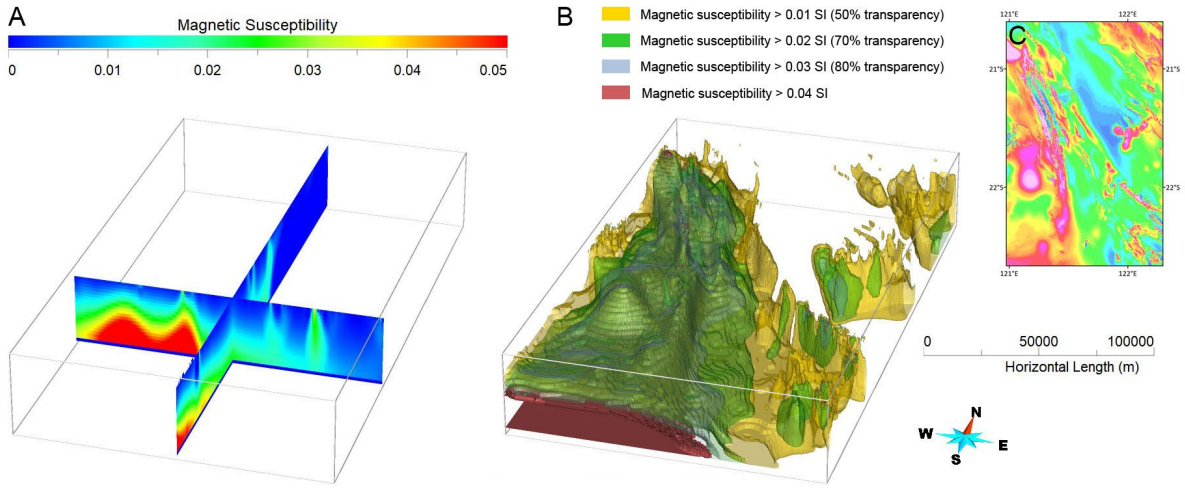

Figure 58: A) Inverted model for the region of interest; B) isosurfaces extracted from the inverted model showing different minimum magnetic susceptibilities; C) location end extension of the inverted model.

Appendix 3 Geochronology

A3.1 Apatite U-Pb

A3.1.1 EPT 2192 266.52

Eleven U-Pb analyses on 11 apatite grains were obtained in sample EPT 2192 266.52 out of which 9 were obtained on matrix apatite and 2 were obtained on vein apatite (*Figure* 59). Ten out of 11 analyses define a regression with a lower intercept age of 1182 ± 26 Ma and a common $^{207}Pb/^{206}Pb_c$ ratio of 1.07 ± 0.02 (MSWD = 1.7, n = 10; *Figure* 60). One analysis obtained on vein apatite is a statistical outlier to this regression, indicating a lower common $^{207}Pb/^{206}Pb_c$ ratio. This outlier analysis is interpreted to be isotopically disturbed, and thus, was not considered in the calculation of the age. The apatite age of 1182 ± 26 Ma defined by the remainder of the analyses is interpreted as the time of cooling below 350-500°C in a detrital component, which is conventionally considered to be the average closure temperature of Pb diffusion in apatite (Chew and Spikings 2015).

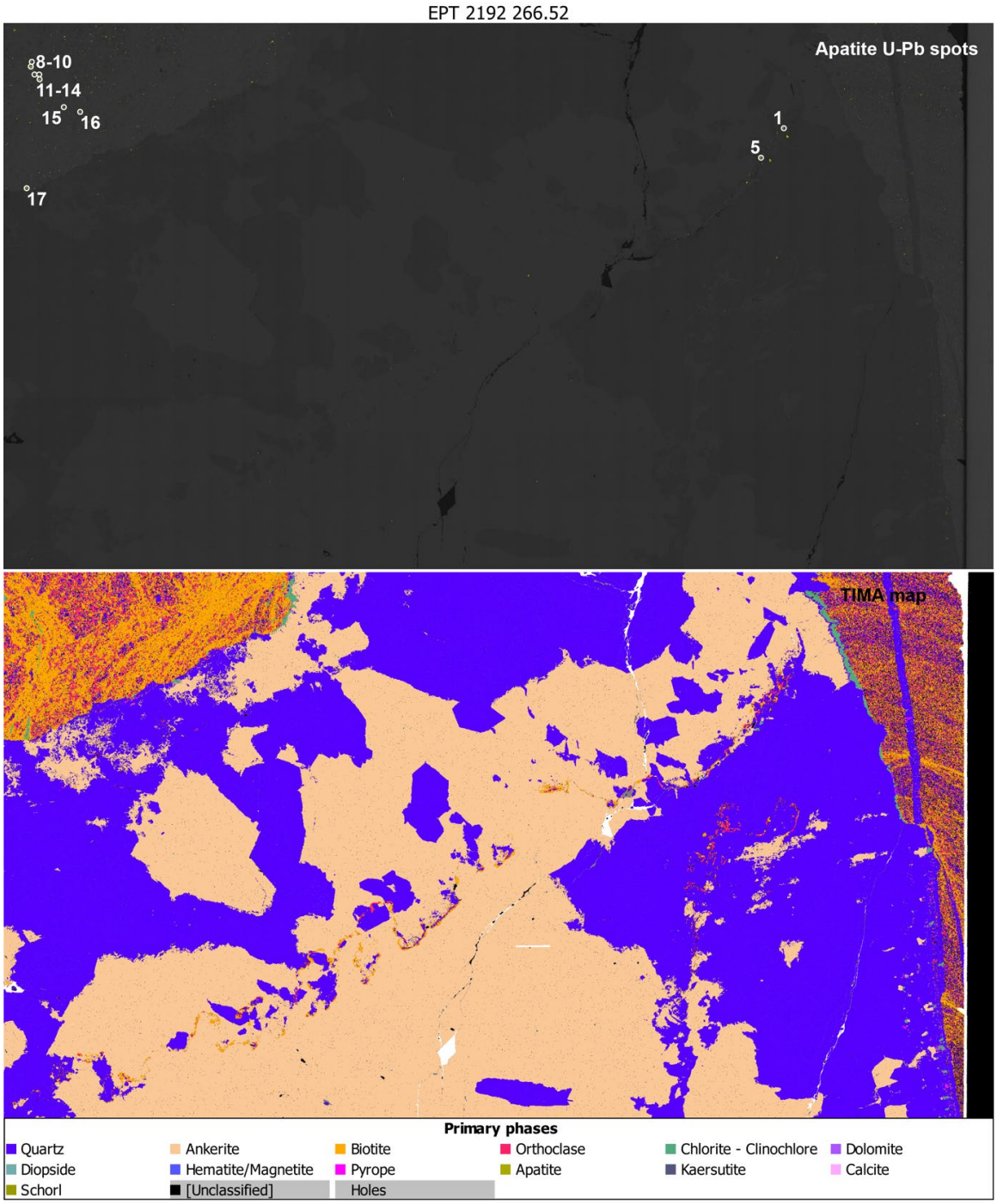

Figure 59. BSE image with apatite highlighted in green (top) and mineral phase map (bottom) of sample EPT 2192 266.52. The spot locations of apatite U-Pb analyses are not to scale.

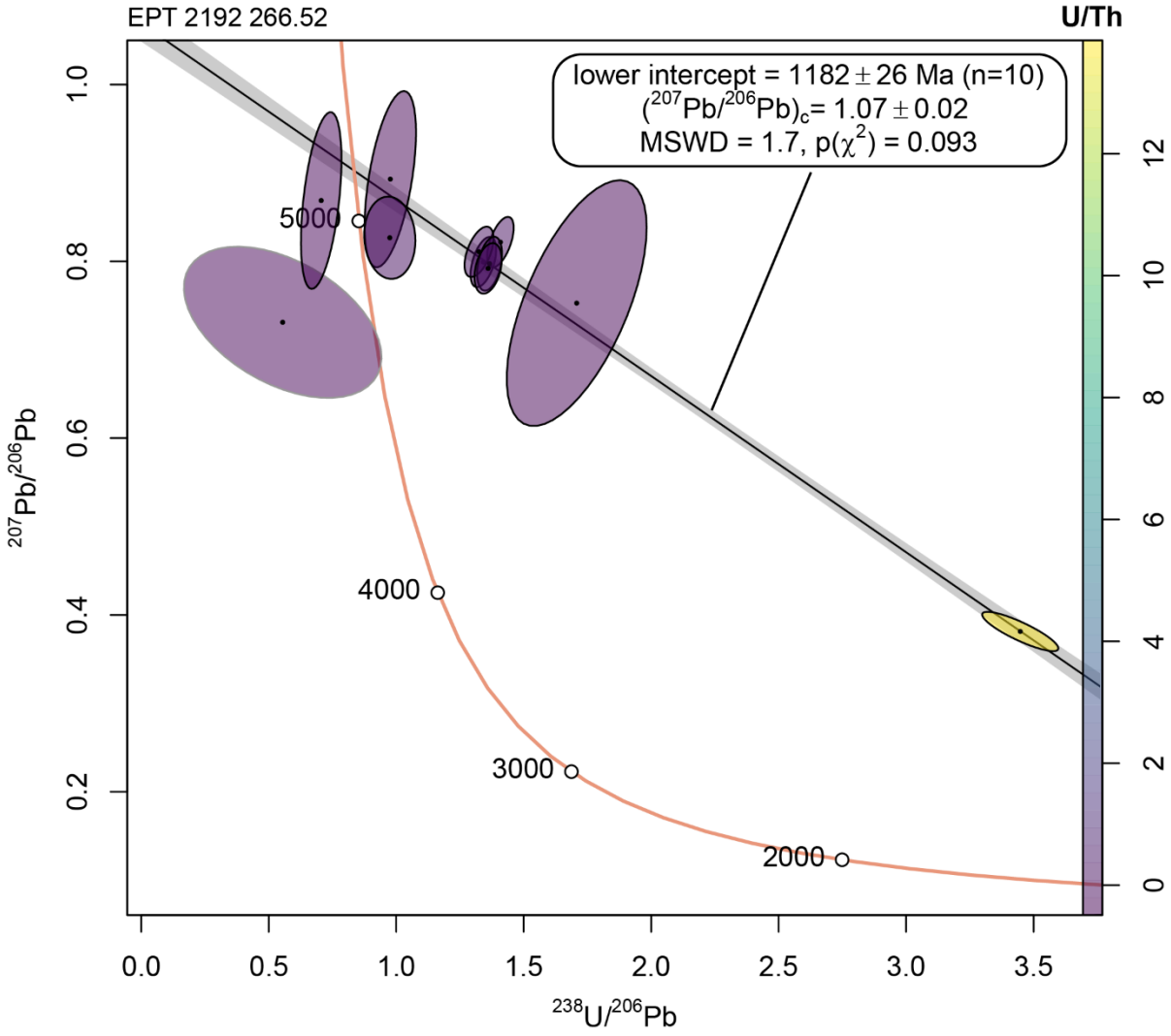

Figure 60. Tera-Wasserburg plot of apatite U-Pb results in sample EPT 2192 266.52 color-coded by U/Th ratio. Error ellipses are shown at the 2σ level. Ellipses with black outline define the regression used in the determination of the intercept age. The regression is shown as black line with grey 95% confidence envelope. The age is quoted as x ± y, where x is the maximum likelihood estimate of the age, y is the analytical uncertainty at 95% confidence level. The ellipse with grey outline is a statistical outlier is not considered in the regression.

A3.1.2 EPT 2192 269.23

Sixteen U-Pb analyses on 16 matrix apatite grains were obtained in sample EPT 2192 269.23 (*Figure* 61). Two broad regressions are defined by the data: 13 analyses are consistent with a regression with a lower intercept age of 1083 ± 168 Ma and a common $^{207}Pb/^{206}Pb_c$ ratio of 0.86 ± 0.03 (MSWD = 1.5, n = 13); 12 analyses are consistent with a regression with a lower intercept age of 684 ± 58 Ma and a common $^{207}Pb/^{206}Pb_c$ ratio of 0.82 ± 0.02 (MSWD = 1.1, n = 12; *Figure* 62). Due to the similar common $^{207}Pb/^{206}Pb_c$ ratios of both age components, a clear differentiation into two groups is only possible for the more radiogenic analyses with $^{238}U/^{206}Pb \geq 2$. One analysis that is a statistical outlier with respect to both regressions is interpreted to be isotopically disturbed, and therefore, not considered in either regression. The two apatite age components at 1083 ± 168 Ma and 684 ± 58 Ma are interpreted to reflect the time of cooling below 350-500°C, which is conventionally considered to be the average closure temperature of Pb diffusion in apatite (Chew and

Spikings 2015). The older age is interpreted to be from a detrital component, whereas the younger as is likely related to the post-depositional history of this sample.

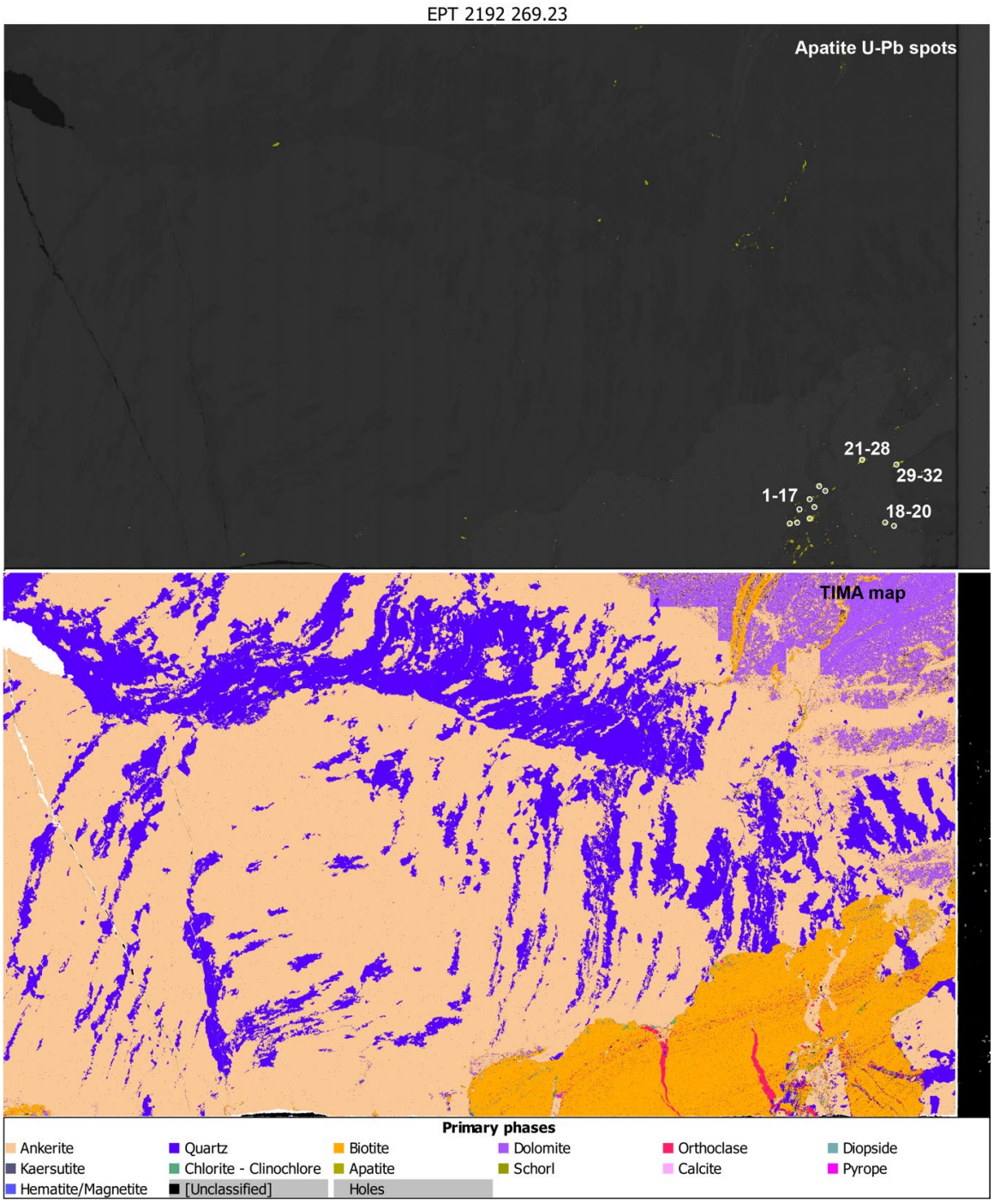

Figure 61. BSE image with apatite highlighted in green (top) and mineral phase map (bottom) of sample EPT 2192 269.23. The spot locations of apatite U-Pb analyses are not to scale.

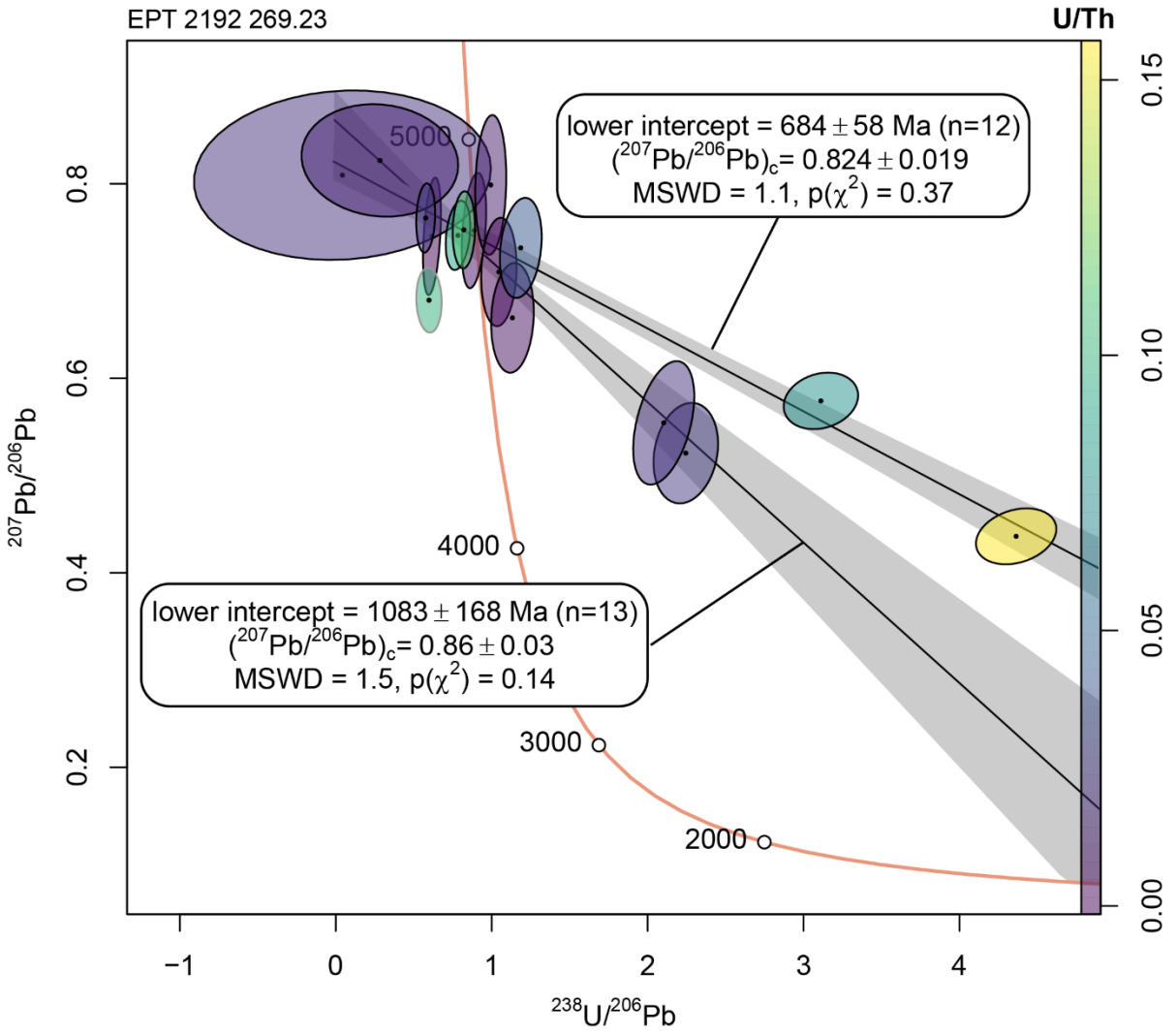

Figure 62. Tera-Wasserburg plot of apatite U-Pb results in sample EPT 2192 269.23 color-coded by U/Th ratio. Error ellipses are shown at the 2σ level. Ellipses with black outline define the two regressions used in the determination of the intercept age. The regressions are shown as black line with grey 95% confidence envelope. The age is quoted as x ± y, where x is the maximum likelihood estimate of the age, y is the analytical uncertainty at 95% confidence level. The ellipse with grey outline is a statistical outlier and is not considered in the regressions.

A3.1.3 EPT 2193 184.71

Fourteen U-Pb analyses on 14 vein apatite grains were obtained in sample EPT 2193 184.71 (*Figure* 63). Two broad regressions are defined by the data: Nine analyses define a regression with a lower intercept age of 1015 ± 232 Ma and a common $^{207}Pb/^{206}Pb_c$ ratio of 0.94 ± 0.03 (MSWD = 1.8, n = 9); ten analyses define a regression with a lower intercept age of 215 ± 41 Ma and a common $^{207}Pb/^{206}Pb_c$ ratio of 0.86 ± 0.01 (MSWD = 1.9, n = 10; *Figure* 64). A clear differentiation into two age components is only possible for the more radiogenic analyses with $^{238}U/^{206}Pb \geq 1.5$. Two analyses that are statistical outliers to both regressions, are interpreted to be isotopically disturbed or derive from an isotopically distinct detrital component and are not considered in either regression. The apatite ages of 1015 ± 232 Ma and 215 ± 41 Ma are interpreted as the time of cooling below 350-500°C, which is conventionally considered to be the average closure temperature of Pb diffusion in apatite

(Chew and Spikings 2015). The older age is interpreted to be from a detrital component, whereas the younger as is likely related to the post-depositional history of this sample.

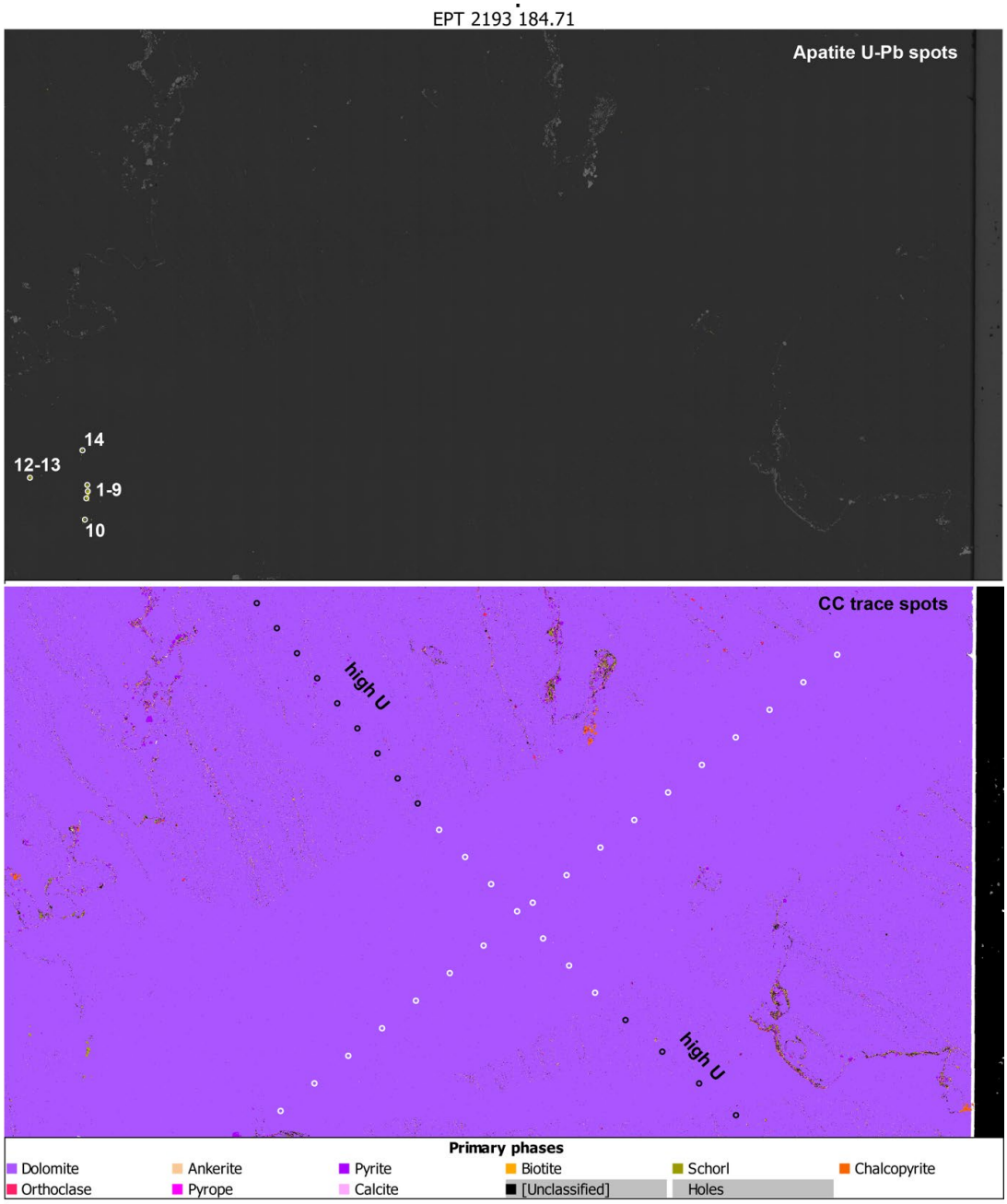

Figure 63. BSE image with apatite highlighted in green (top) and mineral phase map (bottom) of sample EPT 2193 184.71. The spot locations of apatite U-Pb analyses are not to scale. The mineral phase map highlights areas with carbonate U concentration above the limit of detection, which were targeted for carbonate U-Pb analysis.

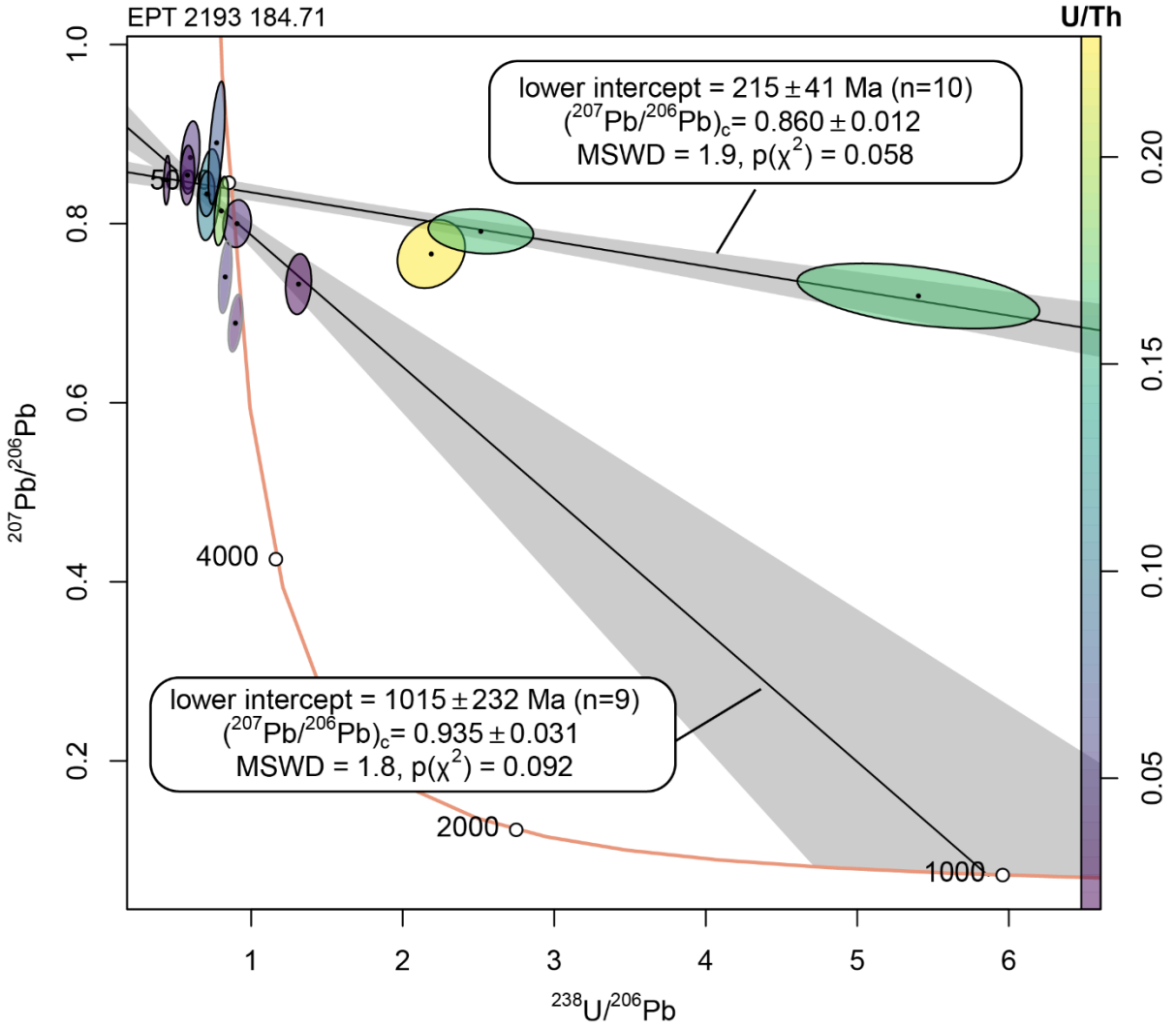

Figure 64. Tera-Wasserburg plot of apatite U-Pb results in sample EPT 2193 184.71 color-coded by U/Th ratio. Error ellipses are shown at the 2σ level. Ellipses with black outline define the regression used in the determination of the intercept age. The regression is shown as black line with grey 95% confidence envelope. The age is quoted as x ± y, where x is the maximum likelihood estimate of the age, y is the analytical uncertainty at 95% confidence level. The ellipses with grey outline are statistical outliers and are not considered in the regressions.

A3.1.4 EPT 2193 305.40

Ten U-Pb analyses were performed on 10 apatite grains. These apatite analyses were associated with feldspar and biotite dominated veins (*Figure* 65). Eight out of 10 analyses define a regression with a lower intercept age of c. 526 Ma and a common $^{207}Pb/^{206}Pb_c$ ratio of 0.838 (MSWD = 10, n = 8; *Figure* 66). This common-radiogenic mixing line shows scatter greater than analytical uncertainties alone and fails to include two analyses, such results clearly point to additional geological complexity in this sample, which, based on the distribution of data could reflect more recent recrystallization process and / or mixtures with other phases (e.g., accounting for the higher uncertainty in some of the analyses). The apatite age of c. 526 Ma is interpreted as the best estimate time of cooling below 350-500°C, for at least a component of these grains, which is conventionally considered to be the average closure temperature of Pb diffusion in apatite (Chew and Spikings 2015).

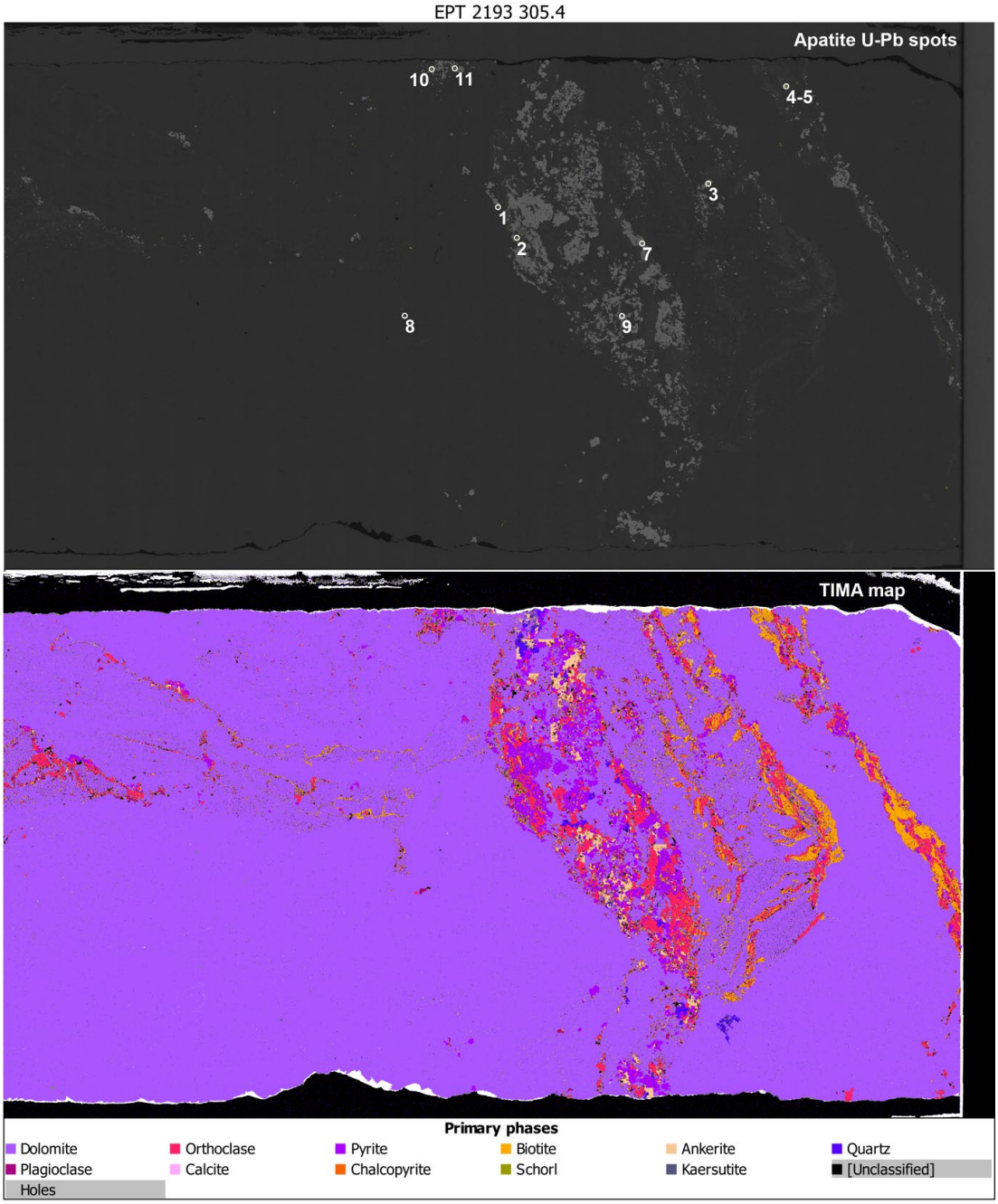

Figure 65. BSE image with apatite highlighted in green (top) and mineral phase map (bottom) of sample EPT 2193 305.40. The spot locations of apatite U-Pb analyses are not to scale.

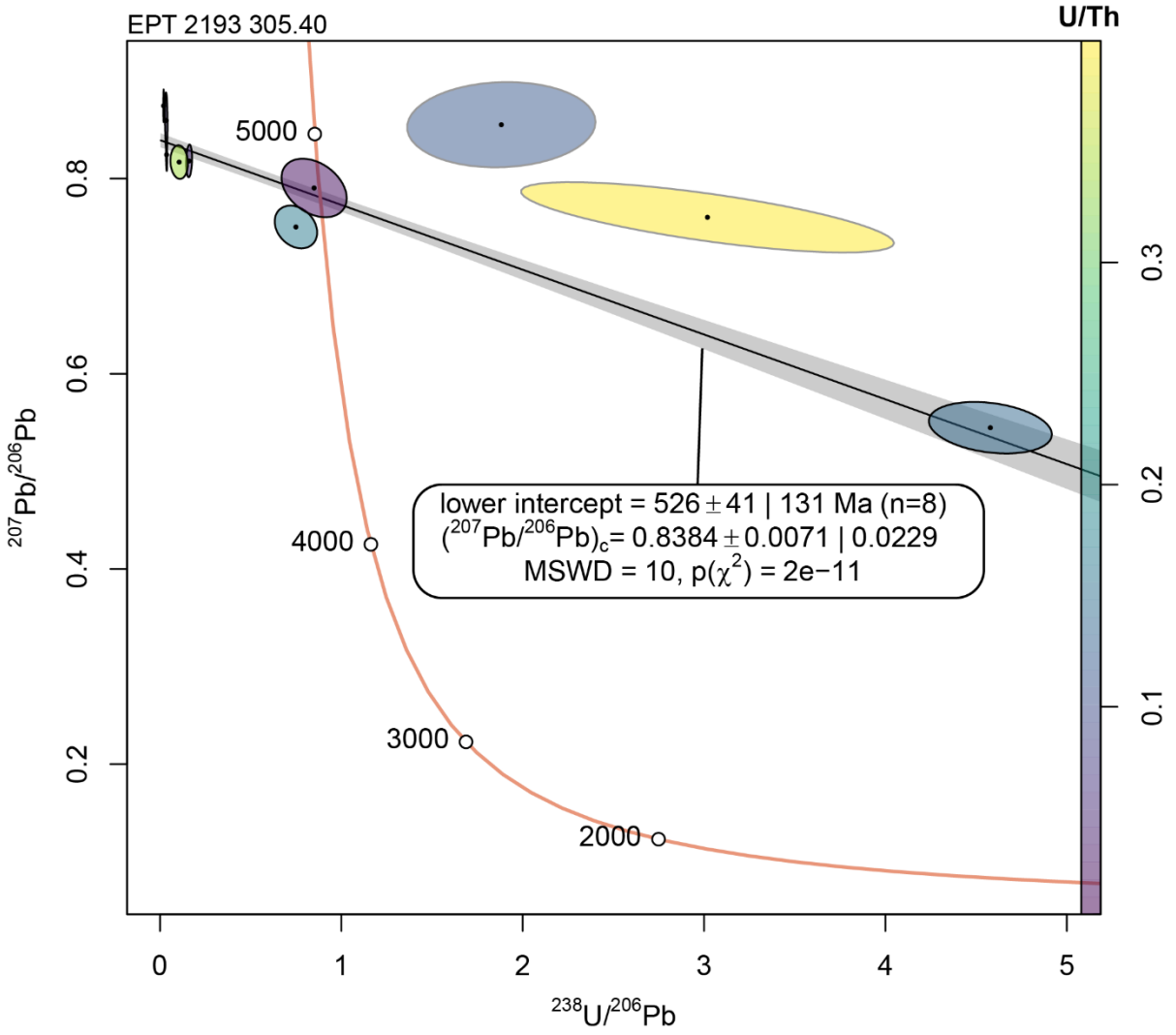

Figure 66. Tera-Wasserburg plot of apatite U-Pb results in sample EPT 2193 305.40 color-coded by U/Th ratio. Error ellipses are shown at the 2σ level. Ellipses with black outline define the regression used in the determination of the intercept age. The regression is shown as black line with grey 95% confidence envelope. The age is quoted as x ± y, where x is the maximum likelihood estimate of the age, y is the analytical uncertainty at 95% confidence level. The ellipses with grey outline are statistical outliers and are not considered in the regression.

A3.1.5 EPT 2280A 385.85

Fifteen U-Pb analyses on 15 apatite grains were obtained in this sample. Analyses were obtained in both vein and matrix domains (Figure 67). Eleven out of 15 analyses define a regression with a lower intercept age of c. 1051 Ma and a common $^{207}Pb/^{206}Pb_c$ ratio of 0.862 (MSWD = 4.9, n = 11; Figure 66). The distribution of all analyses appears colinear with this regression, interpreted to approximate a mixing line between common and radiogenic Pb components. The apatite age of c. 1051 Ma defined by the 11 analyses is interpreted as the average time of cooling below 350-500°C, conventionally considered to be the average closure temperature of Pb diffusion in apatite (Chew and Spikings 2015).

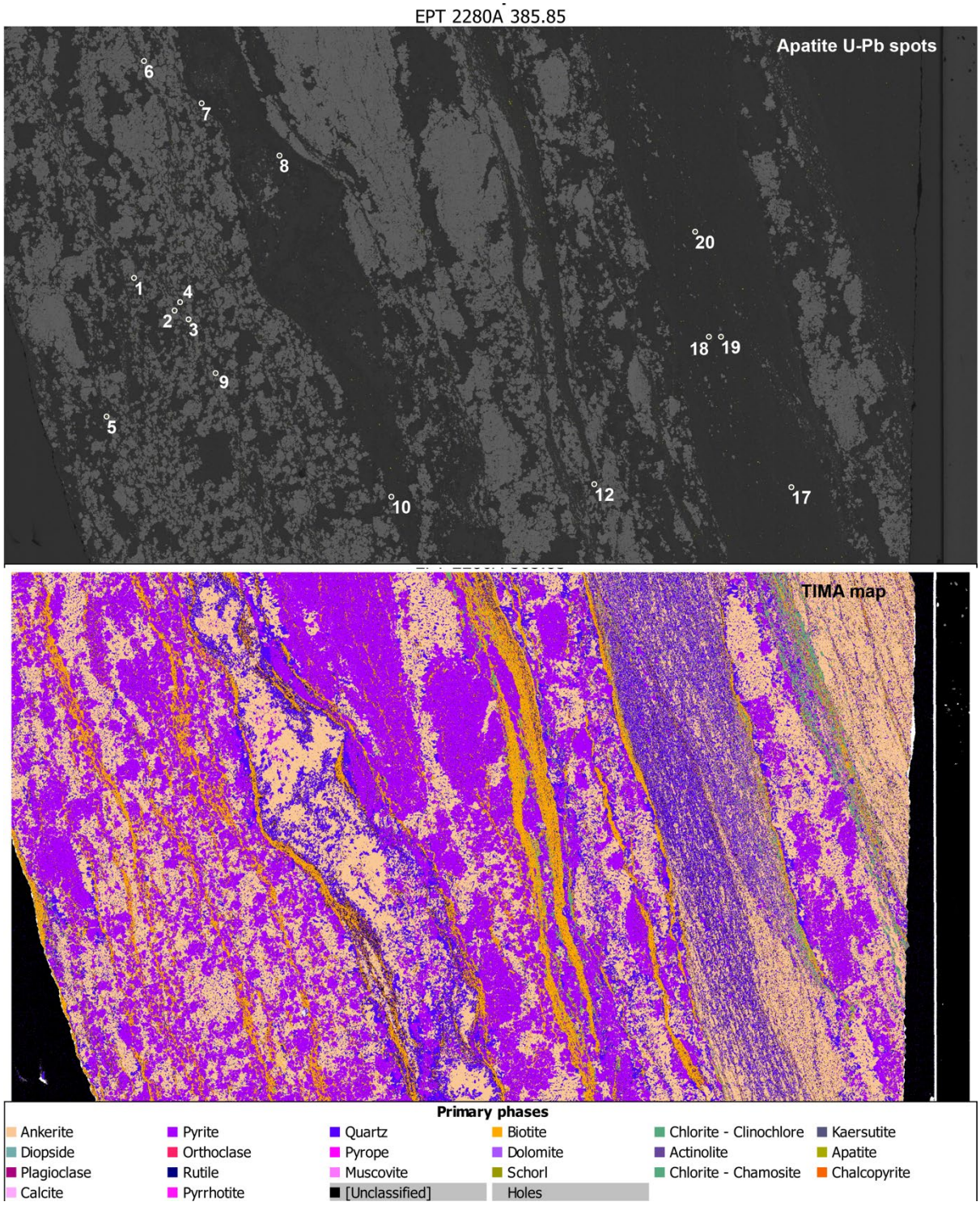

Figure 67: BSE image with apatite highlighted in green (top) and mineral phase map (bottom) of sample EPT 2280A 385.85. The spot locations of apatite U-Pb analyses are not to scale.

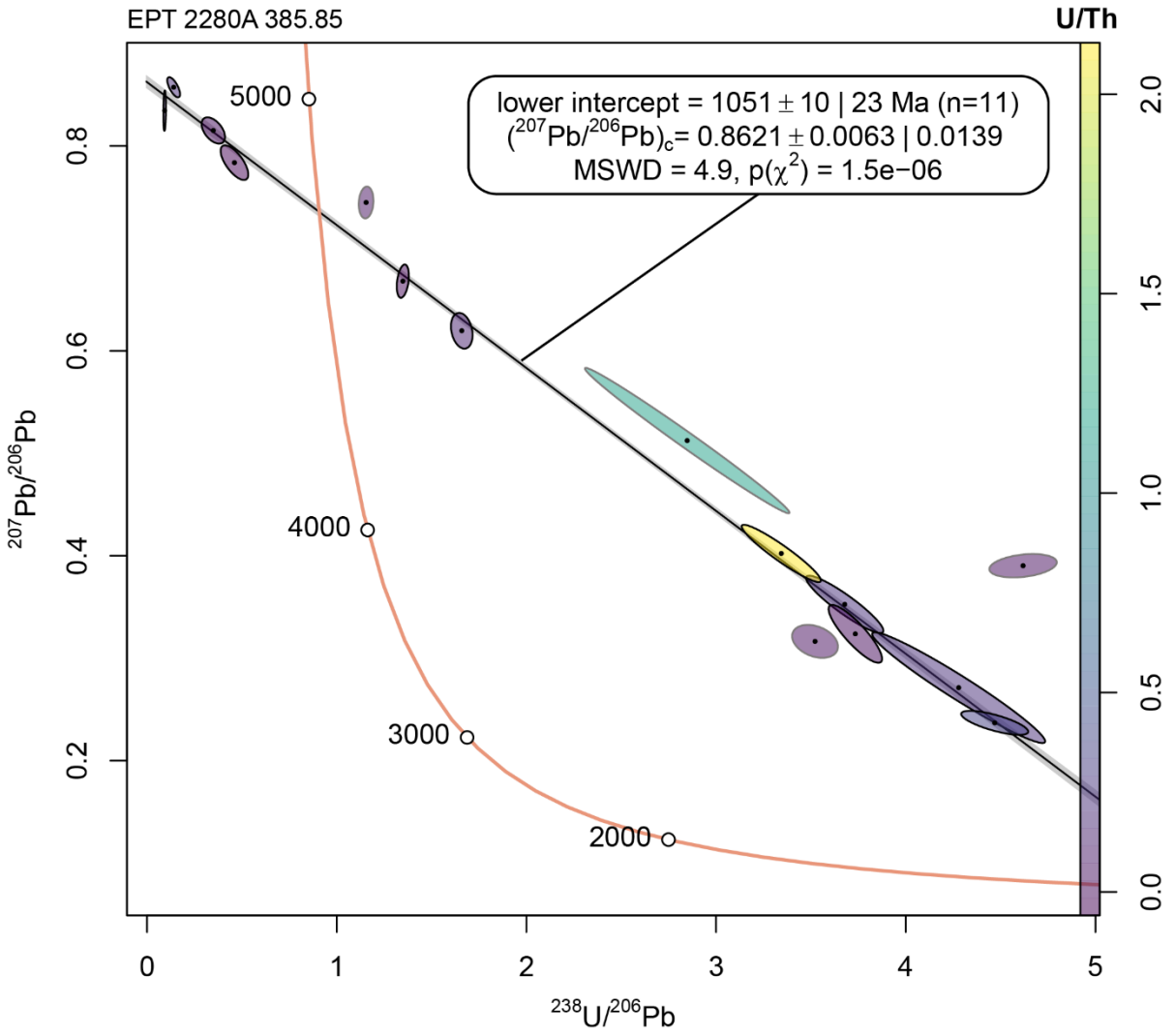

Figure 68: Tera-Wasserburg plot of apatite U-Pb results in sample EPT 2280A 385.85 color-coded by U/Th ratio. Error ellipses are shown at the 2σ level. Ellipses with black outline define the regression used in the determination of the intercept age. The regression is shown as black line with grey 95% confidence envelope. The age is quoted as x ± y | z, where x is the maximum likelihood estimate of the age, y is the analytical uncertainty at 95% confidence level, and z is the the analytical uncertainty at 95% confidence level multiplied by a factor to accound for overdispersion (see Vermeesch, 2018, for details). The ellipses with grey outline are statistical outliers and are not considered in the regression.

A3.1.6 EPT 2280A 420.95

Five U-Pb analyses on 5 apatite grains were obtained in this sample. All apatite resides within a sheared feldspar dominated vein (Figure 69). The data define two apparent common-radiogenic mixing arrays. Three out of five analyses define a regression with a lower intercept age of 551 ± 40 Ma and a common $^{207}Pb/^{206}Pb_c$ ratio of 0.858 ± 0.023 (MSWD = 0.073, n = 3; Figure 68). A second regression (3 out of 5 analyses) also going through the highest common Pb analyses defines a lower intercept age of 1180 ± 27 Ma and a common $^{207}Pb/^{206}Pb_c$ ratio of 0.889 ± 0.028 (MSWD = 0.097, n = 3; Figure 70). The dissimilar apatite dates of 551 Ma and 1180 Ma may reflect the time of cooling, to their Pb retention temperature, for vein grown and inherited apatite, respectively.

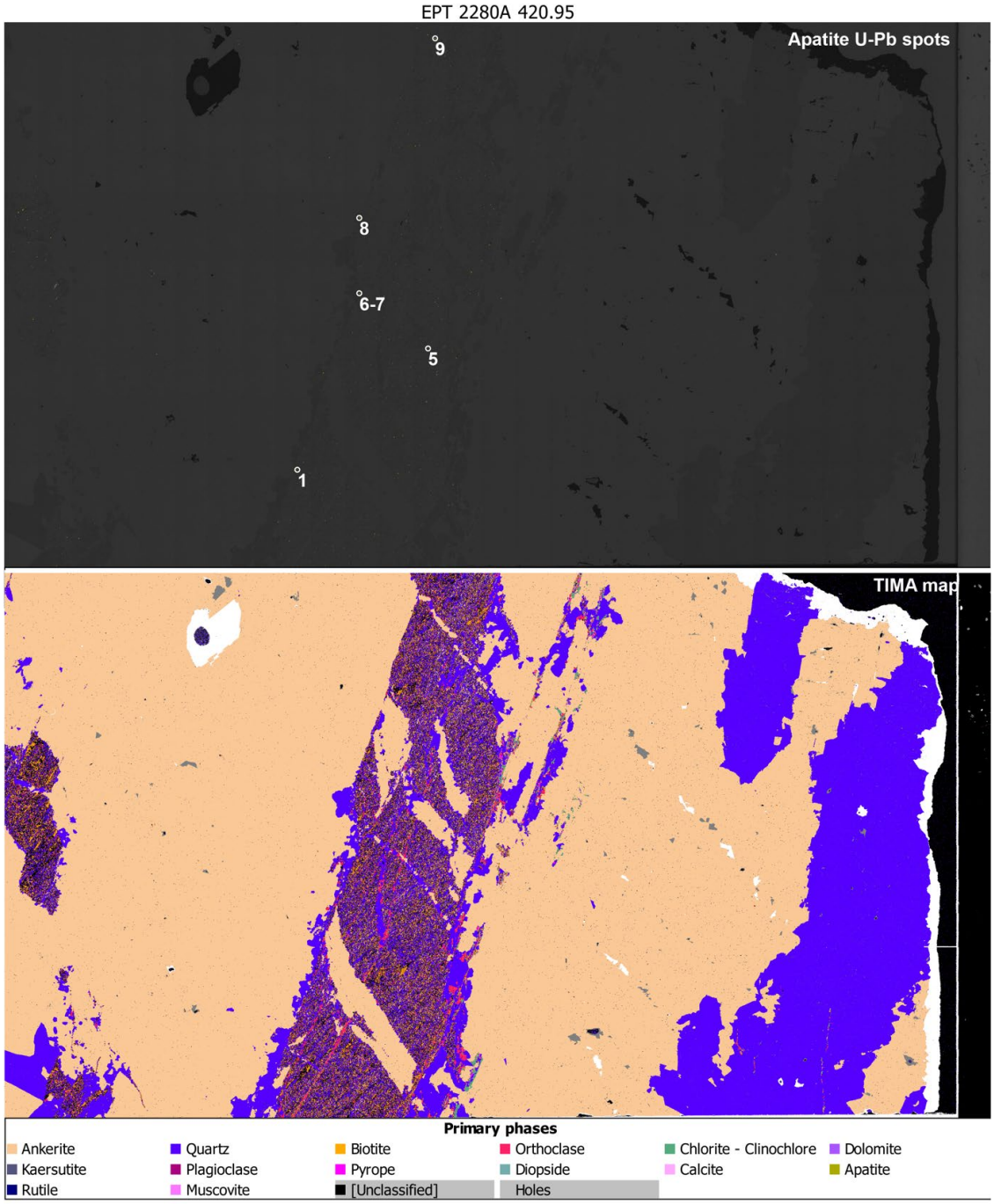

Figure 69: BSE image with apatite highlighted in green (top) and mineral phase map (bottom) of sample EPT 2280A 420.95. The spot locations of apatite U-Pb analyses are not to scale.

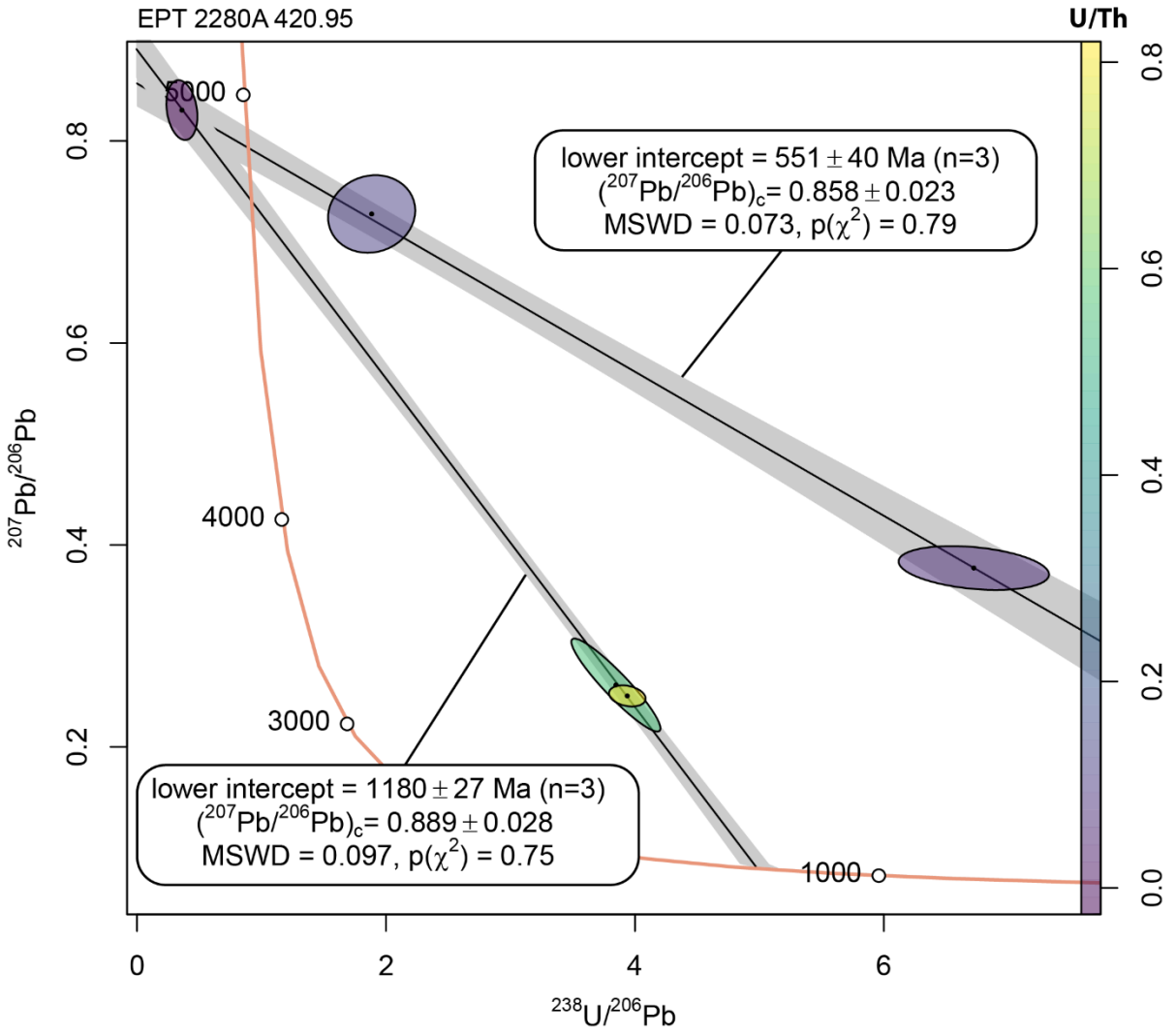

Figure 70: Tera-Wasserburg plot of apatite U-Pb results in sample EPT 2280A 420.95 color-coded by U/Th ratio. Error ellipses are shown at the 2σ level. The regressions are shown as black lines with grey 95% confidence envelopes. The ages are quoted as x ± y, where x is the maximum likelihood estimate of the age, y is the analytical uncertainty at 95% confidence level.

A3.1.7 EPT 2280A 341.47

Twenty-nine U-Pb analyses on 29 apatite grains were obtained in this sample (Figure 71). All analyses were on matrix apatite. The U content in these grains is low and they are dominated by common Pb, hence no meaningful age estimate can be based on radiogenic accumulation. Nonetheless, the common $^{207}Pb/^{206}Pb_c$ for the source fluid growing apatite can be estimated as 0.8508 ± 0.0057 (MSWD = 1.2; using 27 out of 29 analyses with $^{238}U/^{206}Pb$ < 2). Assuming this apatite grew from a normal crustal reservoir consistent with the Pb evolution model of Stacey and Kramers (1975) this would imply a Proterozoic or younger fluid.

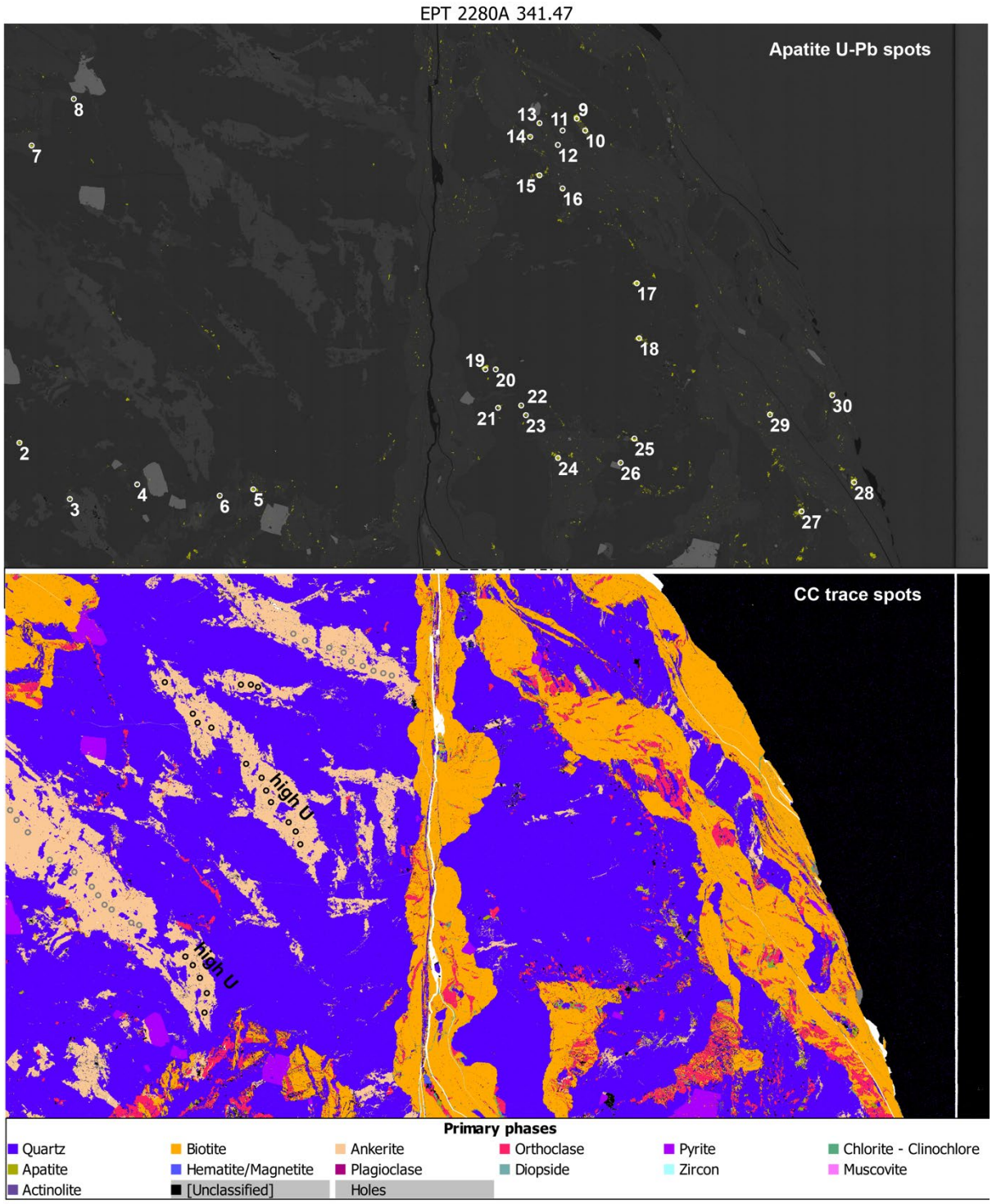

Figure 71: BSE image with apatite highlighted in green (top) and mineral phase map (bottom) of sample EPT 2280A 341.47. The spot locations of apatite U-Pb analyses are not to scale.

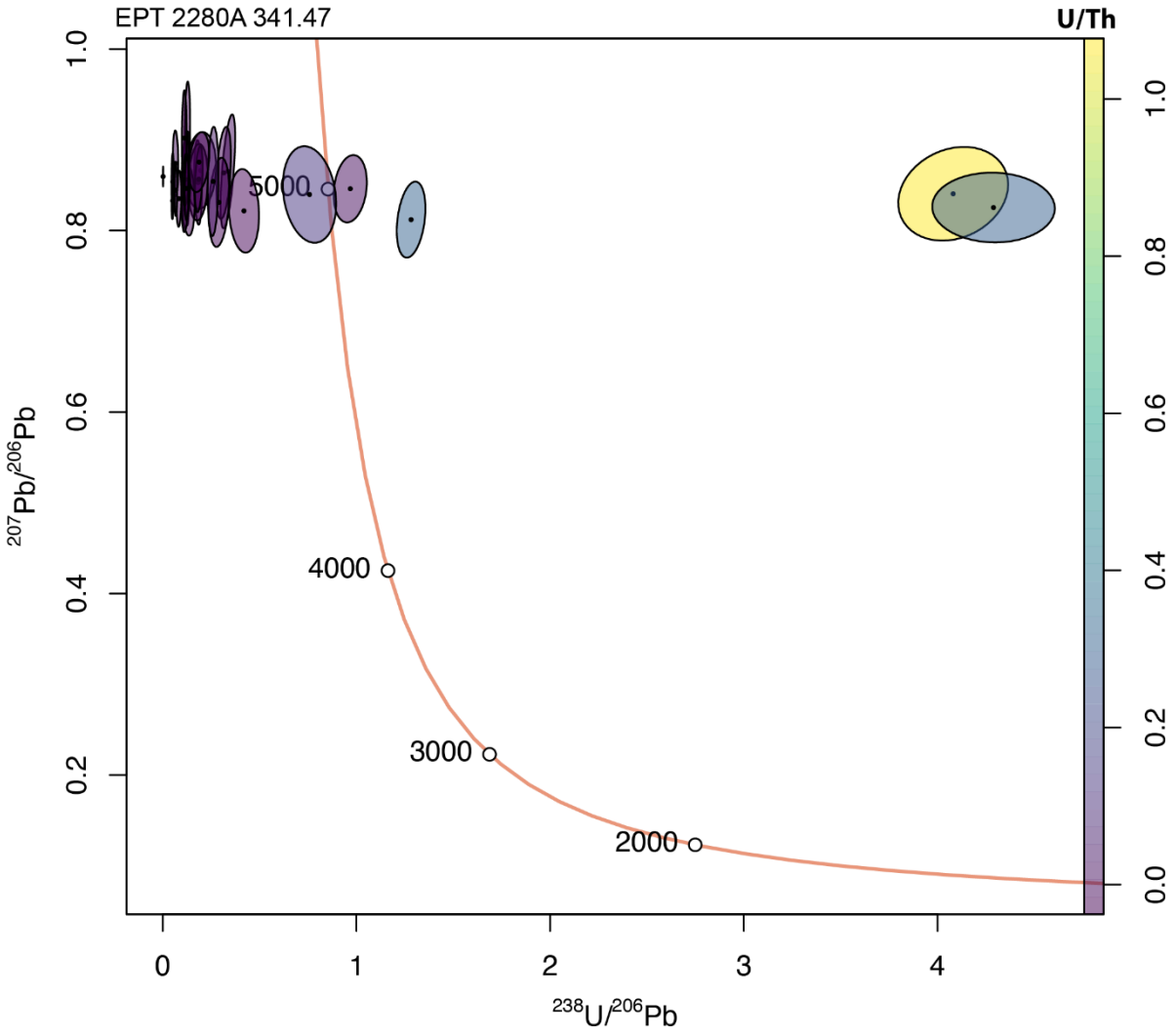

Figure 72: Tera-Wasserburg plot of apatite U-Pb results in sample EPT 2280A 341.47 color-coded by U/Th ratio. Error ellipses are shown at the 2σ level.

A3.1.8 EPT 2280A 265.31

Thirty U-Pb analyses on 30 apatite grains were obtained from this sample. Analyses were obtained in both vein and matrix domains (Figure 73). The U content in these grains is low and they are dominated by common Pb (Figure 74), hence no meaningful age estimate can be based on radiogenic accumulation. Nonetheless, the common $^{207}Pb/^{206}Pb_c$ of the source fluid growing apatite can be estimated and appears to yield a heterogeneous distribution stretching from 0.90 to 0.78, in low U apatite. Such variable common Pb implies that the apatite does not reflect a single growth component.

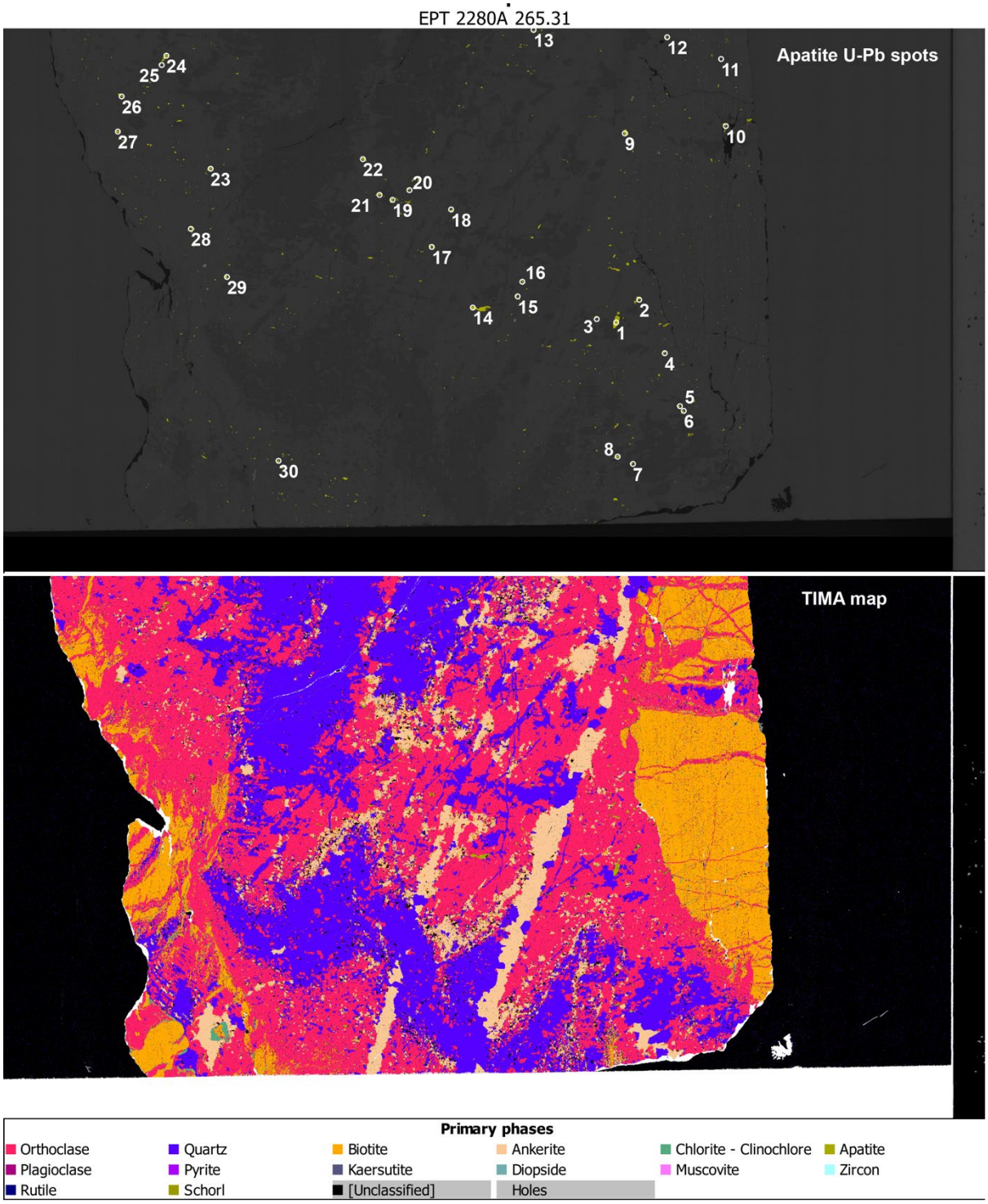

Figure 73: BSE image with apatite highlighted in green (top) and mineral phase map (bottom) of sample EPT 2280A 265.31. The spot locations of apatite U-Pb analyses are not to scale.

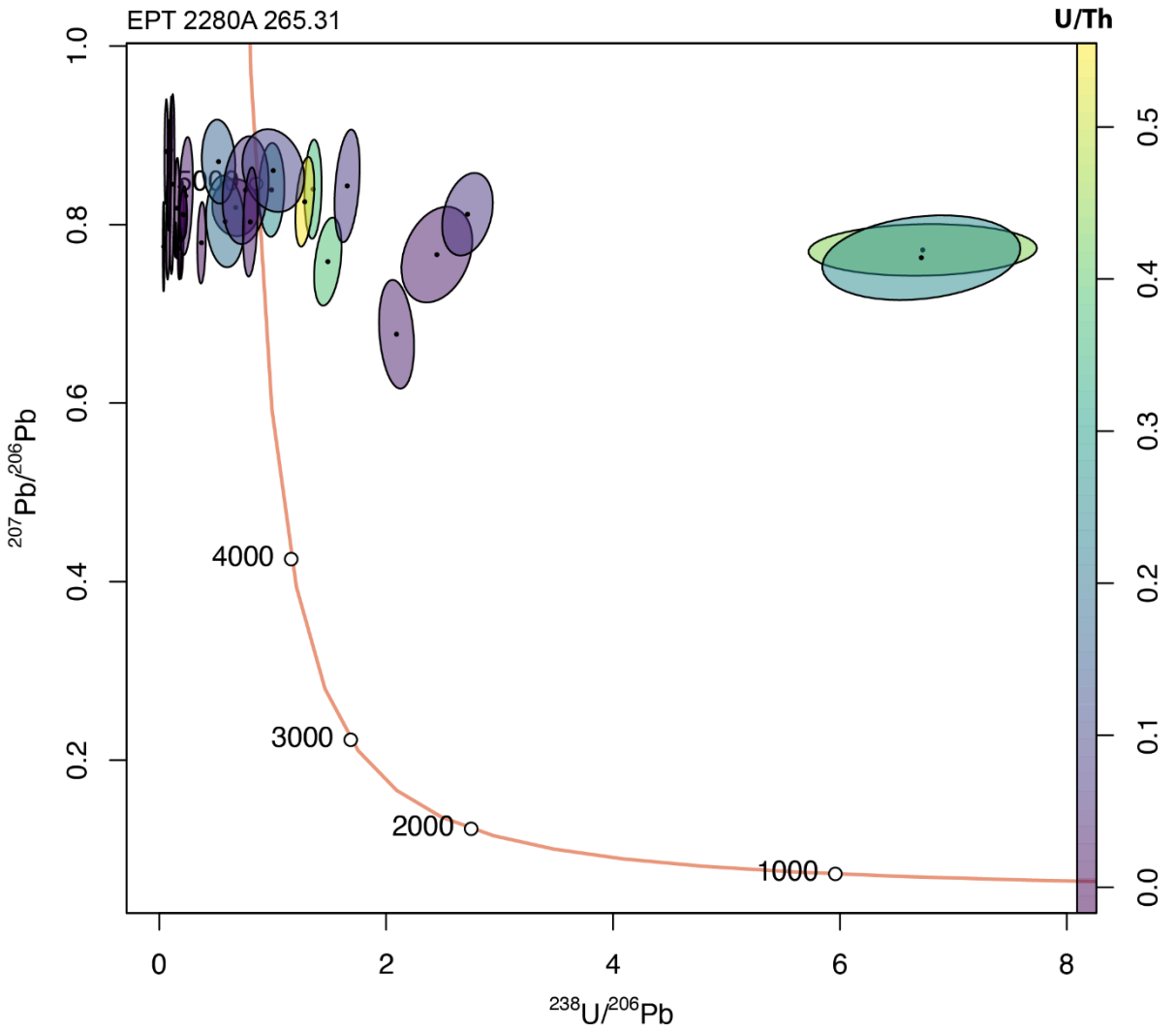

Figure 74: Tera-Wasserburg plot of apatite U-Pb results in sample EPT 2280A 265.31 color-coded by U/Th ratio. Error ellipses are shown at the 2σ level.

A3.2 Carbonate U-Pb

A3.2.1 EPT 2193 184.71

Carbonate in EPT 2193 184.71 was analysed in situ on thin section. Forty-six U-Pb analyses were performed and scatter along a well-defined common-radiogenic mixing line. Four analyses are statistical outliers, as may be caused by ablation of inclusions, fractures, or other within run heterogeneity and are excluded from further consideration. The remaining 44 analyses yield a lower intercept age of 927 ± 33 Ma (n=42/46, MSWD = 7) with an upper intercept implying an initial $^{207}Pb/^{206}$ of 0.806 ± 0.001. This mixing line shows slight excess dispersion over analytical uncertainties alone and may reflect either or both, minor radiogenic Pb loss, prolonged crystallization or a variable initial Pb reservoir. In any case, the general distribution of data is consistent with the average time of radiogenic Pb accumulation in this sample commencing at c. 930 Ma. The common Pb composition is lower than typical terrestrial Pb evolution models for crust of this age and could imply a lower uranium source region as might be expected for mafic crust. The common Pb component is different to the one recorded by apatite in this sample. Such difference in initial Pb, if

geologically meaningful, would imply the source fluid that calcite and apatite grew from was distinct.

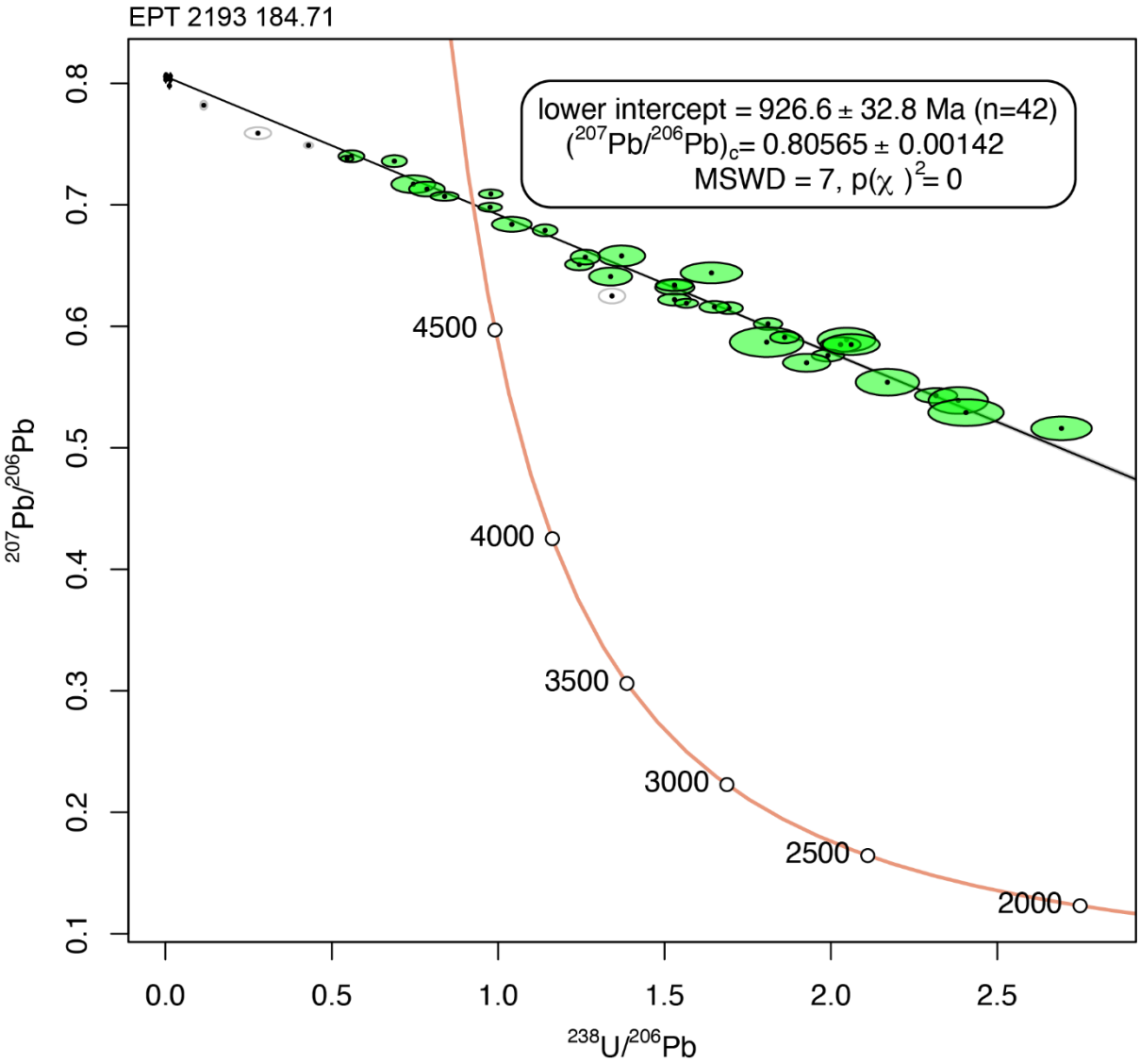

Figure 75: Tera-Wasserburg plot of carbonate U-Pb results in sample EPT 2193 184.71. Error ellipses are shown at the 2σ level. Ellipses with black outline define the regression used in the determination of the intercept age. The regression is shown as black line with grey 95% confidence envelope. The age is quoted as x ± y, where x is the maximum likelihood estimate of the age, y is the analytical uncertainty at 95% confidence level with an additional 3% to account for uncertainty related to matrix correction propagated in quadrature (see text for details). The ellipses with grey outline are statistical outliers and are not considered in regression.

A3.2.2 EPT 2280A 341.47

Carbonate in EPT 22804A 341.47 was analysed in situ on thin section. Fifty U-Pb analyses were performed. All analyses have high to extreme common Pb content with little scatter towards any radiogenic component, meaning that no age can be calculated. Nonetheless, an average common Pb composition can be estimated based on those analyses with lowest U content (15 analyses). A weighted mean of these analyses implies a best estimate initial $^{207}Pb/^{206}Pb$ of c. 0.801. This ratio is similar to calcite in sample EPT 2193 184.71, yet also distinct from apatite in the same sample.

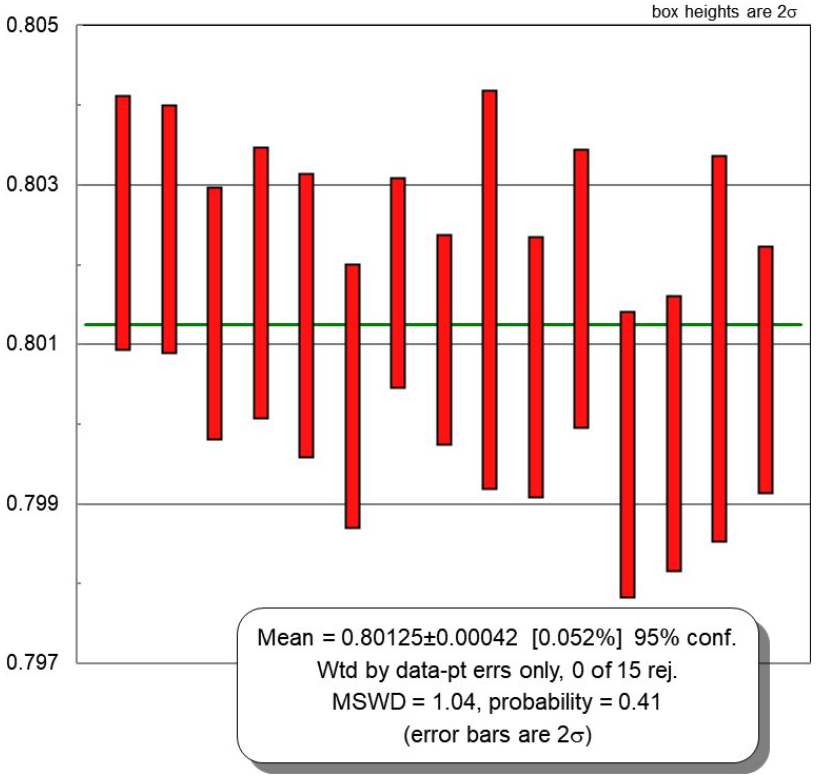

Figure 76: Weighted mean $^{207}Pb/^{206}Pb$ for low uranium calcite in EPT 22804A 341.47. Note this common Pb value implies a source fluid with lower uranium than average crust and is isotopically distinct from the fluid apatite grew in.